WISC

UNIVERSITY OF WISCONSIN • MADISON, WISCONSIN

PLASMA PHYSICS

SPECTROSCOPIC MEASUREMENT OF THE MHD DYNAMO IN THE MST REVERSED FIELD PINCH

RECEIVED
DEC 14 1998
OSTI

James Tharp Chapman

DISTRIBUTION OF THIS DOCUMENT IS UNLIMITED

MASTER

DOE/ER/54345-307

September 1998

NSIN

Printed in the United States of America
Available from
National Technical Information Service
U.S. Department of Commerce
5285 Port Royal Road
Springfield, VA 22161

NTIS Price codes
Printed copy: A07
Microfiche copy: A01

DISCLAIMER

SPECTROSCOPIC MEASUREMENT OF THE MHD DYNAMO
IN THE MST REVERSED FIELD PINCH

by

James Tharp Chapman

A dissertation submitted in partial fulfillment of the
requirements for the degree of

Doctor of Philosophy
(Physics)

at the

University of Wisconsin–Madison

1998

SPECTROSCOPIC MEASUREMENT OF THE MHD DYNAMO IN THE MST REVERSED FIELD PINCH

James Tharp Chapman

Under the supervision of Professor Stewart C. Prager

At the University of Wisconsin–Madison

Abstract

We have directly observed the coupling of ion velocity fluctuations and magnetic field fluctuations to produce an MHD dynamo electric field in the interior of the MST reversed field pinch. Chord averaged ion velocity fluctuations were measured with a fast spectroscopic diagnostic which collects line radiation from intrinsic carbon impurities simultaneously along two lines of sight. The chords employed for our measurements resolved long wavelength velocity fluctuations of several km/s at 8–20 kHz as tiny, fast Doppler shifts in the emitted line profile. During discrete dynamo events the velocity fluctuations, like the magnetic fluctuations, increase dramatically. The toroidal and poloidal chords with impact parameters of $0.3\,a$ and $0.6\,a$ respectively, resolved fluctuation wavenumbers with resonance surfaces near or along the lines of sight indicating a radial velocity fluctuation width for each mode which spans only a fraction of the plasma radius. The phase between the measured toroidal velocity fluctuations and the magnetic fluctuations matches the predictions of resistive MHD while the poloidal velocity fluctuations exhibit a phase consistent with the superposition of MHD effects and the advection of a mean flow gradient past the poloidal line of sight. Radial velocity fluctuations resolved by a chord through the center of the plasma were small compared to the poloidal and toroidal fluctuations and exhibited low coherence with the magnetic fluctuations. The ensembled nonlinear product of the ion velocity fluctuations and fluctuations in the magnetic field indicates a substantial dynamo electric field which peaks during the periods of spontaneous flux generation. During these periods our measurements indicate poloidal dynamo field of 14±7 Volts/m near the plasma core in the direction to generate toroidal flux and a small toroidal dynamo field in the edge region of 1.0±0.3 Volts/m in the direction to drive parallel current. While the absolute magnitudes of the observed dynamo fields are consistent with estimates from equilibrium modeling, discrepancies which remain indicate the need for additional dynamo measurements to demonstrate the numerical balance of parallel Ohm's law by a dynamo electric field the the reversed field pinch.

Acknowledgments

Through the course of my graduate studies I have been supported by the faculty, staff and students of the MST group. I acknowledge below the contributions of those who have enabled the work presented in this thesis and enriched the environment in which it was produced.

Prof. Prager helped me extract interesting physics from the tangled web of diagnostic, analysis, and computational issues and provided a careful reading and editing of this thesis. Dan Den Hartog brought me into this group six years ago by requesting an National Undergraduate Fellow and has since provided mentoring in the careful techniques of experimental physics, willing consideration of research results and plans, opportunities to present work in papers and talks, flexibility in responding to personal requests, and a remarkable diagnostic described in some detail in Chapter 2 of this thesis. The rest of the MST faculty and scientific staff has never failed to open their doors to my questions and ideas: John Sarff helped iron out the technical minutiae of mode analysis and equilibrium modeling; Abdul Almagri provided his magnetic probe, good humor, and skills as a butcher; Gennady Fiksel offered creative experimental ideas many of which actually worked; and Prof. Cary Forest provided a fresh critical perspective which induced some reworking and some rethinking and ultimately contributed to a better piece of research.

The MST technical and engineering staff have been unselfish with their time and expertise: Tom Lovell, Mark Thomas, and Steve Oliva gave assistance back when I was building stuff and/or putting stuff on the machine; John Laufenberg answered the phone on the weekends when we couldn't figure out what was wrong with the MST; Bill Zimmerman, Tom Krajewski, Doug Drescher, and Mikhail Reyfman helped me find the little things I was always looking for; and Roch Kendrick proofread my drawings so they would become neither a source of amusement nor a cause of annoyance in the machine shop. The volume data analysis involved in my research occasionally taxed the computational resources and possibly the patience of Larry Smith and Paul Wilhite although both maintained their sense of humor and appeased me (finally!) with a really nice computer. Dale Schutte got the orders out on time when I purchased several times my personal net worth in parts from Digi-Key and Newark. Kay Shatrawka graciously helped me get through the details and postpone the days work a few minutes with conversation over coffee.

The MST graduate students and post-docs provided a fantastic work and social environment. They include: Jay Anderson, who killed my Frankenstein and conquered the world from Australia; Ted Biewer, my partner in crime through the S-scale run; Brett Chapman, who withstood my repeated attempts to log into his VAX account; (Lt.) Ching-Shih Chiang, the nicest guy to ever violate MST vacuum protocol; Darren Craig, who demonstrates the potential we all might have if we only applied ourselves; Neal Crocker, a Ph.D. physicist for the new millennium; Eduardo Fernandez, a rare instance of a theoretician with sweet moves on the court; Paul Fontana, the last man in the midwest who generates actual laughter through the use of puns; Alex Hansen, who publicly embraced my public codes; Nick Lanier, my office mate, political foil and confidant in all matters MST; Kevin Mirus, who demonstrated, in plain sight, how to write a Ph.D. thesis while maintaining a sense of humor; Carl Sovinec who politely answered my MHD simulation questions from remote desert regions; Matt Stoneking who figured out many useful things and wrote them neatly in a notebook; and John Wright who came just in time to run DEBS for me. I will be lucky to work again with a set of comparably congenial and supportive peers.

I am blessed with a remarkable and supportive family which has always encouraged my genetically inexplicable pursuit of physics. My Mom and Dad bought me science books as a kid because I seemed to read them and listened carefully later on when I tried to explain my research. I could rely on their excitement and praise at times of success and their concern and support at times of stress. Finally, Lizzie dated me before I took my first college physics course, was my partner through the eight years of undergraduate and graduate work that followe, and married me in time to support and encourage me in the final stages of my thesis research.

This work was supported by the U.S. Department of Energy.

Contents

List of Tables

List of Figures

1

Introduction

We have directly measured the coupling of fluctuations in the ion flow and magnetic field in the MST Reversed-Field Pinch (RFP) consistent with an MHD dynamo electric field in the core and edge regions of the plasma. The MHD dynamo mechanism has long been proposed to explain the maintenance of the resistively unstable RFP equilibrium field by balancing parallel Ohm's Law as,

$$\langle E\rangle_{\|} + \langle \tilde{\mathbf{v}} \times \tilde{\mathbf{b}}\rangle_{\|} = \eta\langle J\rangle_{\|}, \tag{1.1}$$

where $\tilde{\mathbf{v}}$ and $\tilde{\mathbf{b}}$ are fluctuations in the fluid flow and magnetic field, respectively, $\langle\ \rangle$ indicates a flux surface average, and ($\|$) subscript indicates alignment with the mean magnetic field. MHD simulations and recent edge measurements in several RFP's have corroborated this hypothesis observing substantial dynamo fields in agreement with Eq. 1.1. Our measurements, conducted with a fast spectroscopic diagnostic, give further evidence for the existence of the $\langle \tilde{\mathbf{v}} \times \tilde{\mathbf{b}}\rangle$ dynamo, providing the first direct experimental observation of components of the $\langle \tilde{\mathbf{v}} \times \tilde{\mathbf{b}}\rangle$ dynamo product in the core region of an RFP. This thesis reports on the methods and results of these measurements.

This introductory chapter seeks to provide the context for our measurements relative to the physics of the dynamo and previous observations. First we review Taylor's model of the RFP equilibrium and demonstrate the imbalance of Eq. 1.1 in this model without the $\langle \tilde{\mathbf{v}} \times \tilde{\mathbf{b}}\rangle$ term. We then describe the dynamo in the strong magnetic field limit relevant to the RFP and relate it to the much-studied, low magnetic field limit of the kinematic dynamo. Next we summarize existing computational and experimental evidence for a $\langle \tilde{\mathbf{v}} \times \tilde{\mathbf{b}}\rangle$ dynamo electric field in the RFP. The introduction concludes with an outline of this thesis which highlights the key novel experimental results which have been obtained.

1.1 RFP Equilibrium and Ohm's Law

In the RFP a dynamo electric field is needed to explain the maintenance of the equilibrium field profiles over the observed time scales. Below we summarize Taylor's theory of plasma relaxation which predicts many features of the RFP equilibrium. We then discuss the $\langle \tilde{\mathbf{v}} \times \tilde{\mathbf{b}}\rangle$ dynamo field necessary to balance Eq. 1.1 for the observed equilibrium fields. For an excellent review of the RFP physics presented briefly here the reader is referred to Chapter 3 of Ortlani and Schnack (1993).

1.1.1 Taylor's Model of Plasma Relaxation

Taylor (1974) conjectured that the magnetic helicity integrated over the entire volume of a turbulent laboratory pinch plasma, K_0, would be conserved,

$$\frac{d}{dt}K_0 = \frac{d}{dt}\int_{V_0} \mathbf{A}\cdot\mathbf{B}\,dV \approx 0. \tag{1.2}$$

From this hypothesis Taylor employed the method of Lagrange multipliers to minimize the magnetic energy of the configuration relative to K_0, yielding the well known "Taylor state",

$$\nabla \times \mathbf{B} = \lambda \mathbf{B}, \tag{1.3}$$

where λ is a constant. In contradiction to Eq. 1.2 for which it may be shown that the global helicity dissapated by the mean currents decays in the same order of η as the global magnetic energy,

$$\frac{dK_0}{dt} = -2\int_{V_0} \frac{\eta}{S}\mathbf{J}\cdot\mathbf{B}\,dV, \tag{1.4}$$

$$\frac{dE}{dt} = -\int_{V_0} \frac{\eta}{S} J^2\,dV. \tag{1.5}$$

However, decay rates should be dominated by dissipation due to fluctuating components which we may approximate by Fourier transforming Eqs. 1.4–1.5 to obtain,

$$\frac{dK_0}{dt} \approx -\frac{2\eta}{S}\sum_k k b_k^2, \tag{1.6}$$

$$\frac{dE}{dt} \approx -\frac{\eta}{S}\sum_k k^2 b_k^2, \tag{1.7}$$

which indicates that high k fluctuations preferentially dissipate energy. A more careful analysis (Bhattacharjee and Hameiri,1986; Boozer, 1986) demonstrates that this conservation holds for the long-wavelength fluctuations which dominate the RFP. In addition, the conservation of helicity relative to magnetic energy has been observed in both numerical simulations and in experiment (Ji, Prager, and Sarff, 1995). Thus, provided that sufficient separation exists between the energy and helicity decay times Taylor's conjecture should be applicable over time scales short compared to the decay times for K_0, during which we would expect the plasma to decay to a state consistent with Eq. 1.3.

1.1.2 Equilibrium Field Profiles

Ultimately the success of Taylor's theory lies in its effective prediction of the observed RFP equilibrium field profiles. Solving for the equilibrium magnetic field configuration consistent with Eq. 1.3 in a periodic cylinder one obtains a cylindrically symmetric Bessel Function Model (BFM) given by,

$$B_\phi = B_0 J_0(\lambda r), \tag{1.8}$$

$$B_\theta = B_0 J_1(\lambda r), \tag{1.9}$$

where J_0 and J_1 are the first and second order Bessel Functions respectively and $\hat{\phi} = \hat{z}$ for a cylinder (Taylor, 1974). The BFM predicts that when a sufficient Volt-seconds are applied to the plasma, λ will increase. J_0 then swings through its first zero at $r < a$ such that B_ϕ reverses direction within the plasma, a signature feature of the RFP equilibrium. The values of λ and B_0 which determine the BFM equilibrium may be related directly to the total toroidal flux and the Volt-seconds applied to the plasma, both of which are controlled by the external circuit. Thus the RFP may be considered a "spontaneous" configuration, arising from the "relaxation" of the plasma into a minimum energy state subject to the constraint of constant global helicity. While fluctuations have been implicated in the dissipation of energy relative to the helicity, the exact mechanism for the relaxation is not addressed by Taylor's theory.

To yield magnetic field profiles which match the equilibrium obtained in experiment, Taylor's model must be modified to allow λ to vary with radius and to include finite pressure gradients (Schoenberg, Gribble, and Phillips, 1982; Sprott, 1988). This yields

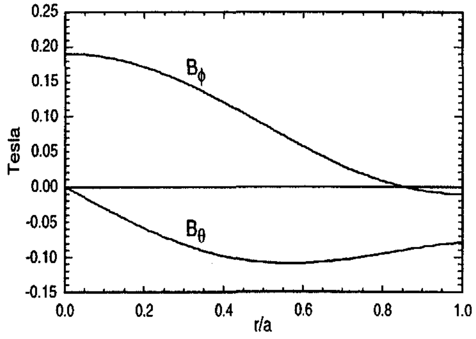

Fig. 1.1.— Magnetic fields modeled from typical MST equilibria assuming a current profile given by a modified Taylor state.

the force balance equation,

$$\nabla \times \mathbf{B} = \lambda(r)\mathbf{B} - \frac{\mu_o \nabla P(r) \times \mathbf{B}}{B^2}, \tag{1.10}$$

which may be fit to the external and global measurements of the magnetic field in experimental discharges (§ 6.1). Fig. 1.1 shows typical magnetic field profiles modeled from Eq. 1.10 for discharge parameters used in this thesis. The key features of this field are poloidal and toroidal fields with comparable peak magnitudes and a toroidal field which reverses direction near the wall. Because the equilibria attained in experiment are not accurately described by Eq. 1.3 we say that they are not fully relaxed into the minimum energy state given by Taylor. Nonetheless, in this thesis we refer to the field profiles which approach a constant $\lambda(r)$ as "relaxed" and describe the relative flattening of $\lambda(r)$ as a relaxation.

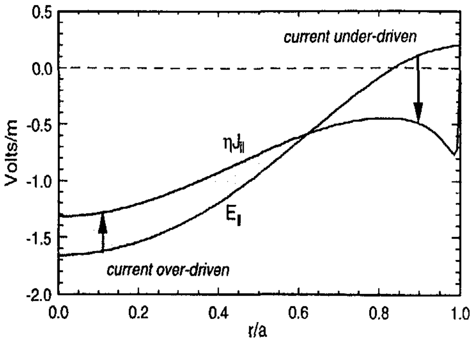

Fig. 1.2.— $\langle E\rangle_{\|}$ and $\eta\langle J\rangle_{\|}$ for an equilibrium modeled from typical experimental discharge parameters.

1.1.3 Imbalance of Mean-field Ohm's Law in the RFP

The current in the RFP is driven externally by a toroidal electric field applied by a transformer. This externally applied field aligns with the magnetic field in the core, driving toroidal current and generating the observed B_θ. However, at the edge the applied electric field is oblique to the equilibrium $\mathbf{B} \approx B_\theta \hat{\theta}$ and thus is unable to drive the edge current necessary to generate the observed core B_ϕ. We consider, for example, the reversal surface where the equilibrium magnetic field is entirely poloidal. At this surface the resistive dissipation of poloidal current is balanced only by the decay of toroidal flux within the surface as,

$$\eta J_\theta = -2\pi \frac{d}{dt} \int_0^{r_{rev}} B_\phi dr, \tag{1.11}$$

where r_{rev} is the reversal radius of the toroidal field. We invoke Eq. 1.3 twice to express J_θ in terms of the integrated toroidal flux obtaining,

$$-\frac{1}{\tau_r}\Phi_\phi = \frac{d\Phi_\phi}{dt}, \tag{1.12}$$

where τ_r is a resistive diffusion time. However, in experiments this decay is not observed, rather the toroidal flux is maintained for as long as an electric field is applied by the transformer. Thus we presume the existence of an auxiliary current drive mechanism which drives current in the edge.

To quantify the approximate imbalance in Ohm's Law over the plasma radius we may overplot $\langle E \rangle_{\|}$ and $\eta \langle J \rangle_{\|}$ (Fig. 1.2). Using estimated values for η we obtain the expected imbalance at the edge where the applied parallel electric field is too small or in the wrong direction to account for the driven current. In addition we obtain an imbalance in the core where the applied field over drives the necessary current. Thus, the applied field acts to peak the current, pushing the equilibrium away from the constant λ relaxed state predicted by Taylor. Clearly, an anomalous drive term is needed to flatten the current profile, suppressing current in the core and driving it in the edge. We must move beyond Taylor's theory to find candidates for that term.

1.2 Dynamos

It has been long proposed that the parallel Ohm's law may be balanced in the RFP by retaining the nonlinear product of fluctuations in the ion velocity and magnetic field averaged over a flux surface (Eq. 1.1). The nonlinear $\langle \tilde{\mathrm{v}} \times \tilde{\mathrm{b}} \rangle$ term would act to drive parallel current in the edge and suppress it in the core to maintain a magnetic field profile characteristic of the relaxed Taylor state. This generation of magnetic flux from flow fluctuations in a conducting fluid is an example of a general class of phenomena called dynamos. The existence and properties of dynamos have been the subject of extensive theoretical efforts and numerical studies with interest stemming in large part from evidence of naturally occurring geophysical and astrophysical dynamos. In this

section we begin with a brief description of kinematic dynamo theory which has been historically employed to describe dynamos occurring in systems dominated by the kinetic energy of the fluid. Extensive monographs exist on this subject including the classic text by Moffat (1978), and the more recent book by Childress (1995). We then outline a nonlinear theory of the MHD dynamo which is applicable to the strong-field regime of the RFP and demonstrate how this theory relates (or fails to relate) to the traditional kinematic dynamo. We end by mentioning an alternative kinetic theory for the relaxation of the RFP current profile and discuss the status of that theory in RFP studies.

1.2.1 Kinematic Dynamo

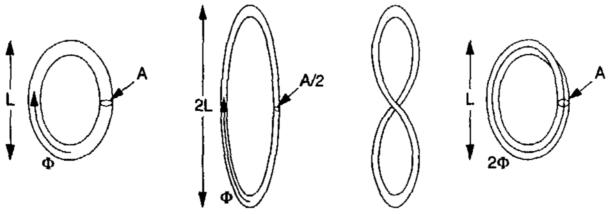

Fig. 1.3.— Illustration of the "Stretch-Twist-Fold" Dynamo.

A simple heuristic example of fluid motion enhancing the magnetic field strength goes by the descriptive name of the "Stretch, Twist, Fold" or STF dynamo (Childress, 1995). The basic idea of this dynamo is shown in Fig. 1.3. We imagine a flux tube, Φ, an ideal plasma with a cross-sectional area, A, and characteristic length, L, such that $V \propto AL$, where V is the volume of the tube. First, the motion of the fluid *stretches* the tube to twice its characteristic length. For an ideal incompressible plasma volume of the tube will be a constant, hence the cross sectional area of the tube becomes $A/2$ while the flux remains Φ. Fluid motions then *twist* the tube into a figure "8" and the *fold* two halves over each other such that the loop occupies its original volume. However, now there is double the flux through A. In principle the STF motion may be repeated to create an arbitrarily strong flux loop. This assumes that the Lorentz force associated with the growing field strength of the loop remain much weaker than the flux enhancing motion of the conducting medium.

The STF is a simple example of a kinematic dynamo mechanism in which the energy of the fluid motion is assumed to dominate the energy of the growing magnetic field. A general approach to the dynamo problem begins with the magnetic induction equation,

$$\frac{\partial \mathbf{B}}{\partial t} = -\nabla \times \mathbf{E} = \nabla \times (\mathbf{v} \times \mathbf{B}) + \eta \nabla^2 \mathbf{B}, \tag{1.13}$$

By separating each quantity $\mathbf{x}$ into a mean, $\mathbf{x}_0$, and fluctuating, $\tilde{\mathbf{x}}$, such that $\langle \mathbf{x} \rangle = \mathbf{x}_0$ and $\langle \tilde{\mathbf{x}} \rangle = 0$, we may linearize Eq. 1.13 into its mean and fluctuating components,

$$\frac{\partial \mathbf{B}_0}{\partial t} = \nabla \times \left(\mathbf{v}_0 \times \mathbf{B}_0 + \langle \tilde{\mathbf{v}} \times \tilde{\mathbf{b}} \rangle \right) + \eta \nabla^2 \mathbf{B}_0, \tag{1.14}$$

$$\frac{\partial \tilde{\mathbf{b}}}{\partial t} = \nabla \times \left(\tilde{\mathbf{v}} \times \mathbf{B}_0 + \mathbf{v}_0 \times \tilde{\mathbf{b}} \right) + \eta \nabla^2 \tilde{\mathbf{b}}. \tag{1.15}$$

Kinematic dynamo theory neglects the $\mathbf{J} \times \mathbf{B}$ back-reaction of the magnetic field onto the fluid motion making Eqs. 1.14–1.15 linear in $\tilde{\mathbf{b}}$. One is then free to specify a $\tilde{\mathbf{v}}$, solve for the resulting $\tilde{\mathbf{b}}$ from Eq. 1.15, and calculate the resulting $\langle \tilde{\mathbf{v}} \times \tilde{\mathbf{b}} \rangle$ to see if it overcomes the effects of resistive dissipation to generate $\mathbf{B}_0$. Such solutions are known to exist and their properties have been extensively studied.

The statistical properties of $\tilde{\mathbf{v}}$ in an isotropic, homogenous turbulent medium which are consistent with $\langle \tilde{\mathbf{v}} \times \tilde{\mathbf{b}} \rangle > 0$ may be determined through expansion of $\langle \tilde{\mathbf{v}} \times \tilde{\mathbf{b}} \rangle$ in terms of the mean field $\mathbf{B}_0$ and its derivatives. This yields the well known result (Moffat, 1978; Parker, 1979; Krause and Radler, 1980; Zeldovich *et al.*, 1983),

$$\mathbf{E}_f \equiv \langle \tilde{\mathbf{v}} \times \tilde{\mathbf{b}} \rangle = \alpha_0 \mathbf{B}_0 - \beta_0 \mathbf{J}_0. \tag{1.16}$$

The α_0 and β_0 coefficients are given by the statistical properties of the fluid fluctuation,

$$\alpha_0 = -\frac{\tau}{3} \langle \tilde{\mathbf{w}} \cdot \tilde{\mathbf{v}} \rangle, \tag{1.17}$$

$$\beta_0 = \frac{\tau}{3} \langle |\tilde{\mathbf{v}}|^2 \rangle, \tag{1.18}$$

where τ is a typical eddy-turnover time and $\tilde{\mathbf{w}} = \nabla \times \tilde{\mathbf{v}}$ is the fluctuating fluid vorticity. Substituting the $\mathbf{E}_f$ from Eq. 1.16 back into Eq. 1.14 we obtain,

$$\frac{\partial \mathbf{B}_0}{\partial t} = \nabla \times (\mathbf{v}_0 \times \mathbf{B}_0 + \alpha_0 \mathbf{B}_0) + (\eta + \beta_0) \nabla^2 \mathbf{B}_0. \tag{1.19}$$

We see here that the presence of fluid fluctuations act through β_0 to enhance the resistive dissipation of $\mathbf{B}_0$. However, if α_0 drives current parallel to the field with the proper geometry the fluid fluctuations may generate $\mathbf{B}_0$. The generation of field through this term is called the α-effect dynamo.

The kinematic description of the dynamo will eventually break down as the magnetic energy grows in magnitude relative to the fluid energy. Eventually the back-reaction of the magnetic field on the fluid fluctuations must be considered. In the weak magnetic field limit these effects are included through the modification (Vainshtein, 1980; Zeldovich *et al.*, 1983; Gruzinov and Diamond, 1994) of Eq. 1.17 to include the Lorentz force,

$$\alpha = \alpha_0 + \frac{\tau}{3\rho} \langle \tilde{\mathbf{j}} \cdot \tilde{\mathbf{b}} \rangle. \tag{1.20}$$

When the the $\langle \tilde{\mathbf{j}} \cdot \tilde{\mathbf{b}} \rangle$ balances the α_0 term the dynamo is said to have saturated. The behavior of these saturated dynamos is a topic of both considerable interest and debate as the dynamos which may exist in astrophysical or geophysical systems are presumed to exist in this state. Recent numerical work (e.g. Cattaneo and Hughes, 1996) suggests that the behavior of dynamos in these saturated regimes differs qualitatively from what might be extrapolated from the kinematic growth phase. Furthermore, as we discuss below, in the strong-field limit applicable to laboratory plasmas the kinematic description breaks down altogether and a physically distinct dynamo mechanism emerges.

1.2.2 MHD Dynamo

The RFP plasma exists in a strong magnetic field regime for which the kinematic description fails to apply. In this limit the fluid velocity and magnetic field fluctuations are inextricably linked such that the magnetic induction equation cannot be linearized. To understand the dynamo in this strong field limit we may start with the generalized Ohm's law which includes the $\mathbf{J} \times \mathbf{B}$ Lorentz force (Spitzer, 1962),

$$-\frac{m_e}{e^2 n_e}\frac{\partial \mathbf{J}}{\partial t} + \mathbf{E} + \mathbf{v} \times \mathbf{B} - \frac{1}{en_e}\mathbf{J} \times \mathbf{B} + \frac{\nabla P_e}{en_e} = \eta \mathbf{J}, \tag{1.21}$$

where m_e and e are the electron mass and charge respectively, n_e is the electron density, and P_e is the electron pressure. We may take the parallel component of Eq. 1.21 averaged over a flux surface obtaining (Ji, *et. al.*, 1995),

$$\begin{aligned} \eta J_{\parallel,0} - E_{\parallel,0} &= \langle \tilde{\mathbf{v}} \times \tilde{\mathbf{b}} \rangle_{\parallel} - \frac{1}{en_e}\langle \tilde{\mathbf{j}} \times \tilde{\mathbf{b}} \rangle_{\parallel} \\ &= \langle (\tilde{\mathbf{v}} - \tilde{\mathbf{j}}/en_e) \times \tilde{\mathbf{b}} \rangle_{\parallel} \\ &\approx \langle \tilde{\mathbf{v}}_{e\perp} \times \tilde{\mathbf{b}}_{\perp} \rangle_{\parallel} \end{aligned} \tag{1.22}$$

where we have neglected parallel fluctuations in pressure and current and made use of $\mathbf{J} = en_e(\mathbf{v}_i - \mathbf{v}_e)$ and the approximation $\mathbf{v} \approx \mathbf{v}_i$. To determine the contributions to $\tilde{\mathbf{v}}_{e\perp}$ we may take the perpendicular component of Eq. 1.21 yielding,

$$\begin{aligned} \tilde{\mathbf{v}}_{e\perp} &= \tilde{\mathbf{v}}_{\perp} - \tilde{\mathbf{j}}_{\perp}/en_e \\ &= \frac{\tilde{\mathbf{E}}_{\perp} \times \mathbf{B}}{B^2} + \frac{\nabla_{\perp}\tilde{P}_e \times \mathbf{B}}{en_e B^2} - \left(\frac{m_e}{e^2 n_e}\frac{\partial \tilde{\mathbf{j}}_{\perp}}{\partial t} + \eta \tilde{\mathbf{j}}_{\perp}\right) \times \mathbf{B}/B^2. \end{aligned} \tag{1.23}$$

We expect the electron inertial and fluctuating Hall term to be negligible. This leaves a single fluid MHD contribution in the form of a fluctuating $\tilde{\mathbf{E}}_{\perp} \times \mathbf{B}_0$ fluid velocity, and a diamagnetic contribution from the fluctuating electron pressure gradient. The MHD contribution to $\tilde{\mathbf{v}}_e$ will appear identically in $\tilde{\mathbf{v}}_i$ which was measured in the work described in this thesis. By substituting our expression for $\tilde{\mathbf{v}}_e$ into Eq. 1.22 we obtain the following form for parallel Ohm's law,

$$\eta J_{\parallel,0} - E_{\parallel,0} = \langle \tilde{\mathbf{E}}_{\perp} \cdot \tilde{\mathbf{b}}_{\perp} \rangle / B_0 + \langle \nabla_{\perp}\tilde{P}_e \cdot \tilde{\mathbf{b}}_{\perp} \rangle / B_0 en_e. \tag{1.24}$$

In this expression the fluctuating velocity is eliminated altogether and the dynamo is expressed entirely as a product of the fluctuating magnetic field with fluctuating electric field and electron pressure terms.

To compare this dynamo mechanism to the kinematic dynamo we examine a more general expression for the α-coefficient derived by Bhattacharjee and Yuan (1995) for the MHD dynamo,

$$\alpha = \frac{\alpha_0 + (\tau/3\rho\eta)(\beta \mathbf{J}_0 \cdot \mathbf{B}_0 + \langle \tilde{\mathbf{E}} \cdot \tilde{\mathbf{b}} \rangle)}{1 + (\tau/3\rho\eta)B^2}, \tag{1.25}$$

where α_0 is the kinematic α-coefficient. In the weak field limit this reduces to $\alpha \approx \alpha_0$ recovering the kinematic expression. However, in the strong field (or high conductivity) limit, $(\tau/3\eta\rho)B_0^2 \gg 1$ this reduces to,

$$\alpha \approx (\beta \mathbf{J}_0 \cdot \mathbf{B}_0 + \langle \tilde{\mathbf{E}} \cdot \tilde{\mathbf{b}} \rangle)/B^2, \tag{1.26}$$

We may substitute this expression back into Eq. 1.16 to obtain the strong field expression for the fluctuation induced electric field,

$$\begin{aligned}\langle \tilde{\mathbf{v}} \times \tilde{\mathbf{b}} \rangle &= \left(\beta \mathbf{J}_0 \cdot \mathbf{B}_0 + \langle \tilde{\mathbf{E}} \cdot \tilde{\mathbf{b}} \rangle\right) \mathbf{B}_0/B^2 - \beta \mathbf{J}_0 \\ &= -\beta \mathbf{J}_{0,\perp} + \langle \tilde{\mathbf{E}} \cdot \tilde{\mathbf{b}} \rangle \mathbf{B}_0/B^2. \qquad (1.27)\end{aligned}$$

Taking the parallel component of this expression we obtain,

$$\langle \tilde{\mathbf{v}} \times \tilde{\mathbf{b}} \rangle_{\|} = \langle \tilde{\mathbf{E}} \cdot \tilde{\mathbf{b}} \rangle / B, \qquad (1.28)$$

This matches the MHD term derived above from the generalized Ohm's law. Thus the dynamo mechanism in the strong field limit of the RFP is a completely distinct mechanism from that responsible for the kinematic dynamo. This is brought about by the domination of α_0 by the MHD terms in the numerator of Eq. 1.25 and the subsequent cancellation of the parallel β-effect with the remaining, non-MHD term in the numerator.

1.2.3 Kinetic Dynamo

A completely different mechanism for the flattening of the current profile has been proposed by Jacobson and Moses (1984). It is known that the large magnetic fluctuations and overlapping island structure in the RFP induce stochasticity in the mean magnetic field such that a field line followed about the machine will wander randomly in radius. This field line wander yields high particle and energy diffusivity (Rechester and Rosenbluth, 1978) as hot core particles stream rapidly parallel to the stochastic fields out of the plasma. This field line diffusion is predicted to exceed the diffusion of the particles due to classical collisional cross-field transport. Jacobson and Moses propose that parallel electron momentum driven by the applied electric field in the core streams along the magnetic field to the edge region where the field is predominantly poloidal. Such

a mechanism would act to flatten the parallel current profile in accordance to Taylor's theory without a $\langle \tilde{\mathbf{v}} \times \tilde{\mathbf{b}} \rangle$ dynamo mechanism.

Recent Fokker-Plank simulation of electron distributions in the RFP with a parallel momentum diffusion set to be consistent with Rechester-Rosenbluth diffusivity suggest that the kinetic dynamo mechanism could produce the observed RFP equilibrium (Giruzzi and Martines, 1994; Martines and Vallone, 1997). However, a self-consistent theoretical treatment of the problem by Terry and Diamond (1990) indicated electron diffusion rates far below those needed to explain the observed flattening of the current profile. Furthermore, experimental measurements of the electron momentum distribution at the edge of MST do not appear to be consistent with the streaming of fast electrons from the core to the edge (Stoneking, PhD Thesis, 1994). While measurements described below and the results reported in this thesis provide strong evidence for MHD dynamo activity in the edge and core region of the MST, detailed commentary on the validity of the kinetic dynamo for the MST falls outside the scope of the present work.

1.3 Evidence for the MHD Dynamo in the RFP

1.3.1 MHD Simulation

The inherently nonlinear nature of the dynamo in the RFP make computational efforts to simulate dynamo effects invaluable. The original numerical simulations of the RFP performed by Sykes and Wesson (1977) employed a periodic $14 \times 14 \times 13$ grid and exhibited strong dynamo activity. Since that time extensive numerical efforts have been devoted to simulation of dynamics in the RFP. For a thorough review of these efforts the reader is again referred to Ortlani and Schnack (1993). These simulations have consistently demonstrated relaxation of the current profile by a dynamo electric field with the RFP equilibrium maintained indefinitely with a constant applied electric field. The dynamo field was observed in linear codes which contained only $m = 1$ resonant modes, while in fully developed nonlinear codes the $m = 1$ contribution still dominated. The inclusion of multiple modes did affect the dynamics of the observed equilibrium with oscillations in the current profile becoming evident. Such effects were more pronounced as the simulations approached Lundquist number regimes similar to those achieved in experiment, with the oscillations approaching the discrete relaxation phenomena observed in experiment. Recent work has employed these simulations to predict low fluctuation regimes which have then been realized in experiment (Sovinec, 1995). Thus far, the numerical work has successfully demonstrated the consistency of the RFP dynamo within the framework of resistive MHD and demonstrated the orgin and characteristics of the fluctuations observed in the RFP. As these simulations continue to approach experimental regimes with advances in algorithms and computational resolution, we expect an increasingly detailed and realistic picture of the dynamo action in the RFP to emerge.

1.3.2 Edge Measurements

Recent experiments by Ji, *et.al.* (1995) have successfully observed the dynamo in the edge of several RFP's. These experiments employed a complex Langumiur probe to measure $\tilde{\mathbf{E}}_\perp$, $\nabla_\perp \tilde{P}_e$ and $\tilde{\mathbf{b}}_\perp$. Calculating $\langle \tilde{\mathbf{E}}_\perp \cdot \tilde{\mathbf{b}}_\perp \rangle$ and $\langle \nabla_\perp \tilde{P}_e \cdot \tilde{\mathbf{b}}_\perp \rangle$ over an ensemble of discrete dynamo events, Ji demonstrated the balance of Eq. 1.24. In relatively collisionless plasmas like those obtained in MST it was found that the $\langle \tilde{\mathbf{E}}_\perp \cdot \tilde{\mathbf{b}}_\perp \rangle$ term dominated the dynamo contribution while the diamagnetic term was found to dominate for the higher collisionality plasmas in the TPE-1RM20 device. Edge measurements continue to constrain the edge dynamo on MST. However, measurement of dynamo activity in the core has required the development of non-perturbing techniques like those described in this thesis.

1.4 Overview of this Thesis

We have employed spectroscopic measurements of intrinsic impurities to measure ion velocity fluctuations in the core and edge regions of the MST plasma. The ensemble averaged product of these fluctuations with magnetic fluctuations yields a substantial $\langle \tilde{\mathbf{v}} \times \tilde{\mathbf{b}} \rangle$ dynamo product in the interior of MST. The chapters describing this measurement are organized as follows. Chapter 2 provides an overview of the hardware, calibration, and data reduction techniques for the spectroscopic diagnostic which enabled the measurements described herein. In the final section of the chapter (§ 2.5) we formally develop expressions describing the capacity of the spectrometer to resolve passively low-k fluctuations in the ion velocity. An understanding of this sensitivity proves critical to subsequent interpretation of velocity fluctuation data. Chapter 3 describes the ensemble techniques employed in the analysis of our data. The first half of the chapter motivates the analysis of the data about discrete manifestations of the dynamo or sawtooth events while the second half details the ensemble software developed for the analysis. In Chapter 4 we describe measurements of the dominant low-k magnetic fluctuations which pervade the interior of MST. While the essence of much of this data is well known, the details of the magnetic fluctuation evolution over the sawtooth and in radius are critical to the proper calculation and interpretation of the core dynamo product. Chapter 5 contains entirely novel measurements of ion velocity fluctuations in the interior of MST. These are found to be highly coherent with amplitudes consistent with the predictions of

MHD. In addition the radial fluctuation profile of the ion velocity fluctuations is found to be significantly limited in contrast to the extended profile of the magnetic fluctuations. Chapter 6 consists of two parts. The first part details dynamic modeling of the RFP equilibrium quantities in an effort to predict the magnitude and direction of the dynamo field necessary to balance Ohm's law. The second part presents the measured dynamo products in the interior of the plasma and compares them to the predictions of the modeling. The observations reported here of substantial dynamo field in the core, peaking to several Volts/m at the sawtooth crash, constitute the central result of this thesis. However, comparison with predictions of the model suggests that substantial improvements in measurement and modeling techniques are needed to demonstrate numerical balance of Eq. 1.1 in the interior of MST.

References

Bhattacharjee, A. and E. Hameiri (1986). Self-consistent dynamolike activity in turbulent plasmas. *Phys. Rev. Lett.* **57**(2), 206–209.

Bhattacharjee, A. and Y. Yuan (1995). Self-consistency constraints on the dynamo mechanism. *ApJ* **449**, 739–744.

Boozer, A. H. (1986). *Phys. Fluids* **29**, 4123.

Cattaneo, F. and D. W. Hughes (1996). Nonlinear saturation of the turbulent α effect. *Phys. Rev. E* **54**(5), R4532–R4535.

Childress, S. and A. D. Gilbert (1995). *Stretch, twist, fold : the fast dynamo.* New York: Springer.

Giruzzi, G. and E. Martines (1994). Kinetic modeling of fast electron dynamics and self-consistent magnetic fields in a reversed field pinch. *Phys. Plasmas* **1**(8), 2653–2660.

Gruzinov, A. V. and P. H. Diamond (1994). *Phys. Rev. Lett.* **72**, 1651.

Jacobson, A. R. and R. W. Moses (1984). Nonlocal dc electrical conductivity of a lorentz plasma in a stochastic magneic field. *Phys. Rev. A* **29**(6), 3335–3342.

Ji, H., A. F. Almagri, S. C. Prager, and J. S. Sarff (1995). Measurement of the dynamo effect in a plasma. *Phys. Plasmas* **3**(5), 1935–1942.

Ji, H., S. C. Prager, and J. S. Sarff (1995). Conservation of magnetic helicity during plasma relaxation. *Phys. Rev. Lett.* **74**(15), 2945–2948.

Krause, F. and K.-H. Radler (1980). *Mean-Field Magnetohydrodynamics and Dynamo Theory.* Oxford: Pergamon.

Martines, E. and F. Vallone (1997). Ohm's law for plasmas in reversed field pinch configuration. *Phys. Rev. E* **56**(1), 957–962.

Moffat, H. K. (1978). *Magnetic Field Generation in Electrically Conducting Fluids.* Cambridge, U. K.: Cambridge U. P.

Ortlani, S. and D. D. Schnack (1993). *Magnetohydrodynamics of Plasma Relaxation.* Singapore: World Scientific.

Parker, E. N. (1979). *Cosmic Magnetic Fieds, Their Orgin and Activity.* Oxford: Clarendon.

Rechester, A. B. and M. N. Rosenbluth (1978). Electron heat transport in a tokamak with destroyed magnetic surfaces. *Phys. Rev. Lett.* **40**(1), 38–41.

Schoenberg, K. F., R. F. Gribble, and J. A. Phillips (1982). Zero-dimensional simulations of reversed-field pinch experiments. *Nuclear Fusion* **22**(11), 1433–1441.

Sovinec, C. R. (1995). *Magnetohydrodynamic simulations of noninductive helicity injection in the reversed-field pinch and tokamak.* PhD dissertation, University of Wisconsin – Madison, Department of Physics.

Spitzer, Jr., L. (1962). *Physics of Fully Ionized Gases.* New York: Interscience Publishers.

Sprott, J. C. (1988). Electrical circuit modeling of reversed field pinches. *Phys. Fluids* **31**(8), 2266–2275.

Stoneking, M. R. (1993). *Fast electron generation and transport in a turbulent magnetized plasma.* PhD dissertation, University of Wisconsin – Madison, Department of Physics.

Sykes, A. and J. A. Wesson (1977). Proc. 8th European Conf. on Cont. Fusion and Plasma Physics, Prague, pp. 80. Czechoslavak Acadamy of Sciences.

Taylor, J. B. (1974). Relaxation of toroidal plasma and generation of reverse magnetic fields. *Phys. Rev. Lett.* **33**(19), 1139–1141.

Terry, P. W. and P. H. Diamond (1990). A self-consistent theory of radial transport of field-aligned current by microturbulence. *Phys. Fluids B* **2**(6), 1128–1137.

Vainshtein, S. I. (1980). *Magnetohydrodynamics* **16**, 111.

Zeldovich, Y. B., A. A. Ruzmaikin, and D. D. Sokoloff (1983). *Magnetic Fields in Astrophysics.* New York: Gordon & Breach.

2

Ion Dynamics Spectrometer

The passive spectroscopic measurement of core ion velocity fluctuations constitutes the central experimental innovation of this work. The development of the Ion Dynamics Spectrometer (IDS), a spectroscopic diagnostic combining high light throughput with fast parallel analog processing, enabled these measurements. § 2.1 of this chapter outlines the IDS from the collection optics, through the spectrometer and the analog processing to the digitizer. § 2.2 details the *in situ* calibration of the system phase and frequency response, single channel transfer function, and volt per photon gain. Then, § 2.3 details the reduction of the measured emission profiles to chord averaged impurity temperatures and velocities. The final sections of this chapter explore two key limitations to the application of the IDS to the dynamo problem. § 2.4 explores the extent to which dynamics observed in minority species reflect those of the majority ion fluid. § 2.5 provides a detailed discussion of chord averaging effects on the ion velocity fluctuation measurements.

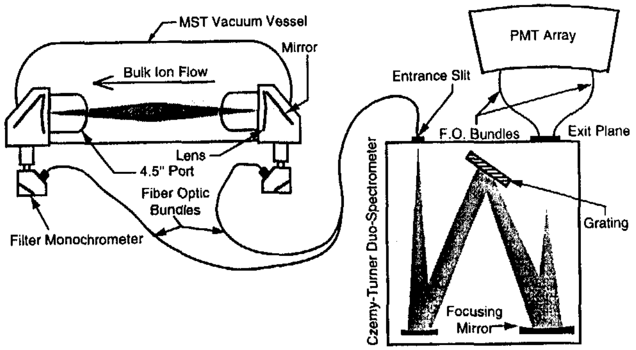

Fig. 2.1.— Overview of the Ion Dynamics Spectrometer configured with opposing toroidal views. Elements are not drawn to scale.

2.1 A Fast Duo-Spectrometer

The IDS extracts chord averaged ion velocity and temperature from the shift and broadening of intrinsic impurity lines (Fig. 2.1). Previous examples of high speed Doppler spectroscopy may be found for example in Carolan (1995 and 1997) and Evensen (1995). While simple in concept, the speed and success unique to the IDS stem from the combination of high-throughput optics, high-gain, high-bandwidth electronics, and completely parallel analog and digital processing. This section briefly describes these components moving through the entire IDS system from the collection optics to the signal digitizers. We begin by identifying the lines of sight employed in this study to resolve the three components of the fluctuating ion velocity $\tilde{\mathbf{v}}$. We then discuss the collection optics that deliver filtered light to the spectrometer and the subsequent separation of that light into 32 wavelength channels. Lastly, we describe the conversion of light from each channel, into a current by photomultiplier tubes and the analog processing that amplifies, filters and digitizes the current signal. This overview attempts to provide a solid understanding

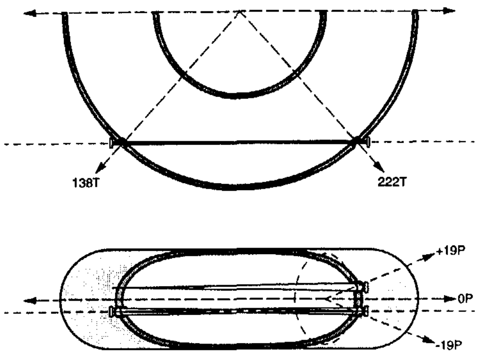

Fig. 2.2.— Toroidal line of sight. Opposing and up-down symmetric views shown.

of the IDS system while omitting many of the technical details. Subsequent sections address some of these details which are specifically relevant to this thesis while design specifications may be found in (Den Hartog and Fonck, 1994).

2.1.1 Lines of Sight

The IDS collects light along two lines of sight oriented to maximize sensitivity to particular components of $\tilde{\mathbf{v}}$. The mean toroidal velocity v_ϕ is measured through the $4\frac{1}{2}$ inch ports at poloidal and toroidal angles of -19P, 138T and -19P, 222T, by opposing the two views along the same toroidal chord.[1] This chord (shown to scale in Fig. 2.2) subtends a toroidal angle of 84° about 180T, approximately 17 cm $(0.33\,a)$ below the midplane of the torus. The midpoint of the chord falls almost directly below the major radius of the torus yielding a radial impact parameter for the chord roughly equal to its vertical displacement from the midplane. By employing the opposing views we may

to compare red shifted and blue shifted emission lines to obtain an absolute measurement of the ion velocity. Alternatively, the views may provide an *in situ* calibration of the unshifted line position, allowing subsequent measurements of ion velocity with non-opposing views (§ 2.3). Measurements of toroidal velocity fluctuation, $\tilde{v}_\phi$ require no calibration of the mean flow making the two chords redundant. For $\tilde{v}_\phi$ measurements we look through the $4\frac{1}{2}$ inch ports at -19P, 222T and +19P, 222T along toroidal chords which mirror each other about the midplane. The up-down symmetry of this configuration allows the extraction of the local velocity fluctuation phase from the chord averaged quantity (§ 2.5). Most $\tilde{v}_\phi$ measurements reported in this study employed the up-down toroidal configuration.

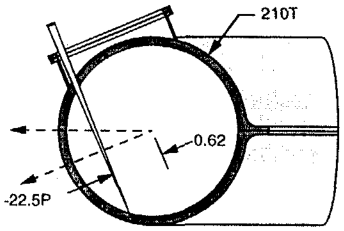

Fig. 2.3.— Poloidal line of sight with impact radius of $0.62\,a$

Poloidal ion velocity, v_θ, was measured using the boxport at 210T, +67.5P, shown in Fig. 2.3. While v_θ measurements may be made in general at several different radii, the $\tilde{v}_\theta$ measurements in this study employed the outermost boxport chord with an impact parameter of $0.62\,a$. Unfortunately, the flow fluctuations measured at this radius are dominantly parallel, compromising the chord's effectiveness for measuring the $v_\perp$ fluctuations producing the dynamo. On the other hand, chords at smaller radii are oblique to

---

[1] Throughout this thesis the convention —P, —T will be used to indicate poloidal and toroidal angles of ports and diagnostics in machine coordinates measured relative to the poloidal and toroidal gaps in the shell.

$\hat{\theta}$ except near the core making any resolution of v_θ difficult. We explore this issue further in our discussion of the $\tilde{v}_\theta$ measurement results.

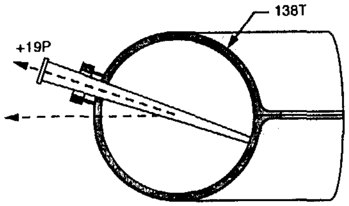

Fig. 2.4.— Radial line of sight.

Radial flows were measured through the $4\frac{1}{2}$ inch port at 138T, +19P along a line of sight passing through the center of the torus (Fig. 2.4). While mean radial flows cancel out from one half of the chord to the other, radial fluctuations with poloidal mode number $m = 1$, which "turn around" as they reach the second half of the chord, are resolved perfectly. This, combined with a direct view through the large port provided a near optimal measurement of radial velocity fluctuations, $\tilde{v}_r$.

2.1.2 Optics

UV-grade fused silica lenses collect the radiation from each chord. For the toroidal views 4 inch lenses look through $4\frac{1}{2}$ inch ports with their aperture constricted by an oblique viewing angle and the 5 cm thick vessel wall. The lenses focus onto the face of the opposing lens in order to reduce the collection of reflected light. This produces a conical collection volume that, according to étendue calculations and ray tracing simulations, collects light from an extended plasma volume with uniform optical weighting along the line of sight. The poloidal view looks directly through a $1\frac{1}{2}$ inch aperture with a 2 inch lens. Likewise, the radial view looks directly through a $4\frac{1}{2}$ inch aperture with an large

7 inch lens. For the toroidal and poloidal views the lens forms the vacuum seal for the system while the radial view looks through a large fused silica window which forms the seal. Light collected by the lens focuses on the entrance slit of small monochromators that filter bright outlying lines capable of contaminating the selected emission line. The width of the monochromator transfer function greatly exceeds the impurity line width and thus does not alter the wavelength distribution of the emitted radiation.

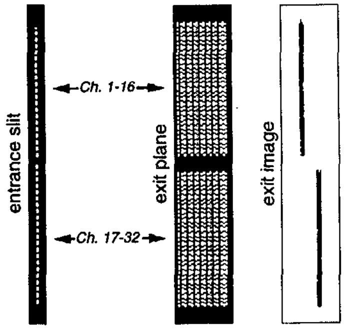

Fig. 2.5.— Entrance and exit planes for spectrometer.

Fiber optic bundles carry the filtered light from the filter monochromators to the spectrometer. The individual fiber optics contain 400-μm-diam pure fused silica cores with a manufacturers specification of less than 3 dB attenuation at 225 nm over their 3 m length. At the spectrometer the fiber optics from each bundle form into a single vertical column several mm high (Fig. 2.5). The fiber optic column from one view sits above the column from the remaining view and both are masked by 178 μm wide rectangles milled into 12.7 μm thick piece of stainless steel. These two rectangles form the entrance slits to a $f/10$ 1.0 m focal length Czerny-Turner spectrometer. The 1180 g/mm grating

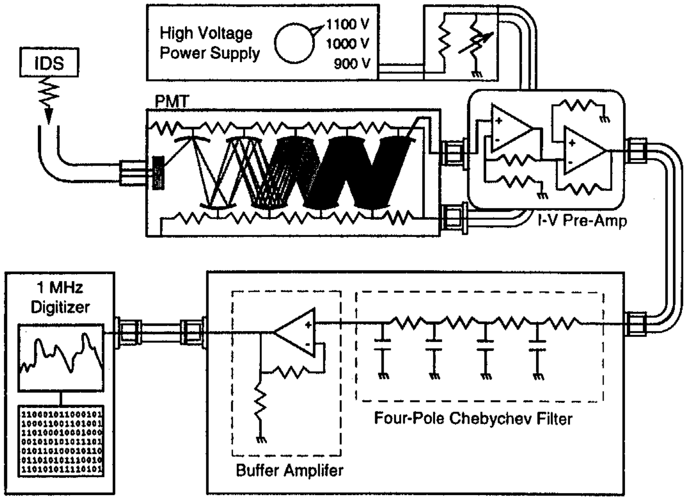

Fig. 2.6.— Cartoon of analog processing for a single IDS channel.

of the spectrometer yields a reciprocal dispersion of 0.12 nm/mm in fifth order at 227 nm. Two sets of 16 tightly packed fiber optic columns form the spectrometer exit plane. The fiber optics in each column contain 200-μm-diam pure fused silica cores yielding single fiber transfer functions approximately 0.024 nm wide. Each column then forms into a single fiber optic bundle carrying the light for that wavelength channel a final 0.5 m to a photomultiplier tube. Before reaching the exit plane light from each view is processed almost identically along parallel optical paths. Now leaving the exit plane the light from each view separates into 16 overlapping wavelength channels to be processed subsequently along a total of 32 nearly identical analog paths.

2.1.3 Electronics

The analog processing components for a single IDS channel are shown schematically in Fig. 2.6. The light for each channel leaves the exit plane fiber optic bundle in an $f/10$ cone before striking a fused silica window photomultiplier tube (PMT) which converts each photon into a cascade of photoelectrons. Calibrations presented in the following section indicate that for typical plasmas, the PMTs typically operate in counting mode, meaning simply that the cascade from one incident photon usually ceases before the next begins. The PMT power supply is typically set to 900 Volts for bright dirty plasmas to 1100 Volts for clean plasmas with little impurity radiation. Individual PMTs biases are set by voltage dividers to roughly half that value. While the PMTs may in principle withstand higher biasing voltages the underlying lack of photon statistics in such cases makes amplification of the individual photoelectron pulses pointless. Current pulses from the PMT enter directly into high-gain I/V amplifiers. These amplifiers contain two very fast operational amplifiers operated in series to convert the small current pulses into measurable signals of several Volts. This voltage travels via BNC cable to a four-pole, low-pass Chebychev filter with a relatively flat response out to 250 kHz. The filtered signal passes through a unity gain buffer amplifier to an Aurora 14 digitizer that digitizes the signal with 12-bit resolution at 1 Mhz.

2.2 Calibration

Three calibrations quantified the performance characteristics of the IDS system. First, an *in situ* calibration of the system phase and frequency response demonstrated the wide bandwidth, non-dispersive character of the analog processing. Second, position, transfer function, and gain of each channel was swept out by a Cd II line, provided by a Cadmium lamp. This revealed overlapping triangular transfer functions with ~0.24 Å FWHM in fifth order, meeting the design specifications. Finally, illumination with an integrating sphere of known intensity provided estimates of the system's Volt per photon gain and overall optical efficiency. These estimates indicate that while sensitive and efficient, the IDS operates in a regime dominated by photon noise, producing inherently noisy signals which may be improved only at the expense of time resolution. This section provides details of the calibration procedure and results in a condensed version of (Chapman and Den Hartog, 1996).

2.2.1 Phase and Amplitude Response

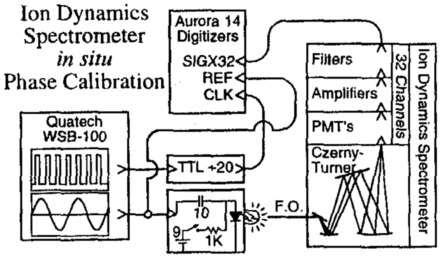

Fig. 2.7.— Schematic of the *in situ* calibration of the IDS response amplitude and phase. The Quatech WSB-100 provides the clock for both the driving signal and the Aurora 14 digitizers.

We performed a highly resolved *in situ* calibration of the entire IDS system phase response from 5 to 500 kHz (Fig. 2.7). The Quatech WSB-100 programmable D/A board, the key component of the calibration, generates an arbitrary function with 12 bit vertical resolution and a 20 MHz clock rate. The signal generator drove a bright LED producing an oscillating light signal that the fiber optics collected and passed through the full IDS system.

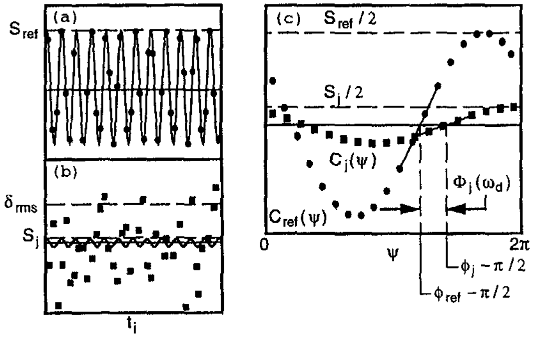

Fig. 2.8.— Extraction of phase information from noisy IDS output signals using correlation analysis. a) An oscillating signal, S_{ref}, drove an LED at ω_d. The digitized data points are plotted with circles. b) The signal output from the j'th channel, X_j, contains both the phase lagged output signal, S_j, and photon noise fluctuations with amplitude δ_{rms}, recorded at the squares. c) Correlation of the driving signal and X_j with a sinusoid at exactly $\omega_o = \omega_d$ over 2π yields the correlation function $C_{ref}(\psi)$ and $C_j(\psi)$ respectively. The phase lag introduced by the channel, $\Phi_j(\omega_d)$, is retrieved as the angle between the two positive going roots of the correlation functions. The relative channel response is calculated as, $R_j(w) = S_j/S_{ref}$.

The 20 MHz WSB-100 data strobe, divided down to 1 MHz by a simple TTL circuit, clocked the digitizers insuring strict synchronization of the driving signal and data collection. The signal output from the j'th channel of the IDS at time t_i can be modeled as

$$X_j(t_i) = S_j \sin(\omega_d t_i + \phi_j) + \delta_j(t_i), \tag{2.1}$$

where S_j and ϕ_j are the absolute amplitude and phase of the signal transmitted through the IDS, δ_j is a random deviate representing the photon fluctuation noise, and ω_d is the LED driving frequency. As Fig. 2.8a depicts, the photon fluctuation noise amplitude dominates the low amplitude transmitted signal recorded at the output of the IDS. The correlation of $X_j(t)$ with a sinusoid of angle ψ at exactly $\omega_o = \omega_d$ over the full record length, L, yields the function (Bendat and Piersol, 1980),

$$C_j(\psi) = \frac{1}{L}\sum_{i=1}^{L} X_j(t_i)\sin(\omega_o t_i + \psi) = \frac{1}{2}S_j\cos(\psi - \phi_j) + \mathcal{O}\Big(\frac{\delta_{rms}}{L}\Big). \tag{2.2}$$

The first term on the right hand side of this equation represents the zero frequency beat wave between the correlated signals, and contains information about both the phase and amplitude of the transmitted signal. The remaining term represents the DC beat wave between the sinusoid and the Fourier component of the noise at the pulsed frequency and is small if $L >> 1$. A linear fit to $C_j(\psi)$ through its positive-going root yields the correlation angle $\psi = \phi_j - \pi/2$ (Fig. 2.8c). We are then able to evaluate $C(\psi = \phi_j)$, making $\cos(\psi - \phi_j) = 1$ and yielding S_j. The amplitude and phase of the reference signal, S_{ref} and ϕ_{ref}, may be obtained identically. This allows calculation of the phase lag, $\Phi_j(\omega_d) = \phi_j - \phi_{ref}$, introduced by the channel and the relative channel response amplitude, $R_j(\omega_d) = S_j/S_{ref}$.

Fig. 2.9 shows the mean system response for the 32 channels. The system exhibits an extremely linear phase response from DC to 250 kHz corresponding to a nondispersive signal delay of 3.64μs. The wide bandwidth of the diagnostic removes the analog electronics as the limiting factor for time resolution of physical phenomena. This limit is currently imposed either by the viewing chord which spatially averages over fast fluctuations of highly localized phenomena, or the low spectral irradiance of the impurity being observed. However, for large scale phenomena of bright impurities the IDS is capable of resolving velocity and temperature dynamics with better than 10μs resolution.

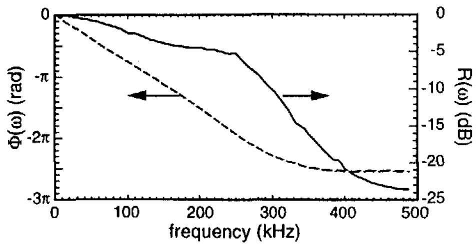

Fig. 2.9.— The calibrated phase and amplitude response from 5-500 kHz. The system response amplitude (solid) drops 5 dB from 5 to 250 kHz and -24 dB from 250 to 500 kHz. Linear system phase response (dashed) corresponds to a nondispersive signal delay of 3.64μs.

2.2.2 Triangular Transfer Function

To measure single channel transfer functions we employed a Cadmium lamp powered by a regulated DC current source. A precision motor drive rotated the spectrometer grating, sweeping the 226.5 nm Cadmium line in 5th order across the exit fiber-optic array. A single sweep of the Cadmium line traced out the instrument functions of sixteen IDS channels, corresponding to one view of the diagnostic. A photo diode detector provided a reference measurement of the lamp brightness.

The area, centroid, and variance of each instrument function were calculated statistically, while the value and location of the instrument function maximum were estimated via a parabolic fit to the peak of each trace pulse. A linear fit to both sides of the peak provided an estimate of the instrument function FWHM. Additional sweeps for each view, which included a neighboring Cadmium line at 283.7 nm in fourth order, provided a conversion factor from the digitized time axis to a wavelength axis equal to the known wavelength separation of the two lines divided by their measured separation in time.

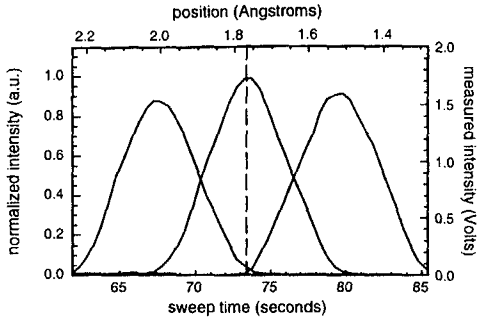

Fig. 2.10.— Three adjacent transfer functions traced out in time by sweeping cadmium line.

Final sweeps in which both IDS views were illuminated determined the relative position of one set of sixteen channels to the other.

2.2.3 Intensity Gain

We estimated the absolute photon response of the IDS using an integrating sphere with a well calibrated luminosity and blackbody spectral response. The sphere, placed directly in front of one of the two collecting lenses, illuminated 16 of the 32 IDS channels. Digitizing the 16 output signals at 1 MHz, 128K records were collected at various PMT bias voltages. The statistics of the photo-electrons emitted by the photo cathode of the PMT should dominate the statistics of the signal y. By assuming the photo-electron emission to be a Poisson process one may use Poisson statistics (Thorn EMI PMT Manual, 1993) to relate the moments of y to the mean number of photo-electron counts per sample, $\langle n_{pe}\rangle$, and the sensitivity of our detection system to the photo-electrons produced by incident photons, G_{pe}, as:

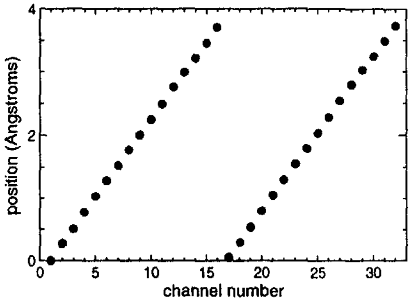

Fig. 2.11.— The calibrated relative positions of the 32 IDS channels demonstrate coverage by both views of roughly 4 Åwith 0.25 Åresolution.

$$\langle y\rangle = G_{pe}\langle n_{pe}\rangle \tag{2.3}$$

$$\langle y^2\rangle - \langle y\rangle^2 = G_{pe}^2\left(\langle n_{pe}^2\rangle - \langle n_{pe}\rangle^2\right) = 2G_{pe}^2\langle n_{pe}\rangle\Delta f\,\tau_{samp}. \tag{2.4}$$

Here Δf is the analog bandwidth of the diagnostic and τ_{samp} is the sampling interval of the system digitizers. Additional corrections to Eq. 2.4 due to PMT dark current and the single electron response pulse distribution should be of order unity [Thorn EMI Electron Tubes, "photomultipliers and accessories", 1993] within the precision of this calibration. However, the calibration data exhibits an unexpected quasi-Gaussian spike in the distribution about the signal baseline, in addition to the expected Poisson distribution (Fig. 2.12a). While the dark current originating within the PMT dynode chain is too small to account for all of the spike, a possible explanation lies in the delta function response of the detection system. Digitizer sampling at 1 MHz of individual PMT photoelectrons in the wings of the response, which rings about zero due to the finite system bandwidth, may effectively pull a portion of the count distribution to negative and near zero values.

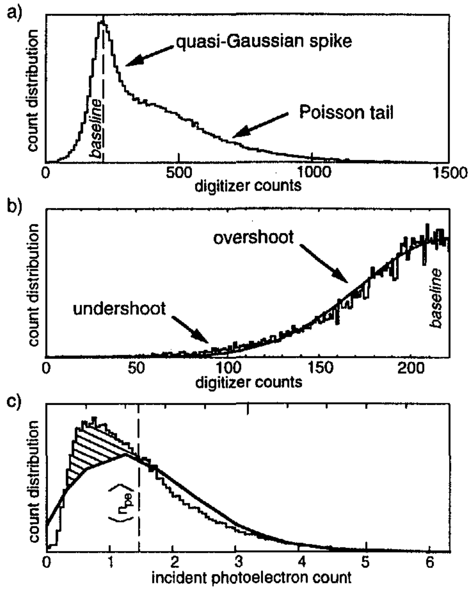

Fig. 2.12.— a) A histogram of digitized signal level yields a curve which appears to be a super position of the expected Poisson curve with a Gaussian spike about the channel baseline. b) A fit to the distribution below the baseline reveals an approximately Gaussian shape. c) Subtraction of the fitted Gaussian from the distribution recovers a distribution above the baseline which more closely approximates a Poisson curve. Here the horizontal axis has been renormalized to the corresponding number of incident photoelectrons and the Poisson curve corresponding to the calculated signal mean and variance is over drawn.

A Gaussian fit to the distribution below the baseline (Fig. 2.12b) subtracted from the whole distribution recovers a distribution which more closely approximates a Poisson curve (Fig. 2.12c). Calculation of the moments of this distribution yields, through Eqs. 2.3–2.4, estimates for $\langle n_{pe} \rangle$ and G_{pe}.

The photon flux incident on a single channel from the calibrated source is given by

$$\Gamma_\gamma = \frac{I_\lambda \eta_{ch} \Delta_{ch}}{\mathrm{hc}/\lambda}, \tag{2.5}$$

where I_λ is the spectral irradiance of the integrating sphere, η_{ch} is the system étendue per channel of $11.7 \times 10^{-5}\,\mathrm{sr\,cm}^2$, Δ_{ch} is the single channel width of 0.024 nm, and λ is 529.1 nm. This yields a $\Gamma_\gamma \approx 400$ photons/μs which when compared to the derived photoelectron flux, $\Gamma_{pe} = \langle n_{pe} \rangle / \tau_{sample} = 1.5\,\mathrm{p.e.}/\mu\mathrm{s}$, corresponds to a total system efficiency of 0.3%. This value agrees well with a value of 2% for the system optical transmission efficiency estimated during the original diagnostic design multiplied by 15%, the quantum efficiency of the PMT's listed in manufacturer's specifications.

PMT bias (Volts)	$G_{p.e.}$ (Volts/p.e.)	$\delta y/y$ 1 Mhz	$\delta y/y$ 100 kHz
1100	0.30	40%	15%
1200	0.70	60%	20%

Table 2.1: Calibrated system gain (Volts/p.e.) and the corresponding noise level at signal amplitude of one Volt before and after binning the signal from 1 Mhz to 100 kHz.

Rearranging Eqs. 2.3 - 2.4 we obtain,

$$\frac{\delta y}{y} \equiv \left(\frac{\langle y^2 \rangle}{\langle y \rangle^2} - 1 \right)^{\frac{1}{2}} = \left(\frac{2 \Delta f \tau_{samp}}{\langle n_{p.e.} \rangle} \right)^{\frac{1}{2}} = \left(\frac{2 \Delta f \tau_{samp} G_{p.e}}{\langle y \rangle} \right)^{\frac{1}{2}}. \tag{2.6}$$

Table 2.1 shows $G_{p.e.}$ and $\delta y/y$ for two PMT settings at a signal level of one Volt. These levels demonstrate the IDS signal degradation as light levels go down forcing higher PMT bias settings. We have generally found signal levels to be dominated by noise above a setting of 1100 V. By binning n_{bin} adjacent samples together one effectively increases $n_{p.e.}$ by n_{bin} and decreases $\delta y/y$ by $1/sqrt(n_{bin})$. Of course this enhanced signal quality comes at the cos of reduced time resolution. For fluctuation measurements we typically choose $n_{bin} = 10$ retaining all fluctuation power below 50 kHz. For equilibrium flow measurements we may bin to even lower frequencies.

2.3 Data Analysis Techniques

The reduction of the raw emission profiles into ion velocities and temperature occurs in two stages. In the first stage an automated routine fits a Gaussian profile to the measured line shape and writes the moments of that profile to the MST database. § 2.3.1 describes the implementation of this stage. The second stage (§ 2.3.4) converts these moments into temperatures and velocities through an application of the Doppler formula. § 2.3.2 and § 2.3.3 describe two intermediate calculations: the calibration of the unshifted line position and the compensation for broadening of the profile by the single channel transfer function. Finally, § 2.3.5 discusses the propagation of photon noise from the raw signal to the derived quantities.

2.3.1 Nonlinear Curve-Fit Routine

The IDS digitizes a voltage proportional to the emission intensity of the plasma about 16 wavelengths for each view. A robust processing engine, `fit.pro`, has been developed to convert this data into physically meaningful parameters characterizing the broadened, shifted emission line (§ B.1.1). A public front-end, `fit.com`, defines several variables specific to the given run (i.e. emission wavelength, PMT Voltage) before accessing `fit.pro` which then loops through a user defined list of shots. For each shot the engine 1) reads the digitized data, 2) preprocesses each channel using calibrated values, 3) fits a five parameter model to the thermal line profile, and 4) writes the fit parameters to the MST data base for subsequent analysis. The next few paragraphs discuss some details of these four steps primarily for the reference of regular IDS users.

The fit engine uses the raw digitized signals prior to their transform into Volts. Since the IDS employs 12-bit digitizers, $d_i \in [0, 4095]$, where d_i is the raw digitized level of the ith channel. After reading d_i, the fit engine bins the data from 1 Mhz to a frequency specified by the user in `fit.com`. For fluctuation analysis we typically fit the data at 100 kHz while the data for the study of mean flows or poorly lit data may be fit at lower frequencies to reduce noise levels. The binning procedure omits saturated points from the average of each bin while fully saturated bins are set to zero and omitted from the fit. Because the omission of too many saturated points from the averaged bin may distort the bins averaged value, the IDS should be run with PMT bias set to avoid regular saturation. Following binning `fit.pro` subtracts the signal baselines determined from their preshot levels and normalizes the signal using the calibrated value appropriate to the PMT setting.

We model the baselined and normalized data, y_i, with a five parameter function,

$$y_i = A_0 \exp\left(-\frac{1}{2}\left(\frac{x_i - A_1}{A_2}\right)^2\right) + A_3 + A_4 x_i. \tag{2.7}$$

The first three parameters describe a simple Gaussian profile while the last two account for baseline levels of bremsstrahlung radiation. This simple model adequately describes the thermally broadened C V line at 2271 Å used for measurements in this study. Lines with significant non-thermal structure may require refinements to account for pressure

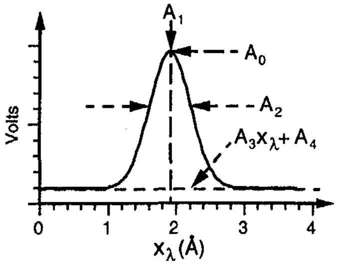

Fig. 2.13.— Gaussian plus linear baseline yield five fit parameters

broadening or fine structure. To determine the moments of y_i, `fit.pro` employs a nonlinear curvefit routine (§ B.1.2) modeled on the general routine described by Bevington (Bevington, 1963). The initial estimates of A_j supplied to the nonlinear routine are given by,

$$A_0 = \max(y_i), \quad A_1 = \frac{\sum y_i x_i}{\sum y_i}, \quad A_2 = \frac{\sum y_i (x_i - A_1)^2}{\sum y_i},$$
$$A_3 = \min(y_i), \quad A_4 = 0. \tag{2.8}$$

Note that we initialize the values of A_1 and A_2 to the centroid and variance of the y_i distribution. In the limit of noiseless data with perfect resolution this guess gives the correct moments of Eq. 2.7. However, these statistical estimates have demonstrated a strong sensitivity to noise in outlying channels producing a large amount of scatter and a systematic over estimation of the variance (Den Hartog, Almagri, and Prager, 1995). This sensitivity arises from the overly general nature of the statistical analysis which fails to incorporate knowledge of the domain of y_i. The nonlinear fit incorporates this knowledge by specifying the model in Eq. 2.7. This has the practical effect of deemphasizing noise in the outer channels and providing cleaner values for A_i.

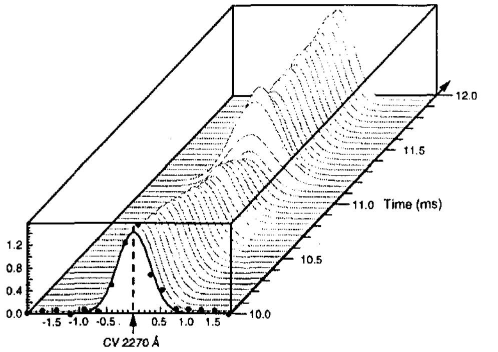

Fig. 2.14.— Fits to 2 ms of IDS data over a sawtooth crash.

The nonlinear convergence algorithm acts to minimize,

$$\chi^2 \equiv \frac{\sum (y_i - f(x_i))^2}{N_{pnt} - N_{par}}, \tag{2.9}$$

where $f(x_i)$ is given by Eq. 2.7, N_{pnt} is the number of points being fit (16), and N_{par} is the number of parameters being fit to (5). This is done through a combination of gradient descent at values far from convergence, and a second order functional minimization of χ^2 at values near convergence. If the values of A_j diverge the routine resets their initial values, perturbs them by a small amount and attempts again to find a convergent solution. If the divergence persists the routine sets A_j to the statistical values determined by Eq. 2.8. The routine records these as negative numbers to inform the user of the points obtained from statistical analysis and those obtained from the nonlinear routine. The measurements presented in this thesis exclude the divergent points from the analysis.

For each shot `fit.pro` saves the fit parameters A_i of each view, the χ^2 of the fits, and a time trace to the MST data base. In addition the wavelength of the emission line, the mass of the impurity ion and the calibrated position of the unshifted wavelength are stored as scalars. Fig. 2.14 shows data fit at 20 kHz spanning 2 ms. The data y_i for the first time point shown is plotted over the fitted Gaussian to illustrate typical fit quality. Note the sawtooth crash near 11 ms which broadens the distribution and increases its amplitude. Physically this corresponds to a sharp spike in the C^{+4} temperature and emissivity. Less visibly the centroids shift to the left at the crash indicating a sharp deceleration of the plasma. The normalized χ^2 varies little over the sawtooth, rising only slightly following the crash.

2.3.2 Calibration of Unshifted Emission Line Position

The Gaussian centroid, A_1, is calculated in Angstroms with respect to the calibrated, relative positions of the 32 single channel transfer functions (Fig. 2.11). To calculate an absolute velocity one needs to calibrate the position on that axis, x_λ, which corresponds to the unshifted wavelength, λ_0, of the observed impurity species. Knowledge of x_λ allows the user to calculate the true wavelength of the shifted centroid, λ_1, as,

$$\lambda_1 = A_1 - x_\lambda + \lambda_0. \tag{2.10}$$

The IDS facilitates the calibration of x_λ by providing for simultaneous measurement of ion velocity along a single toroidal chord from opposing directions. For such a measurement one expects the red/blue shift of the line measured with one view to be equal and opposite to the blue/red shift of the line measured with the opposing view,

$$A_1^{r/b} - x_\lambda = -A_1^{b/r} + x_\lambda. \tag{2.11}$$

This allows for the straight forward calculation of x_λ as,

$$x_\lambda = \frac{1}{2}(A_1^{b/r} + A_1^{r/b}). \tag{2.12}$$

The engine `fit.pro` performs this calibration once for the shot at the beginning of the run, reducing the noise in the calculation by averaging Eq. 2.12 over the shot,

$$x_\lambda = \frac{1}{2}\langle A_1^{b/r} + A_1^{r/b}\rangle_{shot}. \tag{2.13}$$

This value is written with the moments to the database for this and all subsequent shots of the run for use in calculating the flow. The calibration may be further improved by performing a weighted average,

$$x_\lambda = \frac{\sum(A_1^{b/r} + A_1^{r/b})\,w}{2\sum w}, \tag{2.14}$$

where,

$$w = \sqrt{\left(\frac{A_0^{b/r}}{\chi^{b/r}}\right)^2 + \left(\frac{A_0^{r/b}}{\chi^{r/b}}\right)^2} \tag{2.15}$$

By performing the sums in Eq. 2.14 over an ensemble of several shots one may obtain a calibration of x_λ providing single view resolution of the flow to within a few m/s.

Several practical comments concerning the calculation of x_λ are included here for the benefit of future IDS users. First, in performing an ensemble calculation of x_λ or in applying a calibration of x_λ from one point in the run to a different point in the run one must insure that the value of x_λ is truly stationary over the shots in question. At higher Å/turn gearings of the IDS dial, a mechanical drift of the dial position has been observed to produce a slow shot to shot drift in the position of x_λ which can accumulate to an equivalent flow drift of several km/s. This drift may be minimized by setting the gearing of the IDS dial to a lower Å/turn setting prior to the run, by positioning the IDS dial such that its handle points down, and by avoiding bumps to the IDS spectrometer housing during the course of the run. Even with the above precautions separate x_λ calibrations should be made throughout the run to check for drift. Second, for runs employing only the opposing toroidal view setup with both views similarly illuminated calibration of x_λ is unnecessary. For calculation of the ion flow one must calculate,

$$\begin{aligned} \Delta\lambda^{b/r} &= \lambda_1^{b/r} - \lambda_0 = A_1^{b/r} - x_\lambda, \quad \text{or} \\ \Delta\lambda^{r/b} &= \lambda_1^{r/b} - \lambda_0 = A_1^{r/b} - x_\lambda. \end{aligned} \tag{2.16}$$

However, with opposing toroidal views we may combine these expressions with Eq. 2.11 to obtain,

$$\Delta\lambda^{b/r} = -\Delta\lambda^{r/b} = \frac{1}{2}(A_1^{b/r} - A_1^{r/b}). \tag{2.17}$$

This expression which includes only the separation of the two centroids improves the noise statistics of Eq. 2.16 by a factor of $1/\sqrt{2}$ while eliminating the need for x_λ. Eq. 2.16 should only be used when nonopposing views are employed or when light levels (hence noise levels) of the two views differ by a large amount due to lens coatings. Finally, fluctuation studies require no calibration of x_λ as we typically filter mean flow contributions from the signal.

2.3.3 Deconvolution of Transfer Function from $f(\lambda)$

The roughly triangular transfer function of each IDS channel exhibits a FWHM approximately equal to the separation between the channels. The measured intensity distribution is actually a convolution of the thermal distribution and this transfer function. This convolution broadens the measured distribution producing fitted values of A_2

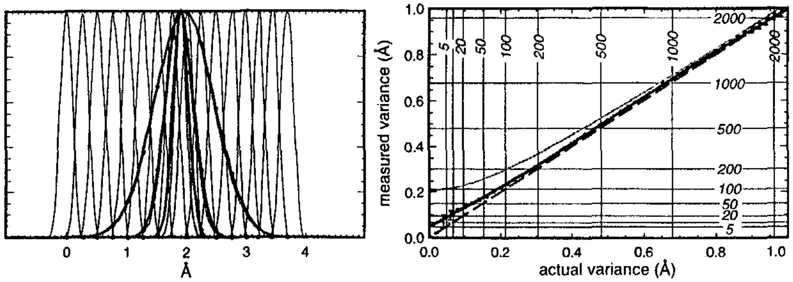

Fig. 2.15.— Finite width transfer functions act to slightly broaden thermal lines. Shown (left) are simulated (gray) and fitted (black) lines of C Vat 20 eV, 100 eV, and 500 eV. Mapping of fitted values (right) is accomplished with polynomial fit to simulated values. Broadening becomes insignificant at high temperatures.

which are systematically larger than the true distribution variance σ_λ. Fig. 2.15a shows the transfer functions for the first 16 IDS channels plotted versus wavelength. Three sets of distributions are plotted over the transfer functions corresponding to C Vtemperatures of 20 eV, 100 eV, and 500 eV. The grey curve in each set corresponds to the original simulated distributions. These distributions were then convolved numerically with the transfer function to obtain a simulated sixteen point measurement. This measurement was then fit as described above to obtain a the Gaussian distribution plotted in black. For each case the fitted distribution is broader than the original though the difference at the two higher temperatures is barely visible. To correct for this broadening we need a mapping from the measured variance to the actual variance of the distribution. Fig. 2.15b shows three mappings for A_2 values corresponding to C Vtemperatures from 5 eV to 2 keV where the dashed line corresponds to the identity map,

$$\sigma_\lambda = A_2. \tag{2.18}$$

By approximating the transfer functions with Gaussians we may analytically calculate this mapping to be, since the convolution of two Gaussians is a Gaussian,

$$\sigma_\lambda = \sqrt{A_2^2 - \sigma_{t.f.}^2}, \tag{2.19}$$

where $\sigma_{t.f.}$ is the typical variance of a Gaussian fit to the measured transfer functions. This mapping is shown with the grey line in Fig. 2.15b for a $\sigma_{t.f.} \approx 0.2$. Note, this curve would map an apparent temperature of 100 eV down to an actual temperature of 10 eV though the effect becomes less dramatic at higher temperatures. To test Eq. 2.19 we performed simulated measurement over the range of variances shown to obtain an empirical mapping. Surprisingly, this mapping, shown in black, is much closer to the identity map of Eq. 2.18 than the quadratic map of Eq. 2.19. This result currently lacks a satisfactory explanation although suspicion centers on the discrete sampling of the convolved Gaussian by the 16 channels. By fitting a third order polynomial to the simulated points we are able to apply this mapping to A_2 before converting those values to temperatures

2.3.4 Doppler Formula

After calculating $\Delta\lambda$ and σ_λ from A_1 and A_2 as described above, we may describe the distribution of radiated light as,

$$f(\lambda) \propto \exp\left(-\frac{(\lambda - \lambda_0 - \Delta\lambda)^2}{2\sigma_\lambda^2}\right). \tag{2.20}$$

To convert Eq. 2.20 into a velocity distribution we employ the Doppler formula,

$$v = \left(\frac{\lambda - \lambda_0}{\lambda_0}\right) c, \tag{2.21}$$

to rewrite Eq. 2.20 as,

$$f(v) \propto \exp\left(-\frac{\left(v - \frac{c\Delta\lambda}{\lambda_0}\right)^2}{2\left(\frac{c\sigma_\lambda}{\lambda_0}\right)^2}\right). \tag{2.22}$$

We may use this distribution to solve for the expectation value of v,

$$\langle v \rangle = \frac{\int dv\, v\, f(v)}{\int dv\, f(v)} = \frac{c\Delta\lambda}{\lambda_0}, \tag{2.23}$$

and the expectation value of v^2,

$$\langle v^2 \rangle = \frac{\int dv\, v^2 f(v)}{\int dv\, f(v)} = \left(\frac{c\sigma_\lambda}{\lambda_0}\right)^2. \tag{2.24}$$

Thus, $\Delta\lambda$ and σ_λ yield our impurity velocity and temperature respectively as,

$$v_Z = \frac{c\Delta\lambda}{\lambda_0} \approx 3.0 \times 10^5 \left(\frac{\Delta\lambda}{\lambda_0}\right) \text{km/s}, \tag{2.25}$$

$$T_Z = m_Z \left(\frac{c\sigma_\lambda}{\lambda_0}\right)^2 \approx 9.3 \times 10^8 m_Z \left(\frac{\sigma_\lambda}{\lambda_0}\right)^2 \text{eV}, \tag{2.26}$$

where all wavelengths are in Angstroms and m_{ion} is in amu. These calculations performed in the post-processing routine `[jchapman.public.flow]flow.pro` (§ B.1.3).

2.3.5 Error Propagation

Optical noise in the raw IDS signal propagates through the nonlinear fit routine to produce substantial noise levels in the the centroid and variance returned by the routine. We have relied on montecarlo simulation techniques to observe the behavior of the error propagation. For these simulations we generated thermal distributions corresponding to C Vdistributions with temperatures from 50 eV to 500 eV and random velocities of several km/s. To these distributions we added white Poisson noise of various levels to simulate the optical noise in the input channels. We discovered that $\hat{\chi}$ defined as,

$$\hat{\chi} \equiv \frac{\sqrt{\chi^2}}{A_0}, \tag{2.27}$$

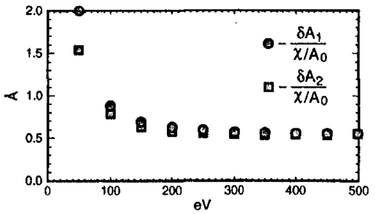

Fig. 2.16.— Simulations yield output noise levels which vary directly with the normalized χ^2 of the fit. Both moments show similar sensitivity at medium to high temperatures.

varied roughly linearly with the level of the input noise. However, this dependence varied somewhat with the distribution of the photon statistics in the simulated noise. In addition for all noise models the increase of $\hat{\chi}$ became more aggressive at large noise levels as the fits became marginally divergent. This behavior at large noise levels motivates the binning of the raw data to the lowest frequency feasible prior to fitting the profiles as opposed to binning the output high frequency, noisy fits. A second, more robust, result was that at a given temperature the uncertainty in both A_1 and A_2 exhibited a strong linear dependence on $\hat{\chi}$. This result held for the full range of temperatures and for various models of input noise. Fig. 2.16 shows the slope of the dependence for both moments plotted against the temperature of the simulated distribution. Note that the slope varies little for moderate to high temperatures while it blows up at low temperatures where the width of the distribution becomes comparable to the channel spacing. Surprisingly, both moments exhibit the same absolute error for a given $\hat{\chi}$ above 100 eV given roughly by,

$$\delta A_1 \approx \delta A_2 \approx \frac{\hat{\chi}}{2}. \tag{2.28}$$

When one then propagates δA_1 and δA_2 through Eqs. 2.25–Eq. 2.26, one obtains a relative sensitivity of ion velocity to input noise which is far stronger than the sensitivity of temperature as $\Delta\lambda \ll \sigma_\lambda$. In practice these simulation results have led us to measure the noise floor of the ion velocity power spectrum to characterize the overall noise power, and then to distribute that power in time proportional to $\hat{\chi}(t)$ (Eq. 2.27).

2.4 Minority Species Dynamics

Difficulties stemming from Hydrogen's 13.6 eV ionization potential impede direct spectroscopic measurements of the majority species. Almost all of the Hydrogen ionizes in the cool plasma edge producing an intensity distribution dominated by a large cold spike. Charge exchange of core ions does produce a hot secondary distribution reflecting dynamics in the MST interior. However, this effect may only be resolved in the wings of the total distribution after several e-foldings of the cold primary distribution. Attempts to characterize the temperature of this secondary distribution have been inconclusive as the low radiation levels in the wings of the hot distribution barely register with the IDS. An effort to discern ion flow from this distribution would prove daunting, and resolving fast fluctuations in that flow more daunting still. Consequently, the IDS design optimally resolves UV radiation emitted from ionized minority species intrinsic to the MST plasma. These species possess a wide range of ionization potentials allowing measurement of different regions in the plasma through the selection of different spectral lines.

2.4.1 Perpendicular Flow for Different Species

Our desire to characterize the flow behavior of the majority species motivates us to relate this behavior to that of the observed minority species. A simple general argument may be advanced from the equation governing the perpendicular flow in each species,

$$\mathrm{v}_{Z,\perp} = \frac{\mathbf{E}\times\mathbf{B}}{B^2} + \frac{\mathbf{B}\times\hat{r}\, p_Z'}{eB^2\, Zn_Z}, \tag{2.29}$$

where the prime denotes a radial derivative. Simple estimates of Eq. 2.29 indicates the flow over the interior of the plasma to be driven predominantly by the species independent $\mathbf{E}\times\mathbf{B}$ term. In addition we anticipate the velocity fluctuations contributing to the dynamo to be $\tilde{\mathbf{E}}\times\mathbf{B}$ (§ 1.2.2) driven, suggesting that the fluctuation results presented here may be generalized to the majority species. Near the edge, pressure gradients become significant yielding a nontrivial diamagnetic contribution. The diamagnetic term may be expanded as,

$$\mathrm{v}_{Z,\nabla p} = \frac{\mathbf{B}\times\hat{r}\, T_Z}{eB^2 Z}\left(\frac{n_Z'}{n_Z} + \frac{T_Z'}{T_Z}\right), \tag{2.30}$$

yielding a dependence on the normalized temperature and density gradients with an overall multiplier of T_Z/Z. In general T_i evolves gradually and we can expect through thermal equilibration that $T_Z \approx T_i$[2], reducing the dependence of the second term to T_i'/Z. This effect should predominate near the edge where T_i drops dramatically potentially yielding an under-representation of the bulk flow $(Z =^{+} 1)$ by the minority species $(Z \sim^{+} 2)$. The second term depends on the normalized derivative of the emission profile which varies widely amongst species. Species like C^{+4} which radiate near the core tend to have broad emission profiles with correspondingly small values of n_Z'/n_Z. On the other hand, species like CIII radiate from narrow shells near the edge with two large gradients in n_Z delineating their radial boundaries. These gradients produce opposing $\mathrm{v}_{Z,\nabla p}$'s of roughly equal magnitudes separated by only a few cm's . As the IDS line of sight will pass through both flows this contribution should nearly cancel producing only a slight broadening in the measured line profile.

---

[2] While thermalization does not hold $T_Z \approx T_i$ during a sawtooth crash when ion heating proceeds more rapidly than energy thermalization, CXA measurements of T_i during the crash indicate that the majority species exhibits sawtooth dynamics similar to those observed in the minority.

n_i $(10^{19}\mathrm{m}^{-3})$	T_i (eV)	$\bar{\nu}_S^{\alpha/i}$ (kHz)			
		C^{+4}	C^{+2}	B^{+3}	O^{+4}
0.2	20	33.5	8.4	20.9	25.1
0.5	120	5.7	1.4	3.6	4.3
0.8	200	4.2	1.1	2.6	3.2
1.1	350	2.5	0.6	1.6	1.9

Table 2.2: $\bar{\nu}_E^{\alpha/i}$ for edge plasma and three core plasma conditions with $m_i = Z_i = 1$ and $\ln\Lambda_{\alpha i} = 16$.

2.4.2 Energy and Momentum Relaxation

Eq. 2.29 omits cross-species collisional terms which could produce parallel flows in MST similar in magnitude to $v_\perp$. These collisional terms also act to equilibrate the temperature between species. Here we will determine the typical relaxation rates for the energy and momentum of two different thermal species. The energy relaxation rate for two thermal distributions is given by the expression (Callen, 1997),

$$\bar{\nu}_E^{\alpha/\beta} = \frac{n_\beta\, q_\alpha^2 q_\beta^2\, \ln\Lambda_{\alpha\beta}}{\pi^{\frac{3}{2}}\epsilon_o^2\, m_\alpha m_\beta\, v_{T_{\alpha\beta}}^3}, \tag{2.31}$$

where,

$$v_{T_{\alpha\beta}} \equiv (v_{T_\alpha}^2 + v_{T_\beta}^2)^{\frac{1}{2}} = \left(\frac{2T_\alpha}{m_\alpha} + \frac{2T_\beta}{m_\beta}\right)^{\frac{1}{2}}. \tag{2.32}$$

From Eq. 2.32 we can see that the minority species will equilibrate far more rapidly to the ion fluid than the electron fluid with,

$$\bar{\nu}_E^{\alpha/i} \approx \left(\frac{m_i}{m_e}\right)^{\frac{3}{2}} \bar{\nu}_E^{\alpha/e}. \tag{2.33}$$

	λ_Z (Å)	Z	m_Z (amu)	U_Z (eV)
C III	2296.9	$^{+}2$	12.011	47.9
O V	2781.0	$^{+}4$	15.999	113.9
B IV	2821.7	$^{+}3$	10.811	259.3
C V	2270.9	$^{+}4$	12.011	392.0

Table 2.3: The wavelength, charge, mass, and ionization potential for the four commonly observed impurity emission lines.

For the case of an impurity species equilibrating with the majority ions Eq. 2.31 becomes,

$$\bar{\nu}_E^{\alpha/i} = \frac{n_i\, e^4\, Z_\alpha^2 Z_i^2\, \ln\Lambda_{\alpha i}}{\pi^{\frac{3}{2}}\, \epsilon_o^2\, m_\alpha m_i\, v_{T_{\alpha i}}^3} \approx 2\times 10^6 \left(\frac{n_i\, m_i^{\frac{1}{2}}\, Z_\alpha^2 Z_i^2 \ln\Lambda_{\alpha i}}{m_\alpha T_i^{\frac{3}{2}}}\right)\ \mathrm{s}^{-1}, \tag{2.34}$$

where,in the final expression, masses are given in amu, temperatures in eV, and densities in $10^{19}\mathrm{m}^{-3}$. Eq. 2.34 assumes $T_\alpha \approx T_i$ and $m_\alpha \gg m_i$ allowing the approximation of Eq. 2.32 by $v_{T_{\alpha i}} \approx (2T_i/m_i)^{1/2}$. The momentum relaxation rate of two thermal species is given by

$$\bar{\nu}_S^{\alpha/\beta} = \frac{n_\beta\, q_\alpha^2 q_\beta^2\, \ln\Lambda_{\alpha\beta}}{3\pi^{\frac{3}{2}}\, \epsilon_o^2\, m_\alpha m_{\alpha\beta}\, v_{T_{\alpha\beta}}^3}, \tag{2.35}$$

where,

$$m_{\alpha\beta} \equiv \frac{m_\alpha m_\beta}{m_\alpha + m_\beta}. \tag{2.36}$$

Thus the momentum relaxation rate of the minority species with the bulk ions is given by,

$$\bar{\nu}_S^{\alpha/i} = \frac{n_i\, e^4\, Z_\alpha^2 Z_i^2\, \ln\Lambda_{\alpha i}}{3\pi^{\frac{3}{2}}\, \epsilon_o^2\, m_\alpha m_{\alpha i}\, v_{T_{\alpha i}}^3} \approx \frac{\bar{\nu}_E^{\alpha/i}}{3} \approx 7\times 10^5 \left(\frac{n_i\, m_i^{\frac{1}{2}}\, Z_\alpha^2 Z_i^2 \ln\Lambda_{\alpha i}}{m_\alpha T_i^{\frac{3}{2}}}\right)\ \mathrm{s}^{-1}. \tag{2.37}$$

where we again assume $m_\alpha \gg m_i$ for which Eq. 2.36 simplifies to $m_{\alpha i} \approx m_i$. Note that the ion velocity equilibrates roughly three times more slowly than the ion energy.

Table 2.2 shows approximate momentum relaxation rates for four commonly observed impurity species in different plasma conditions. The top row is representative of cool edge conditions while the remaining three rows match the hotter conditions in the core for increasing plasma current. The bulk plasma flow typically equilibrates with impurities in < 1 ms, fast enough to insure that the mean parallel flows and temperatures of different species match over the shot. However, collisional equilibration alone does not insure that rapid ($\sim 10\mu$s) dynamics at the sawtooth crash proceed identically in all species.

2.4.3 Impurity Emission Profiles

Limited control over the spatial resolution of the IDS is achieved through the selection of the impurity species viewed. While impurities like C^{+4} with high ionization potentials should be found predominantly in the MST core, easily ionized species like C III should be constrained to a relatively thin shell near the plasma edge. The Impurity Monochromator Array (IMA) was developed to measure these distributions by collecting light along five poloidal chords (Woehrer, 1996). The impact parameters of the chords extends from $r_i/a = 0.00$ to $r_i/a = 0.82$ providing reasonable coverage of the core region and comparatively poor resolution of the edge. Light collected along the five chords is transmitted through fiber optics to the monochromators where radiation of the desired wavelength is converted by PMT's into the measured signal. A coarse relative calibration of the five PMT's is improved by rotating the chords viewed by each PMT every few shots and analyzing the data in an ensemble which spans several rotations.[3] Light levels from the five channels are then inverted into an eleven point profile using a procedure which combines a spline fit with Abel inversion.

---

[3] I have developed an improved *in situ* calibration procedure which may be conducted at the beginning of the run to avoid rotation. The code associated with this procedure may be found in `[jchapman.public.imp_ mono]cal_ mono.pro`.

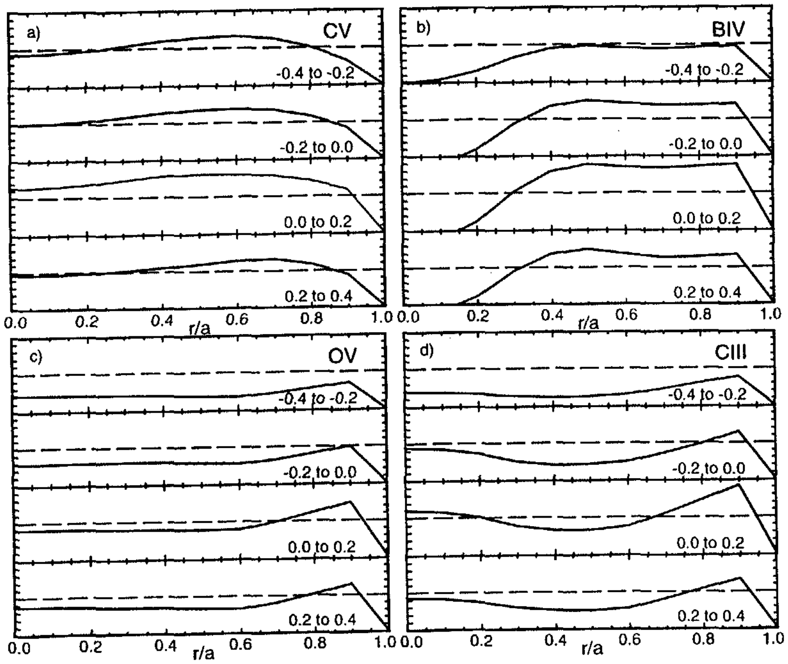

Fig. 2.17.— Inverted impurity emission profiles of a) C V, b) BIV, c) OV, and d) CIII averaged over 0.2 ms windows relative to the sawtooth crash. The dashed lines is drawn to assist visual comparison of same species distributions.

Fig. 2.17 shows the five chord inverted profiles for the four impurities commonly measured by the IDS (Table 2.3). The profiles were averaged over four 200 μs long windows centered about the sawtooth. C V is the most broadly distributed with significant emission from the core, though the peak emission occurs at $r/a \approx 0.6$. BIV also emits from a broad region though its profile is more hollow. While profiles of both OV and CIII are edge peaked and therefore poorly resolved, the ratio of light from the outer to inner chord is higher for CIII indicating that it is more edge peaked. The rise in the CIII profile near the core is probably an artifact of the inversion process coupled with errors in the normalization. While radiation levels rise overall at the sawtooth crash their radial distributions exhibit little change allowing the conclusion that the radial location of the IDS measurements remains stationary over the sawtooth cycle.

2.4.4 Flow and Temperature Profiles

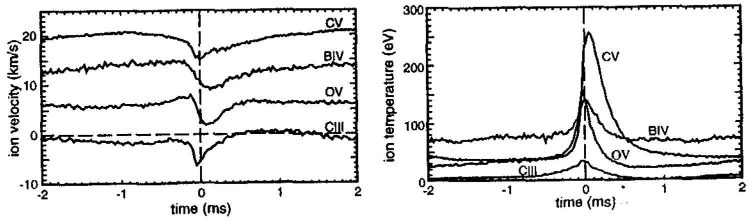

Fig. 2.18.— Impurity a) flow and b) temperature over a sawtooth crash shows core species flowing more rapidly at higher temperatures than those near the edge.

Fig. 2.18 shows the measured toroidal flows and temperatures of the four impurity species ensembled over a sawtooth crash. The flow speed of the impurities decreases as one moves from the core to the edge of the plasma with CIII actually flowing in a direction opposite to that of the core ions. The direction of the core ions corresponds to an $E_r \times B_\theta$ drift as indicated in Eq. 2.29. At the sawtooth crash the ion flow decelerates ~ 5 km/s for each of the species. This does not appear to represent a locking to the lab frame as evidenced by CIII which actually accelerates relative to the shell at the crash. The deceleration appears abruptly in the edge species and then appears to propagate inward toward the core. The deceleration may produced by the viscous coupling of the ion fluid with the core tearing modes. The temperature profiles all exhibit the anomalous heating spike at the sawtooth crash. Note the temperatures of the ions are colder towards the edge with the CIII temperature of order 10 eV. Finally, note the temperature of the impurities peaks later as we move toward the core of the plasma.

2.5 Passive Chord Averaging

While passive collection of radiation enables nonperturbing measurements of core dynamics, the chord averaged nature of the measurement compromises the spatial resolution of the IDS. The IDS line of sight averages over small scale fluctuation structures and attenuates low k structures by a factor that depends on both the wavenumber of the mode and its radial structure. In addition the simultaneous sampling of different phases of the velocity fluctuation raises the question of how the ultimate phase of the chord averaged measurement relates to the phase at a known reference point. Finally, we expect toroidal, poloidal, and radial chords to measure $\tilde{v}_\phi$, $\tilde{v}_\theta$, and $\tilde{v}_r$, respectively. However, casual inspection reveals nonzero projections of $\hat{r}$ and $\hat{\theta}$ onto the toroidal chord and $\hat{r}$ onto the poloidal chord. How does the chord blend these different components together? This section develops exact expressions relating the chord averaged IDS measurements to to the local velocity fluctuation structures. These expressions embody two key results. First, a line integral of $\tilde{\mathbf{v}}$ over the line of sight may be replaced by a radial

convolution with a known instrument function, w_n. Second, the phase of the chord averaged measurement matches the local fluctuation phase at a point of symmetry defined below. Later in this thesis these results will enable an estimation of the relative phase and amplitude of $\langle \tilde{v}\tilde{b} \rangle$ in the core.

In the following sections we first demonstrate analytically that by fitting a Gaussian profile to a chord averaged emission profile, we effectively recover the line averaged velocity and temperature of the observed impurity. Next, we employ this result in outlining the general procedure for calculating the instrument function of a line of sight. We then derive and present w_n for the toroidal chord, followed by an analogous, though far simpler, presentation for the poloidal and radial chords.

2.5.1 Integrated Emission Profiles

The distribution in wavelength of line radiation from the observed impurities should be a Doppler broadened and shifted Gaussian, provided thermal broadening dominates other sources of line structure. We represent this distribution at some point l with the expression,

$$f(\lambda, l) = A_f(l) \exp\left(\frac{-(\lambda - \lambda_f(l))^2}{2\sigma_f^2(l)}\right). \tag{2.38}$$

The IDS integrates $f(\lambda, l)$ along its line of sight obtaining,

$$\langle f(\lambda) \rangle = \int dl f(\lambda, l), \tag{2.39}$$

which is not generally Gaussian. For example, the "two temperature" distribution of the H_α line exhibits a large narrow distribution corresponding to ionization at the cool edge. However, away from the spike, the wings of the distribution correspond to hot, charge-exchange ions in the core. Despite this fact, we routinely observe integrated distributions of core and edge impurities to be extremely well fit by a Gaussian function, providing ion velocities and temperatures which we believe to reflect local ion dynamics. In the following paragraphs we derive expressions relating the moments of the Gaussian fit of $\langle f(\lambda)\rangle$ to the local moments of the impurity emission. These expressions confirm that, to good approximation, the moments of the fit correspond to the line integrated moments of the local distribution.

Here we derive these moments providing intuitive results, modified only slightly by the more rigorous treatment which follows. First we define the intensity of impurity emission at a point along the line of sight by the integral of $f(\lambda)$ over λ,

$$I_f(l) = \int d\lambda f(\lambda, l) = \sqrt{2\pi}\sigma_f(l)A_f(l), \tag{2.40}$$

where $f(\lambda)$ is a Gaussian with local amplitude, $A_f(l)$, and variance, $\sigma_f(l)$. Now we retrieve the centroid of the the line-integrated distribution by calculating its first moment with λ,

$$\langle\lambda_f\rangle = \frac{\int d\lambda\lambda \int dl f(\lambda, l)}{\int d\lambda \int dl f(\lambda, l)} = \frac{\int dl I_f(l)\lambda_f(l)}{\int dl I_f(l)}, \tag{2.41}$$

where $\lambda_f(l)$ is the local centroid of $f(\lambda)$. This matches our expectation that the centroid of $\langle f(\lambda)\rangle$ equals the path averaged centroid of $f(\lambda)$ weighted by $I_f(l)$. Calculating the second moment of $\langle f(\lambda)\rangle$ we find,

$$\langle\sigma_f\rangle = \frac{\int d\lambda(\lambda - \langle\lambda_f\rangle_l)^2 \int dl f(\lambda, l)}{\int d\lambda \int dl f(\lambda, l)} = \frac{\int dl I_f(l)\left(\sigma_f^2(l) + (\lambda_f(l) - \langle\lambda_f\rangle_l)^2\right)}{\int dl I_f(l)}. \tag{2.42}$$

The first term on the RHS gives the chord averaged variance of $f(\lambda)$ weighted by $I_f(\lambda)$ in direct analogy to Eq. 2.41. The second term reflects the broadening of the integrated distribution by variations in the velocity profile over the line of sight. A instance of such broadening was mentioned for the case of CIII which exhibits opposite diamagnetic flows

of similar magnitude at the boundaries of its emission shell. In a limiting case of two CIII shells of equal brightness moving with respect to each other at 10 km/s, the broadening due to this term yields a temperature enhancement of ~ 1.5 eV. Thus, except for cases of cold ions with extremely sheared velocity profiles, this term should be dominated by the line averaged variance.

As discussed in §2.3 the distribution moments calculated directly from $\langle f\rangle_l$ prove overly sensitive to noise in the distribution. Therefore, we fit the distribution to a Gaussian, $g(\lambda)$, and employ the moments of that Gaussian in our subsequent calculations. Here we derive rigorous expressions for these moments by performing analytically what `fit.pro` performs numerically. This entails minimizing,

$$\chi^2 = \int d\lambda (g - \langle f\rangle_l)^2, \tag{2.43}$$

with respect to the amplitude (A_g), centroid (λ_g), and variance (σ_g) of $g(\lambda)$. Setting the partial derivatives of χ^2 with respect to the three parameters equal to zero, yields the minimization condition,

$$\int d\lambda\, \lambda^m g\, \langle f\rangle_l = \int d\lambda\, \lambda^m g^2, \quad m \in \{0, 1, 2\}. \tag{2.44}$$

We may perform the RHS integrals easily to obtain the moments of g^2. To evaluate the LHS integrals we place the product $g\,\langle f\rangle_l$ into the form of a Gaussian,

$$g\,\langle f\rangle_l = \int dl\ A_{fg} \exp\left(-\frac{(\lambda - \lambda_{fg})^2}{2\sigma_{fg}^2}\right), \tag{2.45}$$

where,

$$A_{fg} = A_g A_f \exp\left(-\frac{(\lambda_f-\lambda_g)^2}{2(\sigma_f^2+\sigma_g^2)}\right), \qquad (2.46)$$

$$\lambda_{fg} = \frac{\sigma_g^2\lambda_f+\sigma_f^2\lambda_g}{\sigma_f^2+\sigma_g^2} \qquad (2.47)$$

$$\sigma_{fg} = \frac{\sigma_f\sigma_g}{(\sigma_f^2+\sigma_g^2)^{1/2}}. \qquad (2.48)$$

The near unity exponential term in Eq. 2.46 results from completing the square to obtain the Gaussian exponent of Eq. 2.45. Using Eq. 2.45 - 2.48 we may evaluate the LHS of Eq. 2.44 to obtain three simultaneous equations:

$$\sqrt{2}\int dl A_{fg}\sigma_{fg} = A_g^2\sigma_g, \qquad (2.49)$$

$$\sqrt{2}\int dl A_{fg}\sigma_{fg}\lambda_{fg} = A_g^2\sigma_g\lambda_g, \qquad (2.50)$$

$$\sqrt{2}\int dl A_{fg}\sigma_{fg}(\lambda_{fg}^2+\sigma_{fg}^2) = A_g^2\sigma_g(\lambda_g^2+\sigma_g^2/2). \qquad (2.51)$$

These equations may be combined and rearranged to obtain implicit expressions for λ_g and σ_g:

$$\lambda_g = \frac{\int dl\, I'_f\,\lambda_f}{\int dl\, I'_f}, \qquad (2.52)$$

$$\sigma_g^2 = \frac{\int dl\, I'_f\,\left(\sigma_f^2+2(\lambda_f^2-\lambda_g^2)-\frac{2(\lambda_f-\lambda_g)^2}{1+\sigma_g^2/\sigma_f^2}\right)}{\int dl\, I'_f}. \qquad (2.53)$$

The weighting function, I'_f, is given by,

$$I'_f = \sqrt{2\pi}A_f\,\sigma_f \exp\left(-\frac{(\lambda_f-\lambda_g)^2}{2(\sigma_f^2+\sigma_g^2)}\right)\left(\frac{1}{2}+\frac{\sigma_f^2}{2\sigma_g^2}\right)^{-\frac{3}{2}}. \qquad (2.54)$$

This differs from I_f (Eq. 2.40) by two factors which deviate weakly from unity where $f(\lambda, l)$ deviates from $g(\lambda)$. Except for these small corrections to I'_f, Eq. 2.52 replicates Eq. 2.41. Likewise, Eq. 2.53 mirrors Eq. 2.42 except for the the weak dependence on velocity dispersion. For realistic plasmas this amounts to a small correction to an already small correction. Because the corrections to Eq. 2.52 - 2.53 are both impossible to calculate from the data and tiny relative to the random error from the optical noise, we shall ignore them in subsequent calculations. Instead, derivations in the following sections assume $\lambda_g \approx \langle\lambda_f\rangle_l$ and $\sigma_g \approx \langle\sigma_f\rangle_l$.

2.5.2 IDS Instrument Functions

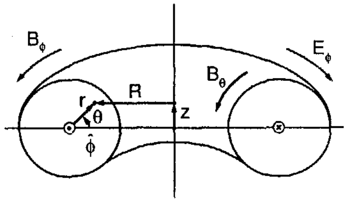

Fig. 2.19.— Toroidal geometry used for calculations.

The measurement of global velocity fluctuations with a chord-averaging, passive diagnostic constitutes a key experimental innovation of this work. This section develops a method to calculate instrument functions relating the amplitude and phase of chord averaged velocity fluctuations to the local amplitude and phase of the fluctuation in the plasma interior. For these calculations we represent velocity fluctuations by their Fourier components,

$$\tilde{\mathbf{v}} = \sum_{m,n}\sum_{j} v_{m,n,j}\; e^{i(m\theta+n\phi+\omega_{m,n}t+\delta_{m,n,j})}\;\hat{j}, \qquad (2.55)$$

where $m \in \{0,1\}$, $n \in \{0,5,6,7,\dots\}$, and $\omega_{m,n}$ is the natural frequency of the mode. All calculations employ the right-handed geometry shown in Fig. 2.19 which reverses the sense of the poloidal angle from that of the MST naming convention. For these, both $v_{m,n,j}$ and $\delta_{m,n,j}$ are considered arbitrary functions of radius which are constant on a flux surface.

We now consider the chord averaged value of a single Fourier component from the sum in Eq. 2.55. For a particular chord the chord average may be written,[4]

$$\tilde{v}_x = \frac{1}{2L_x}\int_{-L_x}^{+L_x} dl_x\, I_Z \sum_j \tilde{v}_j\, \hat{l_x}\cdot\hat{j}, \tag{2.56}$$

where, for convenience, we omit the normalization integral of the impurity emission, I_Z and drop the m and n subscripts. In these expressions $x \in \{T, P, R\}$, where T, P, and R are labels for the toroidal, poloidal, and radial chords respectively. We may expand the jth component of the sum in Eq. 2.56 yielding,

$$\begin{aligned} \tilde{v}_{x,j} &= \frac{1}{2L_x}\int_{-L_x}^{+L_x} dl_x\, I_Z\, v_j e^{i\delta_j}\, e^{i(m(\theta-\theta_x)+n(\phi-\phi_x))}\, \hat{l_x}\cdot\hat{j} \\ &\qquad \times\, e^{i(m\theta_x+n\phi_x+\omega t)}, \end{aligned} \tag{2.57}$$

where we have extracted the fixed angles θ_x and ϕ_x from the integral. We define these angles to satisfy the symmetry conditions,

$$\theta_x = (\theta(l_x) + \theta(-l_x))/2, \tag{2.58}$$

$$\phi_x = (\phi(l_x) + \phi(-l_x))/2. \tag{2.59}$$

Physically, this symmetry anchors the phase of the chord averaged signal to the local fluctuation phase at $\theta = \theta_x$, $\phi = \phi_x$ by insuring the exact cancellation of phase contributions from l_x by those at $-l_x$. Mathematically, the symmetry permits Eq. 2.57 to be rewritten as,

$$\tilde{v}_{x,j} = \frac{1}{a}\int_{r_{o,x}}^{a} dr\, I_Z\, v_j e^{i\delta_j}\, w_{j,x}\, e^{i(m\theta_x+n\phi_x+\omega t)}, \tag{2.60}$$

where $r_{o,x}$ is the impact radius of the chord. The instrument function, $w_{j,x}$, incorporates three effects: the projection of $\hat{j}$ onto the line of sight, the radial weighting of the line of sight (dl_x/dr), and the intersection of the m, n mode with the line of sight. Each effect depends solely on the known geometry of the chord, making it possible to calculate $w_{j,x}$ exactly. By casting the line integral into the form of Eq. 2.60 we have converted the complex and somewhat arduous task of accounting for a line integral into the one-time task of calculating $w_{j,x}$ for each chord. Substituting Eq. 2.60 back into Eq. 2.56 we obtain the complete expression,

$$\tilde{v}_x = \sum_{m,n}\frac{1}{a}\int_{r_{o,x}}^{a} dr\, I_Z \sum_j \left(v_{m,n,j} e^{i\delta_{m,n,j}}\, w_{m,n,j,x} e^{i(m\theta_x+n\phi_x)}\right) e^{i\omega t}. \tag{2.61}$$

This expression contains the properly weighted contribution of each component and each Fourier mode to the measured signal.

We may also be interested in the sensitivity of the chord to modes parallel and perpendicular to the mean magnetic field. Given a model of $\mathbf{B}$, the appropriate instrument function may be determined readily from the geometric functions derived above. Using a cylindrical model of the mean field where, $\mathbf{B} = B_\theta(r)\hat{\theta} + B_\phi(r)\hat{\phi}$, the parallel ($\|$), cross-field ($\wedge$), and perpendicular ($\perp$) instrument functions are given by:

$$w_{\|,x} = \hat{b}\cdot\mathbf{w} = (B_\phi w_{\phi,x} + B_\theta w_{\theta,x})/B, \tag{2.62}$$

$$w_{\wedge,x} = (\hat{r}\times\hat{b})\cdot\mathbf{w} = (B_\theta w_{\phi,x} - B_\phi w_{\theta,x})/B, \tag{2.63}$$

$$w_{\perp,x} = \hat{r}\cdot\mathbf{w} = w_{r,x}. \tag{2.64}$$

---

[4] This expression employs Eq. 2.41 to equate the measured centroid of the integrated intensity distribution to the the line averaged centroid of the local distribution weighted by the local emission intensity.

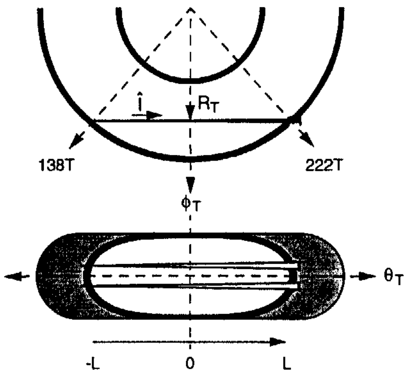

Fig. 2.20.— Toroidal view.

These calculations also may be performed for two dimensional toroidal equilibria, though results should vary little from the cylindrical estimation.

2.5.3 Toroidal Chord Instrument Functions

Velocity fluctuation measurements with the toroidal chord ($x \to T$), employ the setup shown in Fig. 2.20. With ϕ_T set to the angle bisecting the toroidal chord this view obeys the odd symmetry condition of Eq. 2.59. However, $\theta(l)$ exhibits an even symmetry about this midpoint making Eq. 2.58 impossible to satisfy with a single chord. We surmount this difficulty by measuring fluctuations simultaneously with chords placed above and below the midplane. We then average the signal from each view adding a second integral to Eq. 2.57 for the additional view. This composite integral retains the single-chord toroidal symmetry about ϕ_T while achieving the missing poloidal symmetry

with,

$$\theta_T = (\theta^{top}(l_T) + \theta^{bot}(l_T))/2 = \pi. \tag{2.65}$$

Physically toroidal phase contributions from one half of each chord exactly cancel contributions from the other half, while poloidal phase contributions from the top chord cancel contributions from the bottom chord.

The projections of $\hat{\phi}$, $\hat{\theta}$, and $\hat{r}$ onto $\hat{l_T}$ are given by,

$$\hat{l_T} \cdot \hat{\phi} = +\cos(\phi - \phi_T), \tag{2.66}$$

$$\hat{l_T} \cdot \hat{\theta} = -\sin(\phi - \phi_T)\,\sin(\theta - \theta_T), \tag{2.67}$$

$$\hat{l_T} \cdot \hat{r} = +\sin(\phi - \phi_T)\,\cos(\theta - \theta_T), \tag{2.68}$$

where we have chosen to align $\hat{l_T}$ and $\hat{\phi}$ at ϕ_T. Inserting Eq. 2.66 with Eq. 2.57, modified to include both chords, we employ the symmetry about $\theta - \theta_T$ and $\phi - \phi_T$ to collapse the composite integral over two chords into a single integral over half of one chord,

$$\begin{aligned}\tilde{v}_{T,\phi} &= \frac{1}{L_T}\int_0^{L_T} dl_T\, I_Z\, v_\phi e^{i\delta_\phi} \cos(m(\theta - \theta_T))\cos(n(\phi - \phi_T))\,\cos(\phi - \phi_T) \\ &\quad \times e^{i(m\theta_T + n\phi_T + \omega t)}.\end{aligned} \tag{2.69}$$

Likewise, inserting Eqs. 2.67-2.68 we obtain analogous expressions for $\tilde{v}_{T,\theta}$ and $\tilde{v}_{T,r}$. Changing the variable of integration from l_T to r these expressions may be cast into the form of Eq. 2.60,

$$\tilde{v}_{T,j} = \frac{1}{a}\int_{r_{o,T}}^{a} dr\, I_Z\, v_\phi e^{i\delta_j}\, w_{T,j} \quad e^{i(m\theta_T + n\phi_T + \omega t)}, \tag{2.70}$$

where $r_{o,T} \approx 0.3\,a$. The instrument functions, $w_{T,j}$, are given by,

$$w_{T,\phi} \;=\; g_T \cos(m(\theta-\theta_T))\cos(n(\phi-\phi_T))\cos(\phi-\phi_T), \tag{2.71}$$

$$w_{T,\theta} \;=\; g_T \sin(m(\theta-\theta_T))\sin(n(\phi-\phi_T))\sin(\phi-\phi_T)\sin(\theta-\theta_T), \tag{2.72}$$

$$w_{T,r} \;=\; i g_T \cos(m(\theta-\theta_T))\sin(n(\phi-\phi_T))\sin(\phi-\phi_T)\cos(\theta-\theta_T). \tag{2.73}$$

The function g_T contains radial weighting of the line,

$$g_T = \frac{a}{L_T}\frac{dl_T}{dr} = \frac{a\,r\,R}{L_T\,(R^2-R_T^2)^{\frac{1}{2}}\,(R-R_o)}, \tag{2.74}$$

where the two divergences reflect tangencies to $\hat{\phi}$ at R_T and $\hat{\theta}$ at R_o. The terms containing m and n produce the "averaging out" of high k fluctuations and determine the attenuation of low k fluctuations. The final terms arise from the projection of $\hat{i}$ along $\hat{l}$.

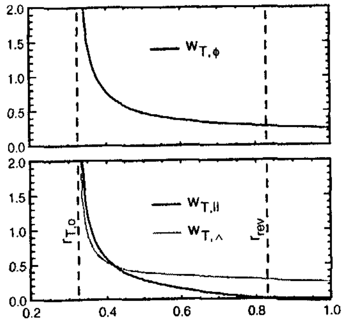

Fig. 2.21.— $w_{T,\phi}$ for $m = n = 0$. Both $w_{T,\theta}$ and $w_{T,r}$ vanish.

By setting $m = n = 0$ in Eq. 2.71 - 2.73 we obtain $w_{T,\phi}$ for equilibrium toroidal flows (Fig. 2.21). Both $w_{T,\theta}$ and $w_{T,r}$ vanish, reflecting the cancellation of equilibrium radial and poloidal flows over the toroidal chord. The divergence of $w_{T,\phi}$ at its impact parameter $r/a = r_{T,o}/a \approx 0.3$ contains both diverging terms in g_T which nearly coincide as the chord passes just below (and above) R_o at its point of tangency. While the sensitivity of the measurement peaks near the impact radius, significant resolution remains at larger radii allowing measurement of toroidal flows over much of the plasma radius. However, in edge flow measurements, significant attenuation arises from the oblique projection of the chord onto $\hat{\phi}$ at larger radii. Projecting $w_{T,\phi}$ onto $\mathbf{B}(r)$ calculated from a cylindrical equilibrium model of standard discharge parameters, we obtain its parallel and cross-field projections. At larger radii where $B \approx B_\theta$, we find $w_{T,\wedge} \gg w_{T,\|}$, while nearer the impact radius parallel sensitivity rises to approximately equal cross-field sensitivity. This suggests that toroidal flows measured near the edge may be primarily $\mathbf{E}\times\mathbf{B}$ driven cross flows rather than viscously dragged parallel flows. While not shown, $w_{T,i}$ for the $m=0$, $n=1$ mode closely resembles its equilibrium counterpart. However, unlike equilibrium

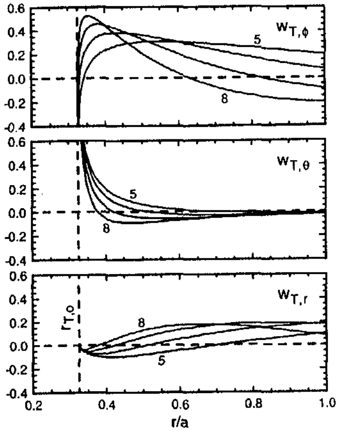

Fig. 2.22.— $w_{T,\phi}$, $w_{T,\theta}$, and $w_{T,r}$ for $m=1$, $n=5-8$.

flow resolution, $w_{T,r}$ for $m=0$, $n=1$ becomes non-zero near the plasma edge.

Setting $m=1$, $n=5-8$ we obtain the toroidal chord instrument functions for the dominant $m=1$ fluctuations. These functions acquire their oscillatory nature from the mode dependent terms of Eqs. 2.71 - 2.73. For $m=1$, $n=5$, $w_{T,\phi}$ exhibits a relatively flat response from $r_{o,T}$ to the edge. However, the fluctuation power for this intermittent core mode may not extend to the the impact parameter so the mode might be "missed" by the IDS. Fortunately, for $m=1$, $n=6-7$, a majority of the fluctuation power should fall under the positive bell of $w_{T,\phi}$. This should provide optimal resolution of these dominant modes for dynamo measurements in the plasma interior. The oscillations increase at larger values of n with $w_{T,\phi}$ for $n=8$ passing through zero midway to the edge. This zero roughly coincides with estimates of the $n=8$ resonant surface suggesting that an opportunistic canceling of this mode may occur. For $n=9$–10 (not shown) the secondary negative bell dominates $w_{T,\phi}$ suggesting that these modes may be observed with phases rotated 180° from their lower n counter-parts. For still larger values of n, $w_{T,\phi}$ passes through zero several times, "averaging out" these shorter wavelength fluctuations. Unlike the case of equilibrium flows, $w_{T,\theta}$ and $w_{T,r}$ are non-zero for $m=1$ fluctuations. $w_{T,\theta}$ grows near $r_{o,T}$ while $w_{T,r}$ extends at a low level over the outer region. In addition we note from Eq. 2.73 that $w_{T,r}$ is imaginary shifting the phase of the chord averaged $\tilde{v}_r$ 90° from the local phase at (ϕ_T, θ_T).

Projecting $\mathbf{w}$ onto the equilibrium field we obtain the parallel and cross-field sensitivity of the toroidal chord (Fig. 2.23). This projection combines $\tilde{v}_\theta$ sensitivity near $r_{o,T}$, where B_ϕ is significant, with $\tilde{v}_\phi$ sensitivity farther out where $B_\theta \gg B_\phi$ to yield a large cross-field sensitivity. Cross-field sensitivity is critical to our measurement as the velocity fluctuations which contribute to a dynamo should be entirely in the cross-field and perpendicular directions. Significant sensitivity to $\tilde{v}_{\|}$ appears near the impact parameter. Parallel fluctuations might arise from the radial advection of a parallel flow gradient by the perturbed magnetic field. While we explore this effect in some detail later on, we only mention here that we expect this effect to be small near the core because $v_{\|}(r)$ varies little over the plasma interior. Thus, while the response of the IDS toroidal chord exhibits complex structure, analysis of $\mathbf{w_T}$ reveals the chord to be well positioned to resolve the dominant cross field velocity fluctuations which we expect to contribute to the $\langle \tilde{\mathbf{v}} \times \tilde{\mathbf{b}} \rangle$ product.

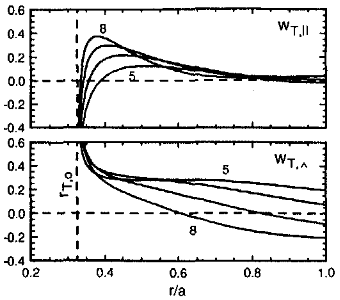

Fig. 2.23.— $w_{T,\|}$ and $w_{T,\wedge}$ for $m=1$, $n=5-8$.

2.5.4 Poloidal and Radial Chord Instrument Functions

The poloidal chord ($x \to P$) presents a comparatively simple geometry (Fig. 2.24). The chord has no toroidal extent satisfying Eq. 2.59 trivially as $\phi(l_P) = \phi(-l_P) = \phi_P$. Unlike the toroidal chord a single poloidal chord exhibits the odd poloidal symmetry necessary to satisfy Eq. 2.58 with θ_P equal to the poloidal angle bisecting the chord.

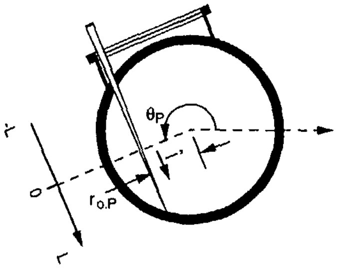

Fig. 2.24.— Poloidal view.

The projections of the velocity components onto $\hat{l}_P$ are given by,

$$\hat{l}_P \cdot \hat{\phi} = 0, \quad \hat{l}_P \cdot \hat{\theta} = \cos(\theta - \theta_P), \quad \hat{l}_P \cdot \hat{r} = \sin(\theta - \theta_P), \tag{2.75}$$

where we chose to align $\hat{l}_P$ and $\hat{\theta}$ at θ_P. Substituting these expressions into Eq. 2.57 we may quickly construct integrals in the form given by Eq. 2.60. The poloidal chord instrument functions for these integrals are,

$$w_{P,\phi} = 0, \tag{2.76}$$

$$w_{P,\theta} = g_P \cos(m(\theta - \theta_P)) \cos(\theta - \theta_P), \tag{2.77}$$

$$w_{P,r} = i g_P \sin(m(\theta - \theta_P)) \sin(\theta - \theta_P). \tag{2.78}$$

In this case the radial weighting of the line of sight,

$$g_P = \frac{a}{L_P}\frac{dl_P}{dr} = \frac{a\,r}{L_P\,(r^2 - r_{o,P}^2)^{\frac{1}{2}}}, \tag{2.79}$$

contains a single divergence at the point of tangency to $\hat{\theta}$.

Two effects stem from the exclusive projection of $\hat{l_P}$ onto $\hat{\theta}$ and $\hat{r}$ (Eq. 2.75). First, the chord is completely insensitive to toroidal flows of any wavenumber (Eq. 2.76).

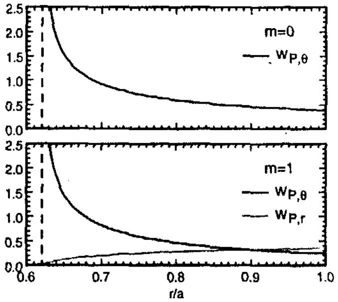

Fig. 2.25.— $w_{P,j}$ for $j \in \{\theta, r\}$.

Second, the poloidal chord instrument functions exhibit no dependence on the toroidal mode number n of the fluctuation. This removes much of the structure discussed for $\mathbf{w_T}$ which yielded attenuation, cancellation, inversion, and/or elimination of $\tilde{v}_n$ depending on the choice of n. For the poloidal chords the resolution of toroidal modes depends only on the intersection power from that mode with the poloidal line of sight. This means that higher n modes averaged out by the toroidal chord may be resolved, though lower n modes, resonant in the core, may have little power at $r \geq 0.6\,a$.

The poloidal chord resolution of equilibrium v_θ (Fig. 2.25) resembles the toroidal chord resolution for equilibrium v_ϕ. $w_{P,\theta}$ diverges at $r_{o,P}$ while retaining significant sensitivity at larger radii. The chord exhibits no sensitivity to equilibrium radial flows which exactly cancel from one half of the chord to the other. For $m = 1$ fluctuations $w_{P,\theta}$ becomes somewhat smaller and $w_{P,r}$ becomes finite and imaginary. Projecting $\mathbf{w_P}$ onto the equilibrium magnetic field (Fig. 2.26) reveals $w_{P,\|} \gg w_{P,\wedge}$ for both $m = 0$ and $m = 1$. This suggests that while the poloidal chord may be wonderfully sensitive to high n, $m = 1$ velocity fluctuations, it may be relatively insensitive the cross-field component

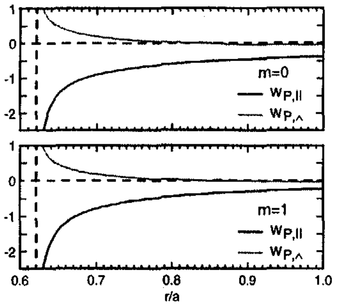

Fig. 2.26.— $w_{P,j}$ for $j \in \{\|, \wedge\}$.

which contributes to the dynamo. These issues will be discussed in greater depth later in the context of the velocity fluctuation measurements.

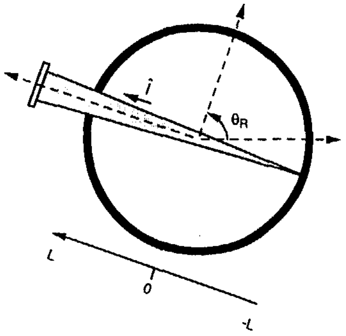

Fig. 2.27.— Radial view.

The radial chord ($x \to R$) exhibits the simple geometry shown in Fig. 2.27. This geometry achieves the necessary toroidal symmetry, just like the poloidal chord, by lacking any toroidal extent. The chord achieves poloidal symmetry about the angle θ_R of a line normal to the chord. This may be seen as a degenerate case of the poloidal chord in which $r_P \to 0 = r_R$ with the result that,

$$(\theta(l_R) - \theta_R) = -(\theta(-l_R) - \theta_R) = \frac{\pi}{2}. \tag{2.80}$$

This clearly will simplify the exponent inside the integral in Eq. 2.60. Also simplifying the calculation the projections of $\hat{l}$ along the line of sight are given simply by,

$$\hat{l_R} \cdot \hat{\phi} = \hat{l_R} \cdot \hat{\theta} = 0, \quad \hat{l_R} \cdot \hat{r} = 1. \tag{2.81}$$

Substituting these expressions into Eq. 2.57 and reducing into the form of Eq. 2.60 one obtains the instrument functions:

$$w_{R,\phi} = w_{R,\theta} = 0, \quad w_{R,r} = \frac{1}{2}(1 - \cos(m\pi)). \tag{2.82}$$

Absent from these expressions is g_R, which for the radial line of sight is given by $g_R = \frac{dr}{dr} = 1$. Thus the radial chord resolves perfectly and exclusively fluctuations with odd m. In addition, since the chord passes completely through the plasma, it will resolve any $m = 1$ mode present in the plasma. This unambiguous measurement of $\tilde{v}_r$ is important both in its own right and in quantifying the expected "contamination" of $\tilde{v}_T$ and $\tilde{v}_P$, both of which exhibit finite sensitivity to $\tilde{v}_r$.

2.5.5 Concluding Remarks on Chord Averaging

Several results obtained in this section will be directly applied to subsequent interpretations of $\tilde{v}$ measurements. By convolving estimated profiles of $\tilde{\mathbf{v}}(r)$ with the instrument functions derived above we shall obtain estimates for the sensitivity of each view to the modes present in the plasma. These estimates will enable us to infer the local amplitude of velocity fluctuations in the interior from the chord averaged values. These sensitivity estimates will be corroborated by the measured coherence of $\tilde{v}_x$ with individual magnetic modes. Next, estimates of a flat $\delta_{\tilde{v}}(r)$ profile will allow mapping of the relative measured phase between $\tilde{b}$ and $\tilde{v}_r$ to the local $\langle \tilde{\mathrm{v}} \times \tilde{\mathrm{b}} \rangle$ angle in the plasma interior. Finally, estimates of sensitivity to parallel and cross-field fluctuations will allow us to distinguish between fluctuations arising from advection and those producing a dynamo field.

References

Bendat, J. S. and A. G. Piersol (1980). *Engineering Applications of Correlation and Spectral Analysis.* New York: John Wiley and Sons.

Bevington, P. R. (1969). *Data reduction and error analysis for the physical sciences.* New York: McGraw-Hill.

Callen, J. D. (1997). Plasma kinetic theory. published class notes for PHYS/NEEP/ECE 725.

Carolan, P. G., N. J. Conway, C. A. Bunting, P. Leahy, R. O'Connell, R. Huxford, C. R. Negus, and P. D. Wilcock (1997). Fast charged-coupled device spectrometry using zoom-wavelength optics. *Rev. Sci. Instrum.* **68**, 1015–1018.

Carolan, P. G. and R. O'Connell (1995). A multichord spectrometer using an 8 × 8 anode photomultiplier. *Rev. Sci. Instrum.* **66**, 1184–1188.

Chapman, J. T. and D. J. Den Hartog (1996). Calibration techniques for a fast duo-spectrometer. *Rev. Sci. Instrum.* **68**, 285.

Den Hartog, D. J., A. F. Almagri, and S. C. Prager (1995). Data reduction techniques for a fast duo-spectrometer. *Rev. Sci. Instrum.* **66**, 444.

Den Hartog, D. J. and R. J. Fonck (1994). A fast spectroscopic diagnostic for the measurement of plasma impurity ion dynamics. *Rev. Sci. Instrum.* **65**, 3238.

Evensen, H. T., R. Durst, R. J. Fonck, and S. F. Paul (1995). Optical diagnostic to measure ion temperature and parallel velocity fluctuations on the tokamak fusion test reactor. *Rev. Sci. Instrum.* **66**, 845–847.

ThornEMI (1993). photomultipliers and accessories. Technical report, Thorn EMI Electron Tubes.

Woehrer, D. (1996). Inversion of impurity profiles using the impurity monochromator array. PLP-1186.

3

Sawtooth Ensemble Analysis

The results presented in the subsequent chapters were achieved over large ensembles of sawtooth events. The sawtooth represents a discrete manifestation of the dynamo in the MST. By averaging the sawtooth over a large ensemble we should effectively average over the flux surface which rotates past our stationary diagnostics. The first half of this chapter examines the phenomenology of this cycle, discusses a simple model of sawtooth behaviour and provides basic definitions critical to sawtooth ensemble analysis. The second half presents details of the analysis itself, outlining the analysis software and defining the ensembled quantities.

3.1 Sawtooth Relaxations in MST

3.1.1 The Sawtooth Cycle

The evolution of the total toroidal flux over a shot (Fig. 3.1) is largely determined by the MST external circuit. The flux rises with the plasma current during the initial portion of the discharge and soon enters the "flattop" region of the shot which may be maintained for tens of milliseconds before decaying with the discharge and ultimately terminating

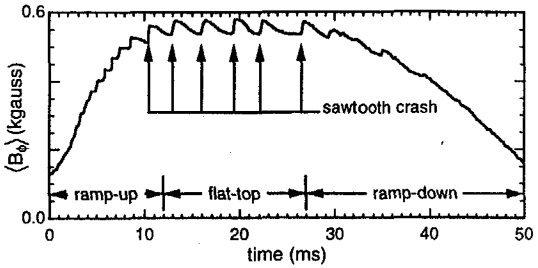

Fig. 3.1.— Volume averaged toroidal field of standard low current discharge. Note well defined sawteeth generating flux during the central "flat-top" period.

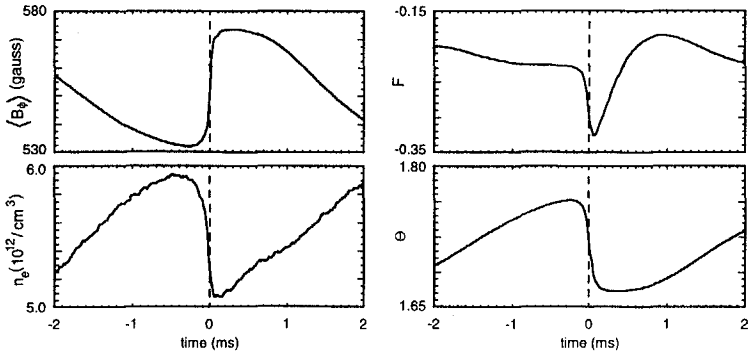

Fig. 3.2.— Key equilibrium quantities ensemble averaged over a sawtooth cycle. Moving from top to bottom: the volume averaged toroidal field, the line averaged central electron density, the reversal parameter, and the pinch parameter.

50–60 ms after the firing of the discharge. We restricted our analysis entirely to the flat-top region of the plasma during which a steady-state RFP equilibrium is most nearly achieved. During the flattop region we see $\langle B_\phi \rangle_V$ decay and grow in a quasi periodic "sawtooth" cycle. The signature event of this cycle is the "sawtooth crash" (Hokin, 1991; Beckstead's PhD thesis,1990) during which $\langle B_\phi \rangle_V$ rapidly jumps by roughly 5–10% of its mean value (Fig. 3.2). These jumps occur robustly in rotating MST discharges with an average period ranging from 1 to 10 ms depending on the plasma conditions.[1] The crashes are global events affecting all observable equilibrium quantities in a reproducible fashion. Fig. 3.2 shows the ensemble averaged sawtooth dynamics of several key equilibrium quantities. During the crash the central electron density drops and edge density rises as the sawtooth flattens the electron density profile and degrades particle confinement (Lanier, 1996). The central electron temperature also drops indicating a reduction in the energy confinement time (Biewer, 1997). The loss of confinement during the crash accompanies a general degradation of the plasma condition as impurity levels and the accompanying radiated power increase dramatically. Two parameters which describe the magnetic geometry of the RFP discharge also evolve over the cycle. The reversal parameter, defined as the ratio of the edge toroidal field to the volume averaged toroidal field ($F \equiv B_\phi(a)/\langle B_\phi \rangle_V$), becomes dramatically more negative during the crash before being pulled back close to its original value. The pinch parameter, defined as the ratio of the edge poloidal field to the volume averaged toroidal field ($\Theta \equiv B_\theta(a)/\langle B_\phi \rangle_V$), drops due mostly to the rise of $\langle B_\phi \rangle_V$ in denominator. Both effects reflect a flattening of the parallel current profile, $\lambda(r) \equiv J_\parallel/B$ toward the constant λ predicted in Taylor's model. The toroidal plasma current, $I_p = 2B_\theta(a)/\mu_o a$, remains relatively constant over the cycle, varying less than 1% over the sawtooth cycle.

One model describes the RFP sawtooth cycle as a discrete relaxation of a resistively peaked current profile (see for example Ortlani and Schnack, 1993). In this model the equilibrium, Fig. 3.3, oscillates with the sawtooth about a critical current gradient with

---

[1] Sawteeth appearing in locked discharges occur at irregular intervals with poorly defined features.

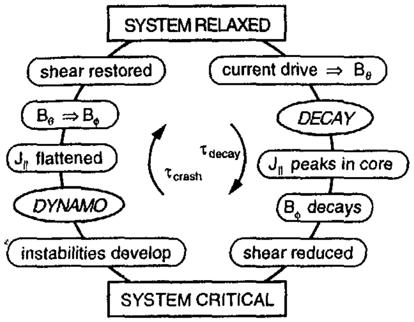

Fig. 3.3.— The sawtooth cycle may be divided into decay and dynamo phases. In the decay phase the transformer generates poloidal flux while a thermal instability slowly peaks the parallel current on axis. In the dynamo phase unstable $m = 1$ tearing modes grow rapidly converting poloidal flux into toroidal flux and flattening the current profile.

a slow *decay* phase steepening the gradient and a fast *crash* phase relaxing it. We shall describe this cycle starting with the plasma "relaxed" into a minimum energy state (§ 1.1) characterized by a strong reversal of the toroidal field in the outer region of the plasma, a poloidal and toroidal field of similar peak magnitudes, a parallel current profile which is relatively flat over the inner regions of the plasma, and a safety factor, $q(r) \approx \frac{rB_\phi}{RB_\theta}$, which exhibits strong stabilizing shear. Two easily understood mechanisms drive the system from this state. First, the toroidal field, maintained by neither poloidal current drive nor external coils, dissipates resistively. Second, externally driven toroidal current peaks in the hot plasma core where the resistivity, $\eta \sim T^{-3/2}$, is lower. Dissipation of this current further heats the core leading to the thermal instability which slowly peaks the current profile, driving the discharge from its relaxed state. This *decay* phase occupies most of the sawtooth cycle. If unchecked it would lead to the loss of reversal and termination of the RFP discharge in a few ms. However, at a critical gradient in $\lambda(r)$ the decay phase abruptly ends as free energy from the large current gradient drives the rapid growth of core resistive instabilities. These instabilities relax the plasma back into its minimum energy state, flattening the current profile, enhancing the stabilizing magnetic shear, and reconnecting poloidal flux into toroidal flux. In addition to the relaxation of the magnetic geometry, the instabilities induce stochastic field line transport over the plasma interior resulting in the observed particle and energy loss. The *crash* phase of the sawtooth cycle ends with the plasma returned to its relaxed state. In this model the RFP equilibrium may be viewed as a complicated oscillation driven about a critical gradient in the current profile. Thus to obtain a full experimental understanding of dynamo quantities in this equilibrium we seek to characterize their behavior over this full cycle.

3.1.2 Definition of the Sawtooth Window

To conduct an ensemble over many sawtooth cycles we first identify the time in the cycle with which we may align the zero of the ensemble window time axis. For this purpose we identify the"sawtooth crash time", t_c, defined as the point in the sawtooth cycle at which toroidal flux is generated most rapidly. We locate this point from the derivative of B_ϕ which appears as a voltage across the toroidal gap of the MST (V_{tg}). An automated sawtooth selection code scans the V_{tg} for spikes above a preset threshold and then locates those spikes more precisely through a parabolic fit to their local maxima. The extremely sharp nature of these spikes allows the identification of t_c to within a few μs.

In addition to the sawtooth crash time we must determine the interval about t_c which most nearly captures a full sawtooth cycle. This interval may be estimated by

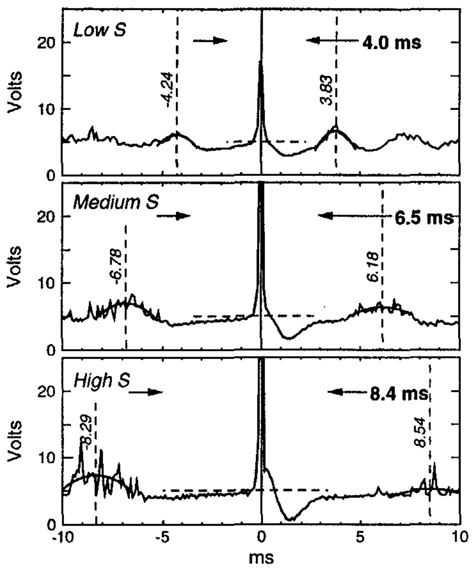

Fig. 3.4.— An ensemble average of V_{tg} with the crash time referenced to zero. Dashed lines mark the most probable time of neighboring crashes and the grey area denotes the chosen sawtooth window. Plasma conditions for each regime in § 3.3

ensemble averaging the V_{tg} over a window that includes sawteeth before and after the selected crash. These neighboring V_{tg} spikes act as finite width delta functions effectively converting the average into a probability histogram for crash locations. The peaks in this histogram on either side of the selected crash yield the most probable interval from the preceding to the current crash, δt_-, and current to the following crash, δt_+. Fig. 3.4 shows V_{tg} ensembles conducted at low, medium and high plasma current settings. Note the well defined bumps in the ensembled trace indicating the typical locations of neighboring sawteeth with the dotted lines indicating the peaks of those bumps. We

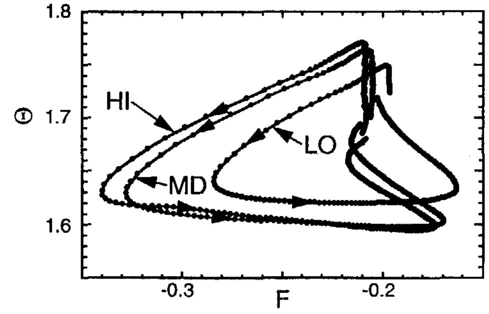

Fig. 3.5.— F-Θ sawtooth trajectories for the three current settings. The circles appear at regularly spaced time intervals.

chose a sawtooth window width of roughly $(\delta t_- + \delta t_+)/2$ adjusted about the crash to best close the $F - \Theta$ trajectory (Fig. 3.5) of the sawtooth cycle.[2]

Comparing the three ensembled traces in Fig. 3.4. one immediately notes the extension of the sawtooth period with plasma current. Scaling this period with the dimensionless Lundquist number, defined as the ratio of the restive to Alfvèn times $(S \equiv \tau_a/\tau_r)$, we obtain $T_{st}/\tau_a \propto S^{0.57}$ or $T_{st} \propto (\tau_a \tau_r)^{1/2}$. This hybrid timescale may be understood by referring back to our phenomenological model of the sawtooth. Examining each phase of the cycle separately we find that the decay phase scales roughly with τ_r while the crash times scales roughly with τ_a. Thus, at higher S we observe an extended decay phase punctuated by increasingly abrupt crashes. Conversely, at low S the decay and dynamo phases become less distinct as the relaxation extends into the decay. This may explain why simulations which must run at S values below those achieved in MST

---

[2] Specifically we solved the equation, $T_{st} = \zeta\delta t_- + (1-\zeta)\delta t_+$, for the $\zeta \approx 0.5$ which most nearly closed the $F - \Theta$ trajectory.

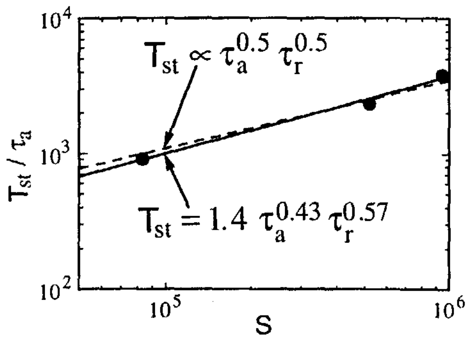

Fig. 3.6.— T_{st} scales with S with a timescale midway between a resistive and Alfvén time.

rarely observe distinct sawteeth

3.2 Sawtooth Ensembling Techniques

This section details the techniques employed to produce the ensembled quantities presented in this thesis. We begin with a general discussion of the extraction of meaningful fluctuations from dynamic, noisy signals. While the previous sections provided motivation for sawtooth ensembles, this discussion motivates the manner in which we conduct those ensembles. We then discuss the software employed to conduct those ensembles. Much of this discussion is for the benefit of researchers who employ these routines and may be skimmed by the readers interested in the results of this thesis. Lastly we define the exact quantities which are calculated in the ensemble, devoting separate sections to traditional and wavelet analysis.

3.2.1 Sawtooth Signal Components

In general we may decompose a signal $x(t)$ windowed about a sawtooth into three components (Fig. 3.7),

$$x(t) = x_o(t) + \tilde{x}(t) + N_x(t), \tag{3.1}$$

where $x_o(t)$ represents the flux-surface averaged or secular evolution of $x(t)$. In the case of core ion velocity measurements $x_o(t)$ describes the deceleration of the fluid at the sawtooth crash. The second term on the RHS of Eq. 3.1, $\tilde{x}(t)$, represents fluctuations in $x(t)$. Typically these are spatial fluctuations which rotate with the plasma past fixed measurements at Doppler shifted frequencies. For ion velocity measurements this term contains dynamo fluctuations. Finally, $N_x(t)$ represents measurement noise in $x(t)$. In an ensemble average of $x(t)$ over many sawteeth we assert,

$$\langle x(t)\rangle \approx \langle x_o(t)\rangle \equiv \bar{x}_o(t), \tag{3.2}$$

$$\langle \tilde{x}(t)\rangle \approx \langle N_x(t)\rangle \approx 0. \tag{3.3}$$

This follows our common sense notion that by averaging the sawtooth signals over a large enough ensemble noise and fluctuation will cancel out leaving the average secular evolution. However the assertion, $\langle \tilde{x}(t)\rangle \approx 0$ rests on equating a flux surface average, over which MHD fluctuations are known to vanish, and an ensemble average. This equivalency holds only if the measured phase of $\tilde{x}(t)$ exhibits no preferred value relative to the sawtooth crash. This may be only approximately true very close to the sawtooth crash where we occasionally observe magnetic fluctuations locking to the lab frame repeatedly with the same phase. Unfortunately, these phase locked components of $\tilde{x}(t)$ prove impossible to distinguish from $x_o(t)$ with current analysis techniques.

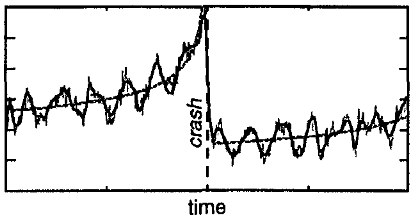

Fig. 3.7.— Cartoon of sawtooth signal contains secular (dashed), fluctuating (solid) and noise (grey) components.

In the identification of fluctuation power and fluctuation products we seek to minimize contamination from the secular evolution. Three simple methods have been employed to accomplish this: subtraction of $\bar{x}_o(t)$, high-pass filtering of $x(t)$, and careful sawtooth selection. The subtraction of $\bar{x}_o(t)$ provides one simple method to diminish the secular contribution to the ensembled signal. Though the details of the relaxation event vary from sawtooth to sawtooth we observe the equilibrium evolution to be relatively consistent. Thus we may model the secular component of the sawtooth cycle as

$$x_o(t) = (1 + \varepsilon_x(t))\bar{x}_o(t), \tag{3.4}$$

where $\langle \varepsilon_x(t) \rangle = 0$. Extending this definition to the measured fluctuation power and fluctuation products we obtain,,

$$\langle (x - \bar{x}_o)^2 \rangle = \langle \varepsilon_x^2 \rangle \bar{x}_o^2 + \langle \tilde{x}^2 \rangle + \langle N_x^2 \rangle, \tag{3.5}$$

$$\langle (x - \bar{x}_o)(y - \bar{y}_o) \rangle = \langle \varepsilon_x \varepsilon_y \rangle \bar{x}_o \bar{y}_o + \langle \tilde{x}\tilde{y} \rangle, \tag{3.6}$$

where we have omitted the explicit dependence of all quantities on t. By subtracting $\bar{x}_o$ we reduce the contamination of the self and cross products by $\bar{x}_o^2$ and $\bar{x}_o\bar{y}_o$ respectively.

In the analysis code we perform this subtraction prior to the calculation of all ensemble quantities. Contamination of the products which persists in Eq. 3.5-3.6 varies directly with the power of the secular component, $\bar{x}_o^2$ and $\bar{x}_o\bar{y}_o$, and the mean-squared variation of the secular component from sawtooth to sawtooth, $\langle \varepsilon_x^2 \rangle$ and $\langle \varepsilon_x \varepsilon_y \rangle$. High-pass filtering may provide substantial reduction of the secular power provided sufficient separation exists in frequency space between $\tilde{x}$ and x_o. Away from the sawtooth this condition is satisfied as $\tilde{x}$ fluctuates rapidly with Doppler frequencies of 10 - 30 kHz while the equilibrium evolves slowly with characteristic frequencies below 3 kHz. Unfortunately, this separation narrows near the crash as the fluctuations decelerate with the plasma and the equilibrium evolves more rapidly. The variation of the secular component among sawteeth ($\langle \varepsilon_x^2 \rangle$ and $\langle \varepsilon_x \varepsilon_y \rangle$) may be reduced by carefully constraining the sawtooth ensemble. We impose these constraints in three steps. First, the ensembles presented in this study were selected from the "flat-top" region of more than 200 similar discharges taken during adjacent run days. The plasma current, reversal parameter, and electron density of discharges during this run were held as constant as operationally feasible. Second, individual sawteeth were manually selected from reversal parameter traces with similar sawtooth waveforms (Fig. 3.9a). Finally, the events in the ensemble were characterized by global plasma parameters near the crash allowing outliers to be excluded from the ensemble (Fig 3.9b). By combining subtraction, filtering, and screening we were able to greatly reduce secular contamination of the fluctuation signals.

The random scatter in the ensembled products due to noise decreases as the square root of the number of events. When the initial noise level in the data, N_x, is significant we seek to balance this benefit of increased statistics against the need for a tightly constrained ensemble. At low current we constructed large rigorously constrained ensembles of several hundred sawteeth though statistics decreased at higher currents where sawteeth became both more variable and more widely spaced. While with sufficient statistics $\langle N_x \rangle \rightarrow 0$, the $\langle N_x^2 \rangle$ term on the RHS of Eq. 3.5 remains. This term amounts to a noise floor which must be quantified in order to correctly determine the fluctuation power $\langle \tilde{x}^2 \rangle$. If known, the random error associated with $x(t)$ for each event may be propagated through the ensemble to determine this floor. However, it is usually more accurate to apply knowledge of the noise behavior in frequency and time to determine the noise floor of the ensembled power. This approach is applied later on with considerable success to subtract a large noise floor from the ensembled IDS signal resolving a comparatively small amount of velocity fluctuation power (§ 5.1).

3.2.2 Sawtooth Ensemble Software

The following paragraphs contain a brief overview of the software developed to analyze signals over a carefully constrained sawtooth ensemble. This code is publicly available and employed by several researchers for the analysis of widely varying data. Thus this description serves both to detail the creation and analysis of ensembles presented in this study, and as a brief introduction to the software for others wishing to conduct similar studies. Those interested in employing this software are encouraged to read these comments carefully and to examine the generously commented code found in `[jchapman.public.st_ corr]` and the Appendices of this thesis. On the other hand, those interested primarily in the measurements presented in this thesis may skim this description without compromising subsequent comprehension of results.

Sawtooth ensemble analysis proceeds in two basic steps: the generation of an ensemble and the analysis of signals averaged over that ensemble. A number of routines

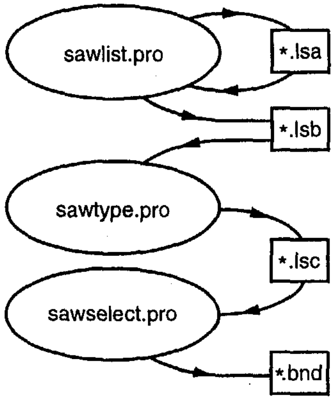

Fig. 3.8.— Routines and file used for the creation of a sawtooth ensemble.

operate together to accomplish the first step by generating a series of increasingly detailed lists. The routine, `sawlist.pro`, first generates a simple shot list containing the shot number and date of each discharge and times indicating the portion of the discharge to be analyzed. The code stores this shot list in a formatted file with a `*.lsa` suffix (§ B.3.1).[3] After generating the shot list `sawlist.pro` loops through the ensemble to identify candidate sawteeth from peaks in the V_{tg}. From these candidates the user manually selects clean, well separated events (Fig. 3.9a). Those wishing to skip the time consuming task of manually selecting the sawteeth in the ensemble, may choose to rely on an automatic selection routine. However no algorithm currently can distinguish "clean" sawteeth from spurious events as effectively as the human eye (and brain). The times of the selected events are stored in a formatted file with a `*.lsb` suffix (§ B.3.2). For those wishing to

---

[3] These shotlists are also used for running the automatic IDS fitting routine, `fit.pro` (§ B.1.1), and the automatic magnetic mode analysis routine, `modes.pro` (§ B.5).

conduct other types of ensembles the routine `triglist.pro` generalizes `sawlist.pro`, producing `*.lsb` files with events occurring at regular intervals (i.e. every 5 ms from 10 - 30 ms) or events triggered at times specific to particular experiments (e.g., PPCD fire time).

After creating a sawtooth ensemble with `sawlist.pro` the user runs a second routine, `sawtype.pro`, to characterize each sawtooth by the discharge parameters around the sawtooth events. In `sawtype.pro` the user selects the parameters to be "typed" for a particular ensemble. These parameters may be signals stored in the data base (i.e. plasma current, electron density, reversal parameter) or signals derived by user defined routines (i.e. mode frequency). The routine then loops through the events in the `*.lsb` file and averages the chosen signals over user defined windows referenced to the individual sawteeth. The routine stores this information in a third file with a `*.lsc` suffix (§ B.3.3) together with all the sawtooth and shot information contained in the `*.lsb` file. This file contains the final and most complete characterization of the sawtooth ensemble.

After typing the sawtooth list may be "bound" by `sawselect.pro` to exclude outliers and constrain the ensemble. This final routine produces scatter plots of the typed quantities and invites the user to define the upper and lower limits of inclusion (Fig. 3.9b). This process must be approached carefully as careless imposition of limits may needlessly and drastically reduce the size of the ensemble. For example, excluding 20% of three uncorrelated quantities will reduce the ensemble by a factor of two. Typically several adjustments must be made before the user achieves an appropriate balance between maintaining sufficient statistics in the ensemble and reducing the variance amongst the included sawtooth events. Once chosen the limits are stored in a separate short file with a `*.bnd` suffix (§ B.3.4). The creation of the `*.lsc` and `*.bnd` files completes the first

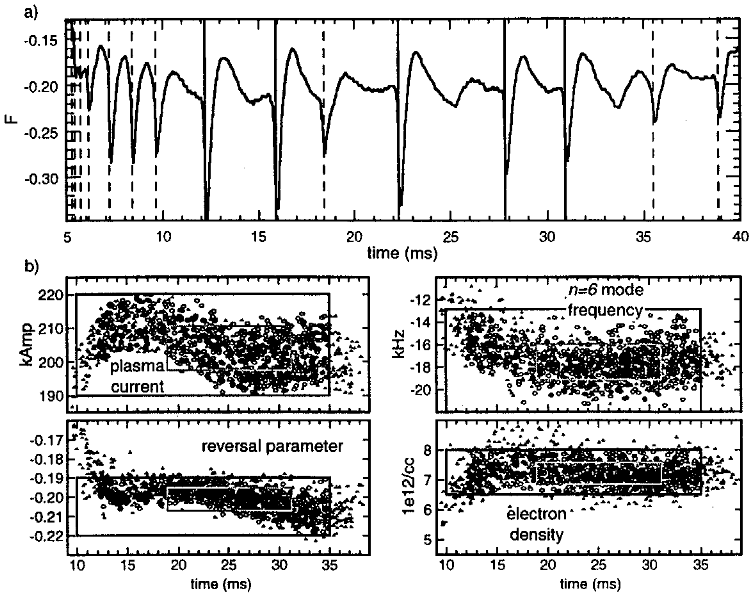

Fig. 3.9.— a) The user manually selects sawteeth from the reversal parameter which exhibit typical "ring-back" sawtooth features and sufficient spacing from neighboring sawtooth. b) The entire ensemble is then characterized with respect to equilibrium plasma parameters and bound manually by the user. The plus's and triangle's represent included and excluded events respectively.

step of constructing a clean, well constrained sawtooth ensemble.

The user now embarks upon the second step of the analysis, the correlation of fluctuating signals over the ensemble. First the user creates a routine to pass the appropriate signals to the correlation engine. This routine takes as its inputs the shot number and date of the discharge and the time bounds of the signal. This information is read by the correlation engine from the `*.lsc` files and then passed to the user defined routine. The routine's outputs consist of a one-dimensional time trace and a two-dimensional data array containing a signal in each row. These signals must be binned and aligned properly such that the single time trace passed by the routine matches each row in the signal array. The routine also outputs string arrays containing the names and units of the individual signals. Any normalization, baseline subtraction, filtering, etc. of the signals must be accomplished by the user prior to being passed to the correlation engine. By requiring individual users to handle the acquisition and preprocessing of their signals the correlation engine becomes a completely generic ensemble analysis tool. The signal routine employed for several of the $\langle \tilde{\mathrm{v}} \times \tilde{\mathrm{b}} \rangle$ measurements reported in this thesis may be found in § B.4.1.

Three analysis engines are available to calculate ensemble quantities. The simplest, `st_aver.pro` (§ B.4.2), loops once through the ensemble to produce the sawtooth average of each quantity. To run the routine the user sets global variables specifying the names of the typed sawtooth listing (`*.lsc`), the bounding file (`*.bnd`), and the user defined signal routine. The engine then opens the sawtooth list and bounding file and begins to loop through the shots in the ensemble. For each shot the routine examines the typed values of the selected sawteeth and excludes those falling outside the range specified by the bound file. Those shots with valid sawteeth are passed to the signal routine which returns the array of signals to be averaged. The routine then loops through the valid sawteeth in that shot extracting a window about each sawtooth from the signal array and adding it to an ensembled array. The user defines the window for each ensemble prior to running the averaging routine. After looping through all shots in the ensemble the routine normalizes the ensembled array by the number of included events and saves the ensembled quantities to file. This routine is typically employed to sawtooth average unfiltered operational signals for the analysis of equilibrium sawtooth dynamics.

The two remaining engines, `st_corr.pro` and `st_wvlt.pro` (§ B.4.3), operate in an analogous fashion. However these routines then loop through the ensemble twice. In the first loop the calculate the ensemble quantities exactly as in `st_aver.pro`. Then in the second pass the routines subtract sawtooth averaged quantities from each windowed signal to extract the fluctuating portion of the signal from its secular evolution (Eq. 3.5-Eq. 3.6). Both routines then ensemble the time resolved products and spectra of every signal with every other signal. In addition `st_wvlt.pro` ensembles wavelet coefficients defined over both frequency and time. The routine finally calculates the coherence and phase of the ensembled products and stores all ensembled quantities to file.

3.2.3 Time Series and Fourier Ensemble Analysis

We now turn to the ensembled quantities calculated and stored by the algorithms outlined above. This section describes the time resolved products and spectra output by both `st_corr.pro` and `st_wvlt.pro`. A discussion of wavelet analysis ensues in the following subsection. All the quantities described are stored in generic IDL save files in a manner described in § ??. We define $x_i(t)$ to be the i'th fluctuating signal extending over a sawtooth window. For every $x_i(t)$ we may construct a phase shifted counterpart $p_i(t)$ as,

$$p_i(t) \equiv \int df\, e^{i2\pi ft} e^{i\,\mathrm{sgn}(f)\pi/2} \left(\int dt'\, e^{-i2\pi ft'} x_i(t') \right), \tag{3.7}$$

where $\mathrm{sgn}(f)$ returns the sign of f. In words, p_i is obtained from x_i by shifting the phase of its Fourier components by 90° (Ji, 1995). The first loop of the correlation engine obtains both $\langle x_i \rangle$ and $\langle p_i \rangle$. By subtracting these averages from the individual signals in the second loop we obtain the fluctuating signals, $\tilde{x}_i$ and $\tilde{p}_i$. We now average $\langle \tilde{x}_i^2 \rangle$, $\langle \tilde{x}_i \tilde{x}_j \rangle$, and $\langle \tilde{x}_i \tilde{p}_j \rangle$ over the ensemble. These will be referred to respectively as the self, direct, and shifted products. Frequently, the coherence of two signals in time is defined in signal analysis literature from the self and direct products as,

$$\gamma^c_{ij}(t) \equiv \frac{\langle \tilde{x}_i \tilde{x}_j \rangle}{(\langle \tilde{x}_i^2 \rangle \langle \tilde{x}_j^2 \rangle)^{\frac{1}{2}}}. \tag{3.8}$$

However, γ^c_{ij} incorporates both the coherence of the two signals and their relative phase,

$$\gamma^c_{ij}(t) = \gamma_{ij}(t)\cos(\Phi_{ij}(t)). \tag{3.9}$$

Here $\gamma_{ij}(t)$ is the true coherence of the two signals. This is to say that $\gamma_{ij}(t)$ is the fraction of the power in x_i and x_j which maintains a non-random phase with respect to the other signal. This non-random relative phase is then given by $\Phi_{ij}(t)$. From Eq. 3.8–3.9 it is impossible to determine, for example, whether a near zero value of γ^c_{ij} arise from the signals being incoherent or out of phase. We overcome this difficulty by using the shifted product to define,

$$\gamma^s_{ij}(t) \equiv \frac{\langle \tilde{x}_i \tilde{p}_j \rangle}{(\langle \tilde{x}_i^2 \rangle \langle \tilde{x}_j^2 \rangle)^{\frac{1}{2}}} = \gamma_{ij}(t)\sin(\Phi_{ij}(t)). \tag{3.10}$$

Eqs. 3.8–3.10 may easily be rearranged to solve for the coherence and phase as,

$$\gamma_{ij}(t) = (\gamma^{c\,2}_{ij} + \gamma^{s\,2}_{ij})^{\frac{1}{2}} = \left(\frac{\langle \tilde{x}_i \tilde{x}_j \rangle^2 + \langle \tilde{x}_i \tilde{p}_j \rangle^2}{\langle \tilde{x}_i^2 \rangle \langle \tilde{x}_j^2 \rangle} \right), \tag{3.11}$$

$$\Phi_{ij}(t) = \tan^{-1}\left(\frac{\gamma^s_{ij}}{\gamma^c_{ij}} \right) = \tan^{-1}\left(\frac{\langle \tilde{x}_i \tilde{p}_j \rangle}{\langle \tilde{x}_i \tilde{x}_j \rangle} \right). \tag{3.12}$$

This technique allows the determination of signal coherence and phase in time much as it may be defined through spectral analysis in frequency. Extensive simulations have demonstrated this reliability of the technique and for further assurance we have checked that $\tilde{p}_i$ for the cosine component of a spatially resolved magnetic mode matches $\tilde{x}_i$ for the sine component of the same mode.

The routines `st_corr.pro` and `st_wvlt.pro` apply standard ensemble Fourier analysis to the signals (e.g. Bendat and Piersol, 1980). Each fluctuating signal, $\tilde{x}_i$ is multiplied by a Hanning window to reduce leakage to high frequencies from finite data lengths, and zero-meaned to remove any DC Fourier component. An FFT of the modified signal yields the complex Fourier transform F_i. This calculation may be written in continuous form as,

$$F_i(f) = \int dt\, e^{-i\,2\pi\, f\, t}\,(w(t)\tilde{x}_i(t) - \langle w(t)\tilde{x}_i(t)\rangle_t), \tag{3.13}$$

where $w(t)$ is the Hanning window. The routine then ensembles the auto-spectral power, $P_{ii} = \langle F_i F_i^* \rangle$, and the complex cross-spectral power, $P_{ij} = \langle F_i F_j^* \rangle$. The ensembled spectra are normalized by the number of events and by $1/(\langle w^2 \rangle_t - \langle w \rangle_t^2)$ to account for the effects of windowing. In addition the routines convert the two sided spectra to one sided spectra by truncating the redundant negative frequencies and multiplying all but the DC and Nyquist frequencies by two to preserve fluctuation power.[4] Coherence and phase are derived in standard fashion from the ensembled cross spectra as,

$$\gamma_{ij}(f) = \left(\frac{P_{ij} P^*_{ij}}{P_{ii} P_{jj}} \right)^{\frac{1}{2}}, \tag{3.14}$$

$$\Phi_{ij}(f) = \tan^{-1}\left(\frac{\Im(P_{ij})}{\Re(P_{ij})} \right). \tag{3.15}$$

For completely uncorrelated signals the expectation value of $\gamma_{ij}(f)$ is given approximately by $1/\sqrt{N_{event}}$. Though more complicated expressions have been derived simulations and practical application have indicated that this simple expression provides a robust estimate of the coherence baseline.

---

[4] In IDL the FFT normalization convention yields, $\sum_f P_{ii} = \sum_t \tilde{x}_i^2/N_t$, where N_t is the number of time points. Dividing P_{ii} by $df = 1/(t_{max} - t_{min})$ converts the spectra into the more physically meaningful units of power per frequency.

3.2.4 Wavelet Analysis

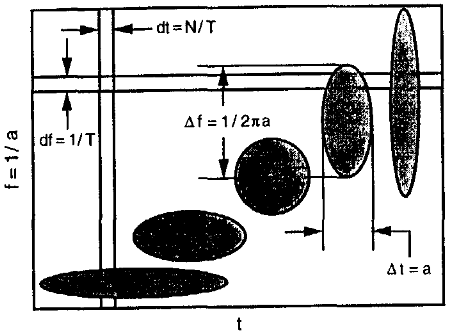

Fig. 3.10.— The resolution of wavelets (dark) is governed by the uncertainty relation $\Delta f \Delta t = 1/2\pi$. Fourier analysis and time series (light) analysis represent the extremes of this resolution.

The spectral and time series analysis discussed above offer complementary pictures of fluctuation phenomena over the sawtooth. Time series analysis provides power, coherence, and phase information with a resolution in time limited only by the sampling rate of the signal, and a total lack of frequency resolution. Conversely, spectral analysis provides the same information with a high resolution in frequency set by the inverse signal length but no time resolution. Wavelet analysis moves smoothly between these two extremes providing information about the fluctuation at a certain frequency and a certain time with a particular resolution in each. This is particularly useful for understanding the evolution of fluctuations over a sawtooth where we observe the frequency spectrum of the fluctuations to exhibit a strong time dependance. To understand the function of wavelets we imagine a perfectly-realized, two-dimensional phase-space distribution in frequency and time of signal power resolved (Fig. 3.10). We can recover the measured $\tilde{x}_i^2(t)$ by averaging the distribution over a narrow time increment and all frequencies. Conversely, to recover the measured $P_{ii}(f)$, we average over the entire window in a narrow frequency interval. Combined these two methods provide an incomplete picture of the phase-space distribution of power. For example a power spectrum peaked at f_o with the corresponding self product peaked at t could indicate that the phase-space distribution peaks at the intersection of f_o and t or that significant fluctuation power at f_o persists over the whole window while a sudden burst of fluctuation power at another frequency yields the spike at t.

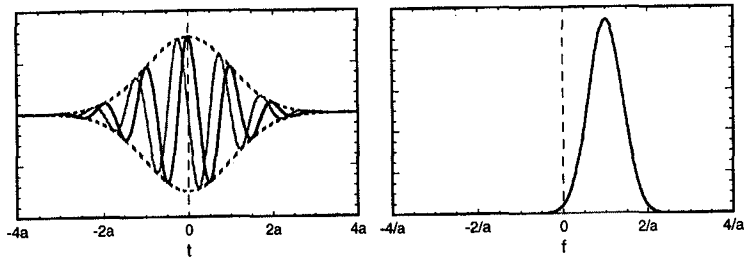

Fig. 3.11.— a) The Moirlet wavelet (real-solid; imaginary-grey) and b) the Fourier transform of the wavelet.

To address the ambiguities inherent in the traditional analysis we have developed wavelet analysis routines which provide information between the two extremes of time series and spectral analysis (Miligen, *et.al.*, 1995). For the analysis presented in this thesis we employed a wavelet basis function $M(t, f_o)$ defined as,

$$M(t, f_o) = (\pi/f_o^2)^{1/4}\, e^{-t^2 f_o^2/2}\, e^{i2\pi t}, \tag{3.16}$$

a complex sinusoid multiplied by a Gaussian envelope (Fig. 3.11a). We now define our complex wavelet transform coefficient through the convolution,

$$\varphi_i(t, f_o) = \int dt'\, \tilde{x}_i(t - t')\, M(t', f_o). \tag{3.17}$$

$\varphi_i(t, f_o)$ contains both the phase and power of the fluctuation averaged over a phase-space region centered around t, f_o. The Fourier transform of $M(t, f_o)$ (Fig. 3.11b) yields a real Gaussian centered about f_o,

$$\tilde{M}(f_o, f) \propto \int dt\, e^{-i\,2\pi\, f t}\, M(f_o, t) \propto e^{2\pi^2 (f/f_o - 1)^2}. \tag{3.18}$$

Employing the convolution theorem we may equivalently define $\varphi_i(t_o; f_o)$ as the inverse Fourier transform of the product of $F_i(f)$ and $\tilde{M}(f_o, f)$. The ensemble analysis engine, `st_wvlt.pro`, defines the wavelet coefficients in this fashion to reduce computational time.

By inspection one may see that the resolution of the wavelet packet $M(f,t)$ is given by the width of its Gaussian envelope, $\Delta t = 1/f_o$. Analogously, the resolution of the wavelet in frequency space is given by the width of $\tilde{M}(f_o, f)$, $\Delta f = f_o/2\pi$. Comparing the two expressions one discovers that the product of the resolutions is constant yielding the uncertainty relation,

$$\Delta t \Delta f = \left(\frac{1}{f_o}\right)\left(\frac{f_o}{2\pi}\right) = \frac{1}{2\pi}. \tag{3.19}$$

Thus, as one increases f_o, compressing the wavelet packet to obtain higher time resolution, one increases Δf, expanding the Gaussian in frequency space to include more frequencies about f_o. The regions resolved in our frequency-time phase space are shown as ellipses in Fig. 3.10. The uncertainty relation fixes the areas of these ellipses preventing "perfect" resolution of fluctuation power distribution in phase space. However, the

ability to adjust the position and the relative dimensions of the resolved regions provide far greater flexibility in determining the characteristics of that distribution.

The ensemble code calculates $\varphi_i(f_o, t)$ at frequencies unevenly spaced every $\sim \Delta f/2$. This two-fold redundancy provides smooth contours in frequency and time while retaining a reasonable degree of computational efficiency. The routine then proceeds to define ensemble products in direct analogy to the Fourier analysis outlined above. We define the wavelet auto and cross spectra as,

$$W_{ii}(f,t) = \langle \varphi_i(f,t) \varphi_i^*(f,t) \rangle, \tag{3.20}$$

$$W_{ij}(f,t) = \langle \varphi_i(f,t) \varphi_j^*(f,t) \rangle. \tag{3.21}$$

After normalizing the ensembles we then define the wavelet coherence and phase as,

$$\gamma_{ij}(f,t) = \left(\frac{W_{ij} W_{ij}^*}{W_{ii} W_{jj}}\right)^{\frac{1}{2}}, \tag{3.22}$$

$$\Phi_{ij}(f,t) = \tan^{-1}\left(\frac{\Im(W_{ij})}{\Re(W_{ij})}\right), \tag{3.23}$$

again in direct analogy to the Fourier analysis.

3.3 Sawtooth Ensembles in this Thesis

The ensembles conducted for this study are listed below along with their operational parameters. The first subsection gives the plasma parameters for the five primary dynamo runs. These include three runs at low currents and a medium and high current run which provided the measurements for the Lundquist scaling. The next section describes the probe scane performed to measure the profile of $\tilde{\mathbf{b}}$ (§ 4.3.1). Finally, we describe a numerical ensemble conducted with an MHD code at low Lundquist settings. For the experimental ensembles the MST was run with four banks in standard RFP mode.

The bank settings were adjusted throughout to maintain constant plasma conditions. The presentation of the plasma parameters here will be brief as the physics results are discussed later in the thesis.

3.3.1 Lundquist Number Scaling Ensembles

	Low S	Medium S	High S	$\langle \tilde{v_\phi} \tilde{b_r} \rangle$	$\langle \tilde{v}_r b_\theta \rangle$
$N_{s.t.}$	728	457	127	1000	556
I_p (kAmp)	204	357	481	207	199
F	-0.20	-0.21	-0.21	-0.20	-0.17
Θ	1.74	1.75	1.77	1.70	1.67
n_e (10^{13} cm^{-3})	0.72	0.90	1.03	0.69	0.76
$f_{n=6}$ (kHz)	17.5	20.2	9.6	15.7	556
T_e (eV)	160	315	380	N/A	N/A
$Z_{eff}/min(Z_{eff})$	3.0	1.9	1.6	N/A	N/A
$\tau_{s.t}$ (ms)	4.0	6.5	8.4	4.1	3.8
τ_{res} (s)	0.36	1.44	2.08	N/A	N/A
$\tau_{alfvén}$ (μs)	4.4	2.8	2.2	4.3	4.1
S (10^5)	0.82	5.21	9.41	N/A	N/A

Table 3.1: The equillibrium values for each ensemble averaged over a sawtooth period. These are the number of sawteeth ($N_{s.t.}$), the plasma current (I_p), the field reversal parameter (F), the pinch parameter (Θ), the electron density (n_e), the frequency of the $n = 6$ toroidal mode ($f_{n=6}$), the electron temperature (T_e), the Z_{eff}, the sawtooth period ($\tau_{s.t.}$), the resistive time (τ_{res}), the Alfvén time ($\tau_{alfvén}$), and the Lundquist number (S). The first three columns refer to the Lundquist number scan while the last two refer to subsequent measurments of $\tilde{v}_\phi$ and $\tilde{v}_r$.

To understand the behaviour of fluctuations in different regimes we conducted runs at three plasma currents, spanning the operational capabilities of the MST. To obtain the maximum swing in S we more the doubled I_p the dominant scale factor with S while holding the variation in the electron density to a minimum. The electron temperature scaled up with the plasma current while the relative Z_{eff} decreased. The latter may be due to machine conditioning which improved as the run progressed. These settings produce a three point scaling with over an order of magnitude in S achieved. For the Lundquist runs we employed one toroidal IDS chord and one poloidal IDS chord. Later low current runs employed the toroidal chords in the up-down symetric configuration for a phase resolved measurement of $\langle \tilde{v_\phi} \tilde{b}_{\theta,n} \rangle$ and a radial chord with a toroidal chord for our measurement of $\tilde{v}_r$. Not all supplemental diagnostics were available for the later low current runs. However, care was taken to match the operational parameters of the original low current run so we may assume that the unmeasured parameters were fairly consistent.

3.3.2 Radial Scan of Magnetic Fluctuations

We employed the insertable magnetic probe to conduct a radial scan of $\tilde{\mathbf{b}}(r)$ for $r \leq 16$ cm. To commence the scan we inserted the tip of the boron nitride housing 20 cm into the MST, aligned the probe with the vacuum B_ϕ shots, and conditioned the probe with $\sim$ 40 low current discharges. We then conducted sets of six or more discharges withdrawing the probe 1 cm from the plasma between each set. We completed a final set at a tip insertion of 2 cm, and then reinserted the probe to obtain additional sets at tip insertions of 20, 19, and 18 cm. This provided a simple check of the early data against slow evolution of the measured quantities over the run. The sawteeth during these discharges were irregular and poorly defined due to the degradation of the plasma by the insertion of the probe, thus we did not pursue sawtooth ensembling for this data. Instead the signals were ensembled over fixed windows during the flat-top of the discharge and then correlated as described in § 3.2.

Fig. 3.12 illustrates some effects of the probe on plasma conditions as a function

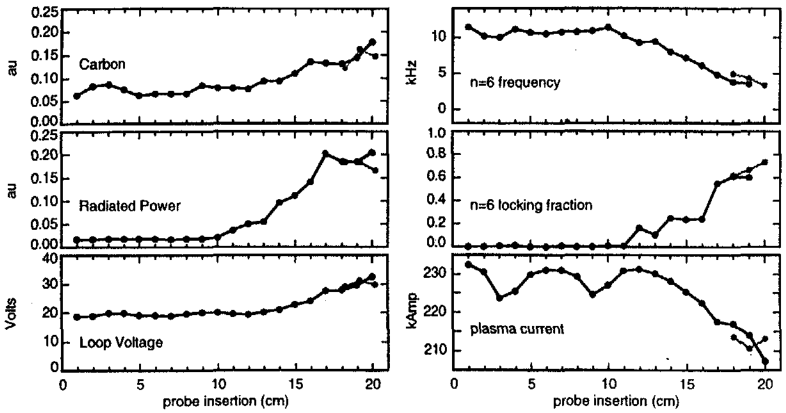

Fig. 3.12.— The plasma sees the magnetic probe as a 0.5 inch-dia boron-nitride limiter. At insertions of greater that 10 cm the incidence of locking, impurity radiation, and loop voltage climb.

of insertion depth. At insertions of fewer than 10 cm the probe appears to have little effect on the plasma condition with impurity radiation levels staying level. However, at insertions deeper than 10 cm, past the reversal surface, the probe increasingly degrades the plasma condition. The locking percentage, defined as the percentage of the shot exhibiting an $n = 6$ mode frequency with an absolute value less than 3 kHz, climbs dramatically from zero locking before 10 cm to near total locking at the deepest insertion. The $n = 6$ mode frequency, averaged over unlocked periods, drops as the probe drags the plasma. The radiated power grows rapidly with insertion past 10 cm indicating an increased plasma-probe interaction which is introducing contaminants into the plasma. At the deepest probe insertion the loop voltage averaged over 30 Volts compared with 20 Volts at shallower insertions. Consequently, the plasma current achieved for the same capacitor bank settings was substantially reduced. This dramatic contamination of the plasma by the probe at the deeper insertions may introduce significant and incalculable errors to the $\tilde{\mathbf{b}}$ measurements at these radii. However, these effects illustrate the need for a passive measurement of the dynamo product using non-perturbing edge coils. Indeed, it is exactly this need which motivates the empirical mapping of $\tilde{\mathbf{b}}(\mathbf{r})$.

3.3.3 MHD Simulation Ensemble

To compare the empirical results with the predictions of MHD we employed the nonlinear simulation code named DEBS (Sovinec, 1995).[5] This code models an RFP equilibrium like that obtained in MST although with Lundquist numbers more than an order of magnitude below those obtained for low current plasmas. For this study we ran the code at an aspect ratio of three and an S of 10^3 until the simulation settled into a stationary equilibrium. We then proceeded to ensemble the Fourier components of the dominant modes over 100 time slices or realizations to average out transient phenomena. Analysis of the ensembled self and cross products between these components proceeded in a manner analagous to that described for actual data.

References

Becksted, J. A. (1995). *Sawteeth in the MST-RFP.* PhD dissertation, University of Wisconsin – Madison, Department of Physics.

Bendat, J. S. and A. G. Piersol (1980). *Engineering Applications of Correlation and Spectral Analysis.* New York: John Wiley and Sons.

Biewer, T. M. (1997). Electron temperature profile evolution profile a sawtooth in the MST–RFP. PLP-1206.

Hokin, S. and *et.al.* (1991). Global confinement and discrete dynamo activity in the MST–RFP. *Phys. Fluids B* **3**, 2241.

---

[5] The DEBS code ensembles presented in this thesis were arranged with and conducted by J. Wright.

Ji, H., A. F. Almagri, S. C. Prager, and J. S. Sarff (1995). Measurement of the dynamo effect in a plasma. *Phys. Plasmas* **3**(5), 1935–1942.

Lanier, N. E. (1996). Electron density fluctuations associated with tearing mode activity. PLP-1191.

Ortlani, S. and D. D. Schnack (1993). *Magnetohydrodynamics of Plasma Relaxation.* Singapore: World Scientific.

Sovinec, C. R. (1995). *Magnetohydrodynamic simulations of noninductive helicity injection in the reversed-field pinch and tokamak.* PhD dissertation, University of Wisconsin – Madison, Department of Physics.

van Miligen, B. P., C. Hidalgo, and E. Sánchez (1995). Nonlinear phenomena and intermittency in plasma turbulence. *Phys. Rev. Lett.* **74**(3), 395–398.

4

Magnetic Fluctuations

Fluctuations in the mean magnetic field of the RFP constitute the better known half of the $\langle \tilde{\mathbf{v}} \times \tilde{\mathbf{b}} \rangle$ dynamo term. Consequently, full characterization of these fluctuations in time, frequency, wavenumber, and radius proved essential to our measurements. To accomplish this we performed a radial scan with a magnetic probe, establishing the phase and amplitude dependence of the three components of $\tilde{\mathbf{b}}(r)$ roughly a third of the way into the plasma. At the plasma edge we employed poloidal and toroidal coil arrays to measure the wavenumber, frequency and time behavior of $\tilde{b}$ over the sawtooth crash. Because of the large radial coherence lengths of these predominantly low-wavenumber fluctuations we were able to combine these measurements to map correlations of $\tilde{v}$ with modes resolved at the edge, to predict behavior of the dynamo product in the core.

Magnetic fluctuations have been long studied in the RFP for the role they play in particle and energy transport, nonlinear three-wave physics, and flattening of the current profile (Hutchinson *et.al*, 1984; La Haye *et.al.*, 1984; Brotherton-Ratcliffe, Gimblett, and Hutchinson, 1987). Thus, many results presented in this chapter are well known and included because they are essential to subsequent meausurements. The key results of this nature are:

- The measured $\tilde{b}_r$ fluctuations rise in amplitude away from the edge exceeding the edge $\tilde{b}_\theta$ amplitude by a factor of three
- The phase of $\tilde{b}_r$ relative to $\tilde{b}_\theta$ at the wall remains at $\pi/2$ over the outer third plasma radius in agreement with MHD which predicts no phase variation over the full plasma radius.
- At the sawtooth crash the total magnetic fluctuation power increases tenfold and the wavenumber dispersion of the power broadens.
- The fluctuations exhibit Doppler frequencies of 10–20 kHz which decrease over the crash as the plasma decelerates.
- The wavenumber dispersion of $\tilde{b}_{\theta,n}$ is dominated by the $m=1$, $n=6$ mode except for immediately following the crash when the $m=1$, $n=5$ dominates.

In addition we present three additional novel results less critical to the thesis :

- Boundary conditions applied to edge measurements of $\tilde{b}_{\theta,n}$ and $\tilde{b}_{\phi,n}$ imply poloidal mode numbers of $m=0$ for $n=1$–4, $m=1$ for $n=6$–9, and $m\approx2$ for $n>11$.
- The relative phase of magnetic coils in the poloidal array exhibits a poloidal dependence consistent with the outward shift of the resonant flux surface.
- The magnitude of $\tilde{b}_\theta$ averaged over the sawtooth cycle scales weakly with S, with most of the scaling stemming from the decreased duty of the fluctuations at high S.

We structure this chapter in three sections. The first section briefly describes the magnetic probe and coil arrays employed for our measurements. Next we establish sign conventions for the description of the fluctuations consistent with the observed perturbation structure and apply boundary conditions to determine the behavior of $\tilde{\mathbf{b}}$ at the edge. Finally, we present the results listed above starting with the key probe and the coil arrays measurements and ending with short sections describing the three new results.

4.1 Magnetic Pickup Coils

4.1.1 The insertable magnetic probe

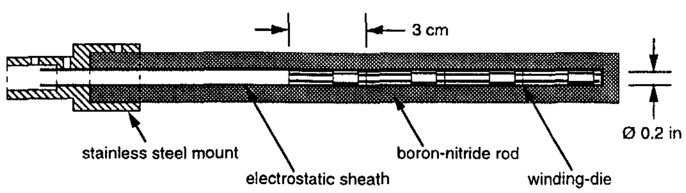

Fig. 4.1.— The insertable magnetic probe contains four winding dies stacked within a boron nitride shield. The die at the probe tip was wound to measure all three field components, while the remaining three contained only $\tilde{b}_r$ windings. The dies were coated with silver paint which serves as an electrostatic shield for the coils.

We employed an insertable magnetic probe to measure $\tilde{\mathrm{b}}(\mathrm{r})$ several centimeters into the plasma.[1] Four boron nitride winding dies make up the core of the probe. Each die is a cylinder 3 cm long and 0.2 inches in diameter with groves milled for windings measuring poloidal, toroidal, and radial magnetic field. In our measurements all four die were wound for $\tilde{b}_r$ measurements, while the die at the probe tip was also would for $\tilde{b}_\theta$ and $\tilde{b}_\phi$ measurements. Due to the finite radial dimension of the coils the $\tilde{b}_\theta$ and $\tilde{b}_\phi$ coils spatially average over 3 cm in radius while the $\tilde{b}_r$ coil averages over 1 cm. The wound die are coated first with a boron nitride paste and then with a silver paint to provide electrostatic shielding. Finally, the coated die are housed inside a 0.5 inch-dia. boron nitride rod to protect the assembly from the plasma. The completed probe is mounted onto a standard probe shaft with six BNC outputs for the four radially separated $\tilde{b}_r$ and the additional $\tilde{b}_\theta$ and $\tilde{b}_\phi$ signals. While the probe has demonstrated measurement

---

[1] The insertable magnetic probe was designed and constructed by A. F. Almagri.

capability at insertions of greater than 25 cm, substantial degradation of the plasma condition occurs at insertions of $\gtrsim$10 cm.

4.1.2 Edge coil arrays

The large coherent structure of the dominant magnetic modes allows edge coils to be used to characterize magnetic fluctuations throughout the plasma. Because these coils do not interfere with the plasma, edge $\tilde{b}$ measurements may be made at multiple positions and then correlated to derive information about the spatial structure of the modes. One common technique employs coil arrays to sample the magnetic perturbation at regularly spaced intervals enabling Fourier decomposition of the measured fluctuations. For most measurements we employed the toroidal array of 64 coil sets evenly distributed in toroidal angle at 241P. Each set consists of $\tilde{b}_\theta$, $\tilde{b}_\phi$, and $\tilde{b}_r$ coils wound on a single die. We typically employ every other poloidal field coil in the array for a total of 32 $\tilde{b}_\theta$ signals providing resolution of the dominant toroidal modes up to $n=15$. However, to insure that high n toroidal modes do not alias down to the low n mode of interest we occasionally employed all 64 $\tilde{b}_\theta$ coils. Poloidal field pickup coils are preferred over the toroidal field pickup coils as the purely toroidal vacuum field prior to the shot allows for the straight forward calibration of B_ϕ pickup due to the slight misorientation of the $\tilde{b}_\theta$ coils. A somewhat more complicated procedure does exist for the correction of the toroidal field coils and, for reasons explained below (§ 4.3.3), some experiments were performed with 32 $\tilde{b}_\theta$ coils and the corresponding 32 $\tilde{b}_\phi$ coils. The conducting wall suppresses radial magnetic fluctuations at the edge so the $\tilde{b}_r$ coils in the edge array are rarely employed. In addition to the toroidal array, we often employed a poloidal array of sixteen coil sets at 180T. For our measurements we typically employed only eight $\tilde{b}_\theta$ coils.

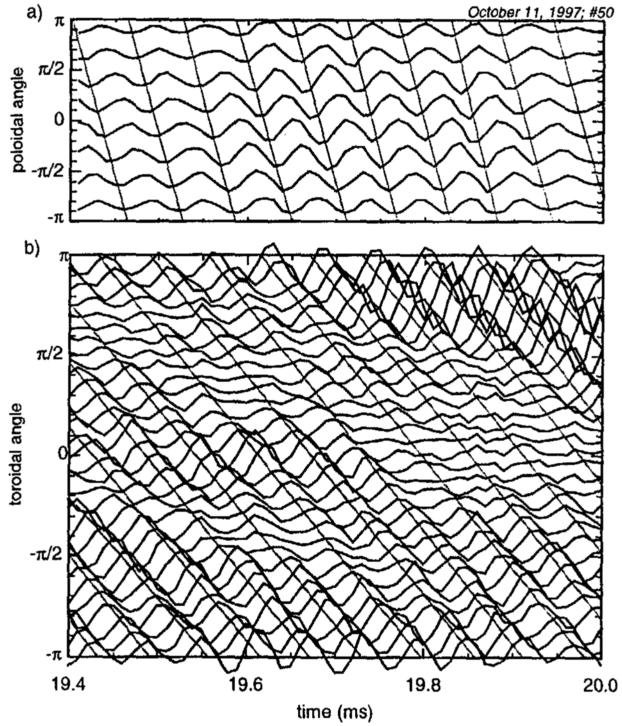

Fig. 4.2.— a) $\tilde{b}_\theta$ fluctuations measured by the eight evenly spaced coils of the poloidal array. The signal from each coil is plotted about the coil's poloidal angle. The grey lines indicate $m=1$ fluctuation wavefronts. b) 32 $\tilde{b}_\theta$ signals fluctuations plotted about the toroidal angle of their respective toroidal array coils. Grey lines highlight the $n=6$ fluctuation wavefronts.

To resolve magnetic modes with amplitudes just a few percent the mean field the relative gains of coils in the toroidal array must be extremely well calibrated. Though coil areas were measured upon the installation of the arrays, uncertainties in that initial calibration, slight errors in the coil orientations, and the accumulated integrator drift combine to produce substantial errors in the recorded coil gains. These errors dominate the actual magnetic fluctuations such that Fourier analysis of coils normalized with the recorded gains yields the locked mode structure of the calibration errors. To overcome this difficulty we employ the toroidal symmetry of the magnetic field averaged over a time window which greatly exceeds the fluctuation period, to perform an *in situ* calibration of the coil gains. This technique has proven extremely effective, even enabling the resolution of the locked mode structure by calibrating the gains over an average of several shots. Because of the substantial poloidal asymmetry in the mean field the same technique may not be used to normalize the poloidal array signals. This generally prevents the straight-forward application of poloidal mode analysis with the poloidal array signals.

4.1.3 Standard Fourier analysis of edge magnetics

We employ standard spatial Fourier decomposition to extract the fluctuating components of individual toroidal modes from the toroidal array signal. We define the time varying cosine, $\tilde{b}_{\theta,n}(t)$, and sine, $\tilde{b}^*_{\theta,n}(t)$, amplitude of the n'th toroidal modes simply as,

$$\tilde{b}_{\theta,n}(t) \equiv \frac{2}{N_c}\sum_i \tilde{b}_\theta \cos(n\phi_i) = b_{\theta,n} e^{i(m\theta_c+\omega t+\delta_{b_n})}, \tag{4.1}$$

$$\tilde{b}^*_{\theta,n}(t) \equiv \frac{2}{N_c}\sum_i \tilde{b}_\theta \sin(n\phi_i) = b_{\theta,n} e^{i(m\theta_c+\omega t+\delta_{b_n}+\frac{\pi}{2})}, \tag{4.2}$$

where ϕ_i is the toroidal angle of the i'th coil, and θ_c is the poloidal angle of the array. In principle we should include high n aliased modes ($n' = kN_c \pm n,\ k \in \{1,2,3,\dots\}$), however, in practice if N_c is large enough the aliased power should be minimal. Physically, $\tilde{b}_{\theta,n}$ may be interpreted as the instantaneous amplitude of the n'th toroidal mode at $\phi = 0$, $\theta = \theta_c$ while $\tilde{b}^*_{\theta,n}(t)$ is the amplitude of that same mode at $\phi = \pi/2n$. $\theta = \theta_c$. The codes which perform the normalization and Fourier analysis of the toroidal array signals may be found in § B.5.

4.2 Fluctuation Geometry and Boundary Conditions

The dominant magnetic modes in MST may be viewed as standing waves which vary harmonically in θ and ϕ but not in r. These modes travel with the plasma past stationary coils in the lab frame at Doppler frequencies of 10–20 kHz while the amplitude of the modes in the plasma frame evolves on the time scales of the sawtooth cycle. Correlation with these global magnetic fluctuations requires consistent definitions of the fluctuation geometry and propagation direction. We specify these below, establishing conventions consistent with the observed fluctuations which will be employed for the remainder of this thesis. We also derive simple relations between the individual components of $\tilde{\mathbf{b}}$ from the edge boundary conditions in MST. We employ the right-handed toroidal geometry shown in Fig. 4.3 and its cylindrical analog for these calculations and throughout the remainder of this thesis.

4.2.1 The sign of m and n

In the RFP most of the fluctuation power resides in a few $m = 1$, $n \gtrsim 2R/a$ modes resonant near the core and the $m = 0$, $n = 1$ mode resonant at the reversal surface (§ 4.3.2). We determine the relative signs of m and n for a single core mode from the resonance

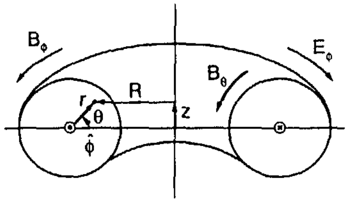

Fig. 4.3.— A right-handed toroidal geometry is employed consistently throughout this thesis. Note the direction of $\hat{\theta}$ is opposite that of the MST naming convention. Cylindrical calculations employ an analogous geometry.

condition,

$$\mathbf{k_{mn}} \cdot \mathbf{B} = \frac{m}{r}B_\theta + \frac{n}{R}B_\phi = 0, \tag{4.3}$$

yielding,

$$\frac{m}{n} = -\frac{rB_\phi}{RB_\theta} > 0, \tag{4.4}$$

where the final inequality derives from the negative ratio of B_θ and B_ϕ in the core (Fig. 4.3). Eq. 4.4 provides the orientation of $\mathbf{k_{mn}}$, however the wavenumber's sign depends on the propagation direction of the perturbations. This may be obtained by inspection of the magnetic fluctuations wavefronts measured by the poloidal and toroidal arrays (Fig. 4.2). The slopes of these wavefronts is consistent with $m = 1$, $n > 0$, and $\omega > 0$ where the equation for the wavefront is given by, $m\theta + n\phi + \omega t =$ cons. We may also take the time derivative of the wavefront equation obtaining the Doppler frequency of the perturbation, $mv_\theta/r + nv_\phi/R + \omega = 0$. With $\omega > 0$ and $n > 0$, assuming $nv_\phi/R \gg mv_\theta/r$, this relation mandates that the toroidal velocity of the modes be negative, $v_\phi < 0$, in agreement with the measured ion flow in the MST core.

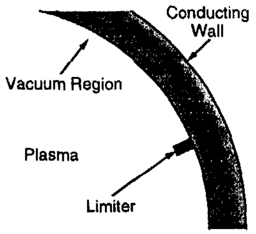

Fig. 4.4.— Graphite limiters create a thin ~ 1 cm vacuum region between the plasma and the 5 cm thick aluminum shell.

The determination of the fluctuation geometry allows us to correlate spatially separated fluctuation measurements provided they share the mode structure of the dominant magnetic fluctuations. The phase measured between two single helicity signals, $\tilde{x}$ and $\tilde{y}$ would be given by,

$$\Phi(\tilde{x}, \tilde{y}) = m(\theta_x - \theta_y) + n(\phi_x - \phi_y) + \delta_x - \delta_y, \tag{4.5}$$

where $\theta_{x(y)}$ and $\phi_{x(y)}$ are the poloidal and toroidal locations of the $\tilde{x}(\tilde{y})$ measurements, and $\delta_x - \delta_y$ is the relative phase of the fluctuations at the same location in the plasma. We typically wish to solve for this relative phase shift, subtracting off the phase incurred from the physical separation of the measurements,

$$\delta_x - \delta_y = \Phi(\tilde{x}, \tilde{y}) - m(\theta_x - \theta_y) - n(\phi_x - \phi_y). \tag{4.6}$$

Throughout this thesis the term "local phase" will refer to the term on the LHS of Eq. 4.6.

4.2.2 Edge Boundary Conditions

Conducting wall and thin vacuum region

The boundary conditions at the edge of the plasma determine the relative phase and amplitude of $\tilde{b}_r$, $\tilde{b}_\theta$, and $\tilde{b}_\phi$ at $r=a$. A highly conductive aluminum shell surrounds the MST plasma suppressing the growth of linear tearing modes and inductively canceling fast radial magnetic field fluctuations at the edge. The resistive shell time is on the order of one second while, for a rotating plasma, the tearing modes typically fluctuate at 10–20 kHz. Thus to the dominant fluctuations the MST wall looks perfectly conducting allowing us to stipulate our first boundary condition,

$$\tilde{b}_r(a,\theta) = 0. \tag{4.7}$$

This condition fails to hold at gaps in the shell which extend about the machine in the toroidal and poloidal direction. Sizable radial field errors grow robustly at the gaps providing a stationary reference frame to which the plasma can lock. However, the discharges chosen for our measurements rotated rapidly past these errors providing to good approximation a symmetric conducting outer boundary. The aluminum MST shell serves also as the vacuum chamber allowing in principle formation of plasma up to the shell wall. However, graphite limiters which protrude approximately 1 cm from the wall prevent this, forming a thin vacuum region about the plasma. This region insulates the plasma from the wall allowing us to stipulate our second boundary condition,

$$\tilde{j}_r(a,\theta) = 0. \tag{4.8}$$

Like Eq. 4.7, this condition breaks down at the toroidal gap and poloidal gap. However, for the rotating discharges selected for our measurements Eq. 4.8 is observed to hold.

Cylindrical application of boundary conditions to $\tilde{\mathbf{b}}$

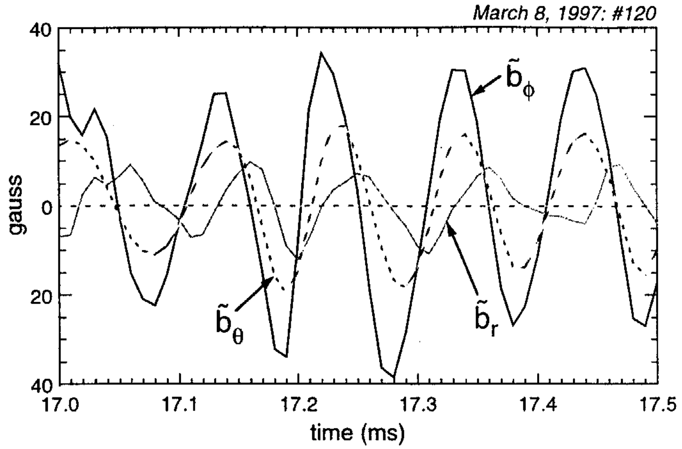

Fig. 4.5.— Measurements of $\tilde{\mathbf{b}}$ near the edge with the insertable probe confirm our calculations showing $\tilde{b}_\theta$ and $\tilde{b}_\phi$ to be in phase, while $\tilde{b}_r$ is $\pi/2$ out of phase.

We now seek to employ the boundary conditions established above to determine the relative phase and amplitude of the components of $\tilde{\mathbf{b}}$ at the vessel wall. For our initial calculations we employ the cylindrical analog to the right-handed toroidal geometry in Fig. 4.3 with the fields and their derivatives evaluated at $r = a$. Eq. 4.8 and Ampere's Law yield the relation,

$$\begin{aligned}
\mu_0 \tilde{j}_r(a,\theta) &= \hat{r}\cdot\left(\nabla\times\tilde{\mathbf{b}}\right)_{r=a} \\
&= \frac{1}{a}\frac{\partial\tilde{b}_\phi}{\partial\theta} - \frac{1}{R}\frac{\partial\tilde{b}_\theta}{\partial\phi} \\
&= in\frac{b_\theta}{R}e^{i(m\theta+n\phi+\omega t+\delta_{b\theta})} - im\frac{b_\phi}{a}e^{i(m\theta+n\phi+\omega t+\delta_{b_\phi})} \\
&= 0.
\end{aligned} \tag{4.9}$$

This may then be solved for the the relative amplitude,

$$\frac{b_\phi}{b_\theta} = \frac{na}{mR}, \tag{4.10}$$

and the relative phase,

$$\delta_{b_\theta} - \delta_{b_\phi} = 0, \tag{4.11}$$

of the toroidal and poloidal magnetic fluctuations. Note, for $m = 0$ fluctuations b_θ must vanish indicating that the $m = 0$ fluctuations resonant at the plasma reversal surface should be largely invisible to the $\tilde{b}_\theta$ pickup coils employed for the dynamo measurements. Measurements with the companion array of $\tilde{b}_\phi$ pickup coils confirms this revealing an $m = 0$, $n = 1$ mode with an amplitude comparable to the dominant $m = 1$ modes (Fig. 4.13). For the dominant $m = 1$ modes the RHS of Eq. 4.10 reduces to ~ 2 indicating toroidal fluctuations roughly twice the magnitude of the measured b_θ. To first order b_θ and b_ϕ are observed to be in phase in agreement with Eq. 4.11. Explanation of slight phase shifts between the two requires the toroidal analysis provided in Appendix A.

While $\tilde{b}_r$ vanishes at the plasma boundary we observe its amplitude to increase monotonically as we enter the plasma. Indeed the coupling believed to drive the poloidal dynamo field, $\langle \tilde{v}_\phi \tilde{b}_r \rangle$, requires a large radial field in the core. To investigate the phase of $\tilde{b}_r$ near the edge together with its radial derivative we combine the divergence free condition for $\tilde{\mathbf{b}}$ with Eq. 4.7 to yield,

$$\begin{aligned} \left(\nabla \cdot \tilde{\mathbf{b}}\right)_{r=a} &= \frac{1}{a}\frac{\partial (r\tilde{b}_r)}{\partial r} + \frac{1}{a}\frac{\partial \tilde{b}_\theta}{\partial \theta} + \frac{1}{R}\frac{\partial \tilde{b}_\phi}{\partial \phi} \\ &= \frac{\partial b_r}{\partial r} e^{i(m\theta + n\phi + \omega t + \delta_{b_r})} \\ &\quad - im\frac{b_\theta}{a}\left(1 + \frac{b_\phi^2}{b_\theta^2}\right) e^{i(m\theta + n\phi + \omega t + \delta_{b_\theta})} = 0. \end{aligned} \tag{4.12}$$

With some manipulation, Eq. 4.12 yields the relations,

$$\frac{a}{b_\theta}\frac{\partial b_r}{\partial r} = m\left(1 + \frac{b_\phi^2}{b_\theta^2}\right). \tag{4.13}$$

and,

$$\delta_{\tilde{b}_\theta} - \delta_{\tilde{b}_r} = \frac{\pi}{2}, \tag{4.14}$$

For the dominant $m = 1$, tearing modes Eq. 4.13 indicates a large growth of $\tilde{b}_r$ from its zero value at the edge. The $\pi/2$ phase shift predicted by Eq. 4.14 is observed with minor corrections which may also be explained through the toroidal analysis in Appendix A.

4.3 Magnetic Fluctuation Measurements

Below we describe the results from a number of measurements which provide a fairly complete characterization of the magnetic fluctuations in MST. We begin with the measured radial profile of the amplitude and phase of the individual components of $\tilde{\mathbf{b}}(r)$. We then describe the behavior of individual toroidal modes resolved by the edge coil arrays. Both of these measurements provide essential background for subsequent analysis of both measured velocity fluctuations and dynamo products. The last three sections contain novel results which are, however, less critical to this thesis. First we define and describe the measured behavior of "average m" for the resolved toroidal modes. We then report the manifestation of toroidal effects in the phase of $\tilde{b}$ as a function of poloidal angle. And lastly, we present scaling results of the magnetic fluctuations with Lundquist number.

4.3.1 Measured magnetic fluctuation profiles

From boundary conditions imposed on the plasma at the edge we were able to derive the relative phase and amplitude of the three components of $\tilde{\mathbf{b}}$. However, moving into the plasma these relations change as $\tilde{b}_r$ and $\tilde{j}_r$ both become non-zero. Our measurement of the dynamo product relies on the estimation of the amplitude and phase of magnetic fluctuations in the interior of the plasma from measurements of $\tilde{b}_{\theta,n}$ at the edge. This motivated the measurements with the magnetic probe of the fluctuations over 15 cm into the plasma. The details of the experimental run may be found in § 3.3.2 and the probe is described above in § 4.1.1. Below we present the profiles predicted by MHD and then compare those profiles to measurements of the fluctuation amplitude and phase. We find that within the range of the probe scan all components of $\tilde{\mathbf{b}}$ increase away from the wall with a relative phase which does not vary. The passing of $\tilde{b}_\theta$ and $\tilde{b}_\phi$ through zero as predicted by MHD was not observed.

MHD predictions

The fluctuation profiles predicted by MHD are shown for each component of $\tilde{\mathbf{b}}(\mathrm{r})$ in Fig. 4.6. MHD predicts $\tilde{b}_r$ to grow to roughly three times $\tilde{b}_\theta(a)$ in the plasma mid region while $\tilde{b}_\phi$ rises sharply from the edge and then passes through zero near the deepest insertion of the fluctuation scan. $\tilde{b}_\theta$ rises more gradually and then turns over mid-radius, passing through zero deep into the plasma. The simulation holds $\tilde{b}_\theta$ and $\tilde{b}_r$ to identical values in core and sets $\tilde{b}_\phi(0) = 0$. Other than π phase shifts which occur when the amplitudes pass through zero the fluctuations maintain a relative phase over the plasma which does not vary from that set by the boundary conditions at the edge.

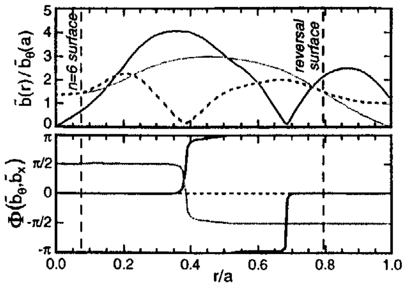

Fig. 4.6.— $n=6$ profiles of $\tilde{b}_\theta$ (dashed), $\tilde{b}_\phi$ (solid), and $\tilde{b}_r$ (grey) amplitudes obtained from ensembled realizations from nonlinear MHD simulations. Amplitudes (top) are normalized to $\tilde{b}_\theta(a)$ while the phases (bottom) are referenced to $\tilde{b}_\theta(r)$. Grey region was scanned empirically by the magnetic probe.

Fluctuation amplitude profiles

We normalized the probe signal prior to ensembling by the rms amplitude of $\tilde{b}_\theta$ measured by the coils in the toroidal array. In this fashion we hoped to compensate partially for the global increase in magnetic fluctuation amplitude observed at deeper insertion depths. Unfortunately, we still are unable to compensate for the effects of the probe on the fluctuation profile at deeper insertions. The normalized signals were then ensembled over a time window extending from 10–20 ms for each insertion depth. Fig. 4.7 shows the normalized rms amplitudes of the signal from the $\tilde{b}_\theta$, $\tilde{b}_\phi$, and $\tilde{b}_r$ coils at the probe tip, where the squared amplitudes were averaged over the ensemble and the time window. As the coil moves into the plasma the measured $\tilde{b}_\theta$ level rises, reaching a plateau at roughly three times it's edge value. The edge $\tilde{b}_\phi$ amplitude nearly doubles the amplitude of $\tilde{b}_\theta$ consistent with Eq. 4.10 with $n=6$ and $m=1$. The toroidal fluctuations rise to a plateau of $\sim 3.5\ b_\theta(a)$ almost immediately and then fall slightly to an amplitude

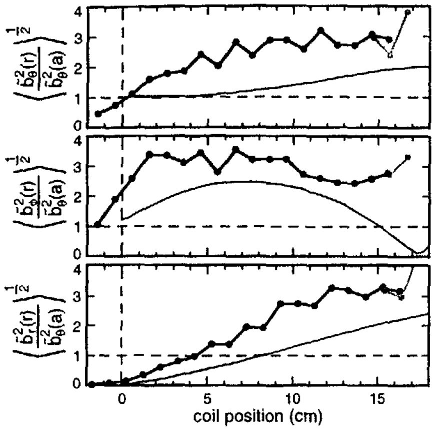

Fig. 4.7.— The rms amplitudes of a) $\tilde{b}_\theta$, b) $\tilde{b}_\phi$, and c) $\tilde{b}_r$ normalized to $\tilde{b}_\theta(a)$ measured by the toroidal array. The grey circles represent rechecks of the deep insertions performed at the end of the scan. The horizontal axis corresponds to the radial midpoint of the coil at each insertion depth. The predictions of DEBS are overplotted with the smooth curve.

of $\sim 2.5\ b_\theta(a)$ perhaps anticipating the pass through zero observed in the simulation. As one moves into the plasma the amplitude of $\tilde{b}_r$ rises steadily from zero to values 3–4 times the edge poloidal field at the deepest insertions. This growth is similar in nature but more aggressive than that observed in the simulation. We will revisit these amplitudes when estimating the size of the core dynamo products.

Correlation of modes over radius

The measured correlation profiles indicate dominant magnetic perturbations which exhibit coherence over the plasma radius. The coherence of the coil signals with the cosine amplitude of the $n = 6$ magnetic mode measured at the edge was calculated ate

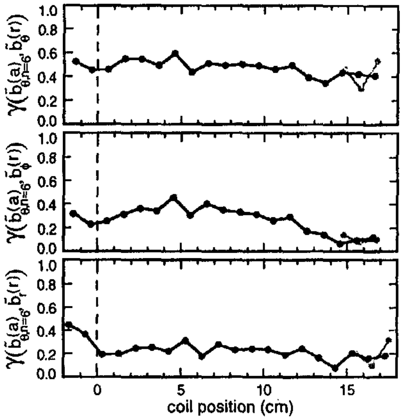

Fig. 4.8.— The correlation of the measured $\tilde{\mathrm{b}}$ with $\tilde{b}_{\theta,n=6}$ measured at the wall. The correlation baseline is less than 5%.

each insertion. The poloidal fluctuations exhibit a coherence of ~ 0.5 with the $n = 6$ mode over the entire region scanned by the probe. This substantial coherence reflects not only the global nature of the $n = 6$ perturbation but its dominance of the toroidal mode dispersion. The coherence for the toroidal and radial fluctuations is somewhat lower though still well above the coherence baseline. The coherence levels for these two components appears to drop off slightly at the deepest insertions. However this drop also occurs in the three radial coils spaced at shallower insertions and may therefore be an artifact of the probe-plasma interaction. Even so, $\tilde{b}_r$ exhibits a coherence of ~ 0.2 at the deepest insertions, only slightly below its value at the wall. Thus, we may feel confident that measurements conducted with edge coils do relate directly to the core fluctuation activity.

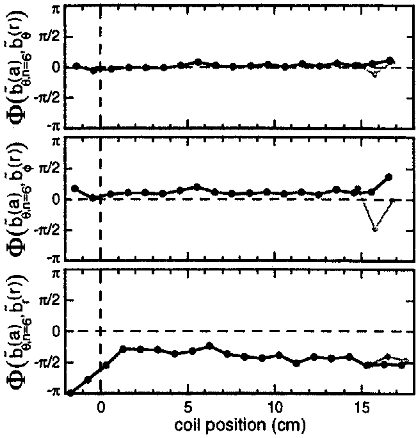

Fig. 4.9.— Measured phase of $\tilde{b}_\theta(r)$ with $\tilde{b}^c_{\theta,n=6}$ measured at the wall shows little variation in the measured phase with radius.

Fluctuation phase profile

The phase of the signals relative to the $n=6$ cosine amplitude was also calculated over the scanned radii. Both $\tilde{b}_\theta$ and $\tilde{b}_\phi$ show almost no phase shift relative to $\tilde{b}^c_{\theta,n=6}$ after appropriate corrections were made for the poloidal and toroidal separation of the probe and array measurements. This edge phase complies with our cylindrical estimate (Eq. 4.11), while the small phase shift of $\tilde{b}_\phi$ may reflect the toroidal effects calculated in § A. The relative phase of $\pi/2$ between $\tilde{b}_r$ and $b^c_{\theta,n=6}$ also agrees with the edge boundary conditions (Eq. 4.14). The phase of all three components exhibits remarkably little radial dependence allowing us to map the edge phase relations directly into the core.

4.3.2 Toroidal Magnetic Modes

Internally resonant modes in MST

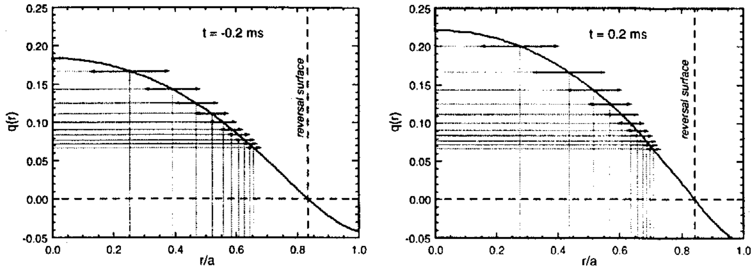

Fig. 4.10.— A cylindrical model of the safety factor profile for a typical, low-current discharge a) before and b) after a sawtooth crash. Vertical dotted lines identify multiple $m = 1$, $n \geq 5$ resonant surfaces while the horizontal arrows represent estimated island widths.

Low-n, $m=1$ magnetic modes resonant in the core dominate the magnetic fluctuation wavenumber spectrum in MST. Resonance occurs when the safety factor, given approximately by $q(r) \approx rB_\phi/RB_\theta$, passes through a magnetic surface satisfying $q(r_{mn}) = m/n$ (Fig. 4.10). At this resonant surface, radial magnetic fluctuations produce magnetic islands which alter the topology of the field over substantial fractions of the plasma radius. For MST q_o usually has values slightly below 0.2 on axis and then decreases with radius passing through zero with B_ϕ near the edge of the plasma. The innermost resonant mode is the $m=1, n=6$ although during a sawtooth crash we typically observe $q(0)$ rising above 0.2 bringing the $m=1$, $n=5$ briefly into resonance. These modes dominate higher n, $m=1$ modes which resonate farther out in the plasma where the plasma exhibits higher stabilizing shear. In addition to the core resonant $m=1$ modes, the MST plasma contains $m = 0$ modes resonant at the reversal surface. These modes are dominated by the $m = 0$, $n = 1$ which may be responsible for the three-wave coupling of adjacent $m = 1$ modes. Usually the $m = 0$ modes lock to the lab frame throughout the discharge making them difficult to observe with the coil arrays. However, careful measurements with the $\tilde{b}_\phi$ coil array reveal $m = 0$, $n = 1$ amplitudes comparable to the dominant $m = 1$ modes. This is especially true at the crash where enhanced nonlinear coupling between the modes is observed to distribute power to $m = 1$ modes with higher n.

Mode dispersion over the sawtooth

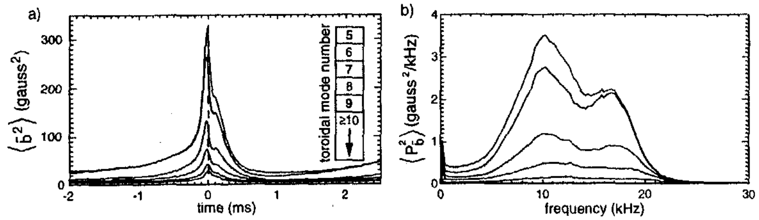

Fig. 4.11.— a) $\tilde{b}^2_{\theta,n}(t)$ ensembled over a sawtooth window. The total magnetic fluctuation power is traced out by the top curve. The light and dark bands indicate the distribution of power among the dominant toroidal modes as indicated by the key. b) The power spectra of the the magnetic fluctuations with the individual mode contributions again denoted by the light and dark bands.

At the sawtooth crash the total magnetic fluctuation power present in all toroidal modes increases dramatically from a total $\tilde{b}^2_\theta$ of 30 gauss^2 to a peak fluctuation power of 300 gauss^2 (Fig. 4.11a). Following the crash the fluctuation power drops nearly 50% in less than 50 μs, plateaus for $\sim$100 μs, and then decays over the next 0.5 ms to its baseline level. The two decay timescales following the crash appear similarly in all of the resonant

$m = 1$ modes, although the $m = 0$, $n = 1$ mode exhibits only the fast decay time scale. This leads to the speculative association of the faster timescale with nonlinear activity.

The wavenumber dispersion of the magnetic fluctuations varies over the sawtooth. Before the sawtooth there exists an almost single helicity, $n = 6$, magnetic fluctuation with a baseline RMS power of 10–20 gauss^2. As the sawtooth approaches the $n = 6$ mode grows and its fluctuation power cascades to higher n broadening the dispersion. The power attains its broadest wavenumber dispersion at the crash where the evidence of nonlinear coupling between the modes is the strongest. Following the crash the power drops off at higher n and appears in a newly resonant $m = 1$, $n = 5$ core mode. As the lowest n resonant mode the $n = 5$ dominates the dispersion, until q drops back below 0.2 and the $n = 6$ resumes dominance.

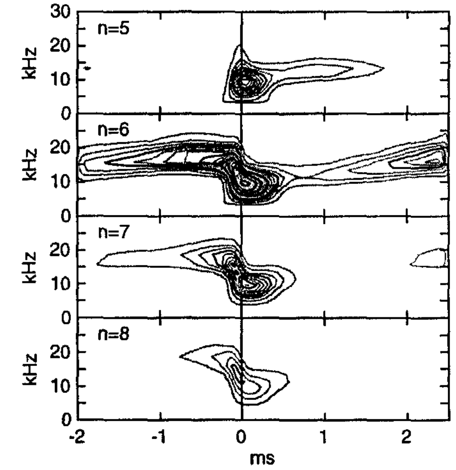

Fig. 4.12.— Contours of constant magnetic fluctuation power density in wavelet power spectra of dominant $m = 1$ modes over a sawtooth.

The ensembled power spectrum (Fig. 4.11b) shows magnetic fluctuation power predominantly in the range of 8–20 kHz. The two peaks in the power spectrum may be understood by referring to the wavelet power spectra (Fig. 4.12) for the four dominant magnetic modes. This shows the power tracking the Doppler frequencies of the modes in time accelerating away from the sawtooth and decelerating sharply at the sawtooth crash. The fast pre-crash mode frequencies give rise to the peak near 17 kHz while the slower postcrash frequencies produce the peak near 10 kHz. Note that the $n=5$ mode, which only appears following the crash, exhibits power only about the lower frequency peak.

4.3.3 "Average m" Calculation

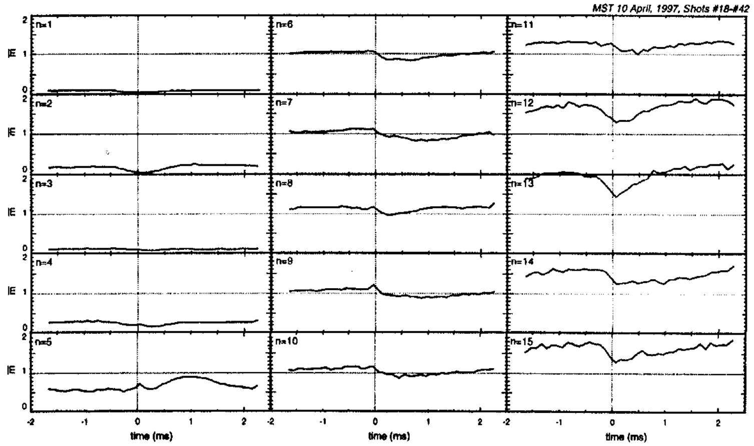

Fig. 4.13.— $\bar{m}$ (Eq. 4.15) over the sawtooth for $n=1$–15.

While we believe the dominant toroidal mode numbers resolved by the toroidal array to correspond to the core dominant $m=1$ modes, full two-dimensional Fourier decomposition is impossible with a single toroidal array. Instead, to obtain approximate poloidal mode information we employed the coincident toroidal arrays of 32 $\tilde{b}_\phi$ and 32 $\tilde{b}_\theta$ pickup coils to measure the full $\tilde{\mathbf{b}}_\mathbf{n}$ at the wall. Using Eq. 4.10 we may then define,

$$\bar{m} \equiv n \frac{a}{R} \left(\frac{\langle \tilde{b}^2_{\theta,n} \rangle}{\langle \tilde{b}^2_{\phi,n} \rangle} \right)^{\frac{1}{2}}, \tag{4.15}$$

where $\bar{m}$, is commonly referred to as the "average m". Unfortunately, this terminology is not wholly accurate as $\bar{m}$ generally does not equal a true power averaged m. That is to say that in general,

$$\langle m \rangle = \frac{\sum_m m\, \tilde{b}^2_{m,n}}{\sum_m \tilde{b}^2_{m,n}} \neq \bar{m}. \tag{4.16}$$

However, without a full two dimensional array of coils we have no way of measuring $\langle m \rangle$. Furthermore, for toroidal modes dominated by a single poloidal mode number, $\bar{m} \approx \langle m \rangle$.

Fig. 4.13 shows $\bar{m}$ for the fifteen resolved toroidal modes ensembled over a low current sawtooth cycle. For $5 \leq n \leq 10$, $\bar{m} \approx 1$ corroborating our expectations that these toroidal modes result from resonant $m=1$ tearing modes. The slight dip in $\bar{m}$ for these n for $t \approx 0$ provides additional indication of enhanced m=0 nonlinear activity at the sawtooth crash. For $n=1$, $\bar{m}=0$ consistent with its resonance at the reversal surface. For $n > 10$, $\bar{m} > 1$ suggesting that these modes include $m=2$ coupling of lower n internal modes. The highest $\bar{m}$ obtains for $n=13$ possibly from three-wave $m=2$ coupling of the dominant $n=6$ and $n=7$ modes.

4.3.4 Poloidal Phase Measurement

Difficulties in properly determining the gains of the coils in the poloidal array, prevents reliable Fourier decomposition of the m spectrum analogous that achieved for the n spectrum with the toroidal array. Instead we have performed a study of the relative

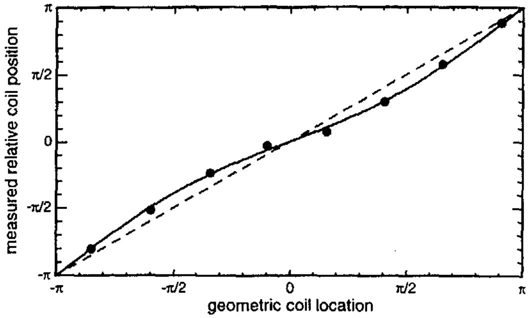

Fig. 4.14.— The measured relative phase of poloidal array coils vs. their poloidal angle. Deviations from the $m = 1$ line are consistent with outwardly shifted flux surfaces.

fluctuation phase between individual coils which should be independent of the coil gains. The relative phase between two poloidally separated measurements of a single helicity magnetic fluctuation should be given by,

$$\Phi(\tilde{b}_i, \tilde{b}_j) = m(\theta_i - \theta_j). \tag{4.17}$$

For $m = 1$ fluctuations measured this reduces to the poloidal separation of the coils. When we calculate the relative phase of the coils we find that to first order the fluctuation exhibits a clear $m = 1$ structure, cycling through 2π once in single poloidal transit (Fig. 4.14). However, the simple relation suggested by Eq. 4.17 does not fully describe the measured phase differences. A closer fit obtains from the expression,

$$\Phi(\tilde{b}_i, \tilde{b}_j) = \theta_i - \theta_j - \Delta(\sin(\theta_i) - \sin(\theta_j)). \tag{4.18}$$

This expression suggests that we could employ Eq. 4.17 by replacing θ with θ' given by,

$$\theta' = \theta - \Delta \sin(\theta), \tag{4.19}$$

where a simple fit to the data yielded $\Delta \approx 0.34$. This transformation of θ most likely represents a conversion from machine geometry to flux surface geometry. In fact Eq. 4.19 roughly corresponds to the correction one would expect from outwardly shifted flux surfaces. However, the size of the shift inferred from Δ ($\sim$ 14 cm) far exceeds that predicted by toroidal models of the equilibrium. Nevertheless, we will employ Eq. 4.19 with the empirical Δ to correct the poloidal position of subsequent fluctuation measurements.

4.3.5 Lundquist Number Scaling

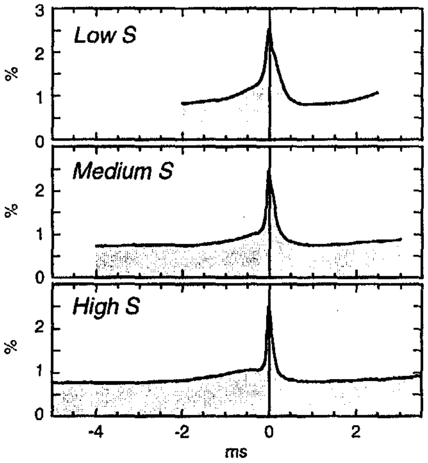

Fig. 4.15.— Ensembles of $\tilde{b}_\theta / B_\theta(a)$ at each S.

We investigated the scaling of magnetic fluctuations with Lundquist number using the three large ensembles described in § 3.3.1. The $\tilde{b}_\theta$ rms amplitude for each S is shown in Fig. 4.15 as a percentage the edge poloidal field. Neither the peak nor the baseline of the normalized fluctuations scales too dramatically remaining at ~1% and ~2% respectively for all three ensembles. Rather, what scales with S is the effective duty cycle of the fluctuations. As noted in our discussion of the sawtooth period scaling (§ 3.1.2) at higher S settings the decay phase extends while the crash phase becomes more abrupt. Thus the relative portion of the discharge during which the enhanced fluctuation levels occur decreases with S even though the actual fluctuation levels at and away from the crash remain unchanged.

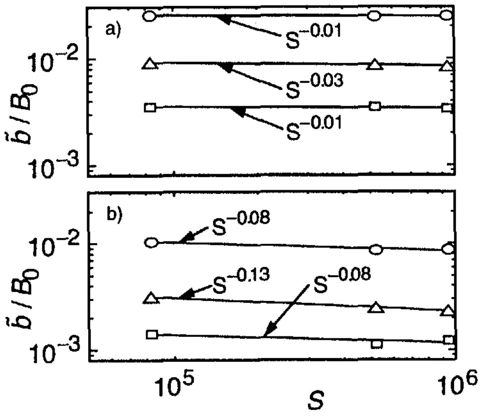

Fig. 4.16.— a) $\max(\tilde{b}_\theta/B_\theta)$ and b) $\langle b_\theta/B_\theta\rangle_{win}$ for the total rms fluctuation amplitude (circle), the $n = 7$ amplitude (triangle) and the $n = 10$ amplitude (square).

This duty cycle effect may be seen in the two scalings shown in Fig. 4.16. The top figure shows the absence of scaling of the peak fluctuation amplitude with S,

$$\max(\tilde{b}) \propto S^{-0.01}. \tag{4.20}$$

A similar result holds for scaling of the baseline fluctuation level. However, by averaging

the fluctuation level over the entire sawtooth cycle one recovers the effect of the decreasing fluctuation duty cycle and obtains a slight scaling of,

$$\langle\tilde{b}\rangle \propto S^{-0.08}. \tag{4.21}$$

These scalings are somewhat weaker than those found by Stoneking *et.al.*(1997), for which fluctuations were averaged over fixed time windows without regard to sawtooth positions.

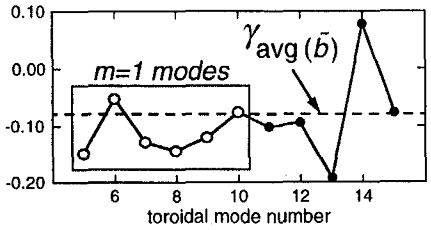

Fig. 4.17.— The scaling exponent for $\text{avg}(\tilde{b}_{\theta,n}/B_\theta(a))$. The dashed line shows the scaling exponent for the total rms magnetic fluctuation amplitude (Eq. 4.21.

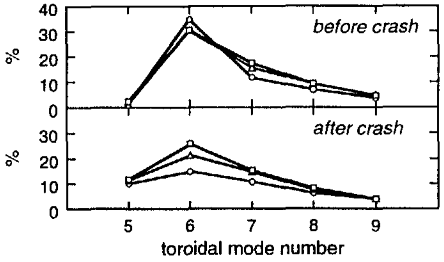

Fig. 4.18.— $\tilde{b}_n^2/\tilde{b}_{rms}^2$ before and after the crash for high (circle), medium (triangle), and low (square) S ensembles.

Fig. 4.16 also shows similar scaling for the $n = 7$ and $n = 10$ modes. These modes become important later on in our discussion of the dynamo measurements. The scaling exponents for the sawtooth averaged fluctuations of other modes is shown in Fig. 4.17. The scaling of the total fluctuation amplitude scales like the $n = 6$ which dominates the $m = 1$ fluctuation energy with the other resonant modes scaling somewhat more strongly as $\sim S^{-0.12}$. Thus, we might expect the dispersion to become more peaked as we move to higher S. This indeed occurs as illustrated in Fig. 4.18 before the sawtooth crash, where we see a slightly higher fraction of the fluctuation power contained in the $n = 6$ mode. However, immediately following the crash the dispersion of the high S ensemble is much broader indicating that the sawtooth crash distributes energy to high n more effectively at higher currents.

References

Brotherton-Ratcliffe, D., C. G. Gimblett, and I. H. Hutchinson (1987). *Plasma Phys. Controlled Fusion* **29**, 161.

Hutchinson, I. H., M. Malacarne, P. Noonan, and D. Brotherton-Ratcliffe (1984). *Nucl. Fusion* **24**, 59.

La Haye, R. J., T. N. Carlstrom, R. R. Goforth, G. L. Jackson, M. J. Schaffer, T. Tamano, and P. L. Taylor (1984). *Phys. Fluids* **27**, 2567.

Stoneking, M. R., J. T. Chapman, D. J. Den Hartog, S. C. Prager, and J. S. Sarff (1997). Experimental scaling of fluctuations and confinement with Lundquist number in the RFP. *Phys. Plasmas* **5**(4), 1004–1014.

5

Ion Velocity Fluctuations

In MHD theory the dynamics of the magnetic field and the dynamics of the ion fluid may be viewed as two aspects of a single dynamic. Thus one expects the existence of large scale perturbations in the magnetic field to imply similar perturbations in the plasma flow. Such fluid velocity fluctuations are observed in MHD computational simulations and predicted in analytic treatments of the RFP. While magnetic perturbations in the RFP have been thoroughly diagnosed through probe and edge measurements, the measurement of fluid fluctuations has proven a greater diagnostic challenge, limited heretofore to indirect observations at the edge.

In this chapter we report on new direct measurements of ion fluid fluctuations in the core region of the MST. These measurements were conducted using the Ion Dynamics Spectrometer, a passive spectroscopic diagnostic with a capacity to resolve fast, large-scale fluctuations. The capacity of the IDS for such measurements is discussed in detail in Chapter 2 (esp § 2.5.2). The key results of these measurements are as follows:

- Toroidal and poloidal ion velocity fluctuations exist in MST with amplitudes of ~1 km/s and distributions in time and frequency resembling those observed for the magnetic fluctuations.

- The velocity fluctuations exhibit strong coherence with the magnetic fluctuations at the tearing mode frequencies prior to the sawtooth crash.
- The phase between $\tilde{v}_\phi$ and $\tilde{b}_\theta$ is consistent with a non-zero dynamo product in the MST core.
- The relative phase between $\tilde{v}_\theta$ and $\tilde{b}_\theta$ is consistent with a superposition of two effects: the advection of a parallel flow gradient past the IDS line of sight and MHD fluctuations producing an electric field.
- The radial profile of $\tilde{v}(r)$ is narrower than that of $\tilde{b}(r)$, consistent with MHD.
- Radial velocity fluctuations in MST are smaller than the measured $\tilde{v}_\theta$ and $\tilde{v}_\phi$ and exhibit a very low coherence with the magnetic fluctuations.
- The normalized magnitude of $\tilde{v}$ has weak scaling with S although its coherence with the magnetics decreases dramatically at higher S.

This chapter employs the well diagnosed magnetic fluctuations as a tool for investigating the structure and dynamics of the velocity fluctuations. While impacting the potential for a nonlinear $\langle \tilde{\mathbf{v}} \times \tilde{\mathbf{b}} \rangle$ dynamo electric field in the MST, we postpone discussion of the dynamo fields generated by the dynamo until next chapter.

We begin this chapter in § 5.1 by describing the distribution of velocity fluctuation power in frequency and time. We then investigate the coherence of these fluctuations with individual magnetic modes in § 5.2 and their phase relative to those modes in § 5.3. In § 5.4 we describe the measurement of radial velocity fluctuations. Finally, § 5.5 briefly presents the scalings of $\tilde{v}$ with S.

5.1 Velocity Fluctuation Power

The ensemble averaged fluctuation power in frequency and time of chord averaged velocity measurements, $\langle P_{\tilde{v}}(f) \rangle$ and $\langle \tilde{v}^2(t) \rangle$, indicate the presence of ~1 km/s ion velocity fluctuations in the MST interior. The chord averaged velocity fluctuation power is concentrated at frequencies of 8–20 kHz and exhibits a sharp burst of fluctuation power during the sawtooth crash. Wavelet power spectra help distinguish the velocity fluctuation power in frequency and time from the overlapping contributions of instrumental noise and sudden changes in the plasma flow.

5.1.1 Power spectra

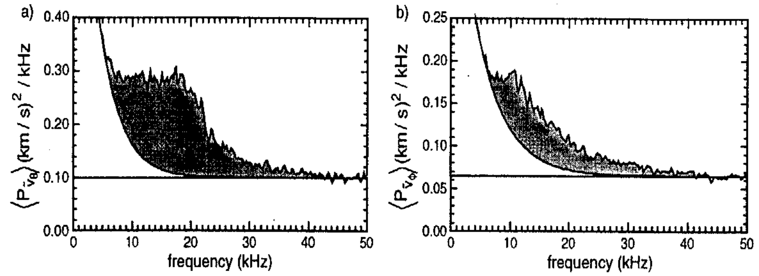

Fig. 5.1.— Power spectra for chord-averaged a) $\tilde{v}_\theta$ and b) $\tilde{v}_\phi$ are divided into estimated regions of power from velocity fluctuations (dark), instrumental noise (light), and secular ($m=0$,$n=0$) variations in the bulk ion flow (white).

$P_{\tilde{v}_\theta}$ and $P_{\tilde{v}_\phi}$, the power spectra of the chord averaged $\tilde{v}_\theta$ and $\tilde{v}_\phi$ respectively (Fig. 5.1), exhibit concentrations of velocity fluctuation power at the frequencies characteristic of the magnetic fluctuations (Fig. 4.11). We isolate and quantify this power by modeling and then subtracting the fluctuation power contributed by instrumental noise and secular ($m = 0$,$n = 0$) variations in the bulk plasma flow. Monte-carlo simulations of photon counting noise propagated through the IDS measurement (§ 2.3.5) yielded output signals with flat power spectra. We adopt this model for the experimental $P_{\tilde{v}}$ fixing the level of the noise floor to equal the average power density from 45–49 kHz where we expect the contributions from fluctuations to be negligible. The fluctuation power of the noise floor determined in this fashion accounts for 52% and 60% of the total chord averaged $\tilde{v}_\theta$ and $\tilde{v}_\phi$ power, respectively.

We expect power from the secular evolution of the plasma flow to peak at low frequency with a high frequency tail due to the rapid changes during the sawtooth crash. Examining the spectra from 0–3 kHz, we observe that the power spectra minus the noise floor, $P_{\tilde{v}}(f) - N_{\tilde{v}}$, falls off roughly as $e^{-\gamma f}$. By extrapolating an exponential fit to this region out to higher frequencies we obtain a rough estimate for the high frequency tail of the secular power contribution. For both measured spectra the power contained between this curve and the noise floor accounts for approximately 20% of the total measured fluctuation power. Because most of this power is at low frequencies where we expect the secular power to dominate, more accurate modeling of the high frequency tail should not change this number by more than a few percent.

Having accounted for noise and secular power in the spectra we are left with a region of velocity fluctuation power comprising 20–30% of the original measured power in the IDS signal. The fluctuations are particularly well resolved in the $\tilde{v}_\theta$ power spectrum, which plateaus from 10–20 kHz where we expect the majority of the velocity fluctuation power to be located. To estimate the true magnitude of the velocity fluctuation we must correct for the attenuation of the velocity fluctuation amplitude by the chord average. For the toroidal chord, extremely simple models of $m=1, n=6$ $\tilde{v}_\phi(r)$ fluctuation profiles upon convolution with the toroidal chord instrument function retain between 12% and 18% of their amplitude. A $\tilde{v}_\phi(r)$ with an optimal profile relative to the instrument function retains only 20% of its amplitude. For the $m=1$, $n=7$ mode, typical profile models retain 10% to 15% of their amplitudes with the optimal mode retaining only 16%. The poloidal chord retains far more of the $\tilde{v}_\theta$ signal with a maximum retention of 69% and more typical retentions of 40–60% for simple models of high n, $m=1$, $\tilde{v}_\theta(r)$ profiles near the edge. These attenuation factors may be summarized as,

$$|\langle \tilde{v}_{\phi,6} \rangle| = \int \mathbf{dl} \cdot \hat{\phi}\; \tilde{v}_{\phi,6} \approx (0.15 \pm 0.03)\, |\tilde{v}_{\phi,6}|, \tag{5.1}$$

$$|\langle \tilde{v}_{\phi,7} \rangle| = \int \mathbf{dl} \cdot \hat{\phi}\; \tilde{v}_{\phi,7} \approx (0.12 \pm 0.02)\, |\tilde{v}_{\phi,7}|, \tag{5.2}$$

$$|\langle \tilde{v}_{\theta,n} \rangle| = \int \mathbf{dl} \cdot \hat{\theta}\; \tilde{v}_{\theta,n} \approx (0.50 \pm 0.08)\, |\tilde{v}_{\theta,n}|, \tag{5.3}$$

where the quantity on the LHS is the amplitude of the chord-averaged fluctuation and the quantity on the RHS is the amplitude of the velocity fluctuation in the plasma times the appropriate attenuation factor. Taking these geometric factors into account we may adjust the integrated velocity fluctuation power in Fig. 5.1 to yield the following estimates of ion velocity fluctuation amplitude:

$$\langle \tilde{v}_\theta^2 \rangle^{\frac{1}{2}} \approx (2.0 \pm 0.3)\,(1.6\ \mathrm{km/s}) \approx 3.2 \pm 0.5\ \mathrm{km/s}. \tag{5.4}$$

$$\langle \tilde{v}_\phi^2 \rangle^{\frac{1}{2}} \approx (6.8 \pm 1.0)\,(1.0\ \mathrm{km/s}) \approx 6.8 \pm 1.0\ \mathrm{km/s}, \tag{5.5}$$

where the geometric correction term of 6.8 ± 1.0 and 2.0 ± 0.3 are calculated by inverting Eqs. 5.1 and 5.3 respectively. With a majority species temperature of ~80 eV in the plasma interior we obtain an order of magnitude comparison with the thermal ion velocity of,

$$\tilde{v} \approx 10^{-2} v_{th}. \tag{5.6}$$

This emphasizes how very small the fluctuating shifts in the velocity distribution function are relative to the distribution's thermal width. Referring back to Eq. 2.25 we may calculate that these fluctuations correspond to $\sim 10^{-2}$ Å shifts in the measured intensity

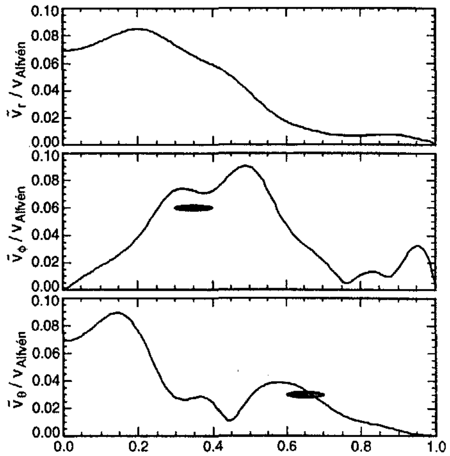

Fig. 5.2.— MHD predictions of$\tilde{\mathbf{v}}(r)$ normalized by the Alfvén velocity. Grey ellipses indicate empirical estimates from IDS measurements.

distribution function, or approximately 4% the width of a single IDS channel. We may further characterize these fluctuations by comparing their energy density with that of the magnetic fluctuations. Using an order of magnitude estimate of $\tilde{b} \sim 10$ gauss we obtain,

$$E_{\tilde{b}} \approx 50 E_{\tilde{v}}. \tag{5.7}$$

This agrees within an order of magnitude with the MHD simulation of the RFP which generally observe magnetic fluctuation energies which greatly exceed the fluid velocity fluctuation energies. The dominance of $E_{\tilde{b}}$ in the MHD dynamo distinguishes it from astrophysical or geophysical dynamos which typically are dominated by the kinetic fluid energy of the system (§ 1.2).

Finally, we normalize $\tilde{v}$ by the estimated Alfvén velocity in the low current regime

obtaining,

$$\langle \tilde{v}_\theta^2 \rangle^{\frac{1}{2}} / v_{Alfv\acute{e}n} \approx 0.03, \tag{5.8}$$

$$\langle \tilde{v}_\phi^2 \rangle^{\frac{1}{2}} / v_{Alfv\acute{e}n} \approx 0.06, \tag{5.9}$$

where we have employed $v_{Alfv\acute{e}n}$ of 110 km/s (Table 3.1). Overplotting these estimates onto the $\tilde{\mathbf{v}}(r)$ profiles modeled with the MHD code (Fig. 5.2) we see remarkable agreement with the measurements, nearly coinciding with the modeled $\tilde{v}_\theta(r)$ and $\tilde{v}_\phi(r)$ curves. While the detailed agreement of the model and measurements may be fortuitous, clearly the velocity fluctuation measured in the core possess a magnitude consistent with the predictions of MHD.

5.1.2 Power distribution over a sawtooth

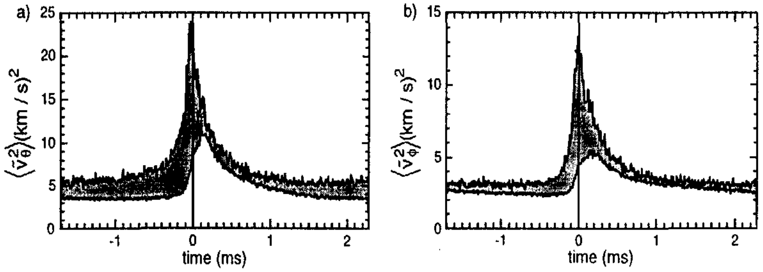

Fig. 5.3.— Average a) poloidal and b) toroidal velocity fluctuation power (dark) over a sawtooth crash. The noise-floor (light) is distributed proportionately to $\langle \hat{\chi}^2 \rangle$ (Eq. 2.27).

The velocity fluctuation power rises sharply at the sawtooth crash reaching peak level of several (km/s)^2 (Fig. 5.3). The noise power estimated from the power spectrum may be distributed in time proportionately to the $\hat{\chi}^2$ according to the error propagation

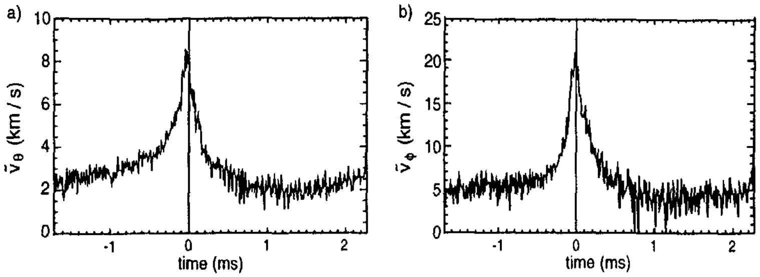

Fig. 5.4.— RMS a) poloidal and b) toroidal velocity fluctuations over a sawtooth after subtraction of the noise baseline and correction for geometric attenuation.

results presented in § 2.3.5 . Subtracting that noise floor we obtain the evolution of velocity power shown in Fig. 5.4. As noted in the power spectra, the poloidal velocity fluctuations are more clearly resolved over the sawtooth, with baseline levels prior to the crash of $\tilde{v}_\theta^2 \approx 2$ (km/s)^2 compared to $\tilde{v}_\phi^2 \approx 0.5$ (km/s)^2. At the crash these values rise dramatically to 16 (km/s)^2 for the poloidal chord and 8 (km/s)^2 for the toroidal chord. Following the crash the $\tilde{v}_\theta^2$ drops precipitously while the decay times for $\tilde{v}_\phi^2$ are comparable to its more gradual rise time. Both fluctuation levels bottom out at barely resolved amplitudes of approximately half their pre-crash baseline. This sawtooth evolution closely resembles that observed for $\tilde{b}^2$ (Fig. 4.11).

Prior to ensemble averaging the fluctuations in time, both signals were high-pass filtered with a cut-off frequency of 3 kHz, removing well over half of the estimated secular power. Nevertheless, the high frequency tail of the secular power, which eludes the digital filter, contributes to the measured fluctuation power in Fig. 5.4. We expect this power to be localized near the sawtooth crash where the fast evolution of the mean flow takes place. Thus the question arises as to how much of the power at the crash reflects the

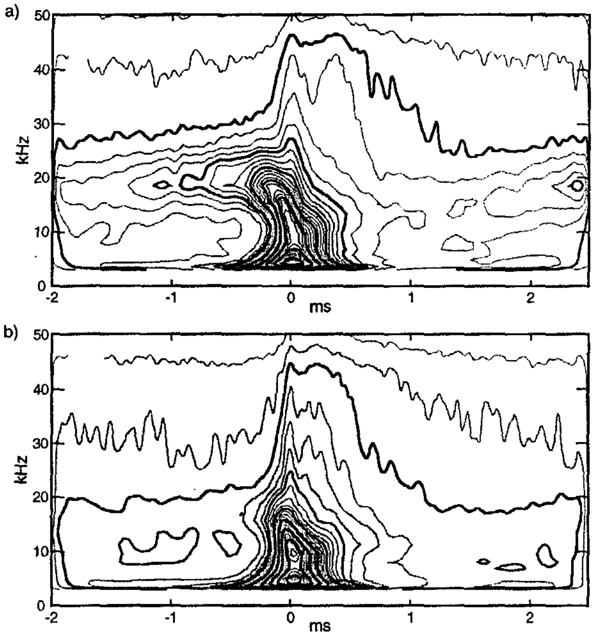

Fig. 5.5.— Contours of constant power density in the averaged a) $\tilde{v}_\phi$ and b) $\tilde{v}_\theta$ wavelet power spectra. Two peaks appear in the bottom contour at 5 and 10 kHz near the sawtooth crash.

growth of velocity fluctuations and how much is due to the fast secular changes. The wavelet power spectra of the fluctuations provides a partial answer to this question (Fig. 5.5). Examining the distribution for $\tilde{v}_\phi$ at the crash, one observes two distinct peaks in the power distribution. The "peak" at ~5 kHz is the high frequency remnant of the secular power peak at 0 kHz removed by the high-pass filter. The apparent broad time duration of this residual secular power about the crash reflects the poor time resolution of the wavelet analysis at low frequencies (Eq. 3.19). A second distinct peak occurs at 10 kHz with the power dropping slowly out to 20 kHz. This peak provides clear evidence of velocity fluctuations concentrated near the crash. Integrating the power beneath the two peaks we find that the power from 3-8 kHz is roughly half of that from 8-20 kHz. This integration gives an approximate correction of two-thirds to the peak velocity fluctuation near the crash. In the $\tilde{v}_\theta$ distribution the two peaks merge into a ridge which extends from the secular to the fluctuation frequencies.

5.2 Coherence of Velocity and Magnetic Fluctuations

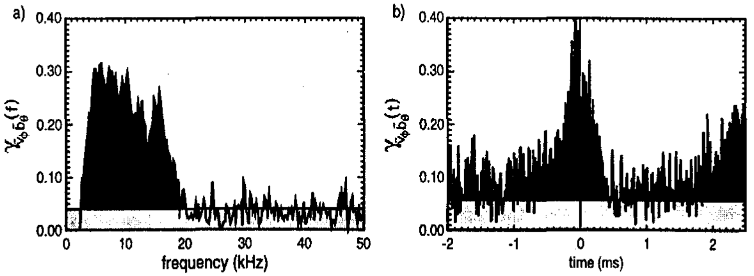

Fig. 5.6.— The measured coherence of the toroidal ion velocity fluctuations with an edge magnetic coil in a) frequency (Eq. 3.14) and b) time (Eq. 3.11). The dashed line represents the coherence baseline.

Above we noted similarities in the frequency distribution of magnetic fluctuation power, $P_{\tilde{b}}$ (Fig. 4.11b), and velocity fluctuation power, $P_{\tilde{v}}$ (Fig. 5.1) and common features in the time evolution of $\tilde{b}^2$ (Fig. 4.11a) and $\tilde{v}^2$ (Fig. 5.3). These observations strongly suggest that the fluctuations in magnetic field and ion flow are dynamically coupled. We confirm this through the measurement of significant coherence between the two quantities in time and frequency. Fig. 5.6 illustrates such coherence between $\tilde{v}_\phi$ and the $\tilde{b}_\theta$ from a single edge coil. In frequency we see a coherence level of 0.2 or higher from 5–15 kHz while in time the coherence peaks immediately prior to the sawtooth. Subsequent paragraphs explore these dynamics in detail characterizing the coherence of $\tilde{b}_\theta$ with $\tilde{v}_\theta$ and $\tilde{v}_\phi$ over the three dimensional domain of time, frequency and wavenumber. We conclude that the distribution of coherence in time and frequency largely reflects the distribution of $\tilde{b}^2(f,t)$ and $\tilde{v}^2(f,t)$. In wavenumber the incidence of coherence does not match the measured dispersion of $\tilde{b}_{\theta,n}$ reflecting instead the changing sensitivity of the IDS chord to the different wavenumbers. Lastly, a sharp rise in coherence prior to the sawtooth crash suggests enhanced fluctuation coupling while a dramatic drop at the crash suggests a scrambling of the fluctuation phase.

5.2.1 Coherence with Individual Modes — Description

The velocity fluctuations measured by the IDS may be expressed as the weighted sum of fluctuations with various wavenumbers,

$$\tilde{v} = \sum_n C_n \tilde{v}_n, \tag{5.10}$$

where C_n depends on the convolution of the radial mode structure with the IDS instrument function and the CV emission profile. If we assume that all activity in the plasma at the resonant wavenumbers in the plasma occurs with a coherent phase relation to the magnetic perturbations we may employ our knowledge of the magnetic perturbations to extract mode information from the velocity fluctuations. The rotation of the low n magnetic modes converts their spatial structure in the plasma frame into a temporal variation in the lab frame. This allows the use of $\tilde{b}_{\theta,n}$ as a set of time dependent basis functions for the spatial Fourier analysis of $\tilde{v}$,

$$\langle \tilde{v}\tilde{b}_{\theta,n}\rangle = \sum_{n'} C_{n'}\langle \tilde{v}_{n'}\tilde{b}_{\theta,n}\rangle \approx C_n\langle \tilde{v}_n\tilde{b}_{\theta,n}\rangle. \tag{5.11}$$

By normalizing this product by the velocity and magnetic fluctuation power (i.e. calculating the coherence), we hope to extract information about both C_n and v_n. Below we present the full wavelet coherence spectra of $\tilde{b}_{\theta,n}$ with $\tilde{v}_\theta$ and $\tilde{v}_\phi$ for $n=6-15$. This allows the simultaneous description of the coherence dynamics over wavenumber, frequency, and time. The following paragraphs will introduce these spectra by describing the important features which are observed. Interpretation of the spectra in terms of underlying physical and instrumental phenomena will be provided in the following subsection (§ 5.2.2).

Coherence of poloidal velocity fluctuations

Subdominant magnetic perturbations with toroidal mode numbers of eight and above exhibit high coherence levels with $\tilde{v}_\theta$. The coherence levels increase steadily over the low n modes from a peak value of just 20% for the dominant $n=6$ mode to a peak value of nearly 50% for relatively small $n=9$ mode. At higher n the coherence drops off slowly maintaining reasonable levels out to the tiny $n=14$ mode, which achieves a higher peak coherence than that achieved by the enormous $n=6$ mode. The distribution of coherence in frequency and time reflects that observed in the single coil coherence levels of Fig. 5.6. The resolved modes exhibit robust coherence over the full sawtooth cycle tracking the accelerations and decelerations of the dominant $\tilde{b}_\theta$ frequencies in time. Just

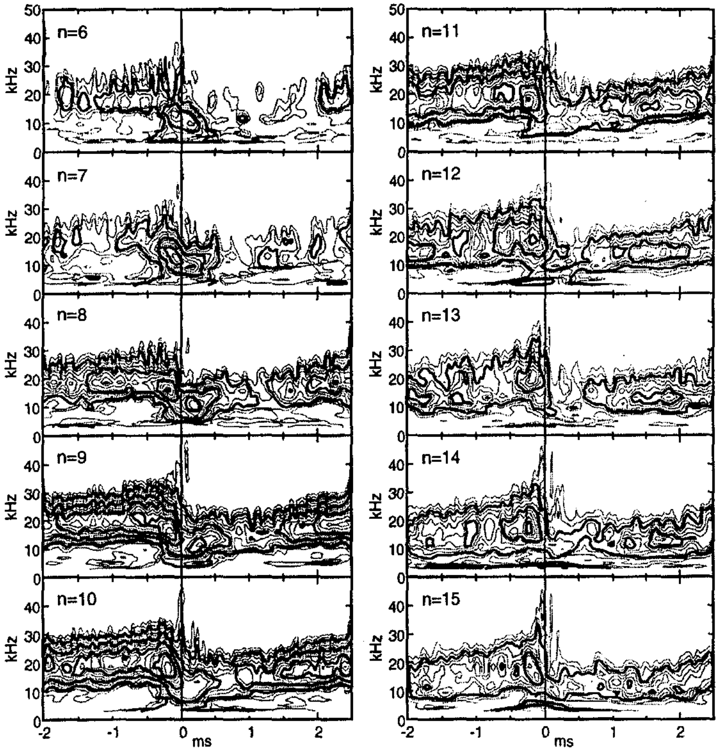

Fig. 5.7.— Wavelet coherence spectra of $\tilde{v}_\theta$ and $\tilde{b}_{\theta,n}$ for $n = 6-15$. Each dark contour represents ten percent coherence. Peak coherence occurs at the sawtooth in the tearing mode frequencies for $n = 9-10$. All contours shown exceed baseline levels.

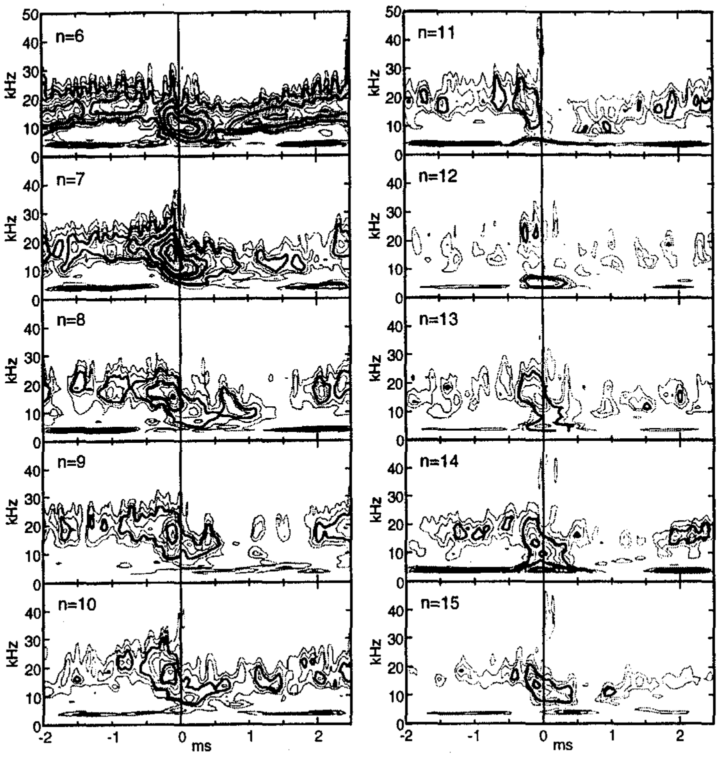

Fig. 5.8.— Wavelet coherence spectra of $\tilde{v}_\phi$ and $\tilde{b}_{\theta,n}$ for $n = 6 - 15$. Chord shows strong, almost exclusive coherence with $n = 6$ and $n = 7$. Each dark contour represents 10% coherence level. All contours shown exceed baseline values.

prior to the sawtooth crash $\gamma_{\tilde{v}_\theta \tilde{b}_\theta}$ peaks along with the $\tilde{v}$ and $\tilde{b}$ fluctuation levels before it drops precipitously at the crash to roughly half its peak value. Modes with $n = 6 - 9$ exhibit a second coherence peak ~0.2 ms after the crash, whereas the higher n modes exhibit only a slow rebuilding back to their pre-crash levels over 1–2 ms.

Coherence of toroidal velocity fluctuations

The large $n = 6$ and $n = 7$ modes dominate the wavenumber dispersion of $\gamma_{\tilde{v}_\phi \tilde{b}_{\theta,n}}(f, t)$ (Fig. 5.8) in sharp contrast to the dispersion observed for $\gamma_{\tilde{v}_\theta \tilde{b}_{\theta,n}}$. The toroidal velocity coherence falls off dramatically for $n \geq 8$ reaching near baseline values over most of the coherence spectrum for $n > 10$. Of the two peak modes the highest coherence appears just prior to the crash for the $n = 7$ where $\gamma_{\tilde{v}_\phi \tilde{b}_{\theta,7}}(f, t) \approx 0.6$.[1] In time $\gamma_{\tilde{v}_\phi \tilde{b}_{\theta,n}}$ behaves similarly to $\gamma_{\tilde{v}_\theta \tilde{b}_{\theta,n}}$, peaking just prior to the crash where it drops dramatically, rebounding a fraction of a ms later in a second peak for $n \leq 9$. However, unlike the poloidal chord only the $n = 6$ exhibits robust coherence over the full sawtooth cycle.

5.2.2 Coherence with Individual Modes — Interpretation

Figs. 5.7-5.8 depict coherence levels for each chord with complex, and often surprising, variations in frequency, time, and wavenumber. To structure our interpretation of these dynamics we enumerate three distinct factors which together determine $\gamma_{\tilde{v}\tilde{b}}$:

1. The presence of fluctuations with amplitudes comparable to or greater than the instrumental noise levels.

2. The actual coherence of the ion velocity fluctuations with the magnetic fluctuations

---

[1] This measurement holds the current record for the highest coherence ever measured between a chord averaged IDS $\tilde{v}$ measurement and a second independent fluctuation. The ability to achieve such a high coherence a signal as noisy as the IDS derives from the combination of large ensemble analysis, spatial Fourier isolation of the dominant $\tilde{b}$ modes, and resolution, via wavelet analysis, of coherence over frequency and time.

in the MST plasma.

3. The sensitivity of the IDS chord to the wavenumber and radial structure of each mode.

Below we attempt to associate phenomena observed in $\gamma_{\tilde{v}_\theta \tilde{b}_{\theta,n}}(f,t)$ and $\gamma_{\tilde{v}_\phi \tilde{b}_{\theta,n}}(f,t)$ with the appropriate factors. First, we examine when the measured coherence reflects the presence of fluctuations and when it reflects the actual coherence of those fluctuations. Then we discuss the interaction of different wavenumbers with the poloidal and toroidal IDS chords, in an attempt to explain the unusual wavenumber dispersion of each view.

Measured coherence of noisy signals

In § 3.2.3 we defined the coherence of two fluctuating signals as the *percentage* of the signals' power which exhibits a non-random relative phase. For noiseless fluctuation measurements, this holds true as the amplitudes of the fluctuations divide out of the measured coherence perfectly. However with the introduction of instrumental noise a portion of the fluctuation power from one or both signals will exhibit a random phase, regardless of the actual coherence of the fluctuations in the plasma. This introduces a dependence of the measured coherence on the relative amplitude of the fluctuations and the instrumental noise. For the IDS measurement with 50% or greater noise levels this effect may be dramatic. We quantify this dependence by rewriting the expression for coherence taking noise into account,

$$\gamma^2_{\tilde{v}\tilde{b}} = \frac{|\langle \tilde{v}\tilde{b} \rangle|^2}{\langle \tilde{v}^2 + N^2_{\tilde{v}} \rangle \langle \tilde{b}^2 + N^2_{\tilde{b}} \rangle}, \tag{5.12}$$

where $N_{\tilde{v}}$ and $N_{\tilde{b}}$ are the velocity and magnetic noise levels respectively. When $\tilde{v}^2 \gg N^2_{\tilde{v}}$ and $\tilde{b}^2 \gg N^2_{\tilde{b}}$ the dependence of $\gamma_{\tilde{v}\tilde{b}}$ on the amplitudes of the fluctuations diminishes,

and more accurately reflects the true coherence of the signals. When the converse is true for either signal the measured coherence reflects both the physical coherence of the fluctuations and the signal to noise ratio of the measurement. This is the limit generally appropriate to the IDS. The dependence of coherence on the presence of substantial fluctuation amplitude explains the basic and expected features in Fig. 5.7–5.8, including the distribution of coherence in frequency and the gross evolution of the coherence over the sawtooth.

The dramatic rise and fall of the coherence near the sawtooth cannot be explained by signal to noise dynamics in Eq. 5.12. Prior to the crash the rising amplitude of the velocity fluctuations in the tearing mode frequencies grow to satisfy $\tilde{v}^2 \gg N^2_{\tilde{v}}$. and rough calculations indicate signal-to-noise effects on the coherence saturate ~0.5 ms before the crash. Nevertheless the measured coherence continues to rise indicating that the fluctuations actually become more coherent prior to the crash. More dramatically, at the crash the drop in coherence precedes and exceeds the decay of the fluctuation amplitudes suggesting a phase scrambling of the fluctuations by the sawtooth. For the dominant modes this randomization is brief and the coherence bounces back following the crash, falling off more gradually after that along with the diminishing fluctuation amplitudes.

Here I propose a scenario which is largely consistent with the observations, that may explain the sudden rise and fall of the measured coherence about the crash. Prior to the crash power concentrates in the dominant modes which lock together forming a structure often referred to as "slinky". The effect of this locking is to make Eq. 5.11 break down as $\langle \tilde{v}_{n'} \tilde{b}_{n,\theta} \rangle$ becomes nonzero for $n' \neq n$. Hence, fluctuation wavenumbers other than the one being correlated with $\tilde{b}_{\theta,n}$ develop a nonrandom phase relationship with the correlated mode and contribute to the measured coherence. In short, phase locking of the modes induces leakage of the coherence with indiviudal modes to the measured coherence of adjacent modes producing a net rise in the overall measured coherence. At the crash two things happen. First, nonlinear coupling distributes power to higher n modes. Second,the modes decouple with their relative phase reset by the crash. This combination pulls power out of the low n dominant modes and then cuts off the leakage of those high n modes back to low n. This produces a coherence crash for the dominant resolved modes. Shortly after the crash, however, the low n modes regain their dominance of the power dispersion producing a return of much of their measured coherence. The phases remain unlocked for several ms leaving the higher n modes with little power and no coherence leakage from the high n modes. Hence, their coherence remains low until the onset of phase locking at the next crash

Coherence vs. n reflects resolution of IDS chord

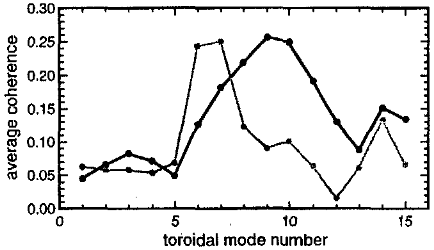

Fig. 5.9.— Coherence of $\tilde{v}_\theta$ (solid) and $\tilde{v}_\phi$ (grey) with $\tilde{b}_{\theta,n}$ averaged in frequency from 7 to 20 kHz, and in time over the full sawtooth cycle.

A prominent exception to the variation of the measured coherence with the fluctuation amplitude may be found in the wavenumber dependence of $\gamma_{\tilde{v}_\theta \tilde{b}_{\theta,n}}$ and $\gamma_{\tilde{v}_\phi \tilde{b}_{\theta,n}}$.

Fig. 5.9 summarizes this dependence for each chord over the 15 resolved wavenumbers. For the poloidal chord we again note the broad resolution of high n modes peaking with $n=9-10$. In contrast the toroidal chord exclusively resolves $n=6-7$ with irregular and generally poor resolution of higher n modes. This contrasting wavenumber dispersion of the two chordal $\tilde{v}$ measurements derives from the differing sensitivities of the two chords to the modes present in MST. To understand these sensitivities we re-examine the IDS instrument functions derived in § 2.5.2. The instrument functions for both chords are plotted in Fig. 5.10 for $n = 6 - 15$. The poloidal chord instrument function diverges roughly as $1/(r/a - 0.6)$ and does not vary with toroidal mode number. The toroidal chord instrument function, on the other hand, penetrates to an impact parameter of $r/a \approx 0.3$ and becomes increasingly oscillatory at higher wave numbers. To estimate the overall sensitivity of the chord to a particular mode we convolve this exact instrument function with the radial profile of the velocity fluctuation. Unfortunately, we possess no direct measurement of $\tilde{v}_n(r)$ making precise calculation of this sensitivity impossible. Still, to gain an approximate understanding of the observed dynamics we conjecture that *$\tilde{v}_n(r)$ is maximum at its rational surface with a radial extent proportional to the magnetic island width of that mode.* We illustrate this conjecture with the shaded Gaussians plotted behind the chordal instrument function in Fig. 5.10. The centroids of these Gaussians are equal to the average estimated position of the resonant surface and their variance is proportional to the estimated island widths.

From Fig. 5.10 a simple explanation for the wavenumber dispersion of $\gamma_{\tilde{v}_\theta \tilde{b}_{\theta,n}}$ emerges. The velocity fluctuation radial profiles for individual modes, $|\tilde{v}_n(r)|$, do not extend over the full plasma radius and the impact parameter of the poloidal chord is simply too far out, radially, to detect the core modes. As the modes increase in n

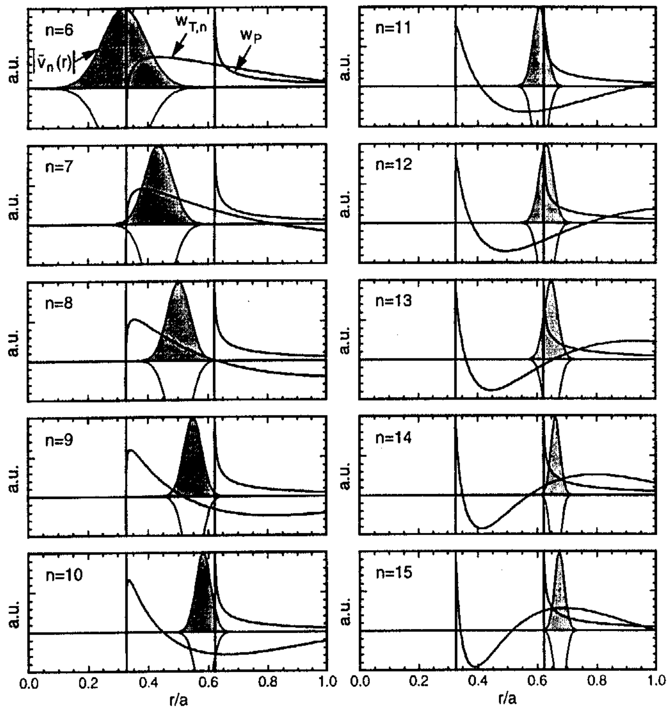

Fig. 5.10.— IDS instrument functions (§ 2.5) for the poloidal chord measurements of $\tilde{v}_{\theta,n}$ ($r_i/a = 0.6$) and toroidal chord measurements of $\tilde{v}_{\phi,n}$ ($r_i/a = 0.3$) plotted for $n = 6 - 15$. The over plotted gaussians are centered about the estimated mode resonance surface with variances proportional to the estimated island widths.

their resonant surfaces move outward and more of their fluctuation power falls along the poloidal line of sight. The peak measured coherence at $n = 9$ suggests that the resonance surface for the modes may lie farther out in radius than the positions estimated by the cylindrical equilibrium model such as might be expected by an outward Shafranov shift of the plasma column. The poloidal chord coherence clearly implies that the velocity fluctuations for each mode extend over a fraction of the machine radius in contrast to the magnetic perturbations which extend coherently from the plasma interior to the wall. The high coherence of the $n = 12$ mode compared to the $n = 6$ mode is particularly striking evidence of this. This result invites measurements to be made at additional impact parameters to produce mode resolved reconstructions of $\tilde{v}_{\theta,n}(r)$.

The complex wavenumber dependence of $\gamma_{\tilde{v}_\phi \tilde{b}_{\theta,n}}$ derives from the convolution of fluctuation power which moves out in radius with n and an instrument function which becomes increasingly oscillatory with increased n. While the impact parameter of the toroidal chord falls outside the estimated position of the $n = 6$ rational surface, much of the fluctuation power in this large mode falls within view of the chord accounting for a large measured coherence. For $n = 7$ the bell of the instrument function moves slightly inward and the rational surface moves slightly outward resulting in the fortuitous overlay of fluctuation power with instrumental resolution. The fact that the maximum coherence peaks is attained for this mode which is roughly half the size of the $n = 6$, indicates that $\tilde{v}_{\phi,n}(r)$ like $\tilde{v}_{\theta,n}(r)$ possesses limited radial extent. As we move to $n = 8 - 9$ the fluctuation power coincides with the null in the instrument function yielding a minimum in the measured coherence. With increasing n the measured coherence moves up and down as the velocity fluctuation profiles coincide with the hills, valleys, and nulls of the toroidal instrument function. This intermittent coherence at high n again suggests sharply defined velocity fluctuation profiles for each mode. If the power from these high n modes were broadly distributed in radius their short wavelengths would be averaged over by the toroidal chord. However, localized, high-n fluctuation power may act like a delta function, picking out the value of the IDS instrument function at the radius of its peak activity. This is one possible explanation for a baseline coherence level achieved for the tiny $n = 12$ mode followed by a jump in coherence for the even tinier $n = 14$ mode. The latter reaches peak coherence levels exceeded only by the dominant $n=6$ and $n=7$ modes. Localized fluctuation amplitudes might also produce time dynamics in $\gamma_{\tilde{v}\tilde{b}}$ as individual high n modes move in and out of view. Unfortunately, our limited knowledge of the precise form or location of $\tilde{v}_n(r)$ prevents the identification of such effects.

5.3 Fluctuation Phase

In this section we examine the phase between the chord averaged velocity fluctuations $\tilde{v}_\theta$ and $\tilde{v}_\phi$ and the fluctuating magnetic field. We begin with the frequency and time behavior of the measured phase for $\langle\tilde{v}_\theta\tilde{b}_{\theta,n=9}\rangle$ and $\langle\tilde{v}_\phi\tilde{b}_{\theta,n=7}\rangle$. Next we derive a map from the measured $\langle\tilde{v}\tilde{b}\rangle$ phase, $\Phi(\tilde{v},\tilde{b})$, to an average local fluctuation phase, $\langle\delta_v - \delta_b\rangle$. Finally, we present and interpret the local phase of $\tilde{v}_\theta$ and $\tilde{v}_\phi$ relative to the magnetics.

5.3.1 Measured chord-averaged phase versus time and frequency

Fig. 5.11a shows the measured phase and coherence between the chord-averaged poloidal ion velocity fluctuation and the cosine amplitude of the $n = 9$ toroidal mode. Prior to the sawtooth as the coherence rises near 0.3, the measured phase becomes more cleanly resolved, however its mean value does not appear to change. Following the crash the mean phase does change, rising nearly 30° and becomes less well resolved as the

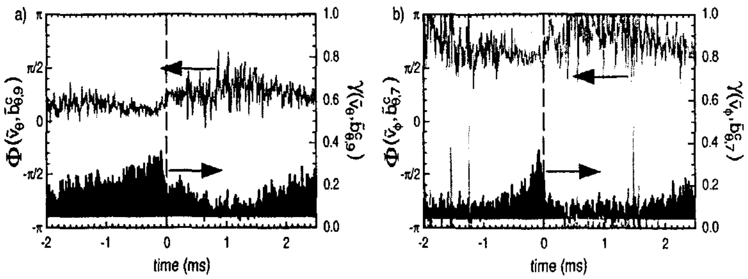

Fig. 5.11.— Grey line denotes the measured phase of a) $\langle\tilde{v}_\theta b_{\theta,n=9}\rangle$ and b) $\langle\tilde{v}_\phi b_{\theta,n=7}\rangle$ over a sawtooth. The darkly shaded region at the bottom of both plots represents the measured coherence while the lightly shaded region represents the coherence baseline.

coherence drops near baseline levels. The measured phase of $\langle\tilde{v}_\phi b_{\theta,n=7}\rangle$ (Fig. 5.11b) exhibits similar time dynamics, although away from the sawtooth the coherence is lower and the phase, therefore, is more poorly resolved.

A partial explanation for the dynamics of the phase versus time may be found in the complementary behavior of the phase versus frequency, (Fig. 5.12). The relative phase of both products decreases as frequency increases. Thus prior to the crash the rapidly rotating high frequency fluctuations sample the lower phase region of the spectra, while after the crash the decelerated modes sample the high-phase, low-frequency portion of the spectra. The negative slope of the phase with frequency is consistent with a uniform time delay of 7.5 μs between $\tilde{v}_\theta$ and $\tilde{b}_{\theta,n=9}$, and a time delay of 9.3 μs between $\tilde{v}_\phi$ and $\tilde{b}_{\theta,n=7}$, where the magnetic fluctuations *lag* the velocity fluctuations in both cases. A check of the analog processing for both $\tilde{v}$ and $\tilde{b}$ measurements found the systems to be synchronous to within one μs following the correction (implemented in the `fit.pro` code) for the 3.64

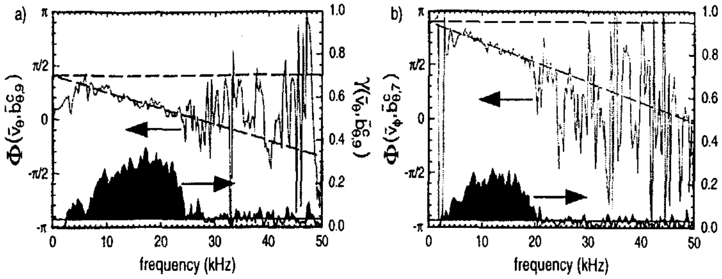

Fig. 5.12.— Grey trace denotes the measured phase of a) $\langle \tilde v_\theta b_{\theta,n=9}\rangle$ and b) $\langle \tilde v_\phi b_{\theta,n=7}\rangle$ over frequency. The dashed line represents a linear fit to the coherent portion of the spectra. The darkly shaded region at the bottom of both plots represents the measured coherence while the lightly shaded region represents the coherence baseline.

μs non-dispersive delay imposed by the IDS analog processing (§ 2.2.1).[2] In addition, the slope of the phase in frequency varies somewhat among $\tilde v \tilde b_{\theta,n}$ products. Thus, we conclude that the observed behavior of the phase accurately reflects the relation of the fluctuations and impose no time delay correction to the measured phase.

5.3.2 Determination of local phase

To understand the value of the measured phase we must return to two expressions derived earlier. The first is the equation for chord-averaged velocity fluctuations (Eq. 2.60) which we rewrite here for the case of $\tilde v_\theta$ measured by the poloidal chord,

$$\tilde v_\theta(t) = \frac{1}{a}\int_{r_o}^{a} dr\, I_{CV}\, w_P\, v_\theta(r) e^{i\delta_v}\ e^{i(m\theta_v + n\phi_v + \omega t)}, \tag{5.13}$$

where I_{CV} is the CV emission profile, w_P is the instrument function for the measurement of $\tilde v_\theta$ with the poloidal chord, θ_v is the poloidal angle of the chord's midpoint, and ϕ_v

---

[2] A 1 μs time lag between the TR612 and the Aurora-14 digitizers was discovered in this check. Both the direction and size of this digitizer lag are inconsistent with the observed phase shifts.

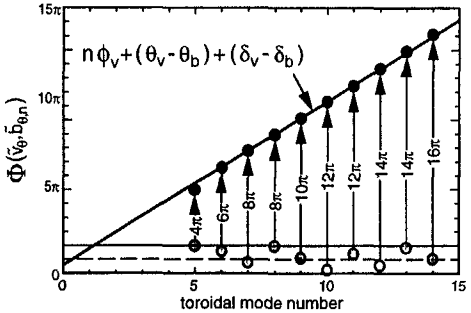

Fig. 5.13.— Grey circles denote the measured phase of $\langle \tilde v_\theta b_{\theta,n}\rangle$ for $n = 5 - 15$. Adding an integer multiple of 2π the points fall along a line with a slope equal to the toroidal angle of the $\tilde v_\theta$ measurement and an intercept which yields the local relative phase of $\tilde v_\theta$ and $\tilde b_\theta$.

is the toroidal location of the chord. This expression expands the measured $\tilde v_\theta$ as a weighted integral of $v_\theta(r)$ and its complex phase angle, $e^{i\delta_v}$. Outside the integral, the time dependent exponential, $e^{i\omega t}$, is multiplied by a reference phase angle determined by the position of the chord and the helicity of the mode. The second expression we need (Eq. 4.1) defines $\tilde b_{\theta,n}$ as,

$$\tilde b_{\theta,n}(t) = b_{\theta,n} e^{i(m\theta_b + \omega t + \delta_b)}, \tag{5.14}$$

where θ_b is the poloidal angle of the toroidal array coils. Using these two expressions we may evaluate the ensemble averaged product of $\tilde v_\theta$ and $\tilde b_{\theta,n}$, obtaining,

$$\langle \tilde v_\theta \tilde b_{\theta,n}\rangle = \frac{1}{a}\int_{r_o}^{a} dr\, I_{CV}\, w_P \left\langle v_\theta(r)\, b_{\theta,n}\, e^{i(\delta_v - \delta_b)}\right\rangle e^{i(m(\theta_v - \theta_b) + n\phi_v)}. \tag{5.15}$$

By taking the $\langle\ \rangle$ inside the integral we express the ensemble averaged quantity as the weighted radial average of the ensemble averaged product of $\tilde b_{\theta,n}$ and the local value of $\tilde v_\theta$ times the relative phase of the local velocity fluctuation and the edge magnetic measurement, $e^{i(\delta_v-\delta_b)}$. We now define an average local phase shift, $\langle\delta_v-\delta_b\rangle$, such that,

$$\langle\tilde{v}_\theta\tilde{b}_{\theta,n}\rangle = \frac{1}{a}\int_{r_o}^{a} dr\, I_{CV}\, w_P\, \langle v_\theta(r)\, b_{\theta,n}\rangle\; e^{i(\delta_v-\delta_b)}\; e^{i(m(\theta_v-\theta_b)+n\phi_v)}, \tag{5.16}$$

where both complex exponentials have been pulled outside the radial integral. This averaged phase shift differs from standard ensemble averaged phase calculations only in its inclusion of a weighted average over radius. Because MHD simulations predict little radial structure to δ_v, we expect this additional average to have little effect

From Eq. 5.16 we recover the phase returned by the ensemble analysis,

$$\Phi(\tilde{v}_\theta,\tilde{b}_{\theta,n}) = \langle\delta_v-\delta_b\rangle + m(\theta_v-\theta_b) + n\phi_v. \tag{5.17}$$

The poloidal velocity measurement beautifully illustrates this expression due to the large number of toroidal modes with which $\tilde{v}_\theta$ exhibits coherence. Fig. 5.13 shows $\Phi(\tilde{v}_\theta,\tilde{b}_{\theta,n})$ for the resolved toroidal mode numbers. The phase for each n was extracted from the wavelet spectrum at the point of maximal coherence in frequency and time. By adding an integer multiple of 2π to the measured phase we are able to align the points to a line with a slope given by the toroidal position of the poloidal chord, ϕ_v. In fact a linear fit to these phases recovers ϕ_v to within 2°. We recover the local phase shift by subtracting $n\phi_v$ and the poloidal separation. Rearranging Eq. 5.17 we express this correction as,

$$\langle\delta_v-\delta_b\rangle = \Phi(\tilde{v}_\theta,\tilde{b}_{\theta,n}) - m(\theta_v-\theta_b) - n\phi_v, \tag{5.18}$$

where we set $m=1$. To accurately correct for the poloidal separation we employed the mapping of $\theta\to\theta'$ given by Eq. 4.19, which accounts for the poloidal asymmetry caused by the outward shift of the plasma (§ 4.3.2).

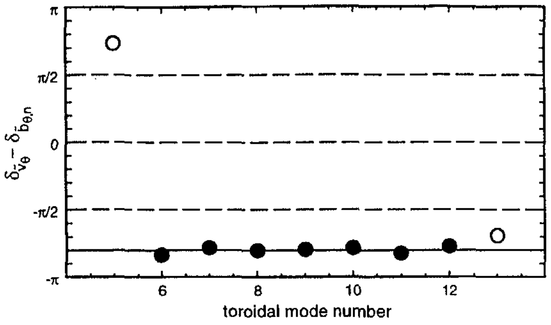

Fig. 5.14.— The local phase of $\tilde{v}_\theta$ and $\tilde{b}_{\theta,n}$ for $n=5-13$ following correction for the geometric separation of the measurements. The horizontal line at -144° represents a coherence weighted averaged of the well resolved modes (filled circles).

5.3.3 Poloidal velocity fluctuation phase

After correcting for the physical separation of the $\tilde{v}_\theta$ and $\tilde{b}_{\theta,n}$ measurements via Eq. 5.18, we obtain an average local phase of,

$$\langle\delta_{v_\theta}-\delta_{b_{\theta,n}}\rangle \approx -140^\circ, \text{for } 6\le n\le 12. \tag{5.19}$$

For poloidal velocity fluctuations to contribute maximally to an equilibrium dynamo field implies a local phase, $\delta_{v_\theta}-\delta_{b_r}$, of either 0 or π. Taking into account the $\pi/2$ phase shift between $\tilde{b}_r(r)$ and $\tilde{b}_\theta(a)$, we obtain an optimal local phase shift, $\langle\delta_{v_\theta}-\delta_{b_{\theta,n}}\rangle$, of $\pm\pi/2$. The measured local phase is "in between" $-\pi/2$ and $-\pi$ indicating the presence of a non-zero dynamo field contribution from this product. However, more than half of the measured $\tilde{v}_\theta$ power is out of phase with $\tilde{b}_r$.

Because the poloidal chord measures fluctuations where the mean magnetic field is primarily poloidal we expect the chord to be extremely sensitive to any $\tilde{v}_\parallel$ fluctuations.

One potential source for $\tilde{v}_{\parallel}$ fluctuations is the advection of an equilibrium $v_{\parallel}$ gradient past the line of sight by radial perturbations in the magnetic field. Simple calculations yield the phase and approximate amplitude of such fluctuations. In a generalized geometry we consider an equilibrium field $\mathbf{B_o} = B_o\hat{z}$ perturbed by a radial magnetic field, $\tilde{b}_x$, yielding a total magnetic field given by,

$$\mathbf{B} = B_o\left(\hat{z} + \frac{b_x}{B_o}e^{i(k_y y + k_z z + \omega t)}\hat{x}\right). \tag{5.20}$$

Integrating the field line equation we obtain an approximate expression for the perturbed x position of the mean field,

$$\tilde{x} \approx \frac{ib_x}{B_o k_z}e^{i(k_y y + k_z z + \omega t)}. \tag{5.21}$$

Now assuming that the parallel fluid flow is constant along the field line we obtain the apparent velocity fluctuation due to advection of that flow by b_x as,

$$\tilde{v}_z = \tilde{x}\,\nabla_x v_z = \frac{ib_x}{B_o k_z}\frac{\partial v_z}{\partial x}e^{i(k_y y + k_z z + \omega t)}. \tag{5.22}$$

This $\tilde{v}_z$ possesses the same wavenumber as the advecting $\tilde{b}_x$ but is phase shifted from $\tilde{b}_x$ by $\pi/2$ We may estimate the amplitude of such an effect in MST at an $r/a = 0.6$ as,

$$|\tilde{v}_\theta| \approx \frac{b_r}{B_\theta m}\frac{\partial v_\theta}{\partial(r/a)} \approx (0.1)(10\,\mathrm{km/s}) = 1\,\mathrm{km/s}, \tag{5.23}$$

This provides an order of magnitude estimate consistent with the measured $\tilde{v}_\theta$. Thus, the $\tilde{v}_\theta$ measurement may be a combination of fluctuations due to parallel flow advection which are $\pi/2$ out of phase with $\tilde{b}_r$ and a lesser contribution of perpendicular dynamo fluctuations which are in phase with $\tilde{b}_r$.

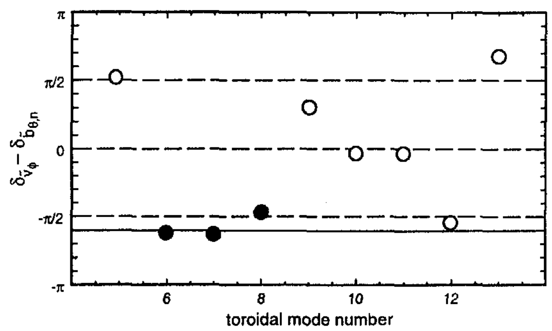

Fig. 5.15.— The local phase of $\tilde{v}_\phi$ and $\tilde{b}_{\theta,n}$ for $n = 5-13$ following correction for the geometric separation of the measurements. The horizontal line at -109° represents a coherence weighted averaged of the well resolved modes (solid circles).

5.3.4 Toroidal velocity fluctuation phase

By substituting the appropriate angles for the top-bottom symmetric toroidal chord we use Eq. 5.18 to solve for the local phase between $\tilde{v}_\phi$ with $\tilde{b}_{\theta,n}$ Fig. 5.15 shows $\langle\delta_{v_\phi} - \delta_{b_\theta}\rangle$ for $n = 5 - 13$. As discussed above, the complex interaction of the toroidal chord instrument function and the velocity fluctuation profile yields clear resolution of the $n = 6 - 7$ modes, marginal resolution for $n = 8$ and generally poor resolution for $n > 8$. In addition, the coincidence in radius of higher n modes with negative regions of the toroidal chord instrument function (Fig. 5.10) produces an apparent phase for the fluctuation which is flipped 180° from its true local value. The poor resolution and phase flipping produce the scatter of phases for higher n compared to the remarkable alignment of the poloidal phases. Our minimal understanding of the $\tilde{v}_n(r)$ radial profile makes interpretation of these high n phases a dubious pursuit.

Fortunately, the dominant $n = 6$ and $n = 7$ modes are well resolved yielding matching phases just below $-\pi/2$,

$$\langle \delta_{v_\phi} - \delta_{b_{\theta,n}} \rangle \approx -105^\circ, \text{for } n=6-7. \tag{5.24}$$

Following the logic presented above, this phase implies that $\tilde{v}_\phi$ is roughly in phase with $\tilde{b}_r$ and thus capable of producing a dynamo field. This is consistent with our analysis of the toroidal chord instrument function which showed that for a typical magnetic field profile $|w_\wedge| \approx 2|w_\parallel|$. Furthermore, we expect the magnitude of $\tilde{v}_\parallel$ to be smaller near the core where the $v_\parallel(r)$ profile flattens. Thus, the toroidal chord, while more complex, appears to provide the needed resolution of dominant $\tilde{v}_\wedge$ fluctuations in the core.

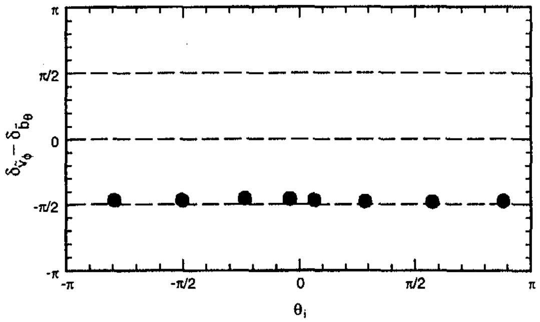

Fig. 5.16.— The local phase of $\tilde{v}_\phi$ and the eight $\tilde{b}_{\theta,i}$ poloidal array coils. The contribution from the geometric separation of the coils has been subtracted (Fig. 4.14).

The relative phase of the velocity fluctuation with a single magnetic coil at θ_i, ϕ_i may be solved for in the manner discussed above as,

$$\langle \delta_v - \delta_{b_{\theta,i}} \rangle = \Phi(\tilde{v}, \tilde{b}_{\theta,i}) - m(\theta_v - \theta_i) - n(\phi_v - \phi_i). \tag{5.25}$$

The difficulty with this expression is that both the $\tilde{v}$ and the $\tilde{b}_{\theta,i}$ measurement contain a superposition of toroidal mode numbers making the correction for toroidal separation ambiguous. We overcome this difficulty by setting $\phi_v \approx \phi_i$ thereby mitigating that dependency from Eq. 5.25. To do this we correlated the toroidal velocity fluctuations ($\phi_v = 180^\circ$) with the $\tilde{b}_{\theta,i}$ from the eight coils in the poloidal array at 180T ($\phi_i = 177^\circ$). The local phases which resulted from this measurement are shown in Fig. 5.16. Note that the phases for each of the eight coils are extremely consistent, with an average value of 85° We employed $n = 6$ in Eq. 5.25 to correct for the 3° toroidal separation. The inclusion of power from higher n modes should alter this phase by no more than 5°. This measurement together with the mode resolved correlation with $\tilde{b}_{\theta,n=6}$ and $\tilde{b}_{\theta,n=7}$ constitute strong evidence of $\tilde{v}_\phi$ fluctuations in the core regions of the MST phased such as to produce a non-zero dynamo electric field.

5.4 Radial Velocity Fluctuations

Throughout the preceding discussion we have denoted the ion velocity fluctuation measurements made along the poloidal and toroidal chords as $\tilde{v}_\theta$ and $\tilde{v}_\phi$, respectively. However, from our derivation of the full toroidal and poloidal chord instrument functions (§ 2.5.2), we know this to be an approximation. While the toroidal chord is minimally sensitive to $\tilde{v}_\theta$ and the poloidal chord is orthogonal to $\tilde{v}_\phi$, both chords exhibit sensitivity to $\tilde{v}_r$. This alone necessitates a separate measurement of $\tilde{v}_r$ in order to quantify the potential contribution of $\tilde{v}_r$ to fluctuations measured by the two chords. In addition, the full cross product for the two parallel components of the dynamo field are given by,

$$E_\phi = \langle \tilde{v}_r \tilde{b}_\theta \rangle - \langle \tilde{v}_\theta \tilde{b}_r \rangle, \tag{5.26}$$

$$E_\theta = \langle \tilde{v}_\phi \tilde{b}_r \rangle - \langle \tilde{v}_r \tilde{b}_\phi \rangle. \tag{5.27}$$

Thus, our ultimate goal of measuring the full $\langle \tilde{\mathbf{v}} \times \tilde{\mathbf{b}} \rangle$ dynamo electric field clearly requires measurement and correlation of $\tilde{v}_r$.

To measure $\tilde{v}_r$ we constructed the large radial view port described in § 2.1 and conducted an ensemble of low current discharges orienting one IDS view along the new radial line of sight and positioning the second view along the traditional toroidal view for direct comparison. This experiment produced two key results. First, the measured power of $\tilde{v}_r$ is similar to that of the chord-averaged $\tilde{v}_\phi$. However, correcting for the substantial attenuation of $\tilde{v}_\phi$ by the toroidal chord geometry we project a core $\tilde{v}_\phi$ amplitude 2–3 times as large as $\tilde{v}_r$. Second, $\tilde{v}_r$ exhibits extremely low coherence with the edge magnetics, barely exceeding the coherence baseline in the tearing mode frequencies in contrast to the robust coherence of $\tilde{v}_\phi$. These two results imply that while $\tilde{v}_r$ power may contribute to the fluctuation power reported above for the toroidal and poloidal chords, that contribution should have little effect on the measured coherence and phase of the two measured quantities. In addition, the absence of $\tilde{v}_r$ coherence implies that the dynamo cross products, Eqs. 5.26–5.27, are dominated by the $\langle \tilde{v}_\theta b_r \rangle$ and $\langle \tilde{v}_\phi b_r \rangle$ terms.

5.4.1 A low noise measurement of $\tilde{v}_r$

The radial view port was designed to maximize the light gathered by looking directly through a 4 1/2 inch port. By employing an eight inch-diameter window as a vacuum seal and a seven inch-diameter lens to focus light onto the filter monochromator, we insured that the fixed diameter of the port served as our limiting aperture. This design produced light levels with the radial viewport which exceeded those of the toroidal view by ~50% (Fig. 5.17a). This enhanced light level reduced the intrinsic photon noise in the emission profiles of the radial view by ~ 20% which then propagated directly to improved nonlinear fits and a reduced $\hat{\chi}$ (Fig. 5.17b). Ultimately the enhanced light levels for the radial port should produce $\tilde{v}_r$ measurements with noise levels reduced from those of the $\tilde{v}_\phi$ measurements taken concurrently.

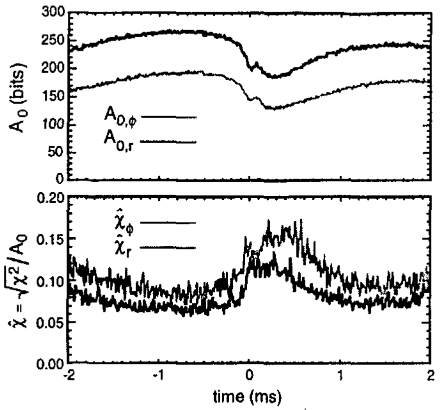

Fig. 5.17.— a) The ensembled amplitude of the fitted Gaussian, A_0, indicates the light collection of the radial port (solid) exceeds that of the toroidal port (grey) by ~50%. b) This results in better fits and lower $\hat{\chi}$ for the radial measurement.

In addition to cleaner $\tilde{v}$ signals the radial chord exhibits a literally perfect instrument function for the resolution of $m = 1$ radial velocity fluctuations (§ 2.5.2). This contrasts sharply to the complex, spatially dependent toroidal instrument functions which optimistically yield ~50% attenuation, with more realistic estimates of ~70% for the dominant modes. Thus, this measurement compares the previously measured $\tilde{v}_\phi$ to a less noisy and more clearly resolved $\tilde{v}_r$.

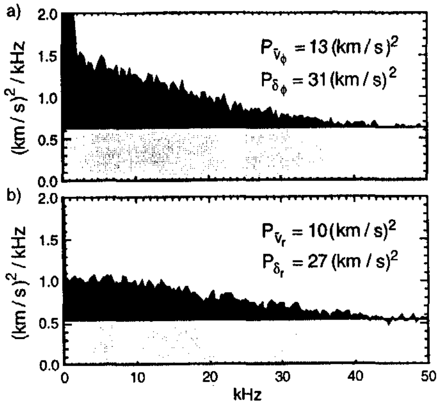

Fig. 5.18.— The ensembled power spectra for a) $\tilde{v}_\phi$ and b) $\tilde{v}_r$. Increased light levels decrease the measured noise floor (light) for $\tilde{v}_r$ compared to $\tilde{v}_\phi$. Following subtraction of the noise floor slightly more fluctuation power (dark) remains for $\tilde{v}_\phi$ than for $\tilde{v}_r$. Integrated noise and fluctuation powers are shown in the figures.

5.4.2 Modest, incoherent radial velocity fluctuations

The ensembled power spectra of the measured $\tilde{v}_\phi$ and $\tilde{v}_r$ are shown in Fig. 5.18. As expected the noise floor for the $\tilde{v}_\phi$ measurement exceeds the more cleanly illuminated $\tilde{v}_r$ measurement. The toroidal velocity fluctuation power above the noise floor is somewhat greater than the corresponding radial fluctuation power. However, some of $P_{\tilde{v}_\phi}$ may stem from secular contributions which should be largely absent from $\tilde{v}_r$ as the latter exhibits little mean flow. Subtraction of the estimated secular power yields comparable levels of measured fluctuation power for the two components within the accuracy of the measurement. Adjustments for the 2–3 fold attenuation of $\tilde{v}_\phi$ by the toroidal chord, yield estimates of $\tilde{v}_\phi$ in the core which are 2–3 times larger than the perfectly resolved $\tilde{v}_r$.

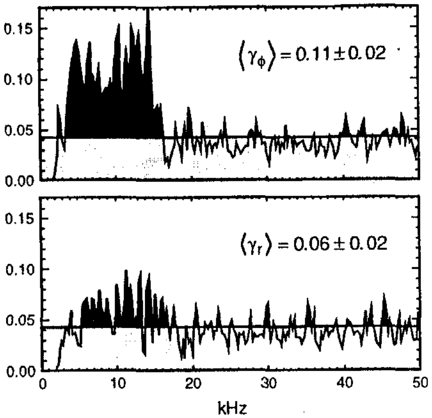

Fig. 5.19.— The measured coherence of a) $\tilde{v}_\phi$ and b) $\tilde{v}_r$ with the edge magnetic coils. $\tilde{v}_r$ exhibits a coherence with the edge magnetics which barely exceeds the coherence baseline.

A striking contrast emerges between the two measured fluctuations when one examines their coherence with an edge magnetic coil. While the toroidal chord exhibits robust coherence of 10–15% in the tearing mode frequencies, the radial fluctuations exhibit a coherence which is just barely resolved above the baseline. This small coherence occurs despite lower noise levels and a perfect geometric resolution of the radial fluctuations. From these results we conclude first that radial velocity fluctuations may contribute small amounts of fluctuation power to the signal averaged over the poloidal and toroidal chords. Second, due to the low coherence of $\tilde{v}_r$ with the edge magnetics we can expect minimal "contamination" of the measured phase and coherence of $\tilde{v}_\theta$ and $\tilde{v}_\phi$ with $\tilde{b}_{\theta,n}$. Finally, with an amplitude several times smaller than the other two components, and a minimal coherence with the magnetic fluctuations, the contributions of $\langle\tilde{v}_r\tilde{b}_\theta\rangle$ and $\langle\tilde{v}_r\tilde{b}_\phi\rangle$ to the E_ϕ and E_θ dynamo fields, respectively, should be negligible compared to the uncertainties introduced in mapping the remaining terms to their core values.

5.4.3 Equilibrium radial velocity and temperature

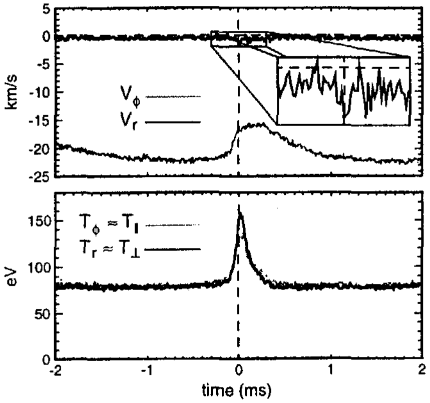

Fig. 5.20.— a) Ensembled v_r indicates a radial flow (solid) consistent with zero with a slight inward Shafronov shift during the sawtooth crash. v_ϕ (grey) reflects typical toroidal core ion flow. b) T_r equals T_ϕ away from the crash indicating an isotropic ion temperature distribution.

This experiment also provided measurements of the mean radial ion velocity and temperature, which we report here although they are somewhat tangential to this thesis. We expect any mean $m=0$ flows (pinch velocities for example) to cancel over the radial chord producing only a slight broadening of the measured velocity distribution. This expectation matches the measured v_r (Fig. 5.20) which is consistent with zero. However, the chord is sensitive to mean $m=1$ flows such as shift by the plasma volume away from or toward the core. Such a flow may occur at the sawtooth crash where a small negative jump in the v_r measurement is observed. A back of the envelope calculation shows that

this ~500 m/s jump which extends ~50 μs corresponds to an inward shift of the plasma of ~3 cm. This is consistent with the expected relaxation of the Shafronov shift during the crash.

The radial and toroidal ion temperatures exhibit identical values over most of the sawtooth period consistent with an isotropic temperature distribution. Immediately before the crash both temperatures rise sharply together with no lag visible between T_ϕ and T_r. A difference of 20–30 eV occurs during the crash as T_r reaches ~160 eV while T_ϕ plateaus at ~130 eV. This difference persists for less than 100 μs at which point both temperatures fall together back to their baseline value of ~80 eV. This result contradicts the measurements on the EXTRAP-T2 device (Sasaki, 1997) which showed strong anisotropy between the $T_\perp$ and $T_\parallel$ of the majority ion species. Further measurements are indicated to resolve this contradiction.

5.5 Lundquist Number Scaling

The extended runs at medium and high currents allowed three point Lundquist number scalings of the velocity fluctuations like those discussed in the previous chapter for the magnetics. Fig. 5.21 shows $\langle \tilde{v}_\phi^2 \rangle^{\frac{1}{2}}$ and $\langle \tilde{v}_\theta^2 \rangle^{\frac{1}{2}}$, in the three Lundquist number regimes with the estimated noise baseline removed. The negative values seen after the crash for the high S regime correspond to errors in our distribution of noise in time. As with the magnetic fluctuations the key effect of scaling is the decreased duty cycle of the fluctuations with baseline of the fluctuations extending while the period of active fluctuation contracts. From this we expect the fluctuation levels averaged over the sawtooth to scale more strongly than either the baseline or the peak levels scale individually.

Normalizing the toroidal and poloidal fluctuations by the Alvfén velocity we achieve

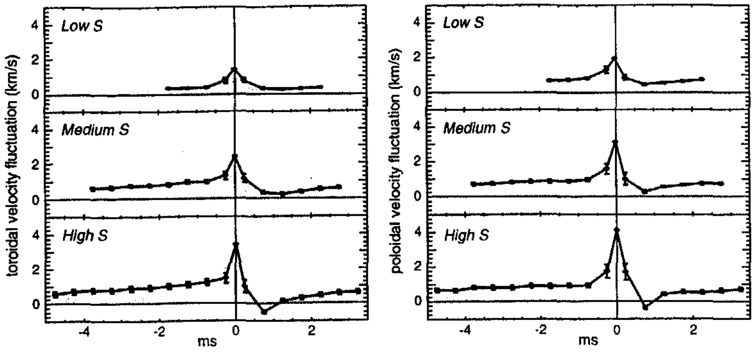

Fig. 5.21.— a) Toroidal (left) and b) poloidal (right) velocity fluctuations for the three Lundquist number settings. The estimated noise baselines have been removed and adjacent points have been binned every 0.5 ms. Error bars derive from the standard deviation of the points binned

the scalings shown in Fig. 5.22. The peak fluctuation levels scale with slightly positive exponents as,

$$\max(\tilde{v}_\phi) \propto S^{0.02}, \tag{5.28}$$

$$\max(\tilde{v}_\theta) \propto S^{0.07}, \tag{5.29}$$

(first reported in Stoneking, 1997). This scaling is fairly consistent with the weak scaling found for the peak levels of the magnetic fluctuations of $\max(\tilde{b}/B_o) \propto S^{-0.02}$ (Eq. 4.20). As expected, the fluctuations averaged over the sawtooth scale more strongly than the peak values due to the decreased fluctuation duty cycle,

$$\mathrm{avg}(\tilde{v}_\phi) \propto S^{-0.19}, \tag{5.30}$$

$$\mathrm{avg}(\tilde{v}_\theta) \propto S^{-0.08}. \tag{5.31}$$

This also is consistent with the scaling of the magnetics for which we found, $\mathrm{avg}(\tilde{b}/B_o) \propto S^{-0.08}$ (Eq. 4.21).

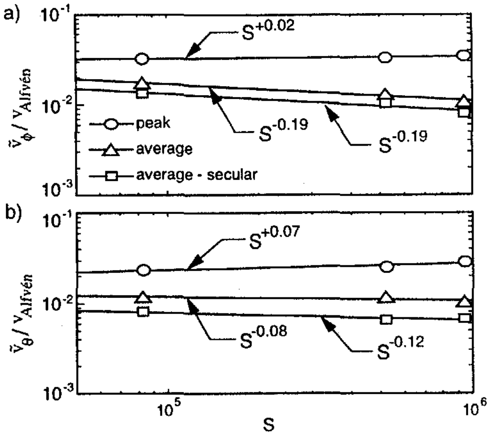

Fig. 5.22.— Scalings of peak (circle) and average (triangle) a) toroidal and b) poloidal velocity fluctuations. Scalings of the average fluctuation amplitude with estimates of secular amplitude subtracted (squares) were not different from those without.

Interpretation of these scalings is complicated by several measurement factors. First, as discussed in previous sections, the measured velocity fluctuation consists of weighted contributions from many modes. The weighting depends on the instrument function of the chord, the emission profile of the CV, and the fluctuation profile for the that mode. With increased S we observe the ion temperature to increase and thus expect CV to burn through in the core. Thus we expect that at high S a measurement of CV dynamics becomes less sensitive to core modes relative to edge modes. In addition $\tilde{v}_n(r)$ may change shape with higher S interacting differently with the instrument function of the chord. Both of these effects change the weighting of the IDS chord for different modes adding uncertainty to our direct comparison of the measurements at different settings.

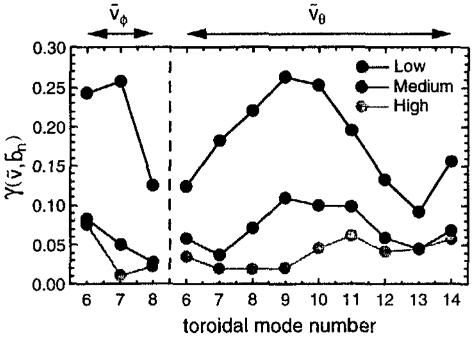

Fig. 5.23.— Coherence of resolved modes averaged from 8-20 kHz for both chords at three S settings. The coherence decreases monotonically for all modes with S.

To investigate the wavenumber content of $\tilde{v}$ at different S settings we may look, as we did in detail for the low S case, at the coherence of the velocity fluctuations with different modes An overview of that coherence for the most clearly resolved modes is shown in Fig.5.23. Note that as anticipated, the relative content of various modes does change with S with $\tilde{v}_\theta$ containing fewer edge modes and $\tilde{v}_\phi$ becoming exclusively sensitive to $n=6$ fluctuations. A more dramatic effect is the decreased coherence of the measured velocity fluctuations and all of the magnetic modes with increased S. Some of the decrease stems from the increased noise levels in the IDS signal at higher currents due to decreased emission levels of CV. However, this effect does not account for all of observed decrease in coherence suggesting that the velocity fluctuations may couple less efficiently to the magnetics at higher S. We will discuss this further when we examine the scaling of the dynamo electric field.

While the resolution of the local $\langle\delta_{\tilde{v}_\theta} - \delta_{\tilde{b}_\theta}\rangle$ phase suffered at higher S due to the low coherence, within the error no significant variations in the phase were observed between the different S ensembles. The up-down toroidal setup was not employed for the medium and high current runs making a similar comparison of the local $\langle\delta_{\tilde{v}_\phi} - \delta_{\tilde{b}_\theta}\rangle$ phase impossible.

References

Sasaki, K., P. Horling, T. Fall, J. H. Brzozowski, P. Brunsell, S. Hokin, E. Tennfors, J. Sallander, J. R. Drake, N. Inoue, J. Morikawa, Y. Ogawa, and Z. Yoshida (1997). Anistropy of ion temperature in a reversed-field-pinch. *Plasma Phys. Control. Fusion* **39**, 333–338.

Stoneking, M. R., J. T. Chapman, D. J. Den Hartog, S. C. Prager, and J. S. Sarff (1997). Experimental scaling of fluctuations and confinement with Lundquist number in the RFP. *Phys. Plasmas* **5**(4), 1004–1014.

6

The Balance of Ohm's Law

At the beginning of this thesis we demonstrated that in an RFP the mean currents and the mean applied electric field do not satisfy a linear parallel Ohm's law, leading to the proposition of a flux surface averaged $\tilde{\mathbf{v}} \times \tilde{\mathbf{b}}$ product providing this balance as,

$$\langle \mathbf{E} \rangle_{\|} + \langle \tilde{\mathbf{v}} \times \tilde{\mathbf{b}} \rangle_{\|} = \eta \langle \mathbf{J} \rangle_{\|}. \tag{6.1}$$

In this chapter we examine the balance of this equation in the interior of MST in two parts. First, we model $\langle \mathbf{E} \rangle_{\|} + \langle \tilde{\mathbf{v}} \times \tilde{\mathbf{b}} \rangle_{\|}$ and $\eta \langle \mathbf{J} \rangle_{\|}$ in Eq. 6.1 and estimate the size and time behavior of the dynamo field from their difference. Second, we project our measured $\langle \tilde{v}_\phi \tilde{b}_{\theta,n} \rangle$ and $\langle \tilde{v}_\theta \tilde{b}_{\theta,n} \rangle$ products into the core yielding empirical estimates of components of $\langle \tilde{\mathbf{v}} \times \tilde{\mathbf{b}} \rangle$ in the interior of MST. The key novel results of the chapter are summarized here:

- During the sawtooth crash the rapid relaxation of the current profile induces a transient electric field of tens of Volts/m which greatly exceeds both the applied field and the electric field necessary to drive current in the plasma.
- During the crash the dynamo term implied by the modeling would act to suppress core current with a field of 20–40 Volts/m and drive edge current with a field of 5–15 Volts/m

- Away from the crash the inductance of the plasma opposes the resistive decay of the equilibrium balancing Ohm's law within the ± 1–2 Volts/m precision of the model.
- From our measurement of $\langle \tilde{v}_\phi \tilde{b}_{\theta,n} \rangle$ we estimate $-\langle \tilde{v}_\phi \tilde{b}_r \rangle \approx \langle \tilde{\mathbf{v}} \times \tilde{\mathbf{b}} \rangle_\theta$ of 14±6 Volts/m at the crash and 1.0±0.4 Volts/m away from the crash in a direction to *drive* parallel current at an $r/a \approx 0.3$–0.4.
- From our measurement of $\langle \tilde{v}_\theta \tilde{b}_{\theta,n} \rangle$ we estimate $\langle \tilde{v}_\theta \tilde{b}_r \rangle \approx \langle \tilde{\mathbf{v}} \times \tilde{\mathbf{b}} \rangle_\phi$ of 1.0±0.3 Volts/m at the crash and 0.14±0.05 Volts/m away from the crash with a small parallel projection in a direction to *drive* parallel current at an $r/a \approx 0.6$–0.7.
- Both dynamo products scale nearly as S^{-1} due to the increasing incoherence of $\tilde{\mathbf{v}}$ and $\tilde{\mathbf{b}}$ at the higher current regimes.

The modeling results provide new insights into the mean field behavior, stressing the importance of the plasma inductance over the sawtooth cycle. In addition, the $\langle \tilde{\mathbf{v}} \times \tilde{\mathbf{b}} \rangle$ *measurements provide provocative evidence of dynamo activity in the core with a time* dependence and magnitude consistent with our expectations. However, substantial uncertainties in the dynamo field projected from measurements and that inferred from modeling demonstrate the need for more sophisticated measurements of mean field and fluctuating quantities before the numerical balance of Eq. 6.1 can be conclusively demonstrated in MST.

This chapter contains two sections. The first section evolves standard RFP equilibrium models over the sawtooth to determine the dynamic mean-field behavior of the MST. The second section presents the measured fluctuation products and describes the correction factors employed to infer $\langle \tilde{v}_\phi \tilde{b}_r \rangle$ and $\langle \tilde{v}_\theta \tilde{b}_r \rangle$ in the core from the measured $\langle \tilde{v}_\phi \tilde{b}_{\theta,n} \rangle$ and $\langle \tilde{v}_\theta \tilde{b}_{\theta,n} \rangle$ products.

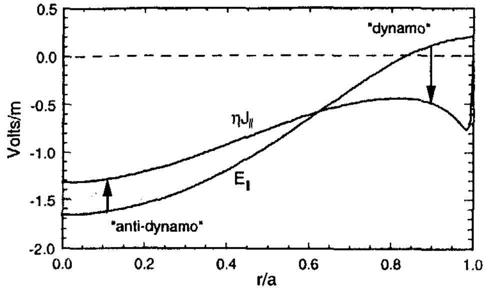

Fig. 6.1.— Static formulation of Ohm's law in the RFP. $E_{\|}$ calculated as parallel projection of applied E_{ϕ}. Shaded region represents discrepancy between applied field and driven current with arrows indicating direction of needed dynamo.

6.1 Mean Field Dynamics

A simple consideration of the time-averaged fields and currents in the RFP demonstrates the imbalance of $\langle \mathbf{E} \rangle_{\|}$ and $\eta \langle \mathbf{J} \rangle_{\|}$ in the RFP. The essence of this argument is that the toroidal electric field applied by the transformer over-drives current in the core and under-drives (or even opposes) current in the edge (Fig. 6.1). With no additional current drive term, the core current will peak and the edge current will dissipate producing a decay of the RFP equilibrium configuration over a few resistive times. Because the application of a toroidal electric field is observed to sustain the RFP equilibrium over many resistive times, we hypothesize an anomalous electric field which suppresses current in the core ("anti-dynamo") and drives current at the edge ("dynamo"). This time-averaged or static formulation of Ohm's law in the RFP captures the mean field behavior on the time scale of the discharge. However, a description of the mean field evolution over the sawtooth cycle must consider electric fields induced by the variation of the magnetic field in time. Our approach in this section will be to model the equilibrium magnetic field from edge and global measurements at each point in time along the sawtooth cycle. We may then solve for the mean electric fields in the plasma induced by the external flux swing of the transformer *and* by the internal redistribution of flux in the plasma. This modeling will yield very different mean field behavior at and away from the crash with equally different implications for the necessary dynamo field. While in our final determination the dynamo field necessary to balance a dynamic Ohm's law behaves in a qualitatively similar fashion to that shown in Fig. 6.1, the sawtooth crash compresses the duration and multiplies the magnitude of the necessary field.

6.1.1 Cylindrical Modeling of the Equilibrium Magnetic Field

In the absence of current profile diagnostics we must rely on equilibrium modeling to investigate mean-field dynamics in MST. Below we describe simple cylindrical equilibrium models of the current profile which we fit to edge and global magnetic measurements. The dynamics of the modeled current profiles exhibit a suppression of core current and flattening of the current profile during the crash.

Models of the parallel current profile

We employed two simple models of $\lambda(r)$ for this study: the "α-model" and the "Modified Bessel Function Model (MBFM)". Both specify the form of $\lambda(r)$ with two adjustable parameters: λ_o, which specifies the parallel current on axis and a second parameter which determines how rapidly the parallel current falls to zero at the plasma edge. The MBFM holds $\lambda(r)$ constant out to a "break radius", r_b, at which point $\lambda(r)$

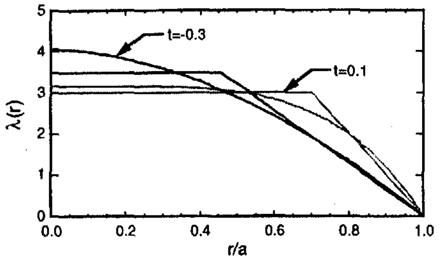

Fig. 6.2.— $\lambda(r)$ fit using the α-model and the MBFM (the MBFM has the sharp corner). The two profiles are fit to equilibria before (solid) and after (grey) the crash.

falls linearly to zero,

$$\lambda(r) = \begin{cases} \lambda_0 & \text{for } r \leq r_b, \\ \lambda_0 \left(\frac{1-r/a}{1-r_b/a} \right) & \text{for } r > r_b, \end{cases} \quad \text{(MBFM)}. \tag{6.2}$$

For the α-model, $\lambda(r)$ falls continuously to zero at a rate determined by the exponent, α, as

$$\lambda(r) = \lambda_0 \left(1 - (r/a)^{\alpha}\right), \quad (\alpha\text{-model}). \tag{6.3}$$

Examples of current profiles obtained from the two models for equilibria before and after the sawtooth are shown in Fig. 6.2. The α-model consistently predicts more current in the core while the MBFM distributes the current broadly over the plasma interior. However, general dynamics in the current profile, such as the predicted flattening of the profile over the sawtooth crash, manifest in similar ways for both models and the two models converge as the parallel current flattens. The α-model and the MBFM were employed in parallel throughout our analysis providing for an estimate of the sensitivity of our results to assumptions about the exact form of $\lambda(r)$.

Force balance equation

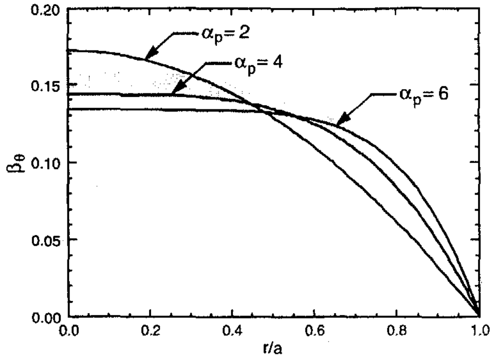

Fig. 6.3.— The normalized pressure profiles employed for the modeling. α_p's of 2, 4, and 6 were used with estimated β_θ varied ±10% at $\alpha_p = 4$ (grey region). β_θ was evolved over sawtooth and α_p was held constant.

To obtain the magnetic field profiles we employ the force balance equation,

$$\nabla \times \mathbf{B} = \mu_o \mathbf{J}_{\|} + \mu_o \mathbf{J}_{\perp} = \lambda \mathbf{B} - \frac{\mu_o \nabla P \times \mathbf{B}}{B^2}. \tag{6.4}$$

This equation may be expressed in cylindrical geometry as a set of coupled differential equations,

$$-\frac{\partial B_\phi}{\partial r} = \lambda B_\theta + \frac{\mu_o}{B^2}\frac{\partial P}{\partial r} B_\phi, \tag{6.5}$$

$$\frac{1}{r}\frac{\partial}{\partial r}(r B_\theta) = \lambda B_\phi - \frac{\mu_o}{B^2}\frac{\partial P}{\partial r} B_\theta. \tag{6.6}$$

For this study we defined the pressure profile using a second α-model,

$$\begin{aligned} P(r) &= P_o \left(1 - (r/a)^{\alpha_p}\right) \\ &= \beta_\theta \left(\frac{B_\theta^2(a)}{2\mu_o} \right) \left(\frac{\alpha_p + 2}{\alpha_p} \right) \left(1 - (r/a)^{\alpha_p}\right), \end{aligned} \tag{6.7}$$

where α_p is the pressure profile shaping parameter and β_θ is the ratio of the volume averaged plasma pressure and the poloidal magnetic field energy density at the wall. Using this form for the pressure we may evaluate the diamagnetic correction in Eqs. 6.5–6.6, obtaining the normalized forms of the PDE's given by,

$$-\frac{\partial B_\phi}{\partial r} = \lambda B_\theta - \frac{\beta_\theta}{2}\left(\frac{B_\theta^2(a)}{B^2}\right)(\alpha_p + 2)\, r^{\alpha_p - 1}\, B_\phi, \tag{6.8}$$

$$\frac{1}{r}\frac{\partial}{\partial r}(r B_\theta) = \lambda B_\phi + \frac{\beta_\theta}{2}\left(\frac{B_\theta^2(a)}{B^2}\right)(\alpha_p + 2)\, r^{\alpha_p - 1}\, B_\theta, \tag{6.9}$$

where $r/a \rightarrow r$, $a\lambda \rightarrow \lambda$ and all fields have been normalized by B_o. Comparing the terms on the RHS of Eqs. 6.8–6.9, we see that the current term dominates the pressure term as,

$$\frac{\text{pressure term}}{\text{current term}} \sim \frac{\beta_\theta}{\lambda} \sim 5 \times 10^{-2}. \tag{6.10}$$

This ordering was borne out by sensitivity tests which demonstrated the modeled fields to be modified substantially by the inclusion of the pressure term but to have little sensitivity to the exact shape or magnitude of $P(r)$.

To estimate β_θ we employed Thomson scattering measurements of the central electron temperature and line averaged measurements of the electron density. By assuming a completely flat electron temperature profile one obtains the expression for the volume averaged electron pressure of,

$$\langle P_e \rangle_V = \frac{\alpha_p}{\alpha_p + 2} P_o = \frac{\alpha_p + 1}{\alpha_p + 2} \langle n_e \rangle_l T_{e0}, \tag{6.11}$$

where $\langle n_e \rangle_l$ is the line averaged density profile, T_{e0} is the central electron temperature, and we have assumed both $P_e(r)$ and $n_e(r)$ to have the form given by Eq. 6.7. We estimate a P_i in a similar fashion employing the chord-averaged IDS measurements of T_i and an estimate of $n_i \approx 2/3\, n_e$. Dividing through by the poloidal field energy at the wall we obtain a $\beta_\theta(t)$ of 10-15% over the sawtooth window (Fig. 6.4d). To estimate the modeling sensitivity to this term we performed our analysis with α_p's of 2,4, and 6 and varied β_θ by ±10% of its mean value with $\alpha_p = 4$ (Fig. 6.3). This sensitivity scan confirmed Eq. 6.10 showing the deviations in the model due to changes in the pressure term to be much less important than assumptions on the current profile.

Experimental inputs to the model

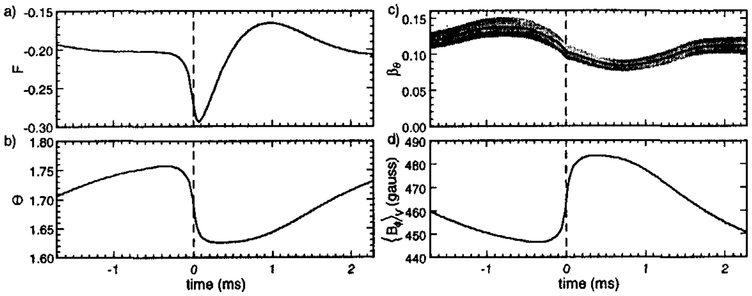

Fig. 6.4.— The ensembled a) F and b) Θ are mapped to the current profile parameters, λ_o and either α (α-model) or r_b (MBFM). c) Finite pressure effect are included through an estimate of β_θ. d) The resulting fields are normalized to the measured $\langle B_\phi \rangle_V$.

The current profile parameters were selected to yield magnetic fields, upon the integration of Eqs. 6.8–6.9 which matched the edge and global magnetic measurements. The measurements employed to characterize the shape of the magnetic equilibrium were the reversal parameter ($F \equiv B_\phi(a)/\langle B_\phi \rangle$) and the pinch parameter ($\Theta \equiv B_\theta(a)/\langle B_\phi \rangle$). This study employed the sawtooth ensemble average of F and Θ over the low-current S-scaling ensemble (Fig. 6.4a–b) which show a sharp negative increase in F and drop in

Θ at the sawtooth crash. Using a simple Newton's method iterative routine we performed the mapping of these ensemble averages, along with the estimated pressure profile, to the corresponding current profile parameters,

$$\{F, \Theta, \beta_\theta, \alpha_p\} \Longrightarrow \{\lambda_0, \alpha \text{ or } r_b\}. \tag{6.12}$$

The iteration routine adjusted the profile parameters until the integrated $\mathbf{B}(r)$ matched the input F and Θ with better than 10^{-5} accuracy. The field magnitudes were then normalized to match the ensembled $\langle B_\phi \rangle_V$.

Estimated model parameters

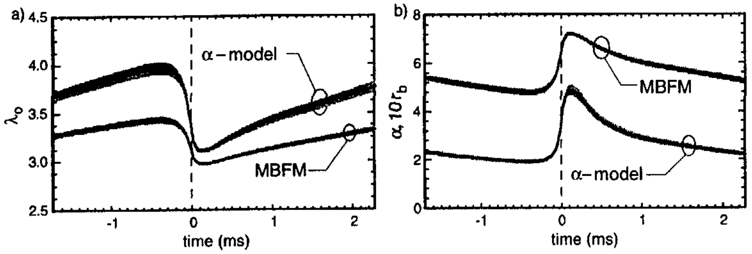

Fig. 6.5.— a) λ_o for α-model and MBFM, b) α and r_b (multiplied by ten) consistent with the experimental inputs (Fig. 6.4). Grey regions correspond to deviations of ±10% β_θ with higher β_θ's mapping to higher α's , higher r_b's, and lower λ_o's.

Fig. 6.5 shows the parallel current parameters consistent with the experimental inputs over a sawtooth cycle. In the MBFM the sawtooth produces an *increase* in r_b from around 0.5 to 0.7, corresponding to a *flattening* of the current profile. The α-model also indicates flattening with α increasing from around 3 before the crash to around 4 after the crash. The $\lambda(r)$ profiles shown in Fig. 6.2 reflect this variation of the profile

about the sawtooth. Both models indicate a suppression of parallel current during the crash. As noted above the α-model predicts higher λ_o for the steep profiles, though the λ_o values of the two models converge as the profiles flatten. This results in a λ_o for the α-model with greater apparent suppression of core current at the sawtooth crash. With higher estimates of β_θ both models predicted lower values of λ_0 and flatter current profiles, although the effects of pressure were minimal. All of the electric and magnetic field sawtooth crash dynamics discussed below may be completely understood as either a manifestation of or a response to the current profile flattening described by these parameters.

6.1.2 Mean Field Electrodynamics

Modeling of the equilibrium over the sawtooth cycle enables us to investigate the evolution of the magnetic flux and to calculate the electric field induced by changes in that flux. Below we qualitatively examine the dynamics of the equilibrium magnetic field and the redistribution of magnetic flux during the sawtooth crash. The two key phenomena observed are the loss of poloidal flux in the plasma core and the generation of toroidal flux in the mid-region of the plasma. The latter is partially offset by a slight loss of toroidal flux in the core and a transient increase in negative toroidal flux at the edge. By calculating the time derivative of the integrated flux we obtain estimates of induced electric fields with peak amplitude of tens of Volts/m during the crash. Below we first describe the evolution of the magnetic field and then describe the electric fields induced by these changes. Again the field described here results from models of the current profile which are constrained by edge measurements but is in no way a unique solution to the parallel current in the MST. By pursuing two models of the parallel current we hope to develop some sense of the sensitivity of the derived field to our approximations in $\lambda(r)$. However, precise numerical comparisons await current profile measurements in the core.

Magnetic field evolution

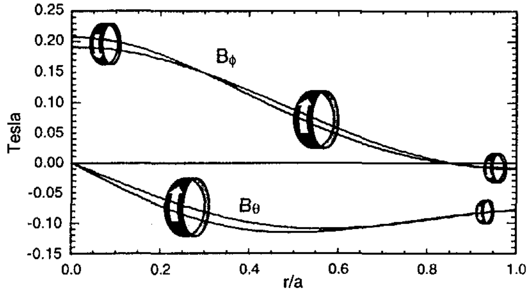

Fig. 6.6.— $B_\phi(r)$ and $B_\theta(r)$ before and after the sawtooth. Arrows indicate direction of field evolution during the sawtooth. Fields were obtained using the α-model and an α_p=4.

Fig. 6.6 shows the toroidal and poloidal magnetic fields before and after a sawtooth crash. The fields were obtained using the α-model, an $\alpha_p = 4$, and the β_θ shown in Fig. 6.4c. We may understand the dynamics of the fields as a direct consequence of the current flattening observed in both models. The sharp decrease in B_θ over the crash simply reflects the suppression of $J_{||} \approx J_\phi$ in the core. This current appears farther out in radius where $J_{||} \approx J_\theta$ producing the observed net increase in B_ϕ. Hence, the flattening of the parallel current profile is often described as a conversion or reconnection of poloidal flux into toroidal flux. In many kinematic dynamo scenarios such a conversion may be brought about from the stretching and twisting of the field lines by the fluid motion. Here the flux dynamics directly reflect the parallel current dynamics. The fluid fluctuations are invoked only to provide an electromotive force to drive those current dynamics.

The toroidal magnetic field exhibits two dynamics during the crash in addition to the increase of B_ϕ in the plasma mid-region. The first is the experimentally observed deepening of the magnetic field reversal at the edge. This appears as the downward spike in F but is less visible in Fig. 6.6. In general, toroidal field reversal reflects a boundary condition applied at the plasma edge. If the plasma were bounded by a perfectly conducting, continuous shell, the integrated toroidal flux in the torus would be fixed. Thus, any increase in J_θ near the edge would induce an image current in the wall, pulling $B_\phi(a)$ more negative and canceling out the generated toroidal flux in the core. This is not the case for the MST shell which contains a toroidal gap which breaks the poloidal continuity of the shell, sustains a voltage, and allows for the time variation of $\langle B_\phi \rangle_V$. Typically a current is driven through the toroidal gap in order to maintain a desired level of reversal. One could imagine a "perfect" toroidal gap circuit, capable of withstanding arbitrary voltages while delivering constant current through the gap. Such a circuit would fix $B_\phi(a)$ while allowing arbitrarily rapid changes in $\langle B_\phi \rangle_V$ operating as the functional opposite of the closed, conducting wall. The toroidal gap circuit of the MST acts between these extremes. Upon the spontaneous generation of B_ϕ in the core by the plasma the toroidal gap circuit responds with a transient image current which produces the observed negative spike in F. The circuit then rings back inductively and settles back to its previous level of J_θ and the corresponding B_ϕ at the wall. Thus, the inductance of the circuit allows for the transient variation of F while the voltage sustained by the gap allows for variations of $\langle B_\phi \rangle_V$ over longer time scales.

In addition to the increase of $\langle B_\phi \rangle_V$ and the deepening of the toroidal field reversal, the models consistently predict a drop in $B_\phi(0)$ over the crash. Computationally this comes about from the normalization of the modeled fields by the measured $\langle B_\phi \rangle_V$. In essence the measured increase in $\langle B_\phi \rangle_V$ is not great enough to account for the modeled increase in B_ϕ in the plasma mid-region even with the jump in negative toroidal flux at the edge. However, the dimensionless mapping of $\{F, \Theta\} \Rightarrow \{\lambda_o, \alpha\}$ fix the shape of the B_ϕ profile. Thus, the normalization reduces the overall magnitude of B_ϕ to match the integrated toroidal flux from the models to the measured toroidal flux integrated over the plasma volume while maintaining the profile shape. This normalization results in the predicted dip in $B_\phi(0)$ as well as an overall decrease in the mean magnetic field energy. While we have no experimental information to confirm or contradict this modeled behavior of $B_\phi(0)$, the drop perhaps indicates the difficulties of integrating approximate models, bound by edge measurements, to predict the behavior of fields near the core. One can imagine slight modifications to the modeling of $\lambda(r)$ which might distribute current differently to match the edge measurements while holding $B_\phi(0)$ constant. This difficulty highlights the need for core current profile measurements to further constrain the modeling of $\lambda(r)$. In the mean time it may be an interesting exercise to explore the behavior of three parameter $\lambda(r)$ models with the *a priori* condition of constant $B_\phi(0)$.

Redistribution of magnetic flux

To examine the redistribution of magnetic flux more carefully we define the radial derivative of the toroidal and poloidal magnetic flux as,

$$\frac{d\Phi_\theta}{dr} = 2\pi R_o B_\theta, \tag{6.13}$$

$$\frac{d\Phi_\phi}{dr} = 2\pi r B_\phi, \tag{6.14}$$

where, R_o is the major radius of the torus. Fig. 6.7 shows a contour plot of these derivatives where for each radius the average value of $d\Phi_\theta/dr$ or $d\Phi_\phi/dr$ over the sawtooth has

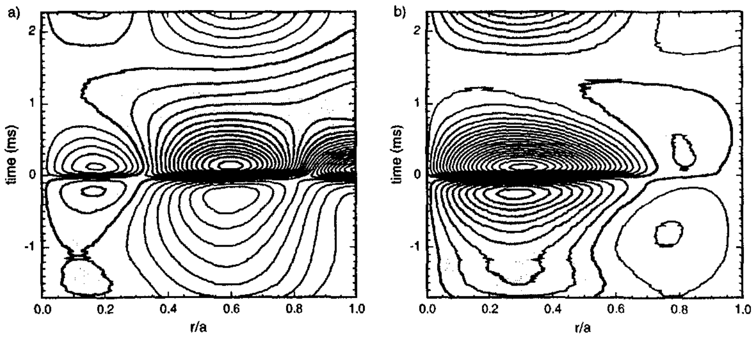

Fig. 6.7.— Evolution of the a) toroidal and b) poloidal magnetic flux in time. Contours drawn for constant $\frac{d}{dr}\Phi - \langle \frac{d}{dr}\Phi \rangle$ where $\langle\ \rangle$ indicates an average in time over the sawtooth cycle. Shaded regions indicate areas of high relative flux magnitudes. For Φ_ϕ this means more positive flux, while for Φ_θ this means more negative flux. Note the density of contours at the sawtooth indicating rapid flux redistribution.

been subtracted. Thus the contours represent constant deviation in the radial density of the magnetic flux from its average value in time. The picture presented here is consistent with the magnetic field evolution described above. During the crash over most of the plasma radius the poloidal flux changes from greater than average value to less than average values, with the most dramatic changes occurring at $r/a \approx 0.3$. The toroidal flux density increases in value over the mid-region of the plasma with the peak increase occurring at $r/a \approx 0.6$. This increase is momentarily offset by a transient increase in negative flux at the wall and a small drop in positive flux at the core. The symmetry of the contours about the crash reflects the inverse natures of the crash and decay phases of the sawtooth cycle, with the former abruptly reversing the redistribution caused by the latter. The exception to this rule is the behavior of the negative toroidal flux at the wall which, as discussed above, reflects the dynamics of the toroidal gap circuit rather than the plasma itself.

Mean inductive electric fields

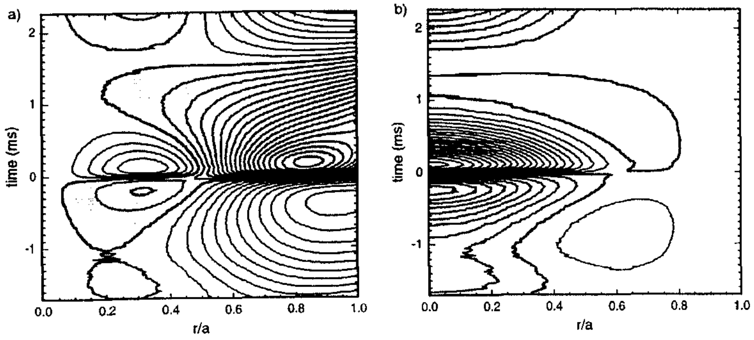

Fig. 6.8.— Contours of constant a) $\Phi_\phi(r,t) - \langle\Phi_\phi(r)\rangle_t$ and b) $\Phi_\theta(r,t) - \langle\Phi_\theta(r)\rangle_t$ over the sawtooth cycle. Shaded areas indicate higher than average integrated flux magnitudes.

To calculate the induced electric fields we must integrate the flux enclosed by poloidal and toroidal loops and take its time derivative. The geometry for the integration of the flux from both components of the magnetic field is shown in Fig. 6.9. Fig. 6.8a shows $\Phi_\phi(r,t) - \langle\Phi_\phi(r)\rangle_t$ where $\Phi_\phi(r) = \int_0^r (d\Phi_\phi/dr')dr'$. Over the inner half of the minor radius the integrated flux decreases slightly during the crash due to the projected drop of $B_\phi(0)$. However, the jump in toroidal flux in the mid-region of the plasma soon dominates and the flux shows a net increase over the outer half of the plasma. Fig. 6.8b shows $\Phi_\theta(r,t) - \langle\Phi_\theta(r)\rangle_t$ where $\Phi_\theta(r) = \int_r^a (d\Phi_\theta/dr')dr'$. This shows a monotonically increasing integrated flux jump as Φ_θ approaches the core. The density of contours in this plot reflects the rapidity of flux change at that radius and foreshadowing the large magnitude of the induced electric field.

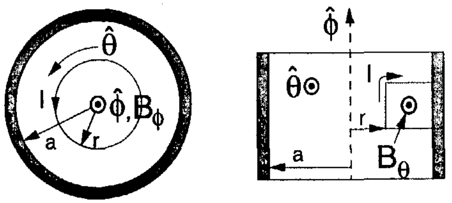

Fig. 6.9.— Geometry for cylindrical calculation of induced electric field. Φ_θ is integrated in rectangle from the edge while Φ_ϕ is integrated in a circle from the core. $\hat{l}$ indicates the direction of the electric field line integration.

The electric fields in the plasma are induced by flux swings external and internal to the plasma. The external flux swing of the iron core transformer induces a toroidal electric field in the $-\hat{\phi}$ direction which appears directly as a voltage across the poloidal gap of the MST shell. We calculate the edge E_ϕ from this voltage (V_{pg}) as,

$$E_\phi(a) = -\frac{d\Phi_{ext}}{dt} = \frac{V_{pg}}{2\pi R_o} \approx 1.7 \text{ Volts/m.} \tag{6.15}$$

The internally induced electric fields arise from the internal redistributions of flux in the plasma described above. The equations which we employed to solve for the total induced field are,

$$E_\theta(r) = -\frac{1}{r}\int_0^r \frac{dB_\phi}{dt} r' dr', \tag{6.16}$$

$$E_\phi(r) = \frac{V_{pg}}{2\pi R_o} - \int_r^a \frac{dB_\theta}{dt} dr', \tag{6.17}$$

again employing the geometry shown in Fig. 6.9. The magnetic flux was integrated numerically using a variation of Simpson's rule and the flux derivatives were calculated using a standard five-point derivative routine.

Fig. 6.10a shows the toroidal inductive electric field in time averaged over the core region of the plasma. An enormous field is induced at the sawtooth crash in the $-\hat{\phi}$

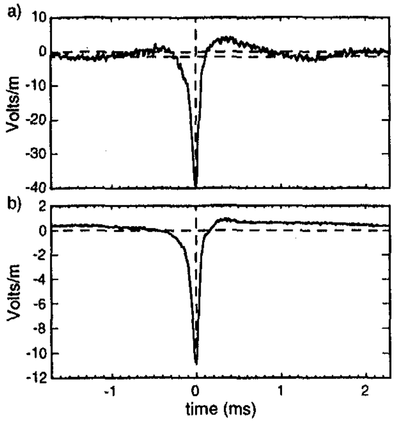

Fig. 6.10.— Inductive a) $E_\phi(t)$ averaged from $r/a = 0.0 - 0.1$ and b) $E_\theta(t)$ averaged from $r/a = 0.7 - 0.8$.

direction. This field is aligned with the applied electric field so as to drive core current, inductively opposing the flattening of $J_{\|}$. Away from the crash the $E_\phi(0)$ is typically more positive than the externally applied field (the lower dotted line). This suggest the opposite behavior of the internally induced field away from the crash as it opposes the gradual peaking of the current profile. As this peaking occurs on a much slower time scale, the inductive back reaction is much smaller. Curiously, following the crash $E_\phi(0)$ crosses zero and reaches positive magnitudes of several Volts/m. Were the plasma infinitely inductive we would expect E_ϕ at the core to equal zero as the inductance of the plasma perfectly cancels the E_ϕ applied by the transformer. This overshoot of the inductance indicates a peaking of J_θ following the crash which cannot be accounted for by the external circuit. This feature persists for both the α-model (shown) and the MBFM and varies little with pressure. If real, it would imply an anomalous current source (i.e.

dynamo electric field) which acts following the sawtooth to *drive* current in the core.

The poloidal electric field near the edge (Fig. 6.10b) also spikes at the sawtooth crash reaching ~10 Volts/m. The edge E_θ is directed in the $-\hat{\theta}$ direction to oppose the distribution of poloidal current in the plasma edge and, equivalently, the generation of core toroidal flux. Away from the crash a positive and smaller E_θ opposes the decay of the edge current with a field strength of ~0.5 Volts/m. Unlike E_ϕ, E_θ arises entirely from internal changes to the magnetic flux and thus typically varies about zero.

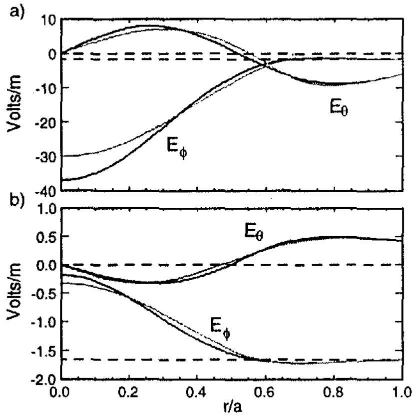

Fig. 6.11.— Inductive $E_\phi(r)$ and $E_\theta(r)$ averaged a) over a 0.1 ms window about the crash and b) over the decay phase defined roughly as $|t - t_c| \geq 0.5ms$. Estimates are shown for both α-model(solid) and MBFM (grey).

We now examine these fields as a function of r averaged over the decay and crash phase of the sawtooth cycle. To obtain a field representative of the crash phase we averaged both fields over a 0.1 ms window centered about the sawtooth crash (Fig. 6.11a). During the crash, $E_\phi(r)$ holds near its externally applied value of ~1.7 Volts/m in the outer half of the plasma. Over the inner half of the plasma the field grows rapidly peaking at a value of ~30 Volts/m at $r = 0$. As discussed above, this enormous induced field is aligned with the externally applied field in the direction to drive current in the core and oppose the redistribution of that current to the plasma edge. $E_\theta(r)$ over the inner half of the plasma acts to drive current opposing the loss of toroidal flux in the very core of the plasma. At mid-radius $E_\theta(r)$ flips sign as the generation of flux in the mid-region of the plasma overtakes the loss in the core for a net increase in $\Phi_\phi(r)$. E_θ opposes the increase $J_\| \approx J_\theta$ over the outer region of the plasma exhibiting a finite value at the plasma edge. In a check of model consistency we confirmed that with excellent accuracy this edge poloidal electric field was given by, $E_\theta(a) = V_{tg}/2\pi a$, where V_{tg} is the ensembled toroidal gap voltage.[1]

By averaging the fields for $|t - t_c| \geq 0.5$ ms we recover the typical behavior of $\mathbf{E}(r)$ during the decay phase of the sawtooth cycle. $E_\phi(r)$ remains close to its externally applied value over the outer region of the plasma and then decreases in magnitude near the core as the inductance of the plasma opposes the resistive peaking of $J_\|$. Likewise, $E_\theta(r)$ inductively opposes the dissipation of edge poloidal current (or, equivalently, core toroidal flux) over the outer region of the plasma. This behavior matches what might be expected of an RFP equilibrium decaying slowly in time. The significantly diminished field magnitudes simply reflect the slower time scales of the flux changes during the decay phase.

---

[1] This agreement confirms the absence of errors in the conversion by analog integrators of the measured V_{tg} to the stored $\langle B_\phi \rangle_V$ signal, the subsequent normalization of the modeled $B_\phi(r)$ by $\langle B_\phi \rangle_V$, the numerical integration of $B_\phi(r)$ to recover Φ_ϕ and the differentiation in time of the flux yielding, finally, the correct $E_\theta(a)$. While physically uninteresting, this loop effectively absolves our modeling of several potential sources of numerical error.

6.1.3 Resistive Current Dissipation

The task of modeling the resistive dissipation term in Ohm's law over the sawtooth is comparatively simple with predicted dynamics over the crash which are comparatively modest. Below we describe our estimation of the plasma resistivity from central electron temperatures measured with Thomson scattering and Z_{eff} inferred from central chord averaged Bremsstrahlung measurements. We then multiply η by $J_\|$ determined from the cylindrical modeling to estimate the parallel electric field necessary to drive modeled current. We find that $\eta J_\|$ ranges from ~2 Volts/m away from the sawtooth crash to ~6 Volts/m at the crash with the increase due entirely to the spike in plasma resistivity. The uncertainties in the estimated profile and magnitude of $\eta J_\|$ are small compared to the induced fields during the crash and thus have little impact on the implied dynamo fields. Away from the crash these uncertainties will dominate our calculation.

Calculation of resistivity

The electron temperature was measured in the core by a Thomson scattering system capable of a single laser fire every discharge. We ran the system along a central chord for ~50 shots in the low current ensemble, triggering the laser to fire at different times relative to sawteeth in the flat-top region of the discharge. By binning the photon counts from neighboring measurements relative to the sawtooth crash time we were able to reconstruct a coarse time evolution of the central electron temperature. Fig. 6.12 shows a smoothed version of our estimated $T_e(t)$ along with a measurement uncertainty of ±15%. Similar measurements at other radii suggest an extremely flat electron temperature profile

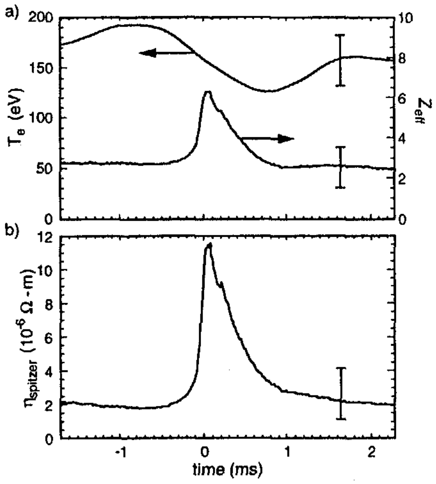

Fig. 6.12.— a) The central electron temperature, T_e, estimated from single point Thomson scattering measurements and Z_{eff} estimated from chord averaged Bremsstrahlung measurements. b) Spitzer resistivity calculated using these values.

motivating the somewhat arbitrary modeling of the electron temperature profile as,

$$T_e(r) = T_e(0)(1 - (T_e(a)/T_e(0) + 1)^8), \tag{6.18}$$

where we set $T_e(a)/T_e(0) = 0.05$.

To characterize Z_{eff} we collected bremsstrahlung radiation which are mostly free from contamination by neighboring spectral lines in the NIR and visible. Unfortunately, these detectors were not absolutely calibrated at the time of the measurement. However, by averaging the emitted radiation over the low, medium, and high current ensembles we could calculate a relative Z_{eff} as a function of time and current regime. Normalizing the relative Z_{eff} by the lowest measured value which occurred during the high current run when the machine had been extensively cleaned, we obtained the estimate shown in Fig. 6.12a. The error bars shown are coarse estimates of the uncertainty in the measurement. At the time of this measurement we had no information about the Z_{eff} profile. However, one would expect the value to increase toward the edge motivating another arbitrary profile definition of,

$$Z_{eff}(r) = Z_{eff,0}(1 + (Z_{eff}(a)/Z_{eff,0} - 1)^8), \tag{6.19}$$

where we set $Z_{eff}(a) = 6$.

Analytic expression for the plasma resistivity has been given by Spitzer (1962) as,

$$\eta = \alpha_e \frac{m_e \nu_e}{n_e e^2} = \left(\frac{\sqrt{m_e} e^2}{4\sqrt{2}\pi\epsilon_o^2}\right)\left(\frac{\alpha_e Z_{eff}}{T_e^{\frac{3}{2}} \log\Lambda}\right), \tag{6.20}$$

where the coefficient $\alpha_e(Z_{eff})$ varies from 0.51 with $Z_{eff} = 1$ to 0.29 for $Z_{eff} >> 1$. Substituting our estimates for T_e and Z_{eff} into this equation we obtain the resistivity shown in Fig. 6.12b. The substantial uncertainties in our estimates produce the roughly 50% error in the calculated value. Substantial diagnostic improvements underway in both Thomson scattering and Z_{eff} diagnostics should enable the calculation of relatively accurate resistivity profiles in the near future.

Estimation of $\eta J_{\|}$

We recover $J_{\|}$ from the current profile modeling easily as $J_{\|} = \lambda B$. The uncertainties in the calculation of η greatly exceed the differences in $J_{\|}$ between the α-model and the MBFM, so we choose the α-model which lacks the sharp, unphysical corner of the MBFM. $\eta J_{\|}$ in the core is shown over the sawtooth cycle in Fig. 6.13. The spike in the dissipated current over the crash reflects the dynamics of the resistivity, in particular $Z_{eff}(t)$. It is interesting to note that were it not for the inductance of the plasma

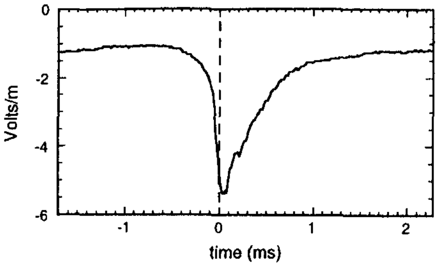

Fig. 6.13.— The estimated $\eta J_{\|}(0,t)$ using the resistivity shown in Fig. 6.12b and the current derived from the α-model.

producing the large electric fields discussed above, this enhanced resistivity during the crash would be more than enough to account for the suppression of current in the core. Of course, such an effect could not be similarly invoked to explain the increased current at the edge during the crash.

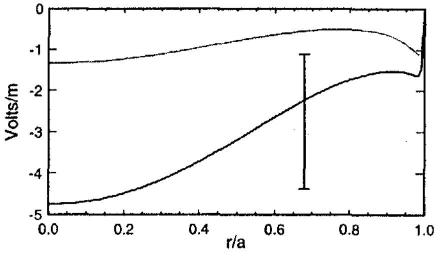

Fig. 6.14.— Profile of $\eta J_{\|}$ during (solid) and away (grey) for the crash. Approximate error bars stem from uncertainties in η.

The estimated profile of $\eta J_{\|}$ drops off roughly with the current as one approaches the edge. This assumes the resistivity profile discussed above which remains nearly constant over the inner 80% of the plasma and then spikes up near the cold resistive edge. The magnitude of $\eta J_{\|}$ scales directly with the five-fold jump in Z_{eff} at the crash. The propagation of substantial uncertainties in the resistivity profile and, to a lesser extent, in the parallel current profile make these profiles accurate only to within a factor of two. These errors will prove to dominate our estimation of the dynamo field away from the crash while the inductive effects discussed above dominate during the crash.

6.1.4 Mean Field Estimate of the Dynamo

To determine the anomalous contribution to Eq. 6.1 we subtract the parallel inductive electric fields from $\eta J_{\|}$. As discussed above both terms contain significant levels of uncertainty stemming from an absence of current profile diagnostics, in the case of $E_{\|}$, and accurate T_e and Z_{eff} diagnostics, in the case of $\eta J_{\|}$. Below we find that away from the crash the two terms cancel within their uncertainty. However, at the crash, the large inductive fields produced by the rapid redistribution of flux imply a dynamo field with a behavior similar to that expected from the static analysis, but possessing a magnitude which is several times larger.

$\eta J_{\|} - E_{\|}$ *at and away from the sawtooth crash*

By taking the scalar component of the inductive electric fields with the mean magnetic field we obtain $E_{\|}$. Not surprisingly, the field induced by the redistribution of parallel current is almost entirely in the parallel direction. We subtract this parallel electric field from the estimated $\eta J_{\|}$ to obtain an estimate of the anomalous electric field needed to balance parallel Ohm's law. Fig. 6.15a shows this field averaged over a 0.1 ms window centered about the sawtooth. The uncertainty in this field due to the subtraction of $\eta J_{\|}$ amounts to approximately ± 4 Volts/m. The sensitivity of the calculation of $E_{\|}$

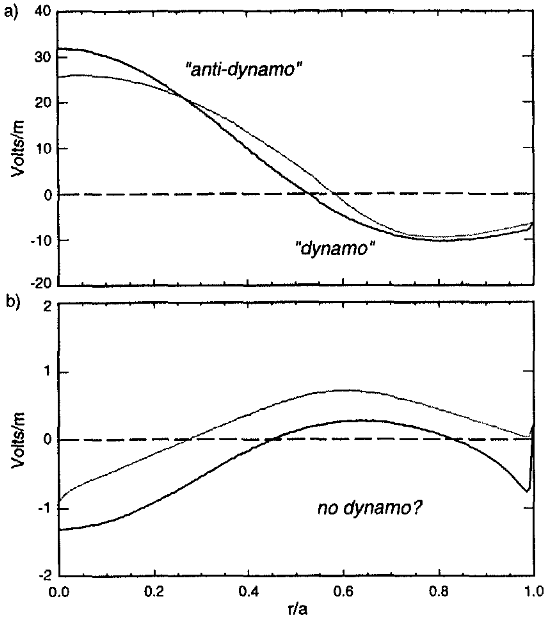

Fig. 6.15.— $\eta J_{\|} - E_{\|}$ a) during and b) away from the sawtooth crash. The fields shown were modeled with the α-model(solid) and the MBFM (grey). The fields away from the sawtooth are consistent with zero within the uncertainties of the model.

to the modeling of the current profile may be estimated by comparing the predictions of the MBFM and the α-model. Despite these considerable uncertainties the modeling provides indication of a substantial imbalance in the core and edge during the crash. In the core a field of 20–40 Volts/m is required to overcome the inductance of the plasma and produce the modeled suppression of core parallel current. Near the edge a field of 5–15 Volts/m in the opposite direction is required to drive the edge current against the inductive back-reaction of the plasma. The sense of the indicated core and edge electric fields is exactly the same as that implied by the static treatment of Ohm's law. However, the discrete nature of the current relaxation combined with the large inductance of the plasma necessitates a much larger field to accomplish the observed redistribution of current. Interestingly, while dynamo action in the MST is typically linked to the generation of toroidal flux (i.e. production of edge J_θ), the loss of poloidal flux (i.e. suppression of core J_ϕ) requires a larger dynamo field.

Fig. 6.15b shows the estimated anomalous fields away from the crash. The uncertainty due to the subtraction of $\eta J_{\|}$ for these fields is approximately ± 0.5 Volts/m. Again, the uncertainty due to modeling of $\lambda(r)$ may be estimated by comparing the predictions of the two models. The field remaining after the subtraction of the two fields suggests a core dynamo term acting to drive current (opposite to its behavior at the crash). However, the field overall may generally characterized as consistent with zero with room for a dynamo term of ± 2 Volts/m. Thus, while lacking the precision necessary to rule out a modest continuous dynamo, the model does not indicate the need for such a term.

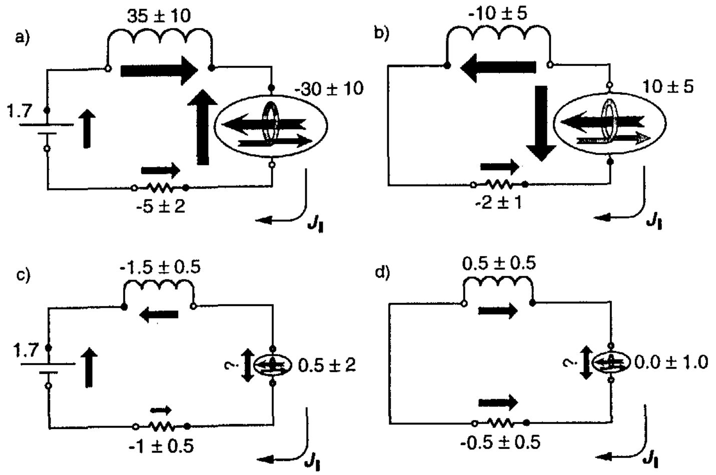

Fig. 6.16.— Applied electric field (voltage source), internally induced electric field (inductor), dissipated current (resistor), and implied dynamo field (MST logo) shown as four circuit elements. The values shown are in Volts/m with arrow representing their direction relative to the parallel current which moves clockwise. Top circuits show the estimated a) core and b) edge terms during the crash while bottom circuits show the c) core and d) edge terms away from the crash.

Simple Circuit Analogy

We summarize the implications of the mean-field modeling with the four circuits shown in Fig. 6.16. During the crash the core is dominated by the internal inductance of the plasma driving current and the dynamo term suppressing current. In the edge the situation during the crash is reversed with the inductance of the plasma opposing the current and the dynamo driving the current. In both cases these terms dominate the applied and the resistive terms by roughly an order of magnitude. The poloidal pitch of the magnetic field at the edge effectively removes the applied field from the circuit. Away from the crash in the core the applied field is roughly balanced by the inductance of the plasma and the dissipated current with no need for a dynamo term. Similarly at the edge the inductance of the plasma balances the resistive dissipation of the poloidal current with no apparent need for a dynamo. Future measurements of the parallel current profile and plasma resistivity combined with modeling which incorporates these additional constraints will, almost certainly, change the values assigned to many of these circuit elements. However, the basic features of these circuits stem directly from the sudden flattening of the parallel current profile. Thus, while numerically approximate, the modeling described above provides a basic understanding of the dynamic balance of Ohm's law in the core and edge which we expect to be refined but not reversed by future measurements.

6.2 Core Dynamo Electric Field

In this section we present the measured dynamo products and provide empirical estimates of $\langle \tilde{\mathrm{v}} \times \tilde{\mathrm{b}} \rangle$ in the interior of MST. These measurements constitute the key novel results of this thesis. In rough order of importance the measurements demonstrate the existence, illustrate the behavior, and approximate the magnitude of a $\langle \tilde{\mathbf{v}} \times \tilde{\mathbf{b}} \rangle$ dynamo field in the interior of MST. The overall behavior of the fields matches many of our expectations, although careful numerical comparisons with the dynamo fields implied by the equilibrium modeling proved inconclusive. Achieving such a comparison through a careful coordination of fluctuation measurements and equilibrium modeling await as the next obvious step in dynamo measurements in MST.

Below we first present the four dominant $\langle \tilde{v}_\phi \tilde{b}_{\theta,n} \rangle$ and $\langle \tilde{v}_\theta \tilde{b}_{\theta,n} \rangle$ products. These will be described in a fairly brief manner as most (if not all) of their features derive from the amplitude, phase, and coherence of the $\tilde{\mathbf{v}}$ and $\tilde{\mathbf{b}}$ fluctuations, presented previously in Chapters 4 and 5. We also present the Lundquist number scaling of these products. Next, we adjust the phase and amplitude of the products to reflect the implied $\langle \tilde{v}_\phi \tilde{b}_r \rangle$ and $\langle \tilde{v}_\theta \tilde{b}_r \rangle$ products in the core. The uncertainties of the amplitude adjustment will dominate the uncertainty in the estimated core dynamo fields. Finally we compare the measured fields with the predictions of the modeling discussed in § 6.1.

6.2.1 Measured Dynamo Products

Time and frequency behavior of $\langle \tilde{v}_\phi \tilde{b}_{\theta,n} \rangle$ *and* $\langle \tilde{v}_\theta \tilde{b}_{\theta,n} \rangle$

The real and imaginary components of the four largest $\langle \tilde{v} \tilde{b}_{\theta,n} \rangle$ products (Fig. 6.17) are consistent with the amplitude, coherence, and phase of the field and flow fluctuations presented in Chapters 4 and 5. Like the amplitudes and coherence of the fluctuations, the products peak in time during the sawtooth with cross-power concentrated in frequency from 8–20 kHz. The relative magnitude of the toroidal and poloidal products simply reflects the amplitude of the core modes coherent with $\tilde{v}_\phi$ relative the edge modes

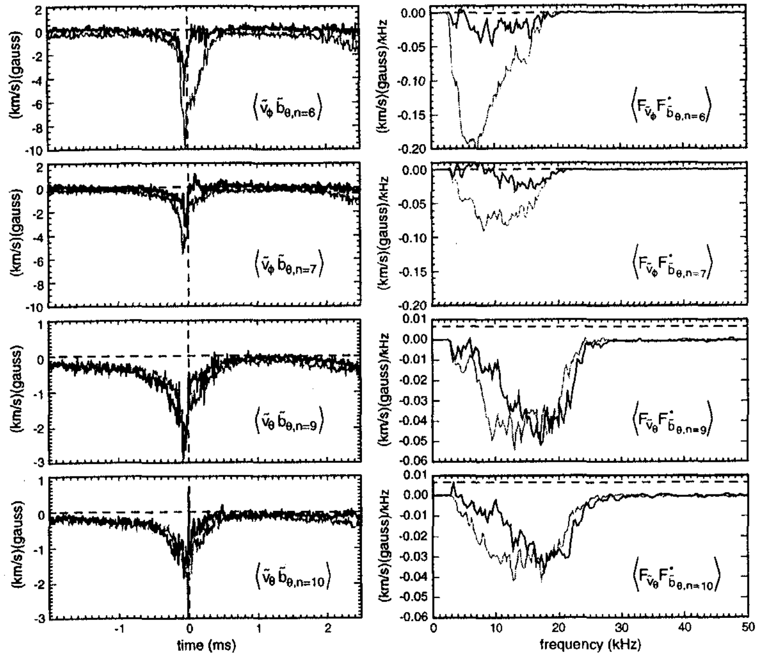

Fig. 6.17.— The ensembled $\langle \tilde{v} \tilde{b}_{\theta,n} \rangle$ products for the two most clearly resolved n for each chord over time (left) and frequency (right). The real (solid) and imaginary (grey) components were calculated using the measured phase corrected for the geometric separation of the measurements. From top to bottom the measured products are $\langle \tilde{v}_\phi \tilde{b}_{\theta,n=6} \rangle$, $\langle \tilde{v}_\phi \tilde{b}_{\theta,n=7} \rangle$, $\langle \tilde{v}_\theta \tilde{b}_{\theta,n=9} \rangle$, and $\langle \tilde{v}_\theta \tilde{b}_{\theta,n=10} \rangle$.

coherent with $\tilde{v}_\theta$. The largest product obtains between $\tilde{v}_\phi$ and the dominant $n=6$ mode, $\langle \tilde{v}_\phi \tilde{b}_{\theta,n=6}\rangle$. The robust coherence of the poloidal products may be seen in the clear resolution of the $\tilde{v}_\theta$ products over the full sawtooth cycle. In contrast the toroidal products, especially $\langle \tilde{v}_\phi \tilde{b}_{\theta,n=7}\rangle$, concentrate their power near the sawtooth. The time dynamics of the coherence discussed in § 5.2 manifest in the gradual rise and abrupt crash of most the products about the sawtooth crash. The exception is the $n=6$ product which encounters a second bump of power immediately following the crash which decays away gradually. This bump is also apparent at much smaller magnitudes and appears as a secondary coherence peak in Figs. 5.7–5.8.

The complex phase of the products shown incorporates the correction for the geometric separation of the measurements described in § 5.3.2. Specifically, defining $\langle \tilde{v}_x \tilde{b}_{\theta,n}\rangle_D$ and $\langle \tilde{v}_x \tilde{b}_{\theta,n}\rangle_P$ as the direct and phase-shifted products of the measured fluctuations returned by the correlation routine (§ 3.2.3), the products shown in Fig. 6.17 are calculated as,

$$\langle \tilde{v}_x \tilde{b}_{\theta,n}\rangle = \Big(\langle \tilde{v}_x \tilde{b}_{\theta,n}\rangle_D + i\langle \tilde{v}_x \tilde{b}_{\theta,n}\rangle_P\Big)\ e^{-i(m(\theta_{v_x}-\theta_b)+n\phi_{v_x})}. \tag{6.21}$$

In this expression θ_{v_x} and ϕ_{v_x} are the angles about which the IDS chord(s) exhibits the odd symmetry defined in § 2.5 and θ_b is the poloidal angle of the toroidal array coils. An analogous mapping provides the complex phase of the Fourier products. These mapped phases match those presented in Chapter 5 with the toroidal products dominated by their imaginary components ($\delta_{v_\phi} - \delta_{b_\theta} = -\pi/2$), and the poloidal components evenly split between real and imaginary components ($\delta_{v_\theta} - \delta_{b_\theta} = -3\pi/2$). The post crash bump in the products exhibits a larger imaginary component appearing as imaginary power at low frequencies in the cross spectra. This agrees with the linear frequency dependence

exhibited by the phase in the Fig. 5.12. As discussed in § 5.3 and below, only the imaginary component of these products maps to $\langle \tilde{v}\tilde{b}_r\rangle$ dynamo activity.

Lundquist number scaling of the dynamo products

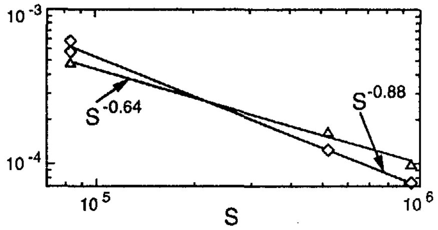

Fig. 6.18.— The S scaling of $\langle \tilde{v}_\phi \tilde{b}_{\theta,n=7}\rangle$ (triangles), and $\langle \tilde{v}_\theta \tilde{b}_{\theta,n=9}\rangle$ (squares) averaged over the sawtooth cycle.

In addition to the low current data presented above we calculated the dynamo products for the medium and high current ensembles to obtain an experimental estimate of the S scaling of the full $\langle \tilde{\mathbf{v}} \times \tilde{\mathbf{b}}\rangle$ product. If the current were entirely dynamo-driven then a non-dimensional formulation of Ohm's law predicts a scaling of,

$$\langle \tilde{\mathbf{v}} \times \tilde{\mathbf{b}}\rangle \propto S^{-1}, \tag{6.22}$$

where the Lundquist number, S, is the ratio of the Alfvén and resistive times. As presented in previous chapters the individual fluctuation amplitudes averaged over the sawtooth cycle present weak empirical scalings of $\tilde{b} \propto S^{-0.08}$, $\tilde{v}_\theta \propto S^{-0.08}$, and $\tilde{v}_\phi \propto S^{-0.19}$ in rough agreement with previous empirical scalings (Stoneking, 1997; Cappello and Biskamp, 1996). However, the full dynamo product yields the much stronger empirical scaling of

$$\langle \tilde{v}_\theta \tilde{b} \rangle \propto S^{-0.64} \quad \text{and} \quad \langle \tilde{v}_\phi \tilde{b} \rangle \propto S^{-0.88}, \tag{6.23}$$

with the exponents derived from the three point linear fits shown in Fig. 6.18. These scalings approach agreement with Eq. 6.22 in sharp contrast to the product of the $\tilde{v}$ and $\tilde{b}$ power, reflecting the dramatic scaling of the coherence between the fluctuations which we noted in § 5.5 (Fig. 5.23). However interpretation of these results is clouded by the edge character of the C V emission profile at higher currents which may illuminate fewer of the large core modes.

6.2.2 Estimation of Core Dynamo Products

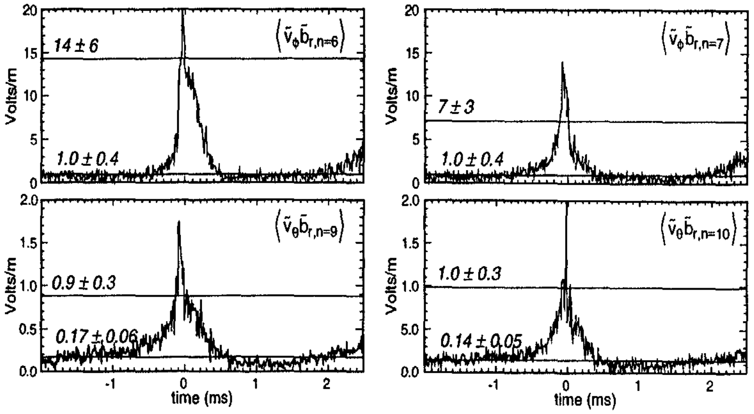

Fig. 6.19.— The estimated real component of $\langle \tilde{v} \tilde{b}_r \rangle$ products for the two most clearly resolved n for each chord. From left to right, top to bottom the estimated products are $\langle \tilde{v}_\phi \tilde{b}_{r,n=6} \rangle$, $\langle \tilde{v}_\phi \tilde{b}_{r,n=7} \rangle$, $\langle \tilde{v}_\theta \tilde{b}_{r,n=9} \rangle$, and $\langle \tilde{v}_\theta \tilde{b}_{r,n=10} \rangle$. Uncertainties in the magnitude stem from the unknown attenuation of the chord and the estimation of $|\tilde{b}_r|$ in the core.

Direction of Core Dynamo Field

To map the measured $\langle \tilde{v}_\theta \tilde{b}_{\theta,n} \rangle$ and $\langle \tilde{v}_\phi \tilde{b}_{\theta,n} \rangle$ products onto core $\langle \tilde{v}_\theta \tilde{b}_r \rangle$ and $\langle \tilde{v}_\phi \tilde{b}_r \rangle$ products we must properly account for the phase shift between $\tilde{b}_r$ in the core and $\tilde{b}_\theta$ at the edge. This mapping rotates the negative imaginary component of the measured products around 90° such that they become positive real components of core $\langle \tilde{v}_\theta \tilde{b}_r \rangle$ and $\langle \tilde{v}_\phi \tilde{b}_r \rangle$ products (Fig. 6.19). To interpret these directions we return to the full expansion of $\langle \tilde{\mathbf{v}} \times \tilde{\mathbf{b}} \rangle$

$$\langle \tilde{\mathbf{v}} \times \tilde{\mathbf{b}} \rangle_\theta = \langle \tilde{v}_\phi \tilde{b}_r \rangle - \langle \tilde{v}_r \tilde{b}_\phi \rangle \approx \langle \tilde{v}_\phi \tilde{b}_r \rangle, \tag{6.24}$$

$$\langle \tilde{\mathbf{v}} \times \tilde{\mathbf{b}} \rangle_\phi = \langle \tilde{v}_r \tilde{b}_\theta \rangle - \langle \tilde{v}_\theta \tilde{b}_r \rangle \approx -\langle \tilde{v}_\theta \tilde{b}_r \rangle, \tag{6.25}$$

where the $\langle \tilde{v}_r \tilde{b} \rangle$ terms are neglected due to the small size and coherence of the measured radial velocity fluctuations (§ 5.4). Thus, our positive $\langle \tilde{v}_\phi \tilde{b}_r \rangle$ measurement implies a $\langle \tilde{\mathbf{v}} \times \tilde{\mathbf{b}} \rangle_\theta$ at $r/a \approx 0.3 - 0.4$ in the $+\hat{\theta}$ direction. Referring back to our right handed geometry we see that this corresponds to a current drive such as to *drive* $J_\parallel$ in the plasma mid-region and generate B_ϕ. Thus the $\langle \tilde{v}_\phi \tilde{b}_r \rangle$ product is consistent with "dynamo" (as in not "anti-dynamo") activity in the middle to core region of the plasma. Our positive $\langle \tilde{v}_\theta \tilde{b}_r \rangle$ measurements imply a $\langle \tilde{\mathbf{v}} \times \tilde{\mathbf{b}} \rangle_\phi$ at $r/a \approx 0.6$–0.7 in the $-\hat{\phi}$ direction. This is the same direction as the applied electric field and thus should also act to drive parallel current inside the reversal surface. However, due to the oblique projection of $\hat{\phi}$ onto the mean magnetic field at the edge, very little of this dynamo field aligns with the edge parallel current. Conversely, if this measured field represents the toroidal projection of a parallel field, it would imply a substantial $\langle \tilde{\mathbf{v}} \times \tilde{\mathbf{b}} \rangle_\parallel$ at this radius. Clearly, edge $\langle \tilde{v}_\phi \tilde{b}_r \rangle$ measurements are needed to confirm this. In addition core measurements of $\langle \tilde{v}_\theta \tilde{b}_r \rangle$ are

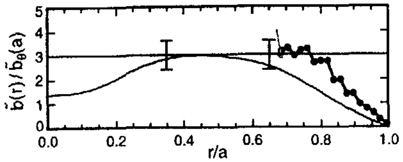

Fig. 6.20.— The MHD modeled (line) and probe measured (dots) $|\tilde{b}_r(r)|$ profile normalized to $\tilde{b}_\theta(a)$ at the wall. Shaded regions indicate approximate location of $\langle\tilde{v}_\phi\tilde{b}_r\rangle$ and $\langle\tilde{v}_\theta\tilde{b}_r\rangle$ measurements. Horizontal line with error bars represents estimated correction factor and its uncertainty.

indicated where the $\langle\tilde{\mathbf{v}}\times\tilde{\mathbf{b}}\rangle_\phi$ field should be strongly anti-dynamo.

Magnitude of Core Dynamo Field

To determine the magnitude of the $\langle\tilde{v}_\phi\tilde{b}_r\rangle$ and $\langle\tilde{v}_\theta\tilde{b}_r\rangle$ products in the core we must estimate two correction factors. The first accounts for the amplitude of $\tilde{b}_r$ in the core relative to the measured $\tilde{b}_\theta$ at the edge (Fig. 6.20) which we estimate as,

$$|\,\tilde{b}_r(r/a=0.3-0.4)\,| \approx |\,\tilde{b}_r(r/a=0.6-0.7)\,| \approx (3.0\pm 0.6)\ |\,\tilde{b}_\theta(r=a)\,|, \tag{6.26}$$

The second correction factor accounts for the attenuation of the velocity fluctuation amplitude by the chord average described in § 5.1. Combining the two corrections we obtain the overall amplitude corrections of,

$$\langle\tilde{v}_\phi\tilde{b}_{r,6}\rangle = (20\pm 8)\quad\langle\tilde{v}_\phi\tilde{b}_{\theta,6}\rangle, \tag{6.27}$$

$$\langle\tilde{v}_\phi\tilde{b}_{r,7}\rangle = (25\pm 10)\ \langle\tilde{v}_\phi\tilde{b}_{\theta,7}\rangle, \tag{6.28}$$

$$\langle\tilde{v}_\theta\tilde{b}_{r,n}\rangle = (6\pm 2)\quad\langle\tilde{v}_\theta\tilde{b}_{\theta,n}\rangle, \tag{6.29}$$

where the quantities on the LHS are the core dynamo products and the quantities on the RHS are the amplitude corrected measured products. Note, the correction factors stemming from the attenuation of the toroidal chord is substantial, while the poloidal chord has a more modest correction of ~ 2 for the attenuation times ~ 3 for the $\tilde{b}_\theta \to \tilde{b}_\phi$ mapping. The errors estimated for these correction factors dominate all other errors (i.e. instrumental, statistical) in our calculation of the magnitude of the core dynamo products

We resolve dynamo field with both chords at and away from the sawtooth crash. Fig. 6.19 shows the real part of the core dynamo products following the above corrections of phase and amplitude. We obtain dynamo fields from the toroidal velocity measurements which peak during the crash with amplitudes of,

$$\langle\tilde{v}_\phi\tilde{b}_{r,6}\rangle = 14\pm 6\ \text{Volts/m, at}\ (r/a=0.3-0.4,\ |t|\leq 0.05), \tag{6.30}$$

$$\langle\tilde{v}_\phi\tilde{b}_{r,7}\rangle = 17\pm 3\ \text{Volts/m, at}\ (r/a \doteq 0.3-0.4,\ |t|\leq 0.05), \tag{6.31}$$

where the values reflect an average over a 0.1 ms window centered about the sawtooth and the uncertainties reflect the uncertainties in the mapping. These greatly exceed the poloidal velocity products during the crash which similarly yield amplitudes of,

$$\langle\tilde{v}_\theta\tilde{b}_{r,9}\rangle = 0.9\pm 0.3\ \text{Volts/m, at}\ (r/a=0.6-0.7,\ |t|\leq 0.05), \tag{6.32}$$

$$\langle\tilde{v}_\theta\tilde{b}_{r,10}\rangle = 1.0\pm 0.3\ \text{Volts/m, at}\ (r/a=0.6-0.7,\ |t|\leq 0.05). \tag{6.33}$$

Away from the crash the average values were calculated by excluding a 1 ms window about the sawtooth. These yielded values which were typically smaller by a factor of 10,

$$\langle\tilde{v}_\phi\tilde{b}_{r,6}\rangle = \quad 1.0\pm 0.4\ \text{Volts/m, at}\ (r/a=0.3-0.4,\ |t|\geq 0.5), \tag{6.34}$$

$$\langle\tilde{v}_\phi\tilde{b}_{r,7}\rangle = \quad 1.0\pm 0.4\ \text{Volts/m, at}\ (r/a=0.3-0.4,\ |t|\geq 0.5), \tag{6.35}$$

$$\langle\tilde{v}_\theta\tilde{b}_{r,9}\rangle = 0.17\pm 0.06\ \text{Volts/m, at}\ (r/a=0.6-0.7,\ |t|\geq 0.5), \tag{6.36}$$

$$\langle\tilde{v}_\theta\tilde{b}_{r,10}\rangle = 0.14\pm 0.06\ \text{Volts/m, at}\ (r/a=0.6-0.7,\ |t|\geq 0.5). \tag{6.37}$$

These values are within the ±1 Volts/m uncertainty of the modeling which predicted little to no dynamo away from the sawtooth.

6.2.3 Comparison with mean-field predictions

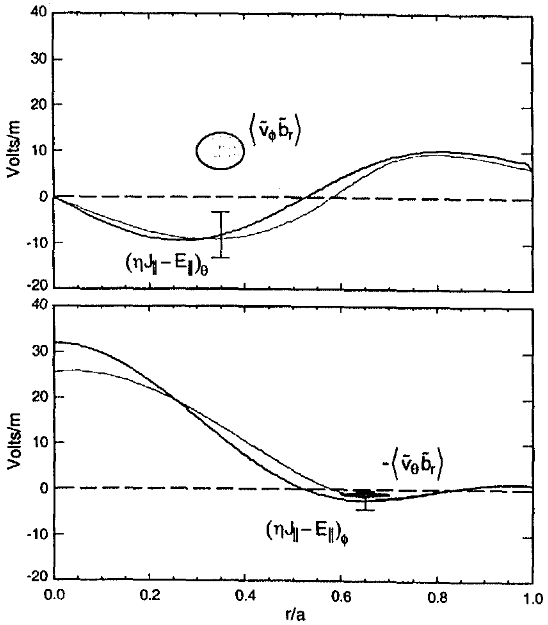

Fig. 6.21.— The a) poloidal and b) toroidal components to $\eta J_\| - E_\|$ estimated from the modeling. The shaded ovals represent the estimated magnitudes of the dynamo fields in the core.

We now seek to compare the empirical estimates of dynamo activity in the core to the field predicted in the previous section by the modeling. We will focus the comparison on the crash time where the modeling provides a clear indication of the direction and relative size of the dynamo product. Fig. 6.21 shows the poloidal and toroidal projections of the parallel dynamo fields predicted by both models during the sawtooth crash. For the $\langle \tilde{v_\phi} \tilde{b_r} \rangle$ measurements we measure a dynamo field of ~10 Volts/m in the $\hat{\theta}$ direction which corresponds to a parallel current drive, or dynamo term. The modeling predicts a field with a similar magnitude but in the opposite direction in the core region coincident with the $\langle \tilde{v_\phi} \tilde{b_r} \rangle$ measurement. The direction of the field in the core reflects the strong "anti-dynamo" term necessary to suppress the core parallel current. which is primarily in the $\hat{\phi}$ direction with a considerably smaller projection in the $-\hat{\theta}$ direction. Thus it may be that meausurement of $\langle \tilde{v_\theta} \tilde{b_r} \rangle$ in the core would yield a strongly "anti-dynamo" E_ϕ which produced a net $E_\|$ in the proper direction. This would indicate the existance of a substantial $\langle \tilde{\mathbf{v}} \times \tilde{\mathbf{b}} \rangle_\perp$ in the core which our modeling would not predict. Thus, with the present modeling the empirically estimated $\langle \tilde{\mathbf{v}} \times \tilde{\mathbf{b}} \rangle_\theta$ field is approximately the right size with the "wrong" sign. However, the total sign of $E_\|$ in the core is not determined. The small projected $\langle \tilde{v_\theta} \tilde{b_r} \rangle$ term is also directed to drive current, in the edge where the modeled field also drives current. Unfortunately, the projection of the estimated $\eta J_\| - E_\|$ in the $\hat{\phi}$ direction is very small in the edge region due to the poloidal pitch of the field lines. Thus we have a small measured field in agreement with a small projected field. Clearly, $\langle \tilde{v_\theta} \tilde{b_r} \rangle$ measurements in the core are indicated where the enormous "anti-dynamo" electric field is projected along with $\langle \tilde{v_\phi} \tilde{b_r} \rangle$ measurements in the edge to measure the clear "dynamo" electric field.

References

Cappello, S. and D. Biskamp (1996). Reconnection processes and scaling laws in Reversed Field Pinch MHD. *Nuclear Fusion* **36**(5), 571–581.

Spitzer, Jr., L. (1962). *Physics of Fully Ionized Gases*. New York: Interscience Publishers.

Stoneking, M. R., J. T. Chapman, D. J. Den Hartog, S. C. Prager, and J. S. Sarff (1997). Experimental scaling of fluctuations and confinement with Lundquist number in the RFP. *Phys. Plasmas* **5**(4), 1004–1014.

7

Summary and Conclusions

Developments in experimental technique

The results presented in this thesis were obtained via several key developments in measurement, analysis, and modeling techniques. The most important new experimental technique was the formal development of the Ion Dynamics Spectrometer to measure the dominant long wavelength velocity fluctuations in MST. This involved expressing the complete effect of averaging velocity over toroidal and polodal chords through radial mode dependent instrument functions. Application of these instrument functions allowed the fluctuation phase and amplitude measured by the spectrometer to be properly adjusted to reflect the local phase and amplitude of fluctuations in the plasma. The subsequent measurement and analysis of $\tilde{v}_\theta$ and $\tilde{v}_\phi$ demonstrated this capacity along with an impressive instrumental ability to resolve rapid and tiny shifts in the centroid of the measured C V emission profile.

The development of standardized sawtooth ensemble techniques enabled the resolution of the distinctive time and frequency characteristics of noisy velocity fluctuation signals. Novel aspects of this analysis include the incorporation of wavelet analysis and careful selection and screening of sawtooth events to create a tightly constrained ensemble. The former allowed for the identification of unique fluctuation features in frequency and time and for the observation of the time dependent velocity and magnetic fluctuation spectra and cross-spectra. The latter allowed for the careful and consistent description of narrow regimes in operational parameter space with minimal contamination from outlying events.

The analysis of the $\langle \tilde{v}_\phi \tilde{b}_{\theta,n} \rangle$ and $\langle \tilde{v}_\theta \tilde{b}_{\theta,n} \rangle$ products demonstrated the power of correlating "single-point" measurements with the dominant Fourier magnetic modes. These modes essentially provide the spatial Fourier basis functions in the reference frame of the plasma converted to a time varying signal in the lab frame. Through the time correlation of a signal with the individual modes we may effectively perform the spatial Fourier decomposition in the rotating reference frame of the plasma. In this study the correlation allowed us to determine the dominant toroidal wavenumbers of the chord-averaged $\tilde{v}_\theta$ and $\tilde{v}_\phi$ and to extract the phase of each wavenumber contribution relative to the magnetic modes.

Summary of experimental results

The measurement of a finite dynamo electric field in the core of the plasma constitutes the key experimental result of this thesis. Specifically, we found that the ensembled nonlinear product of $\langle \tilde{v}_\phi \tilde{b}_r \rangle$ yields a dynamo electric field which peaks during the sawtooth crash to approximately 10 Volts/m in the poloidal direction consistent with the generation of toroidal flux at $r/a \approx 0.3$–0.4. The $\langle \tilde{v}_\theta \tilde{b}_r \rangle$ produces a peak toroidal electric field of approximately 1 Volt/m which is aligned in the toroidal direction with the externally applied electric field at $r/a \approx 0.6$–0.7. Away from the crash both products yield

small but finite products in the same direction as the peak field but with one tenth the amplitude.

The measurement of ion velocity fluctuations of several km/s in the core and edge regions of the MST constitutes the second important contribution of this thesis. These fluctuations peak with the magnetic fluctuations during the crash and exhibit a comparatively small amplitude away from the crash. Fluctuation power averaged over the sawtooth cycle for $\tilde{v}_\theta$ and $\tilde{v}_\phi$ agrees with our expectation from MHD simulation with an amplitude of roughly 5% the Alfvén velocity. Analysis of the wavenumber spectra of the chord averaged $\tilde{v}_\theta$ and $\tilde{v}_\phi$ measurements indicates that the velocity fluctuation level from a particular mode drops off rapidly away from the rational surface of the mode. This contrasts with the magnetic fluctuations which extend over the full plasma radius. This effect is present but less pronounced in the MHD simulation which predict global magnetic modes extending over the full radius and velocity fluctuations for the dominant modes extend over roughly 70% of the plasma radius. Radial velocity fluctuations were somewhat smaller than the other two components and exhibited little coherence with the core magnetic modes. Thus, the measured contribution of $\tilde{v}_r$ to the total $\langle \tilde{\mathbf{v}} \times \tilde{\mathbf{b}} \rangle$ is small relative to the $\langle \tilde{v}_\phi \tilde{b}_r \rangle$ and $\langle \tilde{v}_\theta \tilde{b}_r \rangle$ terms.

Equilibrium modeling of the mean fields indicates that the rapid relaxation of the current profile during the sawtooth crash induces electric fields which dominate both the parallel electric field dissipated by $\eta J_{\|}$ and the toroidal electric field applied by the transformer. To balance Ohm's law these induced fields imply a dynamo term which opposes current in the core and drives current at the edge with a peak magnitude of 20–40 Volts/m. The sense of this implied dynamo term agrees with the conclusions of a static Ohm's law analysis while the magnitude is some ten times larger. The magnitudes inferred from the modeling agree with the dynamo fields observed in the experiment however the direction of the dynamo $E_{\theta,\|}$ predicted in the core contradicts the measured sign of the $\langle \tilde{v}_\phi \tilde{b}_r \rangle$ product.

Both velocity fluctuation and magnetic fluctuation levels scale little with Lundquist number. A weak scaling emerges when the fluctuations are averaged over the sawtooth scale due to the decreasing duty cycle of the fluctuations at high Lundquist regimes. However, the full non-linear dynamo product scales nearly as S^{-1} due to decreasing coherence of the measured fluctuations at high currents. The scaling of the measured dynamo products agrees with the a non-dimensional Ohm's law.

Concluding comments and suggestions for future work

While the current measurements provide clear evidence of dynamo activity in the core of MST, interpretation of the measured field direction is ambiguous. In the core where we expect strong "anti-dynamo" fields acting to suppress core *toroidal* current we measure a core *poloidal* component of the dynamo electric field directed to drive parallel current and generate toroidal flux. One explanation for this discrepancy would be a $\langle \tilde{v}_\theta \tilde{b}_r \rangle$ term in the core which produces a strong "anti-dynamo" toroidal electric field cancelling out the weak parallel projection of the measured "dynamo" E_θ. One might conjecture that if $\langle \tilde{v}_\phi \tilde{b}_r \rangle$ maintained the same sign over the full plasma radius, it would dominated near the edge where the magnetic field is primarily poloidal and the dynamo field should drive current and it would be dominated in the core by a possible "anti-dynamo", E_ϕ term.

Two measurements would clarify this important issue. First, $\langle \tilde{v}_\theta \tilde{b}_r \rangle$ should be measured near the core to confirm the presence of a large, unambiguosly "anti-dynamo" toroidal electric field. This should be combined with the measured $\langle \tilde{v}_\phi \tilde{b}_r \rangle$ term to estimate the total parallel field and confirm that it suppresses core current. This measurement could be carried out immediately, with current hardware and port access. Second, $\langle \tilde{v}_\phi \tilde{b}_r \rangle$ should be measured near the edge to confirm the presence of a large, unambiguously "dynamo" poloidal electric field. This measurement is currently underway with an optical probe extension to the IDS.

Future efforts should be directed toward constraining the numerical balance of parallel Ohm's law in MST. First, this involves improvements in modeling of the mean field terms to Ohm's law. Integration of new $J_{\|}(r)$ measurements with a toroidal equilibrium solver should provide greatly improved estimates of the mean field dynamics while improved measurements of $T_e(r)$ and $Z_{eff}(r)$ will provide better estimates of the plasma resistivity. We expect the improved modeling to agree with features of the modeling described in this thesis which stem from the general flattening of $\lambda(r)$. However, greater numerical accuracy is needed especially in the resolution of a mean-field Ohm's law imbalance (or balance) away from the sawtooth crash.

Second, numerical balance of parallel Ohm's law will involve continued measurements of $\langle \tilde{\mathbf{v}} \times \tilde{\mathbf{b}} \rangle$ in the plasma interior. In addition to the two measurements recommended above long-term pursuits include local $\langle \tilde{\mathbf{v}} \times \tilde{\mathbf{b}} \rangle$ measurements performed using active spectroscopy (CHERS) providing, in principle, for the local measurement of $\langle \tilde{\mathbf{v}} \times \tilde{\mathbf{b}} \rangle$ over the full plasma radius. Coordination of Langmuir probe measurements like those performed by Ji and novel edge $\tilde{\mathbf{v}}$ measurements with the IDS probe will further describe edge dynamo activity. While the measurements presented in this work confirm the presence of an MHD dynamo electric field, future efforts should complete the task of balancing Ohm's law balance over the interior of the reversed-field pinch.

A

Toroidal Calculation of Magnetic Boundary

The results obtained § 4.2.2 for the boundary conditions with a cylindrical analysis hold with only slight modifications in an analogous toroidal analysis. This primarily involves the retention of terms involving the poloidal derivative of b_θ and b_ϕ and neoclassical terms $\mathcal{O}(\frac{a}{R})$. Expanding the toroidal analog to Eq. 4.9 we have,

$$\begin{aligned}
\mu_0\, \tilde{j}_r(a,\theta) &= \nabla r \cdot \left(\nabla \times \tilde{\mathbf{b}}\right)_{r=a} \\
&= \nabla r \cdot \left(\nabla \tilde{b}_r \times \nabla r + \nabla(r\tilde{b}_\theta) \times \nabla\theta + \nabla(R\tilde{b}_\phi) \times \nabla\phi\right) \\
&= \left(\frac{\partial(R\tilde{b}_\phi)}{\partial\theta} - \frac{\partial(r\tilde{b}_\theta)}{\partial\phi}\right)(\nabla\theta \times \nabla\phi)\cdot\nabla r \\
&= i\,n\frac{b_\theta}{R}\, e^{i(m\theta+n\phi+\omega t+\delta_{b_\theta})} - i\,m\frac{b_\phi}{a}\, e^{i(m\theta+n\phi+\omega t+\delta_{b_\phi})} \\
&\quad + \frac{b_\phi}{a}\left(\frac{1}{b_\phi}\frac{\partial b_\phi}{\partial\theta} - \frac{a}{R}\sin(\theta)\right) e^{i(m\theta+n\phi-\omega t+\delta_{b_\phi})} \\
&= 0. \qquad \text{(A.1)}
\end{aligned}$$

The toroidal correction introduces a third term to the RHS of Eq. A.1 which is out of phase with the two cylindrical terms. This term introduces a small phase shift between $\tilde{b}_\theta$ and $\tilde{b}_\phi$ which we solve for obtaining,

$$\sin(\delta_{b_\theta} - \delta_{b_\phi}) = \frac{b_\phi R}{n b_\theta a}\left(\frac{a}{R}\sin(\theta) - \frac{1}{b_\phi}\frac{\partial b_\phi}{\partial\theta}\right), \qquad \text{(A.2)}$$

and,

$$\cos(\delta_{b_\theta} - \delta_{b_\phi}) = \frac{m b_\phi R}{n b_\theta a}. \qquad \text{(A.3)}$$

Here we explicitly see the toroidal correction on the RHS of Eq. A.2 introducing a non-zero phase shift between $\tilde{b}_\theta$ and $\tilde{b}_\phi$. The modification weakly effects the relative amplitudes of the two terms through the cosine in Eq. A.3. Next we expand the toroidal analog to Eq. 4.12 obtaining,

$$\begin{aligned}
\left(\nabla \cdot \tilde{\mathbf{b}}\right)_{r=a} &= \nabla\tilde{b}_r \cdot \nabla r + \nabla\tilde{b}_\theta \cdot \nabla\theta + \nabla\tilde{b}_\phi \cdot \nabla\phi \\
&= \frac{\partial\tilde{b}_r}{\partial r} + \frac{1}{a}\frac{\partial\tilde{b}_\theta}{\partial\theta} + \frac{1}{R}\frac{\partial\tilde{b}_\phi}{\partial\phi} \\
&= \frac{\partial b_r}{\partial r}\cos(m\theta+n\phi-\omega t+\delta_{b_r}) + \frac{1}{a}\frac{\partial b_\theta}{\partial\theta}\cos(m\theta+n\phi-\omega t+\delta_{b_\theta}) \\
&\quad -m\frac{b_\theta}{a}\sin(m\theta+n\phi+\omega t+\delta_{b_\theta}) - n\frac{b_\phi}{R}\sin(m\theta+n\phi+\omega t+\delta_{b_\phi}) \\
&= 0. \qquad \text{(A.4)}
\end{aligned}$$

Employing Eqs. A.2 and A.3 we may solve Eq. A.4 obtaining the expressions,

$$\frac{a}{b_\theta}\frac{\partial b_r}{\partial r}\sin(\delta_{b_\theta} - \delta_{b_r}) = m\left(1 + \frac{b_\phi^2}{b_\theta^2}\right) \qquad \text{(A.5)}$$

and,

$$\frac{a}{b_\theta}\frac{\partial b_r}{\partial r}\cos(\delta_{b_\theta} - \delta_{b_r}) = \frac{1}{b_\theta}\frac{\partial b_\theta}{\partial\theta} + \frac{b_\phi^2}{b_\theta^2}\left(\frac{a}{R}\sin(\theta) - \frac{1}{b_\phi}\frac{\partial b_\phi}{\partial\theta}\right). \qquad \text{(A.6)}$$

The toroidal correction on the RHS of Eq. A.6 again depends on the normalized poloidal derivatives of the fluctuations amplitudes which should be small. Setting this term to zero we recover the cylindrical results in Eqs. 4.13 and 4.14.

B

Computer Code Listings

This appendix contains a partial listing of the code employed for the calculations described in this thesis. Not included in this listing are a large number of supportine subroutines which may be found in the directory `[jchaman.idl]` or in the `[.subroutine]` subdirectory appropriate to the main routine. The sawtooth selection routines `sawlist.pro`, `sawtype.pro`, and `sawselect.pro` were also omitted as most of their large size governs a freindly user interface. In their place truncated sawtooth listings are included which demonstrate the creation of a sawtooth ensemble. Much of this code remains in widespread public use and will hopefully continue to evolve with the needs of its users.

B.1 IDS Data Processing

These routines govern the conversion of raw spectrometer data into impurity temperatures and velocities. A overview of these algorithms may be found in § 2.3.

B.1.1 IDS Fitting Engine

The noninteractive routine `fit.com` serves as the front end for the IDS fit engine. The user defines the variables in this file and submits the job to a VMS batch queue.

The batch routien then defines the necessary variables, compiles the subroutines, and calls the main IDS fit engine. These routines are described in § 2.3.

```
$ set def [jchapman.public.flow]
$ idl
;;;;=================================================================

;;;; FIT.COM
;;;; Ion Dynamics Spectrometer - Gaussian Fit Engine (Batch Startup File)

;;;; J. T. Chapman      University of Wisconsin - Madison   May 27, 1997

;;;;=================================================================

;;;------------------------------------------------------------------

;;; The variable SHOTLIST MUST BE DEFINED FOR FIT.PRO TO WORK.  The shotlist
;;; is an ascii file located in the users directory which contains the shot
;;; numbers, dates, starting times, and ending times for all the shots to be
;;; processed in the batch job.

;;; To make a shot list enter idlv2 and run the main level routine
;;; MAKELIST.PRO. This will prompt you for everything and write a properly
;;; formatted shot file to the directory you specify.

;;; If you desire to use your own routines to write a shot file it must be
;;; formatted as: format='(2x,i3,2x,a11,2x,i5,2x,i5)',shot,date,t1,t2.

;;; The last shot in the shotlist file must be 0.  This signals the routine
;;; that the shotlist has terminated.  The routine will pay attention to no
;;; shots listed beyond the shot labeled 0.

;;; Negative shot numbers signal fit.pro to calculate a new x_lam
;;; using the data from that shot.  If all shots are positive and x_lam is
;;; left undefined the first shot is used for the calibration.  If
;;; x_lam is already defined that value will be used unless a
;;; negative shot number is encountered.

    shotlist = "[myname.mydirectory]myshotlist.lsa"

;;;------------------------------------------------------------------

;;; The variable fit_freq sets the frequency of the signal input to the
;;; non-linear fit routine.  This should set above 10.0 only if you have
;;; some serious time on your hands or are running on something other than
```

```
;;; CHAOS.  Below 1.0 the routine time is dominated by MDS access time and
;;; further reductions do not save much time.  The routine defaults to a
;;; fit_freq=10.0 kHz if the variable is undefined.

    fit_freq = 10.0

;;;------------------------------------------------------------------

;;; This flag sets whether the fit engine plots moments of the fits as the
;;; shots are processed.  This flag should not be raised in
;;; batch mode (the plots have nowhere to go).  Plot fits defaults to 0.

    plot_fits=0

;;; Term type sets the terminal type for the plot routine to use.
;;; If undefined it defaults to a tektronics terminal.

    term_type='tek'

;;;------------------------------------------------------------------

;;; This flag indicates the orientation of the channels to port positions.
;;; The standard orientation (1-16)@138 and (17-32)@222 correspond to a
;;; port_pos=1, the opposite to port_pos=-1.  With these settings
;;; a positive flow corresponds to a flow in the direction of increasing
;;; toroidal angle (i.e. opposite the usual direction of core flow).

    port_pos=1

;;;------------------------------------------------------------------

;;; This variable corresponds to the voltage on the PMT's for the run.
;;; It defaults to 1100 V.  If set to a negative value the value is
;;; set per shot by reading the thumbwheel #316.

    pmt_voltage=1100

;;;------------------------------------------------------------------

;;; These variables contain all the necessary information about the impurity
;;; emmision.  If none of these are set the routine defaults to the settings
;;; for CV.  If just the lam_0 variable is set the routine will set the cor-
;;; responding order, m_ion, and imp_ion.  If a non-standard lam_0 is used
;;; all variables must be defined.

    lam_0 = 2270.9 & order = 5 & m_ion = 12.011 & imp_ion = "CV"
```

```
;   lam_0 = 2296.9 & order = 5 & m_ion = 12.011 & imp_ion = "CIII"
;   lam_0 = 2781.0 & order = 4 & m_ion = 15.999 & imp_ion = "OV"
;   lam_0 = 2821.7 & order = 4 & m_ion = 10.811 & imp_ion = "BIV"
;   lam_0 = 4861.3 & order = 3 & m_ion =  1.008 & imp_ion = "HI"
;   lam_0 = 3203.0 & order = 4 & m_ion =  4.003 & imp_ion = "HeII"
;   lam_0 = 4685.7 & order = 2 & m_ion =  4.003 & imp_ion = "HeII"

;;;------------------------------------------------------------------

;;; This variable is non-zero if the user employs only 16 channels of the
;;; IDS array.  NOTE: x_lam must be pre-calibrated and defined above to
;;; use this option.  The default is one_side=0.

    one_side = 0        ; Channels  1-32 (default)
;   one_side = 1        ; Channels  1-16
;   one_side = 2        ; Channels 17-32

;;;------------------------------------------------------------------

;;; Here I compile all necessary subroutines

.run [jchapman.idl]thinn
.run [jchapman.idl]vtt
.run [jchapman.idl]defined
.run [jchapman.public.flow.subroutines]chanmap
.run [jchapman.public.flow.subroutines]filecode
.run [jchapman.public.flow.subroutines]gausfit
.run [jchapman.public.flow.subroutines]fit_plot

;;; And now I startup the main routine
.run [jchapman.public.flow]fit
;;;;==============================================================
```

The Gaussian fit engine governs the conversion of raw IDS data into the moments of Gaussian profiles. This time consuming task should be submitted using `fit.com` to a queue for overnight processing.

```
;;;;==============================================================

;;;; FIT.PRO
;;;; Ion Dynamics Spectrometer - Gaussian Fit Engine

;;;; This routine is the primary engine for the conversion of raw
```

```
;;;; spectrometer data into profiles of Gaussian fit parameters.
;;;; The program reads data from an XDR file or an MDS data base
;;;; transparent to the engine.  The data is normalized and baselined
;;;; using current normalization parameters and fit using a standard
;;;; non-linear fit routine. The moments of the gaussian fits are then
;;;; written to XDR files on juno for dropping to the MDS data base.

;;;; Version 1.0 (WindowsNT version)
;;;; J. T. Chapman      University of Wisconsin - Madison   June 15, 1995

;;;; Version 2.0 (public and alpha versions non-interactive)
;;;; J. T. Chapman      University of Wisconsin - Madison   May 21, 1997

;;;;====================================================================

;;;--------------------------------------------------------------------

;;; Setup of routine for data fitting

    ;; greeting for log file

    print,format='(80("="))'
    print, " "
    print, " Ion Dynamics Spectrometer - Gaussian Fit Engine"
    print, " J. T. Chapman; University of Wisconsin - Madison; May 21, 1997"
    print, " "
    print,format='(80("-"))'


    ;; fit routine settings and parameters

    !quiet=1        ;...suppressing compile messages

                ;...sampling frequency
    if (not defined(fit_freq)) then fit_freq=10.0
    bin_size=fix(1000.0/fit_freq+0.5)

                ;...plotting parameters
    if (not defined(plot_fits)) then plot_fits=0
    if (not defined(term_type)) then term_type='tek'
    set_plot,term_type


    ;; shot file definition, check, and report

                ;...no shot file defined
```

```
    if (not defined(shotlist)) then begin
      print," ERROR: Shot file not defined."
      goto,EndRoutine
      endif
                ;...shot file not found
    shotlist=strupcase(shotlist)
    dummy=findfile(shotlist)
    dummy=dummy(0)
    if (strlen(strtrim(dummy,2)) eq 0) then begin
      print," ERROR: Shot file not found"
      goto,EndRoutine
      endif
    dummy=" "
                ;...opening shot file
    shotlist=strupcase(shotlist)
    openr,lun_shotlist,shotlist,/get_lun


    ;; permanent IDS calibrations

                ;...calibrated channel positions (5th order)
    openr,lun_centroid,"[jchapman.public.flow.calibration]CENTROID.DAT",$
      /get_lun
    x1=fltarr(16) & x2=fltarr(16)
    readf,lun_centroid,x1,x2
    x1=x1*5.0 & x2=x2*5.0
    free_lun,lun_centroid

    v_sat = 4094.9      ;...saturation of 12 bit digitizer

    t_lag=2.3716e-2     ;...time lag from linear phase (ms)

                ;...coupling of fiber optics to ports
    if (not defined(port_pos)) then port_pos=1

                ;...reporting settings for run
    print," "
    print,"  Processing "+shotlist+" @ "+strtrim(fix(fit_freq),2)+" kHz"
    print," "

;;;--------------------------------------------------------------------

;;; Main Processing Loop Initialization

    ;; Initializing shot and shot loop
```

```
            ;...initializing shot variables
shot=0 & date='today' & t1=0 & t2=0

            ;...reading in first shot
readf,lun_shotlist,format='(2x,i3,2x,a11,2x,i5,2x,i5)',shot,date,t1,t2

            ;...loop is terminated at shot=0
while (shot ne 0) do begin

            ;...setting up MDS data base for shot
  set_db,'mst$data'
  dummy=set_shot(abs(shot))
  dummy=set_date(date)
            ;...determining how to handle x_lam calibration
  if ((not defined(x_lam)) or (shot lt 0)) then $
    calculate_zero_point = 1 $
  else $
    calculate_zero_point = 0


;; IDS PMT normalization

            ;...IDS PMT voltage (default 1100 V)
  if (not defined(pmt_voltage)) then pmt_voltage=1100

            ;...get setting from thumbwheel if undefined
  if (pmt_voltage lt 0) then pmt_voltage=(-1)*thumbi(316)

            ;...set to nearest of 900,1000, or 1100 V
  pmt_voltage_1 = ((( long(abs(pmt_voltage)/100.+0.5)*100 )>900)<1100)

            ;opening appropriate file
  case pmt_voltage_1 of
     900: openr,lun_norm,$
            "[JCHAPMAN.PUBLIC.FLOW.CALIBRATION]NORM0900.DAT",/get_lun
    1000: openr,lun_norm,$
        "[JCHAPMAN.PUBLIC.FLOW.CALIBRATION]NORM1000.DAT",/get_lun
    1100: openr,lun_norm,$
        "[JCHAPMAN.PUBLIC.FLOW.CALIBRATION]NORM1100.DAT",/get_lun
    endcase

  norm = fltarr(32) ;...initialize normalization array

  readf,lun_norm,norm   ;...read in normalizations

  free_lun,lun_norm ;...close up normalization file
```

```
;; Obtaining the impurity emmission information

            ;...assume CV emmission if not defined
  if (not defined(lam_0)) then lam_0=2270.9

            ;...read in lam_0 from thumbwheels
  if (lam_0 lt 0) then lam_0=(-1)*thumbi(310)

            ;...obtaining ion information
  case (float(long(abs(lam_0)*10+0.5))/10.) of
    2270.9: begin & order = 5 & m_ion = 12.011 & imp_ion = "CV"   & end
    2296.9: begin & order = 5 & m_ion = 12.011 & imp_ion = "CIII" & end
    2781.0: begin & order = 4 & m_ion = 15.999 & imp_ion = "OV"   & end
    2821.7: begin & order = 4 & m_ion = 10.811 & imp_ion = "BIV"  & end
    4861.3: begin & order = 3 & m_ion =  1.008 & imp_ion = "HI"   & end
    3203.0: begin & order = 4 & m_ion =  4.003 & imp_ion = "HeII" & end
    4685.7: begin & order = 2 & m_ion =  4.003 & imp_ion = "HeII" & end

    else: if (not (defined(order)*defined(m_ion)) ) then begin
            print, "  ERROR: Unknown impurity wavelength."
        goto,JumpShot
        endif

    endcase

   if (not (defined(one_side))) then one_side=0

   if ((one_side ne 0) and calculate_zero_point) then begin
     print,"  ERROR: Unable to calibrate x_lam with only one side."
     stop
     endif

             ;...reporting shot settings
   if (calculate_zero_point) then $
     print,"  "+date+" #"+strtrim(abs(shot),2)+" ("+strtrim(t1,2)+"-"+$
     strtrim(t2,2)+"): "+imp_ion+" ("+strtrim(fix(lam_0+0.5),2)+$
     " A) X "+strtrim(order,2)+", PMT's @"+strtrim(pmt_voltage,2)+$
     " (x_lam calibrated)." $
   else $
     print,"  "+date+" #"+strtrim(abs(shot),2)+" ("+strtrim(t1,2)+"-"+$
     strtrim(t2,2)+"): "+imp_ion+" ("+strtrim(fix(lam_0+0.5),2)+$
     " A) X "+strtrim(order,2)+", PMT's @"+strtrim(pmt_voltage,2)+"."
```

```
  ;; Setting Boundaries and Sigmas for fit routine:

             ;...boundaries from reasonable physical values
    bound = $
    [[ 0.0,                                      $ ; fit0 > 0
      -(lam_0*1.0e+2)/2.998e+5+2.0,              $ ; velocity>-100 km/s
      0.0                                    ],  $ ; temperature > 0
     [(2^12)*1.5,                                $ ; fit0<1.5*(12 bits)
      (lam_0*1.0e+2)/2.998e+5+2.0,               $ ; velocity<100 km/s
      sqrt(3.0e3/(931.4812e+6*m_ion))*lam_0 ]]     ; temperature<3 keV

             ;...perturbation values of initial conditions
      sigma = [ 2^3,                                    $ ; three bits
               (lam_0*1.0e-1)/2.998e+5,                 $ ; 100 m/s
               sqrt(5e0/(931.4812e+6*m_ion))*lam_0,     $ ; 5 eV
       0,0 ]                    ; baseline stays

;;;-------------------------------------------------------------------

;;; Getting index start and stop time and time array

  ;; Time array from data base

             ;...reading array

    if (one_side le 1) then $
      timevf_full = data('a2_a14_vf1_tm')*1000. $
    else $
      timevf_full = data('a2_a14_vf3_tm')*1000.

             ;...check that it's there

    if (n_elements(timevf_full) le 2) then begin
      print," No IDS data found."
      goto, JumpShot
      endif

             ;...thinning to proper frequency
    timevf_full = thinn(timevf_full,bin_size)


  ;; Finding indices and truncating data

             ;...start and stop indices
    i_start = long( min( where( timevf_full ge t1 ) ) )
    i_stop  = long( max( where( timevf_full le t2 ) ) )
```

```
             ;...baseline subtraction indices
    i_base_1 = 1
    i_base_2 = long( max( where( timevf_full le -0.01 ) ) )

             ;...length of data arrays
    nn = i_stop - i_start + 1

             ;...truncate time array
    timevf = temporary( float( timevf_full( i_start : i_stop )) )

    timevf_full = 0    ;...clear old array

;;;-------------------------------------------------------------------

;;; Normalizing VFS shot data

    vf=fltarr(nn,32)  ;...2-D array of raw signal for all channels

    start_chan=1 & last_chan=32
    case one_side of
      1: last_chan=16
      2: start_chan=17
      else: start_chan=1
      endcase

    for  i=start_chan-1, last_chan-1 do begin

             ;...read data
      vftmp=data(chanmap(i+1))

             ;...skip channel if signal is missing
      if (n_elements(vftmp) le 2) then goto,JumpChan

             ;...find saturated points
      i_v=where(vftmp ge v_sat)

             ;...no saturation -> simple thinn
      if (max(i_v) lt 0) then vftmp = thinn(vftmp,bin_size) $

             ;...thinn data - excluding saturated points
      else begin
             ;... initialize boolean array
        vfbol=fltarr(n_elements(vftmp))+1.0

             ;...set saturate points to zero
```

```
         vfbol(i_v)=0.0 & vftmp(i_v)=0.0

               ;...thinn two arrays
             vftmp = thinn(vftmp,bin_size) & vfbol = thinn(vfbol,bin_size)

               ;...some non-saturated points -> normalize data
         if (max(vfbol) gt 0) then $
           vftmp(where(vfbol gt 0))=vftmp(where(vfbol gt 0))$
                                             /vfbol(where(vfbol gt 0))

               ;...some fully saturated points
         if (min(vfbol) eq 0) then vftmp(where(vfbol eq 0))=0.0

         vfbol=0       ;...clear boolean array

         endelse


    ;; Truncating, baselineing, and normalizing data

               ;...truncate raw data
       vf(*,i) = temporary(float(vftmp( i_start:i_stop )))

               ;...getting valid points
       vfbol = where(vf(*,i))

               ;...subtract off data baseline
       if (max(vfbol) ne -1) then $
         vf(vfbol,i) = temporary(vf(vfbol,i)-avg(vftmp(i_base_1:i_base_2)))

       vf(*,i) = vf(*,i)/norm(i)

           JumpChan:
       endfor

      vftmp=0       ;...clearing data array

;;;---------------------------------------------------------------------

;;; Non-linear Gaussian fit

    ;; Declaration Gaussian fit arrays

                ;...0th moment of fitted Gaussian @ 1{2}
          amp1 = fltarr(nn) & amp2 = fltarr(nn)
```

```
           ;...1st moment of fitted Gaussian @ 1{2}
     cnt1 = fltarr(nn) & cnt2 = fltarr(nn)

           ;...2nd moment of fitted Gaussian @ 1{2}
     vrn1 = fltarr(nn) & vrn2 = fltarr(nn)

           ;...baseline of Gaussian fit
     bas1 = fltarr(nn) & bas2 = fltarr(nn)

           ;...baseline slope of Gaussian fit
     slp1 = fltarr(nn) & slp2 = fltarr(nn)

           ;...Chi-square of non-linear fit @ 1{2}
     chi1 = fltarr(nn) & chi2 = fltarr(nn)

;; Comforting user feedback

;; Main fitting loop

  for j=0L,nn-1 do begin

    if (one_side ne 2) then begin

      y = vf(j,0:15)    ;...filling y array
      x = x1/order  ;...filling x array

            ;...valid points
      val = where(y ne 0.0)

            ;...little/no valid data -> Jump Point
      if (max(val) eq -1) then goto, JumpPoint1
      if (n_elements(val) le 12) then goto, JumpPoint1

      y=y(val) & x=x(val)   ;...getting rid of invalid points

            ;...intitial statistical guess
      a = [  max(y), $
             total(x*y)/total(y), $
             sqrt(total(y*(x-total(x*y)/total(y))^2)/total(y)), $
             (y(0)+y(n_elements(y)-1))/2.0, $
             0.0 ]

            ;...purging math error queue
      dummy = check_math(0,1)

            ;...curvefit routine for 1
```

```
   goodfit = gausfit(x, y, a, bound, sigma, chisqr)

          ;...filling moment arrays
   amp1(j) = a(0)*(2*goodfit-1)
   cnt1(j) = a(1)*(2*goodfit-1)
   vrn1(j) = a(2)*(2*goodfit-1)
   bas1(j) = a(3)*(2*goodfit-1)
   slp1(j) = a(4)*(2*goodfit-1)

          ;...updating chi2_1
   chi1(j) = sqrt(chisqr>0.0)

   endif

 JumpPoint1:

 if (one_side ne 1) then begin

   y = vf(j,16:31)    ;...filling y array
   x = x2/order  ;...filling x array

          ;...valid points
   val = where(y ne 0.0)

          ;...little/no valid data -> Jump Point
   if (max(val) eq -1) then goto, JumpPoint2
   if (n_elements(val) le 12) then goto, JumpPoint2

   y=y(val) & x=x(val)    ;...getting rid of invalid points

          ;...intitial statistical guess
   a = [  max(y), $
          total(x*y)/total(y), $
          sqrt(total(y*(x-total(x*y)/total(y))^2)/total(y)), $
          (y(0)+y(n_elements(y)-1))/2.0, $
          0.0 ]
          ;...purging math error queue
   dummy = check_math(0,1)

          ;...curvefit routine for 1
   goodfit = gausfit(x, y, a, bound, sigma, chisqr)

          ;...filling moment arrays
   amp2(j) = a(0)*(2*goodfit-1)
   cnt2(j) = a(1)*(2*goodfit-1)
   vrn2(j) = a(2)*(2*goodfit-1)
```

```
     bas2(j) = a(3)*(2*goodfit-1)
     slp2(j) = a(4)*(2*goodfit-1)

            ;...updating chi2_2
     chi2(j) = sqrt(chisqr>0.0)

     endif

   JumpPoint2:

   endfor      ;...end of fitting loop

 ;; Calculating zero point if necessary

  if (calculate_zero_point) then begin

             ;...points which were well fit and 10-20 ms
    val = where( (timevf gt 10.) and (timevf lt 20.) )

             ;...calculate average mean position
 if (max(val) ne -1) then begin
     x_lam = avg(cnt1(val)+cnt2(val))/2.0
     calculate_zero_point=0
  endif

    endif

;;;------------------------------------------------------------------

;;; Output of results

     nw=put_data('V.VFS_LAM_0',lam_0,'Angstrom')
     nw=put_data('V.VFS_PORT_POS',port_pos,'au')
     nw=put_data('V.VFS_X_LAM',x_lam,'Angstrom')
     nw=put_data('V.VFS_M_ION',m_ion,'amu')
     nw=put_data('V.VFS_TIME',timevf,'ms')

     if ( port_pos eq 1 ) then begin
       if (one_side ne 2) then begin
         nw=put_data('V.VFS_138_FIT0',amp1,'Volts')
         nw=put_data('V.VFS_138_FIT1',cnt1,'Angstrom')
         nw=put_data('V.VFS_138_FIT2',vrn1,'Angstrom')
         nw=put_data('V.VFS_138_CHI2',chi1,'Volts')
         endif
       if (one_side ne 1) then begin
         nw=put_data('V.VFS_222_FIT0',amp2,'Volts')
```

```
          nw=put_data('V.VFS_222_FIT1',cnt2,'Angstrom')
          nw=put_data('V.VFS_222_FIT2',vrn2,'Angstrom')
          nw=put_data('V.VFS_222_CHI2',chi2,'Volts')
          endif
        endif $
      else begin
        if (one_side ne 1) then begin
          nw=put_data('V.VFS_138_FIT0',amp2,'Volts')
          nw=put_data('V.VFS_138_FIT1',cnt2,'Angstrom')
          nw=put_data('V.VFS_138_FIT2',vrn2,'Angstrom')
          nw=put_data('V.VFS_138_CHI2',chi2,'Volts')
          endif
        if (one_side ne 2) then begin
          nw=put_data('V.VFS_222_FIT0',amp1,'Volts')
          nw=put_data('V.VFS_222_FIT1',cnt1,'Angstrom')
          nw=put_data('V.VFS_222_FIT2',vrn1,'Angstrom')
          nw=put_data('V.VFS_222_CHI2',chi1,'Volts')
          endif
        endelse


    ;; Default plotting routines

    if plot_fits then begin     ;...plotting data?

      if ( port_pos eq 1 ) then $
        fit_plot,abs(shot),date,x_lam,timevf,amp1,amp2,cnt1,cnt2,vrn1,vrn2 $
      else $
        fit_plot,abs(shot),date,x_lam,timevf,amp2,amp1,cnt2,cnt1,vrn2,vrn1

      vtt
      endif
;;;--------------------------------------------------------------------

;;; Wrap of loops and routine

    ;; End of processing loop

    JumpShot:       ;...Jump shot label

                ;...readin next shot
    readf,lun_shotlist,format='(2x,i3,2x,a11,2x,i5,2x,i5)',shot,date,t1,t2

    endwhile        ;...end of shot loop
```

```
    ;; End of routine

    free_lun,lun_shotlist
                ;...saying goodbye
    print," "
    print,format='(80("-"))'
    print," "
        print," Goodbye."
    print," "
    print,format='(80("="))'

    EndRoutine:     ;...end of program
    end

;;;;=====================================================================
```

B.1.2 Nonlinear Fit Routine

The function gausfit has been substantially modified from the IDL `curvefit.pro` routine to optimize its performance for the fit of IDS data. This routine is called by the fitting engine and actually performs the nonlinear convergence of the Gaussian model to the data.

```
function gausfit, x, y, a, bound, sigma, chisqr

;===========================================================================
; Header
;===========================================================================

; NAME:
;       GAUSFIT

; PURPOSE:
;       Non-linear least squares fit to a gaussian.  Using Marquadt method.

; CALLING SEQUENCE:
;       valid = GAUSFIT(X, Y, A, BOUND, SIGMA, CHISQR)

; INPUTS:
;       X:  A row vector of independent variables.
```

```
;       Y:  A row vector of dependent variable, the same length as x.

;       A:  A vector, with as many elements as the number of terms, that
;           contains the initial estimate for each parameter.  If A is
;           double precision, calculations are performed in double
;           precision otherwise they are performed in single precision.

;   BOUND:  A two-dimensional vector, containing the upper lower bounds on
;           the parameters passed in A.  If A falls outside these bounds the
;           fit is attempted again with perturbed initial conditions.

;   SIGMA:  Uncertainty acquainted with each parameter.  If the fit diverges
;           the initial conditions will be randomly perturbed by an amount
;           proportional to sigma.

; OUTPUTS:
;       Returns boolean (0,1) of whether fit was valid

;       A:  A vector of parameters containing fit.

;   SIGMA:  Uncertainty acquainted with the output parameters.

;  CHISQR:  The value of chi-squared on exit

; PROCEDURE:
;       Modified from "CURFIT", least squares fit to a non-linear
;       function, pages 237-239, Bevington, Data Reduction and Error
;       Analysis for the Physical Sciences.

;       "This method is the Gradient-expansion algorithm which
;       combines the best features of the gradient search with
;       the method of linearizing the fitting function."

;       Iterations are performed until the chi square changes by
;       only TOL or until ITMAX iterations have been performed.

;       The initial guess of the parameter values should be
;       as close to the actual values as possible or the solution
;       may not converge.


;=======================================================================
;  Initialize Variables
;=======================================================================

   FALSE = 0.                            ; Booleans defined
```

```
   TRUE  = 1.

   on_error,2                            ; return to caller if error

   count_flambda_max = 10                ; number of flambda jumps
   count_pert_max    = 3             ; number of IC perturbations
   count_iter_max    = 10                ; maximum number of iterations

   tol = 1.0e-2                          ; convergence tolerance

   valid     = TRUE                      ; valid initialized to true
   converged = FALSE                     ; converged is initially false

   nterms  = 5                           ; # of parameters
   npoints = n_elements(y)               ; # of data points in fit
   nfree   = npoints-nterms              ; degrees of freedom

   a_old   = a                           ; saving passed a

   diag = lindgen(nterms)*(nterms+1)    ; subscripts of diagonal elements

;=======================================================================
;  Convergence Iteration
;=======================================================================

;  gaussian procedure calculates partial derivatives
   z     = (x-a(1))/a(2) & z2=z^2
   base  = a(3)+a(4)*x
   yfit  = a(0)*EXP(-z2/2.0)
   pder  = [[yfit/a(0)],[yfit*z/a(2)],[yfit*z2/a(2)],$
            [1+fltarr(npoints)],[x]]
   yfit  = yfit + base

   chisq0 = total((y-yfit)^2)/nfree
   yfit0 = yfit

   count_pert=0
   while ( valid and (not converged) ) do begin
     count_pert=count_pert+1

     flambda = 0.001                     ; reset lambda

     count_iter=0
     while ( valid and (not converged) ) do begin
       count_iter=count_iter+1
```

```
;      evaluate alpha and beta matricies.
        beta   = (y-yfit) # pder
        alpha  = transpose(pder) # pder

;      present chi squared
        chisq1 = total((y-yfit)^2)/nfree

;      invert modified curvature matrix to find new parameters.
        count_flambda=0
        repeat begin
          count_flambda=count_flambda+1

;        find new parameters
          alpha_prime = alpha
          alpha_prime(diag) = alpha_prime(diag)*(1+flambda)
          epsilon = invert(alpha_prime)
          b = a + (epsilon # transpose(beta))

;        calculate new fit
          z    = (x-b(1))/b(2) & z2=z^2
          base  = b(3)+b(4)*x
          yfit = b(0)*EXP(-z2/2.0)
          pder = [[yfit/b(0)],[yfit*z/b(2)],[yfit*z2/b(2)],$
                  [1+fltarr(npoints)],[x]]
          yfit  = yfit + base

          chisqr = total((y-yfit)^2)/nfree ; calculate new chisqr

          flambda = flambda*10.            ; assume fit got worse

;        has the flambda max count been exceeded
          if (count_flambda gt count_flambda_max) then valid=FALSE

          endrep until ((not valid)        or $
                        (chisqr lt chisq1))

       flambda=flambda/100.               ; decreasing flambda by 100/10

; check to see if fit is diverging
       if ( min(b gt bound(*,0)) eq FALSE ) then valid=FALSE
       if ( min(b lt bound(*,1)) eq FALSE ) then valid=FALSE
; check max counts on flambda
       if ( count_iter gt count_iter_max ) then valid=FALSE

; define convergence
       converged = float(abs((chisq1-chisqr)/chisqr) le tol)
```

```
; save new value of a
        a=b

        endwhile

      a=a_old*(1.+sigma*randomn(seed,nterms))  ; perturb initial conditions

      valid=TRUE                               ; try again

      if ( count_pert gt count_pert_max ) then valid=FALSE

      endwhile                                 ; end of perturbation loop
;
    if valid then begin
      a=b                                      ; save fit parameter
      y=yfit                                   ; save fit function
      endif $
    else begin
      a=a_old
      y=yfit0
      chisqr=chisq0
      endelse
;
    return, valid                              ; return valid
;
end
```

B.1.3 Flow and Temperature Calculation

This procedure was written do convert the fitted Gaussian moments to ion flows and temperatures. The theory behind the conversion may be found in §2.3.

```
pro flow,shot,date,t1,t2,t,x,name,units,pmt_voltage=pmt_voltage

; ...setting up mds data base
    set_db,'mst$data'
    dummy=set_shot(shot)
    dummy=set_date(date)

; ...reading in time record for velocity
    tv=data('vfs_time')-3.64e-3
    if (n_elements(tv) le 1) then goto,SkipShot
```

```
;                ...frequency of returned signal
    f_sig=(n_elements(tv)-1)/(max(tv)-min(tv))
    nn=(t2-t1)*f_sig+1
    t=findgen(nn)/f_sig+t1

; ...reading in data records (discarding moment analysis)
    fit1_222=data('vfs_222_fit1')>0.0
    if (n_elements(fit1_222) le 1) then goto,SkipShot
    fit1_138=data('vfs_138_fit1')>0.0
    if (n_elements(fit1_138) le 1) then goto,SkipShot
    fit2_222=data('vfs_222_fit2')>0.0
    if (n_elements(fit2_222) le 1) then goto,SkipShot
    fit2_138=data('vfs_138_fit2')>0.0
    if (n_elements(fit2_138) le 1) then goto,SkipShot

; ...reading in physical and calibrated parameters
    lam_0=max(data('vfs_lam_0'))
    x_lam=max(data('vfs_x_lam'))
    m_ion=max(data('vfs_m_ion'))
    port_pos=max(data('vfs_port_pos'))
    if ((lam_0 le 0) or (x_lam le 0) or (m_ion eq 0) ) then goto,SkipShot

; ...velocity calculated using previously calibrated x_lam
    vel_222=2.998e+5/lam_0*(x_lam-fit1_222)
    vel_138=-2.998e+5/lam_0*(x_lam-fit1_138)

    if (not defined(pmt_voltage)) then pmt_voltage=1000
    pmt_voltage=((fix((pmt_voltage/100.)+0.5)*100)>900)<1100
    case pmt_voltage of
      900:  begin
    pc_138=[-5.914637e-02,1.24626,-0.441226,0.227436]
            pc_222=[-4.288862e-02,1.06984,-0.126103,0.048504]
    end
      1000: begin
    pc_138=[-6.151874e-02,1.27186,-0.510214,0.304937]
    pc_222=[-4.372543e-02,1.08512,-0.159691,0.066536]
    end
      1100: begin
    pc_138=[-5.855970e-02,1.20948,-0.322845,0.137230]
    pc_222=[-4.946594e-02,1.15009,-0.280715,0.144492]
    end
      endcase

    if (port_pos eq -1) then begin
      dummy=pc_138
```

```
      pc_138=pc_222
      pc_222=dummy
      dummy=0
      endif

    fit2_222_cor=0.0
    fit2_138_cor=0.0

    for i_pol=0,3 do fit2_222_cor=fit2_222_cor+pc_222(i_pol)*fit2_222^i_pol
    for i_pol=0,3 do fit2_138_cor=fit2_138_cor+pc_138(i_pol)*fit2_138^i_pol

;         ...T=m*c^2*A2^2/lam_0^2, cons=(c in m/s)^2*(kg/amu)*(eV/Joule)
    tmp_138=(931.4812d+6)*(m_ion)*(fit2_138_cor^2)/lam_0^2
    tmp_222=(931.4812d+6)*(m_ion)*(fit2_222_cor^2)/lam_0^2

; ...invalid points are set to zero
    if (max(where(fit1_222 eq 0)) ge 0) then $
      vel_222(where(fit1_222 eq 0)) = 0
    if (max(where(fit1_138 eq 0)) ge 0) then $
      vel_138(where(fit1_138 eq 0)) = 0

; ...velocities greater than 500 km/s set to zero
    if (max(where(abs(vel_222) ge 500)) ge 0) then $
      vel_222(where(abs(vel_222) ge 500)) = 0
    if (max(where(abs(vel_138) ge 500)) ge 0) then $
      vel_138(where(abs(vel_138) ge 500)) = 0

;                ...temperatures greater than 5 keV set to zero
    if (max(where(abs(tmp_138) ge 5000)) ge 0) then $
      tmp_138(where(abs(tmp_138) ge 5000)) = 0
    if (max(where(abs(tmp_222) ge 5000)) ge 0) then $
      tmp_222(where(abs(tmp_222) ge 5000)) = 0

; ...boundaries of velocity signal
    n1v=max(where(min(abs(t1-tv)) eq abs(t1-tv)))
    n2v=n1v+nn-1

;          ...skipping shot if too many points are missing
    bad_pnt=n_elements(where(vel_222(n1v:n2v) eq 0))
    if ((bad_pnt/float(nn)) ge 0.9) then goto,SkipShot

; ...filling in missing points in velocity and temperature array
    if (bad_pnt gt 1) then begin
      vs=vel_222
      for i=0,19 do begin
        vs=smooth(vs,10)
```

```
      vs(where(vel_222 ne 0.0))=vel_222(where(vel_222 ne 0.0))
      endfor
    vel_222(where(vel_222 eq 0.0))=vs(where(vel_222 eq 0.0))
    vs=0
    endif

;         ...skipping shot if too many points are missing
  bad_pnt=n_elements(where(vel_138(n1v:n2v) eq 0))
  if ((bad_pnt/float(nn)) ge 0.9) then goto,SkipShot

; ...filling in missing points in velocity and temperature array
  if (bad_pnt gt 1) then begin
    vs=vel_138
    for i=0,19 do begin
      vs=smooth(vs,10)
      vs(where(vel_138 ne 0.0))=vel_138(where(vel_138 ne 0.0))
      endfor
    vel_138(where(vel_138 eq 0.0))=vs(where(vel_138 eq 0.0))
    vs=0
    endif

;         ...skipping shot if too many points are missing
  bad_pnt=n_elements(where(tmp_222(n1v:n2v) eq 0))
  if ((bad_pnt/float(nn)) ge 0.9) then goto,SkipShot

; ...filling in missing points in velocity and temperature array
  if (bad_pnt gt 1) then begin
    ts=tmp_222
    for i=0,19 do begin
      ts=smooth(ts,10)
      ts(where(tmp_222 ne 0.0))=tmp_222(where(tmp_222 ne 0.0))
      endfor
    tmp_222(where(tmp_222 eq 0.0))=ts(where(tmp_222 eq 0.0))
    ts=0
    endif

;         ...skipping shot if too many points are missing
  bad_pnt=n_elements(where(tmp_138(n1v:n2v) eq 0))
  if ((bad_pnt/float(nn)) ge 0.9) then goto,SkipShot

; ...filling in missing points in velocity and temperature array
  if (bad_pnt gt 1) then begin
    ts=tmp_138
    for i=0,19 do begin
      ts=smooth(ts,10)
      ts(where(tmp_138 ne 0.0))=tmp_138(where(tmp_138 ne 0.0))
```

```
      endfor
    tmp_138(where(tmp_138 eq 0.0))=ts(where(tmp_138 eq 0.0))
    ts=0
    endif

  x=fltarr(nn,4)

  x(*,0)=vel_222(n1v:n2v)
  x(*,1)=vel_138(n1v:n2v)
  x(*,2)=tmp_222(n1v:n2v)
  x(*,3)=tmp_138(n1v:n2v)

  t=tv(n1v:n2v)

  name=["Ion Velocity @222   ",$
        "Ion Velocity @138   ",$
        "Ion Temperature @222",$
        "Ion Temperature @138"]
  units=["km/s","km/s","eV","eV"]

  return

  SkipShot:
  t=-1 & x=-1
  return

  end
```

B.2 Calculation of IDS Instrument Function

We employed these routines to calculate numerically the mode-dependent spatial instrument functions for the IDS. A complete discussion of the theory underlying these calculations may be found in § 2.5. This routine calculates the toroidal chord instrument function for the up-down configuration. The instrument function is calculated for the relavant toroidal and poloidal mode numbers.

```
;==================================================================

; CHORD_WEIGHT.PRO

; J. Chapman University of Wisconsin - Madison October, 23 1997
```

```
;======================================================================

; Setting run parameters

r_maj = 1.50 ;...major machine radius
r_min = 0.52 ;...minor machine radius

asp = r_maj/r_min ;...aspect ratio

qa = 161 *!pi/180. ;...poloidal angle of ports

p1 = 138 *!pi/180. ;...starting toroidal angle
p2 = 222 *!pi/180. ;...ending toroidal angle

p0 = (p2+p1)/2 ;...mid toroidal angle
pa = (p2-p1)/2 ;...max toroidal angle

; Caculating line of sight path coordinates

wa = (asp-cos(qa)) ;...major radius at port

y = cos(pa)*wa
z = sin(qa)

xa = sqrt(wa^2-y^2) ;...x at the port

nw=128
w=(findgen(nw)+0.5)/nw*(wa-y)+y
dw=(max(w)-min(w))/(nw-1)

x = sqrt(w^2-y^2)
dldw=w/x

r = sqrt(z^2+(sqrt(x^2+y^2)-asp)^2)
p = atan(x,y)
q = atan(z,asp-sqrt(x^2+y^2))

; Calculating 1-D dot-product of velocity field with the IDS line of sight

dot_r = -sin(p)*cos(q) ;...radial component of line of sight
dot_q = -sin(p)*sin(q) ;...poloidal component of line of sight
dot_p = cos(p) ;...toroidal component of line of sight

; Calculating weighting for different m=1 toroidal mode numbers
```

```
n_modes = 12
modes = fltarr(n_modes,2)
modes=[[ 0, 0, 1, 1, 1, 1, 1, 1, 1, 1, 1, 1],$
       [ 0, 1, 5, 6, 7, 8, 9,10,11,12,13,14]]

weight_t=fltarr(nw,n_modes,3)

yr=[[ 0, 0,-1,-1,-1,-1,-1,-1,-1,-1,-1,-1],$
    [ 8, 8, 1, 1, 1, 1, 1, 1, 1, 1, 1, 1]]
for i_m=0,n_modes-1 do begin

  weight_t(*,i_m,0) = $
   cos(modes(i_m,1)*p)*cos(modes(i_m,0)*q)*cos(p)       $
                      *dldw*r/(w-asp)*r_min/xa
  weight_t(*,i_m,1) = $
   sin(modes(i_m,1)*p)*sin(modes(i_m,0)*q)*sin(p)*sin(q)$
                      *dldw*r/(w-asp)*r_min/xa
  weight_t(*,i_m,2) = $
  -sin(modes(i_m,1)*p)*cos(modes(i_m,0)*q)*sin(p)*cos(q)$
                      *dldw*r/(w-asp)*r_min/xa

  endfor

; Calculating the components relative to equillibrium B

restore,'b'
i_b=i_min(abs(t_b+0.05))

bp_i=interpolate(bp(*,i_b),r*(n_elements(r_b)-1))
bz_i=interpolate(bz(*,i_b),r*(n_elements(r_b)-1))
b_i=sqrt(bp_i^2+bz_i^2)

weight_t_b=weight_t

for i_m=0,n_modes-1 do begin

  weight_t_b(*,i_m,0) = ( bz_i*weight_t(*,i_m,0) $
                        + bp_i*weight_t(*,i_m,1) )/b_i
  weight_t_b(*,i_m,1) = ( bz_i*weight_t(*,i_m,1) $
                        - bp_i*weight_t(*,i_m,0) )/b_i
  endfor

; Plotting weights

if (not defined(plot_stuff)) then plot_stuff=1
if (plot_stuff) then begin
```

```
for i_m=0,n_modes-1 do begin

  plot,r,weight_t(*,i_m,0),$
    yr=[-0.5,1>max(weight_t(*,i_m,*))],$
    xtitle='(R-R!d0!n)/a @ z=0.32',ytitle='w!dg!n',$
    title='m='+strtrim(modes(i_m,0),2)+',n='+strtrim(modes(i_m,1),2)
  oplot,r,weight_t(*,i_m,1),line=1
  oplot,r,weight_t(*,i_m,2),line=3

  plot,r,weight_t_b(*,i_m,0),$
    yr=[-0.5,1>max(weight_t_b(*,i_m,*))],$
    xtitle='(R-R!d0!n)/a @ z/a=0.32',ytitle='w!dB!n',$
    title='m='+strtrim(modes(i_m,0),2)+',n='+strtrim(modes(i_m,1),2)
  oplot,r,weight_t_b(*,i_m,1),line=1
  oplot,r,weight_t_b(*,i_m,2),line=3

   endfor
 endif
vtt
stop
restore,file_v_t

r_vt_i=abs(w)*n_elements(r_vt)/(max(r_vt)-min(r_vt))
vt_i=fltarr(nw,n_modes,3)
for i_m=0,n_modes-1 do begin
  vt_i(*,i_m,0)=interpolate(vt,r_vt_i,0)
  vt_i(*,i_m,1)=interpolate(vt,r_vt_i,1)
  vt_i(*,i_m,2)=interpolate(vt,r_vt_i,2)
  endfor

plot,w-asp,weight_t(*,i_m,0),yr=transpose(yr(i_m,*)),$
  xtitle="(R-R!dmaj!n)/R!dmin!n",ytitle="w!d!4p!x!n",$
  title="IDS Instrument Function: m="+strtrim(modes(i_m,0),2)+", n="+$
    strtrim(modes(i_m,1),2)
hline,0 & vline,0 & vline,y-asp & hline,1 & vline,wa-asp

vtt

end
```

B.3 Sawtooth Listings

This section includes partial sawtooth listings generated by the code described in §3.2. The listings below were taken from the low current sawtooth ensemble described

in this thesis.

B.3.1 Shot List

Shotlists are stored in `*.lsa` files which contain the shot number and date and the bounding times for the signals of interest. These files are used for the sawtooth ensemble creation routines, IDS fitting routines, and magnetic mode analysis routines. The files must be formatted using the FORTRAN format string,

`format='(i5,2x,a11,2x,i5,2x,i5)',shot,date,t1,t2,`

to be properly handled by the processing engines. The sawtooth ensemble code or the standalone routine `[jchapman.public.flow]makeshotlist.pro` accomplishes this formatting automatically. A few lines from a sample `*.lsa` are shown below.

```
   43  10-apr-1997      5      40
   44  10-apr-1997      5      40
```

(shots omitted)

```
  136  11-apr-1997      5      40
  138  11-apr-1997      5      40
    0  00-000-0000      0       0
```

B.3.2 Sawtooth List

A sawtooth ensemble listing created by `[jchapman.public.st_corr]sawlist.pro]` contains the shot information plus the individual times of sawteeth included in the ensmble. The final number on the shotlist line denotes the number of sawteeth in the ensemble. If sawteeth are added or deleted manually from the list this number must be adjusted or an error will occur. An identical listing with times not referenced to sawteeth may be produced with `[jchapman.public.st_corr]triglist.pro]`. §3.2 provides an overview of the sawtooth ensemble creation routines. Portions of the `*.lsb` list made from the `*.lsa` list above are shown below.

```
Sawtooth Ensemble Listing - Created Fri Apr 11 19:21:29 1997

 43  10-APR-1997     5    40    3
 2.73600e+01  1
 3.12000e+01  1
 2.01900e+01  1
```

(shots omitted)

```
138  11-APR-1997     5    40    7
 3.27600e+01  1
 2.99500e+01  1
 2.67300e+01  1
 2.35100e+01  1
 1.96800e+01  1
 1.60600e+01  1
 3.71200e+01  1

  0  00-000-0000     0     0    0
<eof>
```

B.3.3 Typed Sawtooth List

The typed sawtooth ensemble listing is a data base containing the times of the sawteeth in the ensemble and the value of equillibrium quantities averaged near the sawtooth. The header to this file contains the signals, chosen by the user, which are used to characterize each sawtooth. Each header line includes the name of the MDS signal or the user defined routine which returns the signal, a description of the signal, the signal units, and the time window relative to the sawtooth overwhich the signal was averaged. The signals shown below were used to characterize the ensembles used for the dynamo measurement. Following the header is the data itself which builds on the structure of the `*.lsb` files. Following each sawtooth time a record for each characterizing signal contains the signal's average, standard deviation, and number of samples over the chosen window. A small segment of a sample `*.lsc` file is shown below.

```
Sawtooth Ensemble Typed Listing - Created Fri Jun 13 14:40:11 1997

 9 records:
 1  IP - Plasma Current (kAmp) from  -1.50 ms to  -0.50 ms
 2  F - Reversal Parameter - before () from  -1.50 ms to  -0.50 ms
 3  F - Reversal Parameter - after () from   0.50 ms to   1.50 ms
 4  THETA - Pinch Parameter () from  -1.50 ms to  -0.50 ms
 5  N_CO2 - Electron Density (cm!E-3!N) from  -1.50 ms to  -0.50 ms
 6  VTG - Peak Toroidal Gap Voltage (Volts) from  -0.10 ms to   0.10 ms
 7  TYP_N6FRQ - n=6 Mode Frequency - after (kHz) from  -1.50 ms to  -0.50 ms
 8  TYP_N6FRQ - n=6 Mode Frequency - before (kHz) from  0.50 ms to   1.50 ms
 9  TYP_NIR - NIR Brem Signal (au) from  -1.50 ms to  -0.50 ms

 43  10-APR-1997     5    40    3
 2.73600e+01
 2.04800e+02   3.14168e-01     100  ip
-1.95394e-01   5.42845e-03     100  f
-1.74221e-01   8.15741e-03     100  f
 1.73506e+00   1.27681e-02     100  theta
 7.03831e+12   1.32551e+11     101  n_co2
 1.09182e+01   4.07957e+00      21  vtg
-1.43148e+01   5.99134e+00     100  typ_n6frq
-1.03096e+01   3.07751e+00     100  typ_n6frq
 1.16790e-01   1.70191e-02     201  typ_nir
 3.12000e+01
```

(records omitted)

```
 2.01900e+01
```

(records omitted)

(shots omitted)

```
   0  00-000-0000     0     0    0
<eof>
```

B.3.4 Bounding File

The sawtooth bouding file (`*.bnd`) is created by `sawselect.pro` from the typed sawtooth file (`*.lsc`). This short file contains the user defined bounds for each of the typed signals plus the bounds for the sawtooth crash time. The bounds below were chosen for the low current sawtooth ensemble.

```
Sawtooth Ensemble Bound File created on Mon Jun 16 13:13:24 1997
Sawtooth Ensemble Typed Listing - Created Fri Jun 13 14:40:11 1997

      10

time of sawtooth crash (ms)
 1.00000e+01   3.50000e+01
IP - Plasma Current (kAmp) from  -1.50 ms to  -0.50 ms
 1.90000e+02   2.20000e+02
F - Reversal Parameter - before () from  -1.50 ms to  -0.50 ms
-2.20000e-01  -1.90000e-01
F - Reversal Parameter - after () from   0.50 ms to   1.50 ms
-1.90000e-01  -1.60000e-01
THETA - Pinch Parameter () from  -1.50 ms to  -0.50 ms
 1.71000e+00   1.77000e+00
N_CO2 - Electron Density (cm!E-3!N) from  -1.50 ms to  -0.50 ms
 6.50000e+12   8.00000e+12
VTG - Peak Toroidal Gap Voltage (Volts) from  -0.10 ms to   0.10 ms
 5.00000e+00   3.00000e+01
TYP_N6FRQ - n=6 Mode Frequency - after (kHz) from  -1.50 ms to  -0.50 ms
-2.50000e+01  -1.30000e+01
TYP_N6FRQ - n=6 Mode Frequency - before (kHz) from   0.50 ms to   1.50 ms
-2.00000e+01  -8.00000e+00
TYP_NIR - NIR Brem Signal (au) from  -1.50 ms to  -0.50 ms
 7.00000e-02   1.70000e-01
```

B.4 Sawtooth Ensemble Analysis

B.4.1 Signal Routine

This signal routine was designed to be called by the sawtooth correlation routines. The procedure returns fluctuating velocity signals and five toroidal magnetic modes. The format of the passed values must be adhered to for all user defined signal routines.

```
;;;;=================================================================

pro SIG_VXB,shot,date,t1,t2,t,x,s,name,units,tlag

;;;;-----------------------------------------------------------------

;;;; This signal routine is employed in the correlation of velocity fluct-
;;;; uations with the magnetic array.  The signals are high-pass filtered
```

```
;;;; to reduce contamination of secular components into the signal.  No
;;;; noise filtering was employed for fear of losing fast fluctuation power.
;;;; The data is correlated with the cosine amplitude of the n=5-9 modes

;;;; J. T. Chapman University of Wisconsin - Madison July 14, 1996

;;;;=================================================================

;;;-----------------------------------------------------------------

;;; Preliminary setup of data base and data arrays

 ;; setting up mds data base

set_db,'mst$data'
dummy=set_shot(shot)
dummy=set_date(date)

 ;; initializing time and frequency arrays

fsig=100.0 ;...output signal frequency
nn=fix((t2-t1)*fsig+1.5) ;...length of ouput array
t=findgen(nn)/fsig+t1 ;...time axis for output array

nf=(nn/256+1)*256 ;...length of buffered frequency axis
f=findgen(nf)*fsig/nf ;...frequency axis
f(nf/2+1:nf-1)=reverse(f(1:nf/2-1))

 ;; setting up filter cuttoffs

cut_noise=45.0 ;...noise above 45 kHz
cut_secular=3.0 ;...secular change below 3kHz

s_n=where(f ge cut_noise) ;...subscripts of noise spectrum
s_s=where(f le cut_secular) ;...subscripts of secular specturum

 ;; initializing data arrays

mag_modes=[10,11,12,13,14] ;...magnetic modes with which to corr.
;mag_modes=[5,6,7,8,9] ;...magnetic modes with which to corr.
;mag_modes=[1,2,3,4,15] ;...magnetic modes with which to corr.

n_mm=n_elements(mag_modes) ;...number of magnetic modes
n_sig=n_mm+2 ;...number of signals

x=fltarr(nn,n_sig) ;...signal array
```

```
name=strarr(n_sig) ;...name array
name(0)="Toroidal Ion Velocity"
name(1)="Poloidal Ion Velocity"
for i_m=0,n_mm-1 do begin
  name(i_m+2)="n="+strtrim(mag_modes(i_m),2)+" Cosine Amplitude"
  endfor

units=strarr(n_sig) ;...units array
units(0:1)="km/s"
units(2:n_sig-1)="gauss"

s=fltarr(n_sig) ;...error array
tlag=fltarr(n_sig) ;...time lag array

;;;-------------------------------------------------------------------

;;; Reading in velocity signals

 ;; aquiring signals from data base

tv=data('vfs_time')-3.64e-3 ;...reading in time record for velocity
nv=n_elements(tv)
if (nv le 1) then goto,SkipShot

n1v=min(where(tv ge t1)) ;...boundaries of time signal
n2v=max(where(tv le t2))
if ((n1v eq -1) or (n2v eq -1)) then goto,SkipShot
tv=tv(n1v:n2v)

;...reading in centroids
fit1_tor=(data('vfs_222_fit1')>0.0)<5.0
if (n_elements(fit1_tor) le 1) then goto,SkipShot
fit1_pol=(data('vfs_138_fit1')>0.0)<5.0
if (n_elements(fit1_pol) le 1) then goto,SkipShot

 ;; converting centroids to velocities

x_lam = 1.88238 ;...calibrated position of line
lam_0 = 2270.90 ;...impurity wavelength

;...Doppler formula!
vel_tor= 2.998e+5/lam_0*(x_lam-fit1_tor)
vel_pol=-2.998e+5/lam_0*(x_lam-fit1_pol)

;...keeping invalid points set to zero
```

```
if (min(fit1_pol) le 0.0) then vel_pol(where(fit1_pol le 0.0))=0.0
if (min(fit1_tor) le 0.0) then vel_tor(where(fit1_tor le 0.0))=0.0

 ;; cleaning up signals
;...zeroing outliers
     vel_pol=clean(vel_pol,m=20,tol=5)
     vel_tor=clean(vel_tor,m=20,tol=5)

;...too many zeros?
pcnt_bad=max([n_elements(where(vel_pol(n1v:n2v) eq 0.0)),$
      n_elements(where(vel_tor(n1v:n2v) eq 0.0))])$
      /float(n2v-n1v+1)
if (pcnt_bad ge 0.1) then goto,SkipShot

;...filling in zeros with nn routine
vel_pol=zerofill(vel_pol,tol=1.0e-6)
vel_tor=zerofill(vel_tor,tol=1.0e-6)

 ;; filtering velocity signals
;...measuring noise level
f_vel_pol=fft([vel_pol(n1v:n2v),fltarr(nf-n2v+n1v-1)],-1)
vel_pol_sig=sqrt(nf*total(abs(f_vel_pol(s_n))^2)/(n_elements(s_n)+1))
f_vel_tor=fft([vel_tor(n1v:n2v),fltarr(nf-n2v+n1v-1)],-1)
vel_tor_sig=sqrt(nf*total(abs(f_vel_tor(s_n))^2)/(n_elements(s_n)+1))

f_vel_pol(s_s)=0.0 ;...filtering out secular component
vel_pol_fil=extrac(float(fft(f_vel_pol,1)),n1v,n2v-n1v+1)
f_vel_tor(s_s)=0.0
vel_tor_fil=extrac(float(fft(f_vel_tor,1)),n1v,n2v-n1v+1)

 ;; placing velocity signals in data array

n1x=max(where(min(abs(t-tv(0))) eq abs(t-tv(0))))
n2x=(n1x+n_elements(tv)-1)<nn
n2v=n2x-n1x

x(n1x:n2x,0)=vel_tor_fil(0:n2v)
x(n1x:n2x,1)=vel_pol_fil(0:n2v)

tlag(0:1)=avg(tv(0:n2v)-t(n1x:n2x))

;;;-------------------------------------------------------------------

;;; Acquiring magnetics

tm=data('modes_time')*1000.
```

```
nm=n_elements(tm)/2
if (nm le 1) then goto,SkipShot
tm=rebin(tm(0:nm*2-1),nm)

n1m=min(where(tm ge t1)) ;...boundaries of time signal
n2m=max(where(tm le t2))
if ((n1m eq -1) or (n2m eq -1)) then goto,SkipShot

n1x=max(where(min(abs(t-tm(n1x))) eq abs(t-tm(n1x))))
n2x=(n1x+n2m-n1m)<nn
n2m=(n1m+n2x-n1x)

for i_m=0,n_mm-1 do begin

  cos_amp=data('modes_'+strtrim(mag_modes(i_m),2)+'_cos')
  if (n_elements(cos_amp) le 1) then goto,SkipShot
  cos_amp=rebin(cos_amp(0:nm*2-1),nm)

;...filtering out secular component
  f_cos_amp=fft([cos_amp(n1m:n2m),fltarr(nf-n2m+n1m-1)],-1)
  f_cos_amp(s_s)=0.0
  cos_amp=extrac(float(fft(f_cos_amp,1)),n1m,n2m-n1m+1)
  x(n1x:n2x,i_m+2)=cos_amp

  endfor

tlag(2:n_mm+1)=avg(tm(n1m:n2m)-t(n1x:n2x))

;;;-------------------------------------------------------------------

    return

    SkipShot:
    t=-1 & x=-1
    return

    end
```

B.4.2 Averaging Routine

This ensemble average routine conducts one pass through the ensemble calculating the signal averages, variance, and power spectra. No correlations between the signals is performed A description of the algorithms in this routine may be found in §3.2.

```
;;;;=================================================================
;;;;
;;;; ST_AVER.PRO
;;;;
;;;; This routine is a simplified version of ST_CORR.  It performs one
;;;; pass through the ensemble and returns the average and power spectra
;;;; of the windowed signals.  No cross products or spectra are calcu-
;;;; lated.  In all other ways this routine is setup in an identically
;;;; to ST_CORR.PRO.  If you have  the sawtooth ensemble for ST_CORR
;;;; you do NOT have to redo it for ST_AVER (and vice-versa).
;;;;
;;;; J. T. Chapman University of Wisconsin - Madison 10/21/96
;;;;=================================================================

;;; Hello and Welcome to the Sawtooth Correlation Routine

print, format='(80("="))'
        print, ' '
        print, 'Sawtooth Window Averaging Routine'
        print, ' '

print, format='(80("-"))'
print, ' '
print, '  Main Level Variables'
print, '    working directory:        '+!working_dir
if (strlen(save_file) eq 0) then $
  print, '    idl save file:            '+'<none>' $
else $
  print, '    idl save file:            '+save_file+'.DAT'
print, '    typed sawtooth listing:   '+saw_list_file+'.LSC'
print, '    sawtooth bounding file:   '+sel_list_file+'.LSC'
print, '    signal routine:           '+signal+'.PRO'
print, '    time before crash:        '+strtrim(prewin,2)+' ms'
print, '    time after crash:         '+strtrim(poswin,2)+' ms'
if verbose then $
print, '    verbose:                  1 (progress messages on)' $
else $
print, '    verbose:                  0 (progress messages off)'
print, ' '
print, format='(80("-"))'
print, ' '

;=====================================================================

; looping through two passes
```

```
init = 1 ;...raising initialization flag

;...opening sawtooth list file
safe_openr,saw_list_file,saw_lun,ext='lsc',dir=!working_dir

;...opening sawtooth selection file
safe_openr,sel_list_file,sel_lun,ext='bnd',dir=!working_dir

;-------------------------------------------------------------------

; starting shot loop

        point_lun,saw_lun,0              ;...rewinding sawtooth listing

dummy=" " ;...reading off header of sawlist file
readf,saw_lun,dummy & readf,saw_lun,dummy
n_records=0
readf,saw_lun,n_records
for i=0,n_records-1 do readf,saw_lun,dummy

shot=0    ;...current shot, 0 for stop processing
date='00-xxx-0000'   ;...date of shot
t1=0    ;...start time of shot
t2=0    ;...end time of shot

;...reading in first shot
SHOT_SET,saw_lun,sel_lun,shot,date,t1,t2,t_crash

while (shot ne 0) do begin ;...main shot loop

;...checking sawteeth windows
  vc=where(((t_crash-prewin) ge t1) and ((t_crash+poswin) le t2))
  if (max(vc) eq -1) then goto,SkipShot else t_crash=t_crash(vc)

  if verbose then $
    print,format='($,"  ",a)',strtrim(filecode(shot,date),2) $
  else print,"  Shot  "+strtrim(shot,2)+" on "+date

;-------------------------------------------------------------------

; obtaining user signals, characterizing basic parameters

  if verbose then print,format='($,"...reading")'

;...reading in signal from user function
```

```
  call_procedure,signal,shot,date,t1,t2,t,x,sx,name,units,tlag

  sig_size = size(x) ;...characterizing signal geometry

;...skipping shot with missing data
  if (sig_size(0) eq 0) then goto, SkipShot

          lsig = sig_size(1) ;...length of signal
  if init then nsig=sig_size(2) ;...number of signals

  dt=(max(t)-min(t))/(lsig-1) ;...time resolution

  sig_val=fltarr(nsig)+1 ;...sig_val defaults to true
  for i=0,nsig-1 do if (avg(x(*,i)^2) eq 0.0) then sig_val(i)=0.0

;-------------------------------------------------------------------

; intialization of arrays

          if ( init ) then begin ;...if initializing necessary

;...number of points in window
    nw=fix((prewin+poswin)/dt+1.5)

            dxav = fltarr(nw,nsig) ;...average sawtooth profile
            dxdxav = fltarr(nw,nsig) ;...average fluctuation product

    sxav = fltarr(nsig) ;...average random power
    sxsxav = fltarr(nsig) ;...average random (power)^2

    dfdfav = fltarr(nw,nsig) ;...spectra of fluctuation products

    sfav = fltarr(nw,nsig)  ;...average random spectral power
    sfsfav = fltarr(nw,nsig) ;...average random (spectral power)^2

;...creating time and frequency axis
    taxis = findgen(nw)*dt-prewin
            faxis = findgen(nw/2+1)/(nw*dt)

    npre = fix((nw-1)*(float(prewin)/(prewin+poswin))+0.5)
    npos = fix((nw-1)*(float(poswin)/(prewin+poswin))+0.5)

            nevent = intarr(nw,nsig) ;...number of sawtooth events

            init = 0                  ;...lowering init flag
```

```
            endif
;----------------------------------------------------------------------

; sawtooth ensemble loop

  n_crash=n_elements(t_crash) ;...number of sawtooth crashes

  if verbose then print,"..."+strtrim(n_crash,2)+" events."
          for i_crash = 0, n_crash-1 do begin

    n0 = max(where(min(abs(t-t_crash(i_crash))) eq $
       abs(t-t_crash(i_crash))       ))

    n1 = (n0-npre)>0
    n2 = (n0+npos)<(lsig-1)

    n1d = (npre-n0+n1)>0
    n2d = (npre-n0+n2)<(nw-1)

    dx = fltarr(nw,nsig) ;...initializing sawtooth arrays

             for i=0,nsig-1 do begin  ;...filling sawtooth arrays
       if sig_val(i) then begin
         dx(n1d:n2d,i) = x(n1:n2,i)
 nevent(n1d:n2d,i) = nevent(n1d:n2d,i)+1
         endif
       endfor

 ;----------------------------------------------------------------------

 ; calculating average profiles

             dxav = dxav + dx ;...updating average profile
             dxdxav = dxdxav + dx^2

     sxav = sxav + sx^2 ;...updating average errors
     sxsxav = sxsxav + sx^4

  ;---------------------------------------------------------------------

  ; calculating spectral quantities (second pass)

              w = hanning(nw) ;...windowing array

      if spec_calc then begin
```

```
                                         ;...calculating transforms
              df = complexarr( nw, nsig )
              for i=0,nsig-1 do if sig_val(i) then $
        df(*,i) = fft( dx(*,i)*w-avg(dx(*,i)*w), -1 )

;...estimating power spectra
      dfdfav = dfdfav + abs(df)^2.

;...average random power^2
      for i=0,nsig-1 do if sig_val(i) then begin

sfav(*,i) = sfav(*,i) + sx(i)^2*abs(df(*,i))^2 $
                         / total(abs(df(*,i))^2)

sfsfav(*,i) = sfsfav(*,i) + ( sx(i)^2*abs(df(*,i))^2 $
               / total(abs(df(*,i))^2) )^2

        endif

      endif

;----------------------------------------------------------------------

    SkipCrash:

             endfor ;...end of sawtooth averaging loop

;----------------------------------------------------------------------

; wrapping up shot ensemble loop

  SkipShot:
;...getting next shot
           SHOT_SET,saw_lun,sel_lun,shot,date,t1,t2,t_crash

           endwhile ;...end of shot ensemble loop

;----------------------------------------------------------------------

; normalizing ensemble quantities

for isig=0,nsig-1 do begin
  vv=where(nevent(*,isig))
  if (max(vv) ne -1) then begin
             dxav(vv,isig)   = dxav(vv,isig)   / nevent(vv,isig)
             dxdxav(vv,isig) = dxdxav(vv,isig) / nevent(vv,isig)
```

```
    sxav(isig)      = sxav(isig)      / max(nevent(vv,isig))
    sxsxav(isig)    = sxsxav(isig)    / max(nevent(vv,isig))
    endif
  endfor

  dfdfav = dfdfav(0:nw/2,*) ;...converting to one-sided spectra
  sfav = sfav(0:nw/2,*)
  sfsfav = sfsfav(0:nw/2,*)

;...normalizing average spectra

  norm_win = [1.0,fltarr(nw/2-1)+2.0,1.0]

  for i=0,nsig-1 do if (max(nevent(*,i)) ne 0) then begin
        dfdfav(*,i) = dfdfav(*,i) * norm_win / avg(w^2)/max(nevent(*,i))
    sfav(*,i)   = sfav(*,i)   * norm_win / max(nevent(*,i))
    sfsfav(*,i) = sfsfav(*,i) * norm_win / max(nevent(*,i))
    endif

; calculating errors


;...error in average products
sdxav=fltarr(nsig)
sdxdxav=fltarr(nsig)
for ii=0,nsig-1 do if (max(nevent(*,ii)) ne 0) then begin
  sdxav(ii)   = sqrt(sxav(ii)/max(nevent(*,ii)))
  sdxdxav(ii) = sqrt(2*sxsxav(ii)/max(nevent(*,ii)))
  endif

;...error in average spectra
sdfdfav=fltarr(nw/2+1,nsig)
; for ii=0,nsig-1 do if (max(nevent(*,ii) ne 0) then begin
;   sdfdfav(*,ii,ii) = sqrt((2*dfdfav(*,ii,ii)*sfav(*,ii) + $
;              sfsfav(*,ii,ii))/max(nevent(*,ii,jj)))
;   endif
;=====================================================================

; fluctation correlation routine wrap-up

;...write variables do save file
if (strlen(strtrim(save_file,2)) ne 0) then $
  save,file=!working_dir+save_file,$
      taxis,faxis,dxav,sdxav,dxdxav,sdxdxav,sxav,sxsxav,$
      dfdfav,sdfdfav,sfav,sfsfav, $
```

```
              nevent,nsig,dt,nw,name,units,tlag

free_lun,saw_lun,sel_lun ;...freeing logical units

;...say Goodbye
print," "
print,"Goodbye."
print," "
print,format='(80("="))'

        end ;...FINE!

;=====================================================================
```

B.4.3 Wavelet Analysis Routine

This correlation engine performs two passes through the sawtooth ensemble. The details of the algorithms employed may be found in § 3.2. This engine is identical to `st_corr` but has added ensemble wavelet analysis.

```
;;;;==================================================================
;;;;
;;;; ST_WVLT.PRO
;;;;
;;;; This routine finds the correlation and coherence of an ensemble of
;;;; windowed signals provided by the user.  The routine loops twice through
;;;; the ensemble.  The first loop finds the average  of the signals, the
;;;; second to analyzes the fluctuating part of subtracting the average.
;;;;
;;;; J. T. Chapman University of Wisconsin - Madison 10/21/96
;;;;
;;;; Wavelet analysis incorportated into sawtooth correlation routine.
;;;;
;;;; E. Martines Consorzio RFX - Padova, Italy 09/09/97
;;;;==================================================================

;;; Hello and Welcome to the Sawtooth Correlation Routine

print, format='(80("="))'
        print, ' '
        print, 'Sawtooth Window Fluctuation Correlation Routine'
        print, ' '
```

```
print, format='(80("-"))'
print, ' '
print, '  Main Level Variables'
print, '    working directory:        '+!working_dir
print, '    idl save file:            '+save_file+'.DAT'
print, '    typed sawtooth listing:   '+saw_list_file+'.LSC'
print, '    sawtooth bounding file:   '+sel_list_file+'.BND'
print, '    signal routine:           '+signal+'.PRO'
print, '    time before crash:        '+strtrim(prewin,2)+' ms'
print, '    time after crash:         '+strtrim(poswin,2)+' ms'
if verbose then $
print, '    verbose:                  1 (progress messages on)' $
else $
print, '    verbose:                  0 (progress messages off)'
print, ' '
print, format='(80("-"))'
print, ' '

;=====================================================================

; looping through two passes

;...raising initialization flag
init = 1

time_read = 0.0
time_calc = 0.0

;...opening sawtooth list file
safe_openr,saw_list_file,saw_lun,ext='lsc',dir=!working_dir

;...opening sawtooth selection file
safe_openr,sel_list_file,sel_lun,ext='bnd',dir=!working_dir

;...two pass outer loop
        for ipass=1,2 do begin

                                        ;...pass message
        if (ipass eq 1) then $
          print,"First Pass: Mean Profile" $
        else $
          print,"Second Pass: Fluctuating Quantities"
        print," "

;--------------------------------------------------------------------
```

```
; starting shot loop

        point_lun,saw_lun,0             ;...rewinding sawtooth listing

dummy=" " ;...reading off header of sawlist file
readf,saw_lun,dummy & readf,saw_lun,dummy
n_records=0
readf,saw_lun,n_records
for i=0,n_records-1 do readf,saw_lun,dummy

shot=0    ;...current shot, 0 for stop processing
date='00-xxx-0000'   ;...date of shot
t1=0    ;...start time of shot
t2=0    ;...end time of shot

;...reading in first shot
SHOT_SET,saw_lun,sel_lun,shot,date,t1,t2,t_crash

while (shot ne 0) do begin ;...main shot loop

;...checking sawteeth windows
  vc=where(((t_crash-prewin) ge t1) and ((t_crash+poswin) le t2))
  if (max(vc) eq -1) then goto,SkipShot else t_crash=t_crash(vc)

  print,"  Shot "+strtrim(shot,2)+" on "+date+", "+strtrim(t1,2)+"-"+$
strtrim(t2,2)+" ms, "+strtrim(n_elements(t_crash),2)+" events."

;--------------------------------------------------------------------

; obtaining user signals, characterizing basic parameters

  if verbose then print,format='($,"  ...reading")'

;...reading in signal from user function
  dumt=systime(1)
  call_procedure,signal,shot,date,t1,t2,t,x,sx,name,units,tlag
  time_read=time_read+systime(1)-dumt

  sig_size = size(x) ;...characterizing signal geometry

;...skipping shot with missing data
  if (sig_size(0) eq 0) then goto, SkipShot

          lsig = sig_size(1) ;...length of signal
          nsig = sig_size(2) ;...number of signals
```

```
  dt=(max(t)-min(t))/(lsig-1) ;...time resolution

;----------------------------------------------------------------------

; creating phase shifted signal

  if verbose then print,format='($,"...phase shift")'

          p = fltarr( lsig, nsig )      ;...phase shifted signal

  lbuf=64-(lsig mod 64) ;...buffer for signal to factor of 64

          phsft = fltarr( lbuf+lsig )   ;...phase shifting array

                                    ;...setting for 90 degree phase shift
          phsft(0:(lbuf+lsig-1)/2) = 1.0
          phsft((lbuf+lsig+1)/2:lbuf+lsig-1) = -1.0

;...recovering phase shifted signal
          for isig=0,nsig-1 do                 $
    p(*,isig) = temporary(extrac(float(fft(                   $
                fft([fltarr(lbuf),x(*,isig)],-1) * complex(0,phsft), $
                  1)),lbuf,lsig))

;----------------------------------------------------------------------

; intialization of arrays

            if ( init ) then begin ;...if initializing necessary

;...number of points in window
      nw=fix((((prewin+poswin)/dt)+0.5)/2)*2

      dx = fltarr(nw,nsig) ;...initializing sawtooth arrays
      dp = fltarr(nw,nsig)

              dxav = fltarr(nw,nsig) ;...average sawtooth profile
      dpav = fltarr(nw,nsig) ;...average phase shifted sawtooth

                                 ;...average fluctuation product
              dxdxav = fltarr(nw,nsig,nsig)

      sxav = fltarr(nsig) ;...average random power
      sxsxav = fltarr(nsig,nsig);...average random (power)^2

;...spectra of fluctuation products
```

```
      dfdfav = fltarr(nw,nsig,nsig)

      sfav = fltarr(nw,nsig) ;...average random spectral power

;...average random (spectral power)^2
      sfsfav = fltarr(nw,nsig,nsig)

;...creating time and frequency axis
      taxis = findgen(nw)*dt-prewin
              faxis = findgen(nw/2+1)/(nw*dt)


      ;; Wavelet analysis array declarations

;...wavelet frequency axis
      if (not defined(wfaxis)) then begin

        if not defined(wfreqmin) then wfreqmin=4.0/(nw*dt)
        if not defined(wfreqmax) then wfreqmax=1.0/(2*dt)

        nwf=fix(2*!pi*alog(wfreqmax/wfreqmin))+1

        wfaxis=wfreqmin*(wfreqmax/wfreqmin)^(findgen(nwf)/(nwf-1))

endif

;...frequency interval size
      dwfaxis        =(shift(wfaxis,-1)-shift(wfaxis,+1))/2.0
      dwfaxis(0)     =(wfaxis(1)-wfaxis(0))/2.0+wfaxis(0)/(2*!pi)
      dwfaxis(nwf-1) =(wfaxis(nwf-1)-wfaxis(nwf-2))/2.0

      dwfaxis      =dwfaxis*(nw*dt)

      fwav=fltarr(2*nw,nwf) ;...defining wavelets if Fourier space

              wftemp=[findgen(nw+1),-reverse(findgen(nw-1)+1.0)]/(2*nw*dt)

      for iwf=0,nwf-1 do begin

;   wav = 1.0/(!pi/wfaxis(iwf)^2)^0.25 * $
;           exp(-0.5*((t-t(0))*wfaxis(iwf))^2) * $
;       complex( cos(2*!pi*(t-t(0))*wfaxis(iwf), $
;        sin(2*!pi*(t-t(0))*wfaxis(iwf) )

;  wav = [ wav, 0.0, reverse(conj(wav(1:*))) ]
```

```
;   fwav(*,iwf) = fft(wav,-1)*(2*nw*dt)

   fwav(*,iwf) = (4*!pi/wfaxis(iwf)^2)^0.25 * $
         exp(-0.5*((wftemp/wfaxis(iwf)-1)*2*!pi)^2)

   fwav(0,iwf) = 0.0

        endfor
      wftemp=0 ;...clearing array

;...wavelet coefficients
      dw   = complexarr(nw,nwf,nsig)

;...average wavelet coefficients
      dwav = complexarr(nw,nwf,nsig)

;...average wavelet products
      dwdwav = fltarr(nw,nwf,nsig,nsig)

              nevent = 0                 ;...number of sawtooth events
              init = 0                   ;...lowering init flag

              endif

;----------------------------------------------------------------------

; sawtooth ensemble loop

  n_crash=n_elements(t_crash) ;...number of sawtooth crashes

          for i_crash = 0, n_crash-1 do begin

;...boudaries of sawtooth event
            n1 = fix(min(where( t ge (t_crash(i_crash)-prewin) )))
            n2 = nw+n1-1

            for i=0,nsig-1 do begin  ;...filling sawtooth arrays
      dx(*,i) = x(n1:n2,i)
      dp(*,i) = p(n1:n2,i)
      endfor

;----------------------------------------------------------------------

; calculating average profiles (first pass)

    if (ipass eq 1) then begin
```

```
            dxav = dxav + dx ;...updating average profile
    dpav = dpav + dp

    sxav = sxav + sx^2 ;...updating average errors
    for ii=0,nsig-1 do for jj=0,nsig-1 do         $
      sxsxav(ii,jj) = sxsxav(ii,jj) + sx(ii)^2*sx(jj)^2

            nevent = nevent + 1 ;...updating number of events

    endif

;----------------------------------------------------------------------

; subtracting average sawtooth profile from window (first pass)

   if (ipass eq 2) then begin

     for i=0,nsig-1 do begin ;...straight subtraction
       dx(0:(n2-n1),i)=dx(0:(n2-n1),i)-dxav(0:(n2-n1),i)
       dp(0:(n2-n1),i)=dp(0:(n2-n1),i)-dpav(0:(n2-n1),i)
       endfor

     endif

;----------------------------------------------------------------------

; calculating fluctuation products (second pass)

   if (ipass eq 2) then        $
         for ii=0,nsig-1 do for jj=0,nsig-1 do begin
      if (ii le jj) then         $
            dxdxav(*,ii,jj) = dxdxav(*,ii,jj) + dx(*,ii)*dx(*,jj)$
      else        $
            dxdxav(*,ii,jj) = dxdxav(*,ii,jj) + dx(*,ii)*dp(*,jj)
          endfor

;----------------------------------------------------------------------

; calculating spectral quantities (second pass)

         w = hanning(nw) ;...windowing array

   if ((ipass eq 2) and spec_calc) then begin

                                              ;...calculating transforms
```

```
              df = complexarr( nw, nsig )
              for i=0,nsig-1 do df(*,i) = fft( dx(*,i)*w, -1 )

;...estimating power spectra
              for i=0,nsig-1 do                 $
        dfdfav(*,i,i) = dfdfav(*,i,i) + abs(df(*,i))^2.

;...average cross spectra off diagonal
          for i=0,nsig-2 do for j=i+1,nsig-1 do begin
            dfdfav(*,i,j) = dfdfav(*,i,j) + float(    df(*,i)*conj(df(*,j)))
            dfdfav(*,j,i) = dfdfav(*,j,i) + imaginary(df(*,i)*conj(df(*,j)))
            endfor
;...average random power
      for i=0,nsig-1 do        $
sfav(*,i) = sfav(*,i) + sx(i)^2*abs(df(*,i))^2        $
                        / total(abs(df(*,i))^2)

;...average random power^2
      for i=0,nsig-1 do for j=0,nsig-1 do         $
sfsfav(*,i,j) = sfsfav(*,i,j)        $
                   + sx(i)^2*sx(j)^2*abs(df(*,i))^2*abs(df(*,j))^2$
  / total(abs(df(*,i))^2)*total(abs(df(*,j))^2)

      endif

;--------------------------------------------------------------------

; calculating wavelet coefficients

    if (ipass eq 2) then begin

      dumt=systime(1)
;...calculating wavelet transform (fwav is real)
      for isig=0,nsig-1 do begin

fsig=fft([dx(*,isig),replicate(0.0,nw)],-1)

           for iwf=0,nwf-1 do $
  dw(*,iwf,isig)=extrac(fft(fwav(*,iwf)*fsig,1),0,nw)

        fsig=0

      endfor

      dwav=dwav+dw ;...averaging wavelet coefficients
```

```
;...averaging wavelet products
      for i=0,nsig-1 do $
   dwdwav(*,*,i,i) = dwdwav(*,*,i,i) + abs(dw(*,*,i))^2
      for i=0,nsig-2 do for j=i+1,nsig-1 do begin
   dwdwav(*,*,i,j) = dwdwav(*,*,i,j) + $
            float(     dw(*,*,i)*conj(dw(*,*,j)) )
   dwdwav(*,*,j,i) = dwdwav(*,*,j,i) + $
  imaginary( dw(*,*,i)*conj(dw(*,*,j)) )
      endfor

      time_calc=time_calc+systime(1)-dumt

    endif

;--------------------------------------------------------------------

            endfor ;...end of sawtooth averaging loop

;--------------------------------------------------------------------

; wrapping up shot ensemble loop

  SkipShot:
;...getting next shot
          SHOT_SET,saw_lun,sel_lun,shot,date,t1,t2,t_crash

          endwhile ;...end of shot ensemble loop

;--------------------------------------------------------------------

; normalizing ensemble quantities

;...average profiles and errors
if (ipass eq 1) then begin
          dxav = dxav/nevent
  dpav = dpav/nevent
  sxav = sxav/nevent
  sxsxav = sxsxav/nevent
  endif
;...average products and spectra
if (ipass eq 2) then begin

          dxdxav = dxdxav/nevent ;...normaling average products

  dfdfav = dfdfav(0:nw/2,*,*) ;...converting to one-sided spectra
  sfav = sfav(0:nw/2,*)
```

```
 sfsfav = sfsfav(0:nw/2,*,*)
;...normalizing average spectra
 norm_win = [1.0,fltarr(nw/2-1)+2.0,1.0]/nevent

 for i=0,nsig-1 do sfav(*,i) = sfav(*,i)*norm_win
         for i=0,nsig-1 do for j=0,nsig-1 do begin
           dfdfav(*,i,j) = dfdfav(*,i,j)*norm_win/avg(w^2)
   sfsfav(*,i,j) = sfsfav(*,i,j)*norm_win
   endfor

 dwdwav = dwdwav/(2*nevent) ;...normalizing wavelet products
 dwav   = dwav/nevent ;...normalizing wavelet coefficients

 endif

;----------------------------------------------------------------------

; end of two-pass super loop

 print," "

endfor

;======================================================================

; calculating ensemble quantities
print," "
print,"Calculating Ensemble Quantities"

;----------------------------------------------------------------------

; calculating errors

sdxav=sqrt(sxav/nevent) ;...error in average profile

;...error in average products
sdxdxav=fltarr(nsig,nsig)
for ii=0,nsig-1 do for jj=0,nsig-1 do                     $
  if (ii eq jj) then                                      $
    sdxdxav(ii,ii)=sqrt(2*sxsxav(ii,ii))/sqrt(nevent)    $
  else                                                    $
    sdxdxav(ii,jj)=sqrt(sxsxav(ii,jj))/sqrt(nevent)

;...error in average spectra
sdfdfav=fltarr(nw/2+1,nsig,nsig)
; for ii=0,nsig-1 do for jj=0,nsig-1 do         $
```

```
;   if (ii eq jj) then                 $
;     sdfdfav(*,ii,ii)=sqrt(2*dfdfav(*,ii,ii)*sfav(*,ii)+sfsfav(*,ii,ii))$
;      / sqrt(nevent)    $
;   else        $
;     sdfdfav(*,ii,jj)=sqrt(sfsfav(*,ii,jj)+dfdfav(*,ii,ii)*sfav(*,jj)   $
;         + dfdfav(*,jj,jj)*sfav(*,ii))/sqrt(2*nevent)


;----------------------------------------------------------------------

; calculating correlation array

correlation=0
if ens_calc then begin

  ;...initializing arrays
          correlation   = fltarr( nw, nsig, nsig )

  ;...looping pairwise through signals
          for i=0,nsig-2 do for j=i+1,nsig-1 do begin

  ;...trick to avoid dividing by zero
            base=sqrt( dxdxav(*,i,j)^2 + dxdxav(*,j,i)^2 )
            base=min(base(where(base ne 0.0)))*0.1

  ;...calculating correlation
            correlation(*,i,j)   =  $
      sqrt( dxdxav(*,i,j)^2 + dxdxav(*,j,i)^2 )/  $
              (sqrt( abs( dxdxav(*,i,i) * dxdxav(*,j,j) ) )>base)

  ;...estimating average phase of signals
            correlation(*,j,i) = atan(dxdxav(*,j,i),dxdxav(*,i,j))

            endfor

  endif

;----------------------------------------------------------------------

; calculating coherence array

coherence=0
if (ens_calc and spec_calc) then begin

;...initializing coherence arrays
        coherence = fltarr(nw/2+1,nsig,nsig)
```

```
;...looping pairwise through signals
          for i=0,nsig-2 do for j=i+1,nsig-1 do begin

;...trick to avoid dividing by zero
    base=sqrt( abs( dfdfav(*,i,i) )*abs( dfdfav(*,j,j) ) )
    base=min(base(where(base ne 0.0)))*0.1

;...calculating coherence array
            coherence(*,i,j)     =  $
         sqrt( dfdfav(*,i,j)^2 + dfdfav(*,j,i)^2 ) /  $
              sqrt( abs( dfdfav(*,i,i) * dfdfav(*,j,j) ) >base)

;...calculation of phase angle
    coherence(*,j,i) = atan( dfdfav(*,j,i),dfdfav(*,i,j) )

            endfor

  endif

;--------------------------------------------------------------------

; calculating wavelet coherence array

wcoherence=0
if (ens_calc and spec_calc) then begin

;..initializing wavelet coherence arrays
          wcoherence = fltarr(nw,nwf,nsig,nsig)

;...looping pairwise through signals
          for i=0,nsig-2 do for j=i+1,nsig-1 do begin

;...trick to avoid dividing by zero
    base=sqrt( abs( dwdwav(*,*,i,i) )*abs( dwdwav(*,*,j,j) ) )
    base=min(base(where(base ne 0.0)))*0.1

;...calculating wavelet coherence array
            wcoherence(*,*,i,j)     =  $
         sqrt( dwdwav(*,*,i,j)^2 + dwdwav(*,*,j,i)^2 ) /  $
              sqrt( abs( dwdwav(*,*,i,i) * dwdwav(*,*,j,j) ) >base)

;...calculation of wavelet phase angle
    wcoherence(*,*,j,i) = atan( dwdwav(*,*,j,i),dwdwav(*,*,i,j) )

            endfor
```

```
  for i=0,nsig-1 do $
    wcoherence(*,*,i,i)=atan(imaginary(dwav(*,*,i)), $
            float(dwav(*,*,i))  )

  endif

;====================================================================

; fluctation correlation routine wrap-up

;...write variables do save file
if (not (defined(save_xdr))) then save_xdr=0
if (strlen(strtrim(save_file,2)) ne 0) then $
  save,file=!working_dir+save_file,xdr=save_xdr,$
      taxis,faxis,wfaxis,dxav,dpav,sdxav,dxdxav,sdxdxav,        $
              sxav,sxsxav,dfdfav,sdfdfav,sfav,sfsfav,dwdwav,dwfaxis,   $
              coherence,wcoherence,correlation,                         $
              nevent,nsig,dt,nw,name,units,tlag,time_calc,time_read,nwf

        free_lun,saw_lun,sel_lun

print," " ;...say Goodbye
print,"Goodbye."
print," "
print,format='(80("="))'

        end ;...FINE!

;====================================================================
```

B.5 Magnetic Mode Analysis

The noninteractive routine `modes_b.com` serves as the front end for the IDS fit engine. The user defines the variables in this file and submits the job to a VMS batch queue. The batch routine then defines the necessary variables, compiles the subroutines, and calls the main mode analysis engine.

```
$ set def [jchapman.public.mode_anal]
$ idl
;;;=================================================================
```

```
;;; MODES_B.COM

;;;; This is an IDL batch routine designed simply to compile
;;;; the subroutines and initialize the variables necessary to run
;;;; MODES.PRO, the primary mode analysis engine.  It is recommended
;;;; that users copy this batch file into their directory where they
;;;; can modify it according to their needs. It is not necessary to
;;;; copy MODES.PRO which is designed to run out of the public directory.
;;;; Any questions or comments regarding the routines in this directory
;;;; should be directed to Jim Chapman (jchapman@juno.physics.wisc.edu).

;;;; J. T. ChapmanUniversity of Wisconsin - Madison      May 22, 1997

;;;;==============================================================

;; Compiling necessary subroutines.
.run [jchapman.idl]deriv_5pt
.run [jchapman.idl]defined
.run [jchapman.idl]thinn
.run [jchapman.idl]vtt

;; Specifying input files
                     ;...The shot list is a list of shots, dates, starting
                     ;   and ending times input by the modes analysis.
                     ;   Such a list may easily be made by running the
                     ;   routine MAKESHOTLIST from this directory.  These
                     ;   lists have a .LSA suffix and are identical to the
                     ;   shotlist produced by the correlation routines.
                     ;   A shot file MUST be specified for the routine to
                     ;   run on your data.
        shot_file = "[myname.mydirectory]myshotlist.lsa"

                     ;...The renormalization file contains the current
                     ;   renormalization for the magnetic coil array.
                     ;   If left undefined the routine will use the default
                     ;   renormalizations in this directory which I will
                     ;   attempt to keep current.  To create you own
                     ;   renormalization file run RENORM_CALC from this
                     ;   directory.
        renorm_file = "[myname.mydirectory]myrenormfile.dat"

;; Specifying run variables

                     ;...n is an integer array of the toroidal mode numbers
                     ;   for which you wish to calculate amplitudes.  If
                     ;   left undefined the routine defaults to calculating
                     ;   modes 5, 6, 7, and 8.
n = [ 5, 6, 7, 8]

                     ;...ncb is an integer specifying the nuber of coils
                     ;   used for toroidal mode analysis.  MODES will
                     ;   work with 16, 32, or 64 coils.  If left undefined
                     ;   ncb defaults to 32 coil analysis.
ncb = 32

                     ;...v_sat_hi and v_sat_lo are the digitizer saturation
                     ;   voltages.  These may be either a single value if
                     ;   the saturation voltages are all the same or an
                     ;   array ncb long if digitizers with different
                     ;   saturation voltages are used.  If left undefined
                     ;   v_sat_hi defaults to 2.5 and v_sat_lo to -2.5.
                     ;    (See note on signal order below if specifying
                     ;     saturation levels for each digitizer.)
v_sat_hi = +5.0
v_sat_lo = -5.0

                     ;...output_freq is the frequency at which the mode
                     ;   amplitudes are output to the data base.  The
                     ;   toroidal array is digitized at 200kHz.  The modes
                     ;   may therefore be written at 200kHz, 100kHz, 66kHz,
                     ;   50kHz, 40kHz, 33kHz, 25kHz, and 10kHz.  The routine
                     ;   defaults to 100kHz
output_freq = 100

                     ;...plot_vel determines whether the n=6 mode velocity
                     ;   will be plotted as the processing continues.  This
                     ;   should only be set to 1 if the mode analysis is
                     ;   being done interactively.  Plot_vel defaults to 0.
plot_vel = 0

                     ;...bpgain sets the integrator gain for MODES.  This
                     ;   may be set to a single integer gain if all gains
                     ;   are identical or an array if different coils have
                     ;   different integrator gains.  If bpgain is set to 0
                     ;   the routine assumes that the shot_file also
                     ;   contains the integrator gains.  Such a set up is
                     ;   useful if the gains change during a run.  A shot
                     ;   list with the gains may be created by running
                     ;   CHECK_GAINS from this directory after creating
                     ;   a normal list with MAKESHOTLIST.  If left undefined
                     ;   bpgain defaults to 20.
```

```
                      ;    (See note on signal order below if specifying
                      ;     gains for each digitizer.)
        bpgain = 20

;; Running the main mode processing engine

.run [jchapman.public.mode_anal]modes

;=====================================================================

; Note on the order of coil signals:

; The coil names are ordered in the array to facilitate mode analysis for
; 16, 32, or 64.  Thus the first 16 names are those signals for 16 coil
; analysis, the first 32 for 32 coil analysis, etc.  Thus, when specifying
; gains or saturation levels for individual signals they must be ordered in
; the array to match the name array below:

;     /     /     / 'BP_241_003','BP_241_025','BP_241_048','BP_241_070',
;     |     |  ncb| 'BP_241_093','BP_241_115','BP_241_138','BP_241_160',
;     |     |  =16| 'BP_241_183','BP_241_205','BP_241_228','BP_241_250',
;     |  ncb|     \ 'BP_241_273','BP_241_295','BP_241_318','BP_241_340',
;     |  =32|       'BP_241_014','BP_241_037','BP_241_059','BP_241_082',
;     |     |       'BP_241_104','BP_241_127','BP_241_149','BP_241_172',
;     |     |       'BP_241_194','BP_241_217','BP_241_239','BP_241_262',
;  ncb|     \       'BP_241_284','BP_241_307','BP_241_329','BP_241_352',
;  =64|             'BP_241_008','BP_241_020','BP_241_031','BP_241_042',
;     |             'BP_241_053','BP_241_065','BP_241_076','BP_241_087',
;     |             'BP_241_098','BP_241_110','BP_241_121','BP_241_132',
;     |             'BP_241_143','BP_241_155','BP_241_166','BP_241_180',
;     |             'BP_241_188','BP_241_200','BP_241_211','BP_241_222',
;     |             'BP_241_233','BP_241_245','BP_241_256','BP_241_268',
;     |             'BP_241_278','BP_241_290','BP_241_301','BP_241_312',
;     \             'BP_241_323','BP_241_335','BP_241_346','BP_241_357'

;=====================================================================
```

The mode analysis engine performs the spatial Fourier analysis and signal normalization of the toroidal array.

```
;=====================================================================
;;;; MODES.PRO - Magnetic Mode Analysis Engine
```

```
;;;; This main level routine performs a spatial Fourier transform on the
;;;; toroidal Bp array signals to generate the cos and sin
;;;; amplitudes of the toroidal harmonic modes in time.  These amplitudes
;;;; are written to the M.* (modified) data base along with the time axis,
;;;; the equillibrium poloidal field amplitude, and the total RMS fluctuation
;;;; amplitude.  The program relies on several variables and input files which
;;;; are specified (or not) in the MODES_B.PRO batch routine.  Copy
;;;; the MODES_B.PRO and the MODES_B.COM into a local directory to modify and
;;;; run.  MODES.PRO does not need to be copied as it is designed to run from
;;;; this directory.  Any questions regarding code in this directory should be
;;;; directed to Jim Chapman (jchapman@juno.physics.wisc.edu).

;;;; J. T. Chapman      University of Wisconsin - Madison      May 23, 1997
;;;; Based on code by J. S. Sarff & A. F. Almagri

;=====================================================================

;; Setting processing session parameters

 ;...setting system variables
        !c=0 & !quiet=1 & !noeras=0

 ;...shot list file name (must exist prior to run time)
        if (not defined(shot_file)) then begin
          print,"ERROR: Must define variable shot_file prior to run."
          goto, EndRoutine
          endif

 ;...checking that shot file exists
        dummy=findfile(shot_file) & dummy=dummy(0)
        if (strlen(strtrim(dummy,2)) eq 0) then begin
          print,"ERROR: Shot list file, "+shot_file+", not found."
          goto, EndRoutine
          endif

 ;...renormalization file
        if (not defined(renorm_file)) then $
          renorm_file = '[jchapman.public.mode_anal]renorm.dat'

 ;...checking that renormalization file exists
        dummy=findfile(renorm_file) & dummy=dummy(0)
        if (strlen(strtrim(dummy,2)) eq 0) then begin
          print,"ERROR: Renormalization file, "+renorm_file+", not found."
          goto, EndRoutine
          endif
```

```
;...reading in renormalization
       rnm = fltarr(ncb)
       openr,lun_rnm,renorm_file,/get_lun
       readf,lun_rnm,ncb_rnm,nshot_rnm
       if (ncb_rnm lt ncb) then begin
         print,"ERROR: Renormalization file, "+renorm_file+", for wrong ncb."
         free_lun,lun_rnm
         goto, EndRoutine
         endif
       readf,lun_rnm,rnm
       free_lun,lun_rnm

;...poloidal mode numbers to calculate
       if (not defined(n)) then n = [5,6,7,8]
       n_n = n_elements(n)

;...number of coils for analysis, code wil work with ncb = 16, 32 or 64
       if (not defined(ncb)) then ncb=32

;...output frequency for mode analysis
       if (not defined(output_freq)) then output_freq=200

;...checking digitizer saturation voltages
       if (not defined(v_sat_hi)) then v_sat_hi=+5.0
       if (n_elements(v_sat_hi) eq 1) then v_sat_hi=v_sat_hi+fltarr(ncb)
       if (n_elements(v_sat_hi) ne ncb) then begin
         print,"ERROR: Length of defined v_sat_hi array unequal to ncb."
         goto,EndRoutine
         endif
       if (not defined(v_sat_lo)) then v_sat_lo=-5.0
       if (n_elements(v_sat_lo) eq 1) then v_sat_lo=v_sat_lo+fltarr(ncb)
       if (n_elements(v_sat_lo) ne ncb) then begin
         print,"ERROR: Length of defined v_sat_lo array unequal to ncb."
         goto,EndRoutine
         endif

;...plot n=6 mode velocity? (default is no)
       if (not defined(plot_vel)) then plot_vel=0

;----------------------------------------------------------------------

; Initializing coil data

       if (not defined(bpgain)) then bpgain=20+intarr(ncb) $
       else if (n_elements(bpgain) eq 1) then bpgain=bpgain+intarr(ncb)
```

```
if (total(bpgain) eq 0) then gain_file=1 else gain_file=0

                                      ;...name of bp coils (explicit)
bpname = ['BP_241_003','BP_241_025','BP_241_048','BP_241_070',$
          'BP_241_093','BP_241_115','BP_241_138','BP_241_160',$
          'BP_241_183','BP_241_205','BP_241_228','BP_241_250',$
          'BP_241_273','BP_241_295','BP_241_318','BP_241_340',$
          'BP_241_014','BP_241_037','BP_241_059','BP_241_082',$
          'BP_241_104','BP_241_127','BP_241_149','BP_241_172',$
          'BP_241_194','BP_241_217','BP_241_239','BP_241_262',$
          'BP_241_284','BP_241_307','BP_241_329','BP_241_352',$
          'BP_241_008','BP_241_020','BP_241_031','BP_241_042',$
          'BP_241_053','BP_241_065','BP_241_076','BP_241_087',$
          'BP_241_098','BP_241_110','BP_241_121','BP_241_132',$
          'BP_241_143','BP_241_155','BP_241_166','BP_241_180',$
          'BP_241_188','BP_241_200','BP_241_211','BP_241_222',$
          'BP_241_233','BP_241_245','BP_241_256','BP_241_268',$
          'BP_241_278','BP_241_290','BP_241_301','BP_241_312',$
          'BP_241_323','BP_241_335','BP_241_346','BP_241_357' ]

bpname = bpname(0:ncb-1)

tname  = 'BP_241_003_TM'              ;...time array

av_bparea = 0.1468681e-03             ;...average coil area

                                      ;...angle of bp coils (radians)
ang    = [003.125,025.312,047.812,070.312,$
          092.812,115.312,137.812,160.312,$
          182.812,205.312,227.812,250.312,$
          272.812,295.312,317.812,340.312,$
          014.062,036.562,059.062,081.562,$
          104.062,126.562,149.062,171.562,$
          194.062,216.562,239.062,261.562,$
          284.062,306.562,329.062,351.562,$
          008.437,019.687,030.937,042.187,$
          053.437,064.687,075.937,087.187,$
          098.437,109.687,120.937,132.187,$
          143.437,154.687,165.937,177.187,$
          188.437,199.687,210.937,222.187,$
          233.437,244.687,255.937,267.187,$
          278.437,289.687,300.937,312.187,$
          323.437,334.687,345.937,356.875 ]*!pi/180.

ang = ang(0:ncb-1)
```

```
;=====================================================================

; Main shot loop

        openr,lun_shot,shot_file,/get_lun

        shot=0 & date='00-000-0000' & t1=0 & t2=0
        readf,lun_shot,format='(i5,2x,a11,2x,i5,2x,i5)',shot,date,t1,t2

        while (shot ne 0) do begin

          if gain_file then readf,lun_shot,bpgain

          set_db,'mst$data'             ;...setting up MDS
          dummy=set_shot(shot)
          dummy=set_date(date)

;----------------------------------------------------------------------

;    Reading in time array and finding bounds

                                ;...reading in time array
          time  = 0
          time  = temporary(data(tname)*1000.0)
          sizef = n_elements(time)

                                ;...checking for time signal
          if (sizef le 2) then goto,JumpShot

                                ;...calculating time interval for full array
          dt    = (time(sizef-1)-time(0))/(sizef-1)

                                ;...calculating rebin factor
          rebin_factor = fix(1.0/(dt*output_freq)+0.5)>1

                                ;...pickup times
          put1  = -9.5
          put2  = -3.0
                                ;...index for bt pickup
          ns1b  = fix( min(where( time ge put1 ) ) )
          ns2b  = fix( max(where( time le put2 ) ) )

                                ;...index for baseline subtraction
          nb1b=100
          nb2b=600
```

```
                                ;...bounds of signal
          n1b   = fix( min( where( time ge t1 ) ) )
          n2b   = fix( max( where( time le t2 ) ) )

          sizeb = n2b-n1b+1

                                ;...truncating time array
          time  = temporary(time(n1b:n2b))

                                ;...rebinning time array
          sizerb = (sizeb/rebin_factor)*rebin_factor

;----------------------------------------------------------------------

;    Reading in bt at the wall for normalization

                                ;...reading btw from the mds data base
          btw     = data('btw_full')
          btw_tm  = data('btw_full_tm')*1000.

                                ;...checking that arrays are there
          n_btw   = n_elements(btw)<n_elements(btw_tm)
          if (n_btw le 2) then goto,JumpShot

                                ;...rebinning btw to match coil signals
          dt_btw  = (btw_tm(n_btw-1)-btw_tm(0))/(n_btw-1)
          if (dt gt dt_btw) then begin
            rb_btw  = fix(dt/dt_btw+0.5)>1
         btw  = rebin(   btw(0:(n_btw/rb_btw)*rb_btw-1),long(n_btw/rb_btw))
         btw_tm= rebin(btw_tm(0:(n_btw/rb_btw)*rb_btw-1),long(n_btw/rb_btw))
            endif else $
          if (dt lt dt_btw) then begin
            rb_btw  = fix(dt_btw/dt+0.5)>1
            btw     = rebin(   btw(0:n_btw-1),long(n_btw*rb_btw))
            btw_tm  = rebin(btw_tm(0:n_btw-1),long(n_btw*rb_btw))
            endif else $
          if (dt eq dt_btw) then rb_btw=1


                                ;...finding bounds of btw array
          n1btw   = fix( min( where( btw_tm ge t1 ) ) )
          n2btw   = n1btw+sizeb-1

                                ;...finding bounds of pickup
          ns1btw  = fix( min( where( btw_tm ge put1 ) ) )
          ns2btw  = ns1btw + ns2b - ns1b
```

```
;----------------------------------------------------------------------

;    Reading in and converting magnetics

          sign = -1             ;...sign convention for bp data

          bpt=fltarr(sizeb,ncb) ;...initializing bp data array

                                ;...looping  read in and normalization
          for  icb = 0, ncb-1 do begin

                                ;...skip coil if there is no signal
            if (bpgain(icb) eq 0) then goto,SkipCoil

                                ;...reading in bp array
            b = data( bpname(icb) )

                                ;...checking for missing data
            n_vpb = n_elements(b)
            if n_vpb le 1 then goto,SkipCoil

                                ;...checking for saturation
            sat = where( temporary( ( b ge v_sat_hi(icb) ) or $
                                    ( b le v_sat_lo(icb) ) ) )

            b = temporary( b / (sign*bpgain(icb)*av_bparea) )

                                ;...subtracting off data baseline
            b = temporary( b - avg( b( nb1b:nb2b ) ) )

                                ;...calculating pickup of poiloidal coils
            b_pickup = avg(temporary(b( ns1b:ns2b )/btw( ns1btw:ns2btw )))

                                ;...truncating data
            b = temporary( b(n1b:n2b) )

                                ;...subtracting eqillibrium field from coils
            b = temporary( b - b_pickup*btw( n1btw:n2btw ) )

                                ;...renormalizing using stored value
            b = temporary( b / rnm(icb) )

            bpt(*,icb)=b        ;...storing data in data array

                                ;...setting saturated points to zero
```

```
            if (max(sat) ne -1) then bpt(sat,icb)=0.0

            SkipCoil:
            b=0 & sat=0         ;...clearing magnetic data array

            endfor

;----------------------------------------------------------------------

;    Zero mean each time record

          bpequil = fltarr(sizeb)       ;...equillibrium field
          bprms   = fltarr(sizeb)       ;...total rms fluctuation

          weight=fltarr(sizeb)  ;...number of valid coils

                                ;...equillibrium field and rms fluctuation amp
          for i=0,sizeb-1 do begin
            val=where(transpose(bpt(i,*)) ne 0.0)
            if (max(val) ne -1) then begin
              bpequil(i)=avg(bpt(i,val))
              bpt(i,val)=temporary(bpt(i,val)-bpequil(i))
              weight(i)=n_elements(val)/float(ncb)
              bprms(i)=sqrt(1.0*avg(bpt(i,val)^2))
              endif
            val=0
            endfor

;----------------------------------------------------------------------

;    Performing spatial Fourier transform on magnetics

          vtt

          print,"Shot "+strtrim(shot,2)+" on "+date+" from "+strtrim(t1,2)+$
            " to "+strtrim(t2,2)+", processing."

          for i_n = 0, n_n-1 do begin           ;...loop through selected n

                                  ;...calculating cos and sin amp
            cos_amp = temporary((2.0/ncb)*bpt#cos(n(i_n)*ang))
            sin_amp = temporary((2.0/ncb)*bpt#sin(n(i_n)*ang))

            cos_amp(where(weight))=$
               cos_amp(where(weight))/weight(where(weight))
            sin_amp(where(weight))=$
```

```
     sin_amp(where(weight))/weight(where(weight))

  print,"    Writing MODES_"+strtrim(n(i_n),2)+"_COS"
  cos_amp = $
    temporary(rebin(cos_amp(0:sizerb-1),sizerb/rebin_factor))
  nw=put_data('M.MODES_'+strtrim(n(i_n),2)+'_COS',cos_amp,'gauss')
  print,"    Writing MODES_"+strtrim(n(i_n),2)+"_SIN"
  sin_amp = $
     temporary(rebin(sin_amp(0:sizerb-1),sizerb/rebin_factor))
  nw=put_data('M.MODES_'+strtrim(n(i_n),2)+'_SIN',sin_amp,'gauss')

  if (plot_vel and (n(i_n) eq 6)) then begin

    amp =  cos_amp^2 + sin_amp^2      ;...mode amplitude

                                      ;...derivatives of sin and cos
    cos_dot = deriv_5pt( cos_amp, dt )
    sin_dot = deriv_5pt( sin_amp, dt )
                                      ;...mode frequency calculation
    frq = (sin_dot*cos_amp-sin_amp*cos_dot)/(amp*2*!pi)

    endif

  endfor

                        ;...writing equillibrium to database
print,"    Writing MODES_EQUL"
bpequil = temporary(rebin(bpequil(0:sizerb-1),sizerb/rebin_factor))
nw=put_data('M.MODES_EQUL',bpequil,'gauss')

                        ;..writing rms amplitudes to database
print,"    Writing MODES_RMS"
bprms = temporary(rebin(bprms(0:sizerb-1),sizerb/rebin_factor))
nw=put_data('M.MODES_RMS',bprms,'gauss')

                        ;...writing time array to database
print,"    Writing MODES_TIME"
time = temporary(rebin(time(0:sizerb-1),sizerb/rebin_factor))
nw=put_data('M.MODES_TIME',time/1000.0,'seconds')

if plot_vel then $
  plot,thinn(time,10),thinn(frq,10),xtitle='time (ms)',$
    ytitle='frequency (kHz)',$
    title='n=6 Mode Frequency: Shot '+strtrim(get_shot(1),2)+$
    ', '+get_date(1),xrange=[t1,t2],xstyle=1,yrange=[-30,30]
```

```
;-----------------------------------------------------------------------

;   End of shot loop.

       JumpShot:

       shot=0 & date='00-000-0000' & t1=0 & t2=0
       readf,lun_shot,format='(i5,2x,a11,2x,i5,2x,i5)',shot,date,t1,t2

       endwhile

     free_lun,lun_shot

;-----------------------------------------------------------------------

; End of processing session.

;   Clearing remaining arrays.
      gbp=0 & ang=0 & bpname=0

;   Saying goodbye.
      print,"Goodbye."
      EndRoutine:

      end

;=======================================================================
```